University of Alberta

A Crack Detection Technique
Using Piezoelectric Actuator/Sensor Systems

By

Guoliang Huang

©

A thesis submitted to the Faculty of Graduate Studies and Research in partial
fufillment of the requirements for the degree of **Doctor of Philosophy**

Department of Mechnical Engineering

Edmonton, Alberta
Spring 2004

Canadä

Abstract

For new and aging engineering structures in aerospace and marine industries, implementation of an effective health monitoring system can replace the schedule-based inspection/maintenance of structures by condition-based maintenance. This thesis is focused on the systematic investigation of a structural health monitoring technique for quantitatively identifying embedded cracks in structures. A piezoelectric actuator/sensor system is used to generate high-frequency elastic wave propagation and a reverse wave technique is developed to locate the damage's position, shape and dimension using the obtained sensor signals.

A theoretical model of piezoelectric actuators surface-bonded to and/or embedded in structures is adopted and developed to describe their electromechanical behavior, and the outgoing wave propagation in the host structure is analytically obtained to understand the effects of the different parameters of the actuator upon the resulting wave field. For a surface bonded actuator, only the deformation along the longitudinal direction is considered due to the free surface. However, for an embedded actuator, a model involving the deformation in both the transverse and longitudinal directions of the actuators is developed. The single actuator solution is then implemented into the Pseudo-Incident Wave (PsIW) method to study the wave propagation induced by multiple actuators. When the outgoing wave reaches the surface of existing damages, the scattering wave propagation will be generated, which is recorded as sensor signals. A one-dimensional sensor model is then used, from which received strain field can be determined by using voltage output of the sensor.

The second part of this thesis is to develop a new and innovative technique to interpret the obtained sensor signals to quantitatively locate the cracks in the structures. A reverse wave technique is developed to form the image of the cracks by "moving"

the recorded sensor signals to their actual spatial locations. To achieve this, the obtained wave signals are used as boundary conditions to induce reversed elastic wave propagation, from which the sizes, shapes and positions of existing cracks can be determined through the developed imaging technique for both the harmonic wave and transient wave cases. The main advantage of this technique is that complicated mode conversion phenomena caused by the crack reflection and wave propagation distortions in the medium are corrected by the back propagation operation, which made this method favorable for detection of multiple cracks of various shapes.

Acknowledgements

I would like to first express my most sincere and deepest gratitude to Dr. Xiaodong Wang, my supervisor, without whose guidance and support I could not have completed this thesis. He taught me several knowledge in this field and gave me many advice and insightful discussions. I am indebted to him for sharing countless hours of time.

The Dissertation Scholarship, Andrew Stewart Memorial Graduate Prize and ASME OMAE Calgary Chapter Graduate Scholarship, which are awarded to me, are thankful for the successful completion of this study.

Finally, I am grateful to my wife, Hong Hu, for her patience, love and understanding which make it possible to complete this work today.

Table of Contents

List of Figures

Chapter 1

Introduction

1.1 Background

Integrity of critical engineering structures such as large-scale space structures, aircraft, satellites, nuclear reactors, etc., needs to be monitored constantly to prevent catastrophic and expensive failure. In order to respond to any possible damage leading to failure of the structures, damages should be detected, evaluated, if possible monitored, even though the structures might be in services. Traditional nondestructive testing/evaluation (NDT/NDE) techniques, such as X-radiographic detection (X-ray) and hydro-ultrasonics (C-scan), are impractical for in service inspection of large structures because these techniques usually are based on laboratory testing and require bulky instruments (Thomas, 1995; Chang, 1995; Giurgiutiu and Zagrai, 2002; Giurgiutiu et al., 2002a,b; Kessler, et al., 2002a,b). Especially for some structures such as aerospace vehicles and buried pipeline, the health monitoring system requires to perform on in-service structures in isolated environments without manual interference. The replacement of our present-day manual inspection with automatic health monitoring would substantially reduce the associated life cycle costs. Hence, there is a need for reliable structural health monitoring (SHM) system that can automatically process data, assess structural condition, and find information of the embedded

1

damages. Motivated by this need, significant efforts of integrating monitoring components such as sensors and actuators to form a SHM system, either surface mounted or embedded into the structures, have been made to monitor adverse "change" to detect incipient damage before catastrophic failure occurs (Boller, 1998,2000). Currently, efforts are focussed on: (1) the development of specialized health monitoring actuators and sensors; and (2) the construction of automated health monitoring systems.

Among the available options for online structural health monitoring systems, piezoelectric sensors offer special opportunities for developing sensor arrays for SHM system, because they are quick in response, with high linearity, small, inexpensive and easily wired into sensor arrays. A SHM system with built in piezoelectric sensors, which is usually called smart SHM system, has attracted much attention due to their low cost in the past decade (Hickman et al., 1991; Tzou et al., 1991; Gandhi and Thompson, 1992; Ha et al., 1992; Kudva et al., 1993; Varadan et al., 1993; Ashley, 1995; Charles et al., 1995; Ayres et al., 1996; Wu, 1999; Koh et al., 2001; Maalej et al., 2002; Mall, 2002). Besides sensors, piezoelectric actuators, whose function is to excite diagnostic signals, can also be integrated into the structures to build an active SHM system. Comparing with conventional passive SHM system (without built in actuators), which can only tell what happened to the structure, i.e. load and strain history, the active SHM system is able to interrogate the structure and find out "how it feels", i.e. the state of its health. Moreover, a major advantage of the active SHM over a passive one is that the active SHM system is subjected to a prescribed actuation and thus increases the possibility of deducing the structure status from the collected sensor data by choosing suitable monitoring system signals. Implementation of such an active SHM system can replace the schedule-based inspection/maintenance of a structure by condition-based maintenance (Mal, 2001; Duune et al., 2001).

A primary issue in constructing an active SHM system is to choose suitable monitoring signals. In general, any wave field such as mechanical (waves in fluids and

2

solids), electromagnetic (electric currents, radar, X-rays) or quantum mechanical (particle beams) fields could be used to monitor the structural health. Each type of wave field has its advantages and disadvantages for inspection and a choice should be made on the basis of the required precautions for the inspection technique, its sensitivity for the relevant material and/or geometrical parameters, and on the ease of operation. Elastic waves in structures, which are sensitive to the change of the geometry and the material parameter, can propagate over long distances and have been considered as a principal candidate of potential signals in the active SHM system (Biemans, 1999; Gobin et al., 2000; Mast, 2001; Dalton et al., 2001; Bakker, 2003). Elastic wave based testing can potentially detect varies of damages such as corrosion, delamination and cracks not only on the surface but also inside the structures. However, the difficulties of applying ultrasonic elastic wave based monitoring lie on that the signals are not instinctually interpretable due to their dispersive characteristics and complicated mode conversion phenomena due to wave reflection (Fu, 1987; Alleyne and Cawley, 1992a,b; Datta and Kishore, 1996; Anchenbach, 2002). This difficulty is further augmented due to the interaction between host structures and incorporated piezoelectric actuators/sensors and complicated electromechanical behaviour in a smart SHM. Many investigations have been conducted in the field of active smart SHM and these researches could be divided into three major categories:

(a) Modelling piezoelectric actuators/sensors in structures to analyze complicated dynamic electromechanical behaviour;

(b) Integrating and optimizing piezoelectric actuators/sensors for desired wave propagation and wave reception;

(c) Developing robust diagnosis algorithm to extract health status information from the received sensor signals.

3

1.2 Elastic wave generation and reception

Traditional technique of generating and receiving elastic waves for structural health monitoring begun in the 1950s (Kino et al., 1980; Pao, 1983; Bar-Cohen, 2000; Bar-Cohen and Lih, 2000). The elastic wave based testing usually requires two transducers as a transmitter and a receiver separately, or just one that functions as both transmitter and receiver, depending on whether the testing scheme is pitch-catch or pulse-echo configuration. In most cases the wave transducers are made of piezoelectric materials, which are capable of generating large strains under electric loads and have excellent dynamic response characteristics. Wu and Gong (1993) employed steel ball impact to generate a transient elastic wave and identified a void or inclusion in plate structures by the measured elastic wave signals using conical transducers. In some acoustic emission studies, lead break was used to emulate the source of elastic waves (Gorman and Prosser, 1996; Hsu et al., 1997). In the past decade, Electro-magetic acoustic transducers (EMATs) and optical fiber sensors were also used to generate and receive elastic waves respectively (Guo et al., 1997). Especially, studies of laser based ultrasonic elastic wave testing are growing rapidly. Unlike other conventional methods, laser based ultrasonic testing does not require couplant or immersion of the specimen in liquids and provides a method to realize non-contact ultrasonic testing (Kromine et al., 2000; Sohn et al., 2001). However, one of the disadvantages of the above ultrasonic wave based NDT technique is that a test is usually executed point by point, thus is time consuming and not suitable for in-service testing.

Recently, many researchers have studied the technique of generating and collecting diagnostic elastic waves using bonded piezoelectric actuators/sensors and thus realizing continuous monitoring of the structural integrity. Piezoelectric materials used are in several forms such as piezoceramics (PZT), piezopolymers, piezoelectric fibers, piezoelectric films, and so on. In Tracy and Chang's study (1998), distributed

4

piezoelectric ceramic disks were surface mounted on a composite structure to generate and receive the diagnostic signals for impact damage detection. The experimental results showed very promising features of integrated actuators/sensors technique for structural health monitoring purposes. Surface bonded piezoelectric ceramics was also used to generate different modes of Lamb waves for damage detection (Lin and Yuan, 2000, 2001a,b). Comparing with piezoelectric ceramics, piezoelectric polymer film has higher dielectric voltage constants and is recognized as better sensor material. It is also flexible and could be easily cut into any shape to fit a complex structural shape. Polyvinylidene Fluoride (PVDF) was bonded on the specimen to excite Lamb waves (Monkhouse et al., 1997). Their experimental results showed that Lamb waves ranging from 0.5 to 4MHz could be efficiently generated. In this design, interdigital electrode patterns on the PVDF substrate were controllable for generating desirable Lamb mode shapes to suppress the dispersive effect, which has been a major barrier to the interpretation of Lamb wave signals. Selecting interdigital electrode pattern to generate desired flexible and longitudinal waves was also studied by Moetakef's group (Moetakef, 1996). In this study, the phased array of piezoelectric transducers combines the functions of several conventional transducers in a single casing. The problem was modelled by finite element method and a comparison was provided with the experimental results. Piezoelectric sensors and actuators may also be embedded inside structures rather than mounted on the surface (Moulin et al., 1999). In the work by Moulin and his colleagues, a piezoelectric element was embedded into a carbon-epoxy composite plate and acted as an actuator to generate elastic waves. The displacement wave field on the plate surface was predicted by a hybrid finite element-normal mode expansion method and the wave was verified experimentally by an optical measurement.

5

1.3 Modelling piezoelectric actuators and sensors

Building a model for the structures integrated with piezoelectric actuators and sensors to understand their electromechanical dynamic behaviour and simulate their resulting wave propagation is a prerequisite for achieving the goal of damage identification. Piezoelectric materials attached to or embedded in structures may largely influence structural behaviour. The efficiency of actuation and sensing is related to not only the material properties of piezoelectric materials but also those of the host structure and the applied loading frequency. The most important parameters should be identified and analyzed to qualify the proposed actuators/sensors technology (Im and Atluri, 1989; Crawley, 1994; Aldraihem and Khdeir, 2000). Due to the presence of the materials discontinuity between the actuators/sensors and the host structure, a complicated stress field is generated, especially for the position near the edges of the actuators/sensors, where stress concentration will occur. For example, the induced stress concentration near the ends of an actuator may result in undesired peeling-off of the actuator from the host structure, which may result in a reduction of the load transfer capability of the structure, and hence the actuator may lose its ability to perform its role. An accurate assessment of the coupled electromechanical behaviour of piezoelectric structures would, therefore, necessitate the detailed study of the load transfer between the piezoelectric actuators/sensors and the host structure for ensuring the efficiency of actuation and sensing.

To avoid the difficulties associated with the complicated interfaces between the actuators and the host medium, some simplified actuator models have been used to simulate the actuation process of embedded and surface-bonded thin sheet actuators. The pin-force model was first developed for a cantilever beam with a layer of PVDF bonded on one side only (Bailey and Hubbard, 1985). The modelling was based on a force equilibrium between the actuator and the beam. A constant actuator force output proportional to the applied voltage was obtained. A more extensive model was

6

later proposed by Crawley and de Luis (1987) to analyze a beam-like structure with surface bonded and embedded thin sheet piezoelectric actuators to study the load transfer between the actuators and the host beam. In this analysis, the axial stress in the actuator was assumed to be uniform across its thickness and the host structure was treated as a Bernoulli-Euler beam. This model was further modified using a Bernoulli-Euler model of a piezoelectric actuator by considering the linear strain distribution along its thickness (Crawley and Anderson, 1990). This model was developed for both embedded and surface bonded actuators and is often called the "consistent strain" model. Im and Atluri (1989) modified the actuator model presented by Crawley and de Luis (1987) by considering both the axial and the transverse shear forces in the beam. A refined actuator model based on a second order axial normal stress field was presented for a beam structure with symmetrically surface-bonded actuator patches (Lin and Rogers, 1993a,b). This model was developed using a plane stress formulation and solved by the principle of stationary complementary energy. A model assuming a linear stress variation through the thickness of the actuators and structure was developed by Dimitriadis et al. (1991). In this spherical pure bending model, the equivalent moment to out-of-phase actuation is based on the moment equilibrium about the neutral axis. Richard and Cudney (1993) presented an analytical model for multiple layer piezoelectric actuators in which Timoshenko's beam theory led to equations of motion for lateral vibration that included rotary inertia and shear deformation effects. Twist, shear and torsion can be generated for the piezoelectric actuator applied to an anisotropic composite structure. A integrated theory was used to model the bending/twisting/shearing actuation of laminated beams (Lee and Sun, 1994).

Plate and shell models have also been extensively used in modelling the piezoelectric structures. A consistent plate model was developed by Crawley and Lazarus (1991). This model is a simple extension from the one-dimensional beam model to

7

the two-dimensional plate model. Lee and Moon (1989) applied the classical laminate plate theory to the design of piezoelectric laminate for bending and torsion modal control. Wang and Rogers (1991) modified the classical laminated plate theory to model actuator-induced bending and extension of laminated plates under static loading. This work provided a theoretical basis of general application of induced strain actuators. The vibration control of a simply supported rectangular plate was studied by Batra and Liang (1996). Thin layers of PZT ceramic were attached to the top and bottom of the rectangular plate, which was assumed to be vibrated at a frequency close to one of its natural frequencies, to achieve the control. For structures with curvatures such as rings and shells, analytical models based on layered shell theory have been proposed to consider the coupling between the in-plane and out-of-plane displacements. An analytical model for multi-layered thin shells with distributed piezoelectric actuators was proposed by Tzou and Gadre (1989). In this work, the theoretical development is based on Love's thin shell theory in which the transverse shear deformation and the rotary inertia are neglected, and the governing equations are established based on Hamilton's principle. An analytical model for thick composite piezoelectric shells was proposed by Tzou and Zhong (1993). Other typical examples for modelling piezoelectric actuators include the works by Hagood et al. (1990); Tauchert (1992); Mitchell and Reddy (1995); Bank and Smith (1995, 1996); Han and Lee (1998); Reddy (1997, 1999); Zhou et al. (2000); Yang and Ngol (1999); Wang and Huang (2000); Benjeddou et al., (2000); Wang and Shen (2001); Wang and Quek (2002); Ryu and Wang (2002). For more complex structures, analytical modelling becomes strenuous, and numerical methods, such as finite element analysis, should be considered to resolve such problems. A finite element model based on the theory of elasticity and the Maxwell's electrical theory of piezoelectrics has been developed by Ha et al. (1992) using the variational principle. Tzou and Ye (1994) developed a three dimensional thin hexahedron piezothermoelastic element for general

8

treatment of piezoelectric systems and their deformation control.

Many researchers have used piezoelectric sheet elements as sensors in active controllable systems (Lee and Moon, 1991; Qui and Tani, 1995; Hoummady et al., 1997; Lim et al., 1999) and in structural health monitoring systems (Samuel and Pines,1997; Chiu, 1997,2000; Wang and Chen, 2000; Giurgiutiu et al, 2000), since such piezoelectric sensors have advantages such as compactness, sensitivity over a large strain bandwidth in the monitored structure. PVDF films were used by Hubbard (1991) for the application to vibration control of beam structures as sensors. Wang (1996) used a PZT wafer to excite a structure and an array of PVDF film sensors to pick up the forced vibration response to generate the different mode shapes through multi-point signal precessing. Lee and Moon (1989) developed PVDF film with special shapes, modal sensors, to sense specific vibration models. The experimental results agreed quite well with the theoretical predictions. Lee and Osullivan (1991) studied various types of generalized piezoelectric strain rate sensors by combining the effective surface electrode and appropriate skew angle.

In contrast to the study of the global response of the piezoelectric structures, much less attention has been paid to the local wave field around sensors and actuators, especially the behaviour of the resulting wave propagation. Wang and Meguid (2000) developed a one-dimensional actuator model to examine the coupled electromechanical behaviour of a thin piezoceramic actuator embedded in or bonded to an elastic medium under in-plane mechanical and electrical loadings, in which the dynamic load transfer and the local stress field around the actuator are studied. In this thesis, this model is used to consider the static coupled electromechanical behaviour of a piezoelectric actuator bonded to an orthotropic elastic medium. The effects of the geometry, the material mismatch, the material anisotropy and interfacial debonding upon the load transfer between the actuator and the host structure

9

are determined and discussed. The dynamic actuator model is further used and modified to consider dynamic electromechanical behaviour of actuators surface-bonded to and/or embedded in an isotropic elastic medium. The wave propagation generated by surface-bonded and embedded piezoelectric actuators is then analytically studied. The interaction between actuators is simulated by using newly developed Pseudo-Incident Wave method. The numerical simulation conducted indicates the effects of the geometry of the actuators, the material combination and the loading frequency upon the resulting wave propagation. The basic properties of the wave field is demonstrated by the analytical solution of the wave field far away from the actuators.

In most of the sensor models used, the coupling between the sensors and the host structures have not been properly studied in detail. Especially, the effect of this coupling upon sensor signals has not received much attention. It should be mentioned that the sensitivity and fidelity of piezoelectric sensors are central to the function of a smart structure as they are used for the structural health monitoring. Recently, Sirohi and Chopra (2000) investigated the behavior of piezoelectric PZT and PVDF as strain sensors surface-bonded to a beam structure. In this study, correction factors to account for sensor-structure interaction effects were analytically derived and experimentally validated over a low frequency range of 5-500Hz. Dynamic mechanoelectrical (sensing) behaviour of embedded piezoelectric sensors was also studied by using finite element method (FEM) for frequencies up to 5KHz (Varadan et al., 1997). By the use of dynamic piezoelectric theory and Mindlin plate theory for flexural wave propagation, the study of piezoelectric sensor for detecting flexural waves was conducted to show the sensitivity of bonded sensors (Veidt et al., 2001). It was demonstrated that for high frequency cases a dynamical piezoelectric sensor model should be used to consider dynamic sensing effects.

10

1.4 Damage Identification

After obtaining the sensor signals, the most important and the most difficult issue is the interpretation of the sensor signals for identifying the embedded damages. Damage identification algorithm is dependent on the process of generation and reception of elastic waves. Preliminary method of interpreting ultrasonic signals is to compare some characteristic parameters between virgin and damaged structures and draw conclusions based on the comparison (Ludwig and Lord, 1988; Schulz et al., 1999). These parameters to be used for interpretation could be wave speed, arrival time, amplitude, attenuation, mechanical impedance, etc., either in time domain or in frequency domain. With a series of advancements related to material science and other inter-disciplinary fields, different diagnosis algorithms are developed, which cover a wide range from conventional techniques, such as modal analysis and optimization, to artificial neural network (ANN), etc. (Tracy et al., 1996). Modal analysis is the most common technique principally because it is simple to implement on any size structure using vibration characteristics of the structure as an indication of structural damage (Pearson et al., 2001). Changes in normal modes can be correlated with loss of stiffness in a structure, and usually analytical models or response history tables are used to predict the corresponding information of damage. However, some damages are too small to affect the global dynamics and hence cannot be readily detected by conventional low-frequency vibration methods. ANN is a typical technique for classifying the obtained monitoring information and near real-time diagnosis could be realized once the network has been well trained. With the help of contemporary computation power, the data required to train the neural network could be obtained from numerical simulation, which could save extensive labor of acquiring large amount of experimental data (Takadoya et al., 1992; Okafor et al., 1996). This method seems to be highly promising for handling a large number of sensor signals. The time of flight technique (TOFT) is one of the successful interpretation techniques to locate

11

the position of a crack by using the travel time of waves in the received data directly (Carino et al., 1986; Lorenz et al, 1991; Capineri et al., 1995; De Hoop, 1995). To use the received data more efficiently, an extended technique from the conventional time of flight, multi-path time of flight technique (MTOFT), which considers multiple wave reflection, is recently developed to characterize surface breaking crack in a plate structure (Bakker et al., 2003).

With the development of smart materials and adaptive structures, some authors have tried to locate the damage using obtained piezoelectric sensor signals to form different in service structural health monitoring systems because of their advantages in low costs, continuous monitoring ability and comparatively high frequency excitations induced by piezoelectric actuators (Boller, 1998). Significant progress has been made in the development of smart structure for aerospace application. Keilers and Chang (1995a, b) used piezoelectrics built into laminated structures to detect a delamination. In this study, they set up a numerical beam model and employed it with measured voltage frequency response function (FRF) from an attached sensor to identify the delamination location. Banks et al. (1995) put forward an optimization model for a cantilever beam based on a least-square error minimization procedure to locate damages using sensor signals in time domain. By combining the above two proposed methods and solving nonlinear optimization programming problems, a two stage identification method using the obtained sensor signals has been proposed to predict damage locations and extents in the composite structure (Fukunga et al., 2001). Acoustic emission (AE) is elastic radiation generated by the rapid release of energy from sources within a material. These elastic waves are detected and converted to voltage signals by small piezoelectric sensors mounted to a convenient surface of the material. By comparing amplitude distribution, the signal arrival time and signal energy at different sensors within the sensor matrix, the actual location of the flaw site can be defined (Nam et al., 1999; Park et al., 2000). This

12

technique is sensitive enough to detect newly formed crack surfaces down to a few hundred micrometers and less. The electro-mechanical (E/M) impedance method for structural health monitoring is a new technology utilizing the emitter-detector properties of active material sensors and the structural mechanical impedance (Rogers and Giurgiutiu, 1997). The method has been shown to be especially effective at ultrasonic frequencies, which properly capture the changes in local dynamics due to incipient structural damage. With an array of surface bonded PZT or PVDF sensor, the detection of disbond under a repair patch was also successfully conducted by using this method (Koh et al., 2001). Lamb wave techniques may prove suitable for structural health monitoring applications since they are able to travel long distances in plates and laminated structures, can be applied with low power, conformable piezoelectric actuators and sensors, and can provide useful information about the state of a structure during operation. The piezoceramics used for this method could also be used as multipurpose actuators or sensors by simply changing the driving frequency. The most successful work using Lamb waves for damage detection has been performed by Cawley's group (Monkhouse et al., 1997). Utilizing interdigital PVDF transducers to generate highly focused and directional waves without higher-mode interference, they have inspected various metallic specimens with encouraging results. The use of embedded piezoelectric wafer active sensors for in situ structural health monitoring of thin wall structure was recently studied by Giurgiutiu's group (2002a,b). Based on their study, the developed electro-mechanical impedance method is suitable for near field damage detection, while guided ultrasonic Lamb waves in conjunction with the pulse-echo technique are suitable for far field damage detection. These above mentioned methods are suitable for certain types of damages in some degrees, however, they usually can recognize only the existence of the damages and very limited quantitative information about the damages could be obtained.

Recently, to establish the quantitative relation between the received sensor signals

13

and unknown damages in materials, efforts have been made to propagate the received scattering waves back to the damages, thus to realize quantitative damage identification, since the scattering waves contain information of the embedded damages (Anchenbach, 2000). One technique is using a sensor array to focus ultrasonic waves at a specific point inside the material for damage identification. Focussing is achieved by controlling the relative time delay between sensor elements. Fink (1992,1993) provided a detailed review on different focussing techniques, especially the usage of time reversed focussing technique in solids. Similar concept has also been used by Deutsch, et al. (1997) in surface crack detection using self-focussing of Lamb waves. In their study, a cross correlation technique is used to determine the time-of-flight differences of back-scattered signals received by elements of a sensor array. The determined time difference was then used to adjust the signals sent out by the sensor array to focus on position of the defect, which is determined by the observation of the maximum amplitude of the back propagated displacement and stress components. Among these methods, the reverse wave method is specifically interesting, which uses the reversed scattering wave in conjunction with an imaging algorithm and can predict distributed damages.

1.5   Reverse wave method

Since the equations for elastic wave propagation only contain second-order time derivatives, the elastic waves have the invariant properties under time reversal, and can ultimately converge at the original source just as if time was going backwards. The main advantage of this method is that wave distortions caused by the geometries of cracks and wave propagation in the medium are corrected by the back propagation operation, which made this method favorable for detection of multiple cracks of various shapes. This method also has limits: it was developed for homogeneous structure applications and focuses on crack detection by using scattering wave propagation.

14

Migration technique, which conducted the reverse wave propagation by using surface signals, has been developed and widely used in geophysics (Claerout, 1985). Based on the signals recorded by a linear array of geophones (receivers), the image of subsurface reflectors is formed by moving or 'migrating' the recorded wave field to their actual spatial locations. Over the past thirty years, research on the migration technique has attained a maturity and is indispensable as an advanced interpretation method for the reflective wave field (Claerbout, 1976; Schneider, 1978; Kuo and Dai, 1984; Chang and Mcmechan, 1984; Wiggins, 1984; Sun and Mcmechan, 1986; Miller et al., 1987; Berkhout 1987; Esmersoy and Oristaglia, 1988; Wappenaar and Haime, 1990; Docherty, 1991, Zhu and Lines, 1998). Due to the similarity of the data collection method in SHM system and geophysics, the concept of migration technique could be modified and implemented in SHM to process the recorded sensor signals and image damages in structures, although the area under investigation and the range of frequency differs between geophysical prospecting and damage identification. Liu, Tsai and Wu (1997) introduced the migration concept into the NDE of concrete structures. In their study, a surface crack was a priori assumed, thus all the imaging process was simplified to find the first arrival time and converted it into the distance by timing the wave propagation velocity. This technique also was systematically studied recently to interpret Lamb waves for identifying damages in a plate with some success (Chien, 1997; Lin and Yuan, 2000, 2001a,b).

In this thesis, to quantitatively determine information of the embedded cracks in structures using high frequency scattering elastic waves, a reverse elastic wave technique is proposed for homogeneous elastic media. The reversed elastic wave propagation will be obtained by solving an elastodynamic boundary problem for both harmonic wave and transient wave. The corresponding image algorithm is developed to find the information of the embedded cracks. For the case of harmonic wave, an image algorithm is developed by using a cross correlation principle. For the case of

15

transient wave, an imaging algorithm based on longitudinal (P) and transverse (S) waves' travel times is proposed.

1.6 Research objectives and thesis organization

The main objectives of the thesis are to conduct a theoretical study of developing a crack detection technique using bonded piezoelectric actuators/sensors and quantitatively determine the information of embedded cracks using the received sensor signals. A typical crack detection system with an array of surface bonded and/or embedded piezoelectric actuators/sensors is suggested as shown in Figure 1.1. Attached piezoelectric elements act as both actuators and sensors. An electric field is applied to one of the piezoelectric actuators and induces diagnostic elastic wave signals. If the waves encounter the surface of a crack, they will be reflected. When the reflected waves reach the sensors, the strain change sensed will generate a voltage output, which will be recorded as raw monitoring data. In this study, the newly developed actuator and sensor models (Wang and Meguid, 2000) will be used to describe the complicated dynamic electromechanical behaviour, the resulting wave propagation and wave reception. In addition, a reverse wave technique is provided to extract the information of the embedded crack from the obtained sensor signals. In the present thesis, the method is developed for the case of structures with homogeneous isotropic material.

The main content of this study is covered in Chapter 2 through Chapter 7. In Chapter 2, the aim is to use a developed actuator model (Wang and Meguid, 2000) to analyze the general electromechanical behaviour of piezoelectric actuators surface-bonded to anisotropic elastic media. The validity of the actuator model is studied. Typical examples are provided to show the effects of the geometry, the material combination and the material anisotropy upon the load transfer. The study is further

16

extended to treat the interfacial debonding between the actuator and the host structure. To simulate the elastic wave propagation, in Chapters 3 and 4, the developed piezoelectric actuator model (Wang, 2000) is modified to consider the dynamic behaviour of surface bonded and/or embedded piezoelectric actuator. The effects of the different material combinations and the loading frequency upon the resulting wave propagation are investigated. The explicit forms of wave field near the actuator and far away from the actuator are further obtained to show the basic properties of the resulting wave. The wave field induced by multiple actuators is studied by implementing the Pseudo Incident Wave (PsIW) method (Wang and Meguid, 1997). The cumulative results generated by the previous chapters are then used in Chapter 5, which provides a study of elastic wave propagation in a cracked elastic medium induced by an embedded piezoelectric actuator. The main objective is to determine the characteristics of the crack using the information of scattering waves, which can be measured by a sensor system. A reverse wave technique is developed for detecting and imaging multiple cracks in plane elastic media using complete transient surface signals in Chapter 6. The focus of this study is to develop a quantitative understanding of the relation between surface signals and the location and characteristics of embedded cracks. As a continuation of Chapter 6, Chapter 7 focuses on the possibility of using piezoelectric sensor signals to quantitatively detect the cracks. A one-dimensional sensor model is used to determine received strain field from the sensor's voltage output. The feasibility of the proposed crack detection technique has been substantiated by the developed reverse wave technique. Chapter 8 summarizes the contributions and conclusions of this study and proposes some perspective topics for the future research.

17

piezoelectric actuator/sensor system
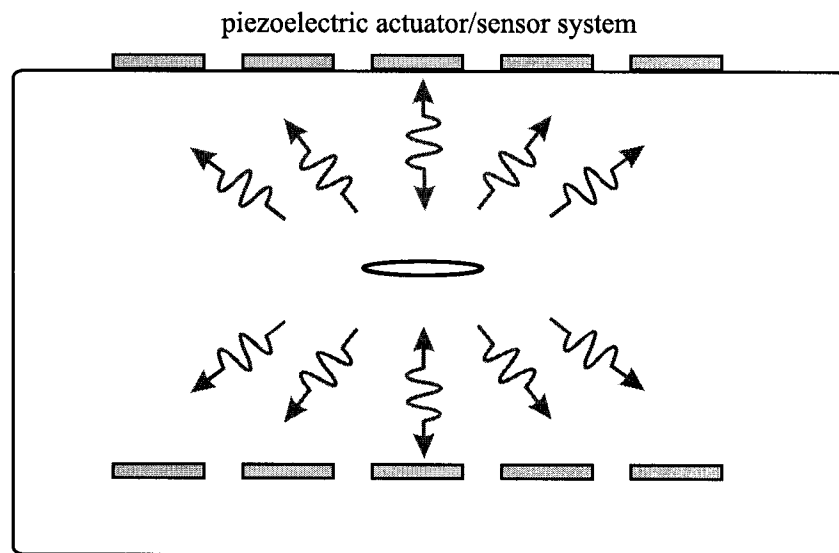
Figure 1.1: An active SHM system

18

Chapter 2

Modelling and Analysis of a Piezoelectric Actuator

In this chapter, we examine the static electromechanical behaviour of a thin piezoceramic actuator surface bonded to an anisotropic elastic medium with a finite thickness under inplane mechanical and electrical loading. Based on the developed one dimensional actuator model (Wang and Meguid, 2000), the actuator is characterized by an electroelastic line model with the poling direction being perpendicular to its length. The purpose of the current work is to study the validity of using this actuator model to simulate the load transfer between actuators and an anisotropic host medium for general cases. The theoretical formulations, governing this electromechanically coupled problem, are derived based upon the use of Fourier transform and solving the resulting singular integral equations in terms of an interfacial shear stress. Typical examples are provided to show the effects of the geometry, the material combination and the material anisotropy of the composite upon the load transfer. The study is further extended to treat the interfacial debonding between the actuator and the host medium.

19

2.1 Formulation of the problem

Consider now the plane strain problem of a piezoceramic actuator bonded to a finite homogeneous anisotropic elastic medium, as illustrated in Figure 2.1. The host medium is assumed to be orthotropic with the principal elastic axes being parallel to y and z axes, respectively. The poling direction of the piezoelectric actuator is assumed to be along the z-axis. The half length, the thickness of the actuator and the thickness of the host medium are denoted as a , h and H, respectively. An electric field E_z is applied along the poling direction of the actuator by applying a voltage $(\triangle V)$ between the upper and the lower electrodes of the actuator, with $E_z = -\triangle V/h$. Because of the piezoelectric property of the piezoceramics, the actuator will deform in both y and z directions and, therefore, induce deformation of the whole structure.

2.1.1 The actuator model

A piezoelectric material produces strains when an electric field is applied, conversely, it generates electric displacement when it is strained. While the former property is used in actuation, the later is used in sensing. The mechanical and electrical properties of the piezoceramic materials can be described as

$$\{\sigma^a\} = [c^a]\{\varepsilon^a\} - [e^a]\{E\}, \quad \{D\} = [e^a]\{\varepsilon^a\} + [\lambda^a]\{E\} \qquad (2.1.1)$$

where

$$\varepsilon^a_{ij} = \frac{1}{2}(u^a_{i,j} + u^a_{j,i}), \quad E_i = -V_{,i}, \quad i,j = x,y,z$$

the superscript $'a'$ represents the actuator, $\{\sigma\}$ and $\{\varepsilon\}$ are the stress and the strain fields, $\{D\}$, $\{E\}$ and V represent the electric displacement, the electric field intensity and the potential, respectively. $[c]$ is a matrix containing the elastic stiffness parameters for a constant electric potential, $[e]$ represents a tensor containing the piezoelectric constants and $[\lambda]$ represents the dielectric constants at a constant strain.

20

The conventional piezoelectric materials are often characterized as a piezoelectric crystal structure with orthotropic structure properties and in-plane isotropy. Thus, Equation (2.1.1), based on the coordinate system used in Figure 2.1, can be expanded as (Park and Sun, 1994)

$$
\left\{
\begin{array}{c}
\sigma_x^a \\
\sigma_y^a \\
\sigma_z^a \\
\sigma_{yz}^a \\
\sigma_{xz}^a \\
\sigma_{xy}^a
\end{array}
\right\}
=
\left[
\begin{array}{cccccc}
c_{11}^a & c_{12}^a & c_{13}^a & 0 & 0 & 0 \\
c_{12}^a & c_{11}^a & c_{13}^a & 0 & 0 & 0 \\
c_{13}^a & c_{13}^a & c_{33}^a & 0 & 0 & 0 \\
0 & 0 & 0 & c_{44}^a & 0 & 0 \\
0 & 0 & 0 & 0 & c_{44}^a & 0 \\
0 & 0 & 0 & 0 & 0 & c_{55}^a
\end{array}
\right]
\left\{
\begin{array}{c}
\varepsilon_x^a \\
\varepsilon_y^a \\
\varepsilon_z^a \\
2\varepsilon_{yz}^a \\
2\varepsilon_{xz}^a \\
2\varepsilon_{xy}^a
\end{array}
\right\}
-
\left[
\begin{array}{ccc}
0 & 0 & e_{31}^a \\
0 & 0 & e_{31}^a \\
0 & 0 & e_{33}^a \\
0 & e_{15}^a & 0 \\
e_{15}^a & 0 & 0 \\
0 & 0 & 0
\end{array}
\right]
\left\{
\begin{array}{c}
E_x \\
E_y \\
E_z
\end{array}
\right\}
$$

(2.1.2)

and

$$
\left\{
\begin{array}{c}
D_x \\
D_y \\
D_z
\end{array}
\right\}
=
\left[
\begin{array}{ccc}
0 & 0 & e_{31}^a \\
0 & 0 & e_{31}^a \\
0 & 0 & e_{33}^a \\
0 & e_{15}^a & 0 \\
e_{15}^a & 0 & 0 \\
0 & 0 & 0
\end{array}
\right]^T
\left\{
\begin{array}{c}
\varepsilon_x^a \\
\varepsilon_y^a \\
\varepsilon_z^a \\
2\varepsilon_{yz}^a \\
2\varepsilon_{xz}^a \\
2\varepsilon_{xy}^a
\end{array}
\right\}
+
\left[
\begin{array}{ccc}
\lambda_{11}^a & 0 & 0 \\
0 & \lambda_{22}^a & 0 \\
0 & 0 & \lambda_{33}^a
\end{array}
\right]
\left\{
\begin{array}{c}
E_x \\
E_y \\
E_z
\end{array}
\right\}
$$

(2.1.3)

where $c_{55}^a = \dfrac{c_{11}^a - c_{12}^a}{2}$, superscript 'T' denotes the transpose of the matrix.

Because of the finite thickness and length of the actuator, determining local stress field using analytical solutions of the original problem may not be feasible. For a thin piezoelectric actuator, for which the thickness is very small compared with its length, the applied electric field will mainly result in an axial deformation. The axial stress and displacement can then be assumed to be uniform across the thickness of the actuator and the interfacial shear stress (τ) transferred between the actuator and the host medium can be replaced by a distributed body force along the actuator. Accordingly, the actuator can be modelled as an electroelastic line subjected to the applied electric field and the distributed axial force, τ, as shown in Figure 2.2. The transverse stress is assumed to be $\sigma_z^a = 0$ due to the free surface of the actuator. For

21

the plane strain problem with $\varepsilon_x^a = 0$, the relation between the stress, the strain and the electric field of this actuator can be obtained by using the constitutive Equations (2.1.2) and (2.1.3) as (Wang and Meguid, 2000)

$$\sigma_y^a = E_a \varepsilon_y^a - e_a E_z \tag{2.1.4}$$

$$D_z = e_a \varepsilon_y^a + \lambda_a E_z \tag{2.1.5}$$

where

$$\begin{aligned} E_a &= c_{11}^a - \frac{(c_{13}^a)^2}{c_{33}^a} \quad plane\ strain \\ e_a &= e_{13}^a - e_{33}^a \frac{c_{13}^a}{c_{33}^a} \quad plane\ strain \\ \lambda_a &= \lambda_{33}^a + \frac{(e_{33}^a)^2}{c_{33}^a} \quad plane\ strain \end{aligned} \tag{2.1.6}$$

are effective material constants.

According to this one dimensional actuator model, by using the equilibrium condition,

$$\frac{d\sigma_y^a(y)}{dy} + \frac{\tau(y)}{h} = 0 \tag{2.1.7}$$

and the traction free conditions at the ends of the actuator,

$$\sigma_y^a(y) = 0, \quad |y| = a \tag{2.1.8}$$

the axial stress in the actuator can be expressed in terms of the shear stress τ as

$$\sigma_y^a(y) = -\int_{-a}^y \frac{\tau(\xi)}{h} d\xi \tag{2.1.9}$$

with

$$\int_{-a}^a \tau(\xi) d\xi = 0 \tag{2.1.10}$$

The resulting axial strain can then be expressed in terms of τ by substituting Equation (2.1.9) into (2.1.4) as

$$\varepsilon_y^a(y) = -\frac{1}{E_a h} \int_{-a}^y \tau(\xi) d\xi + \frac{e_a}{E_a} E_z, \quad |y| < a \tag{2.1.11}$$

22

2.1.2 Elastic medium deformation

Consider now the deformation of the host orthotropic elastic medium with the principal elastic axes being parallel to y and z axes. The host medium will be deformed by the piezoelectric actuator through the interfacial shear stress at $z = 0$. For a plane problem, the constitutive equation is as follows

$$\begin{Bmatrix} \sigma_y \\ \sigma_z \\ \sigma_{yz} \end{Bmatrix} = \begin{bmatrix} c_{11} & c_{12} & 0 \\ c_{12} & c_{22} & 0 \\ 0 & 0 & c_{33} \end{bmatrix} \begin{Bmatrix} \varepsilon_y \\ \varepsilon_z \\ \varepsilon_{yz} \end{Bmatrix} \tag{2.1.12}$$

Using the strain-displacement relation and substituting the constitutive relation into the equilibrium equations give

$$c_{11} \frac{\partial^2 u_y}{\partial y^2} + c_{22} \frac{\partial^2 u_y}{\partial z^2} + (c_{12} + c_{33}) \frac{\partial^2 u_z}{\partial y \partial z} = 0 \tag{2.1.13}$$

$$c_{33} \frac{\partial^2 u_z}{\partial y^2} + c_{22} \frac{\partial^2 u_z}{\partial z^2} + (c_{12} + c_{33}) \frac{\partial^2 u_y}{\partial y \partial z} = 0 \tag{2.1.14}$$

where u_z and u_y represent the displacement components along z and y directions. Applying Fourier transform with respect to y defined by

$$\bar{u}_y(s, z) = \frac{1}{2\pi} \int_{-\infty}^{\infty} u_y(y, z) e^{isy} dy, \quad u_y(y, z) = \int_{-\infty}^{\infty} \bar{u}_y(s, z) e^{-isy} ds \tag{2.1.15}$$

$$\bar{u}_z(s, z) = \frac{1}{2\pi} \int_{-\infty}^{\infty} u_z(y, z) e^{isy} dy, \quad u_z(y, z) = \int_{-\infty}^{\infty} \bar{u}_z(s, z) e^{-isy} ds \tag{2.1.16}$$

the equilibrium equations in the Fourier transform domain can be expressed as

$$c_{33} \frac{\partial^2 \bar{u}_y}{\partial z^2} - c_{11} s^2 \bar{u}_y - is(c_{12} + c_{33}) \frac{\partial \bar{u}_z}{\partial z} = 0 \tag{2.1.17}$$

$$c_{22} \frac{\partial^2 \bar{u}_z}{\partial z^2} - c_{33} s^2 \bar{u}_z - is(c_{12} + c_{33}) \frac{\partial \bar{u}_y}{\partial z} = 0 \tag{2.1.18}$$

From these equations, the general solution in Fourier transform domain can be obtained as

$$\bar{u}_y = \begin{cases} G_1^+ e^{-z_1} + H_1^+ e^{-z_2} + G_2^+ e^{z_1} + H_2^+ e^{z_2} & c_{33} < \frac{1}{2}(\sqrt{c_{11}c_{22}} - c_{12}) \\ (G_1 + H_1 z_0)e^{-z_0} + (G_2 + H_2 z_0)e^{z_0} & c_{33} = \frac{1}{2}(\sqrt{c_{11}c_{22}} - c_{12}) \\ (G_1^- \cos z_4 + H_1^- \sin z_4)e^{-z_3} & \\ + (G_2^- \cos z_4 + H_2^- \sin z_4)e^{z_3} & c_{33} > \frac{1}{2}(\sqrt{c_{11}c_{22}} - c_{12}) \end{cases} \tag{2.1.19}$$

23

and

$$\overline{u}_z = \frac{1}{ic_{33}(c_{12}+c_{33})s^3}\{c_{22}c_{33}\frac{\partial^3\overline{u}_y}{\partial z^3} - s^2[c_{11}c_{22} - (c_{12}+c_{33})^2]\frac{\partial\overline{u}_y}{\partial z}\} \qquad (2.1.20)$$

It should be noted that an isotropic medium will satisfy the relation $c_{33} = \frac{1}{2}(\sqrt{c_{11}c_{22}} - c_{12})$. In above equations,

$$z_0 = \beta_0|s|z, z_1 = \beta_1|s|z, z_2 = \beta_2|s|z, z_3 = \beta_3|s|z, z_4 = \beta_4|s|z$$

$$\beta_0 = \sqrt{u_1}, \beta_1 = \sqrt{u_1 + \sqrt{u_1^2 - u_2}}, \beta_2 = \sqrt{u_1 - \sqrt{u_1^2 - u_2}}$$

$$\beta_3 = \sqrt{\frac{\sqrt{u_2}+u_1}{2}}, \beta_4 = \sqrt{\frac{\sqrt{u_2}-u_1}{2}}$$

$$u_1 = \frac{c_{11}c_{22}+c_{33}^2-(c_{12}+c_{33})^2}{2c_{22}c_{33}}, u_2 = \frac{c_{11}}{c_{22}}$$

G_1^+, H_1^+, G_2^+, H_2^+, G_1, H_1, G_2, H_2, G_1^-, H_1^-, G_2^-, H_2^- are unknown functions of s to be determined from the boundary conditions of the problem.

For the elastic medium, the boundary conditions at two free surfaces should be satisfied as

$$\sigma_{yz}(y,0) = \begin{cases} -\tau(y) & |y| < a \\ 0 & \text{otherwise} \end{cases}, \quad \sigma_z(y,0) = 0, \qquad (2.1.21)$$

$$\sigma_{yz}(y,H) = 0, \quad \sigma_z(y,H) = 0 \qquad (2.1.22)$$

Using above boundary conditions, the unknown functions in (2.1.19) and (2.1.20) can be determined and the resulting strain along $z = 0$ can be obtained by conducting inverse Fourier transform as:

$$\varepsilon_y(y,0) = \frac{2}{\pi\overline{E}}\int_{-a}^{a}\frac{\tau(\xi)}{y-\xi}d\xi - \frac{1}{\pi}\int_{-a}^{a}\int_{0}^{\infty}[\overline{F}(s) - \frac{2}{\overline{E}}]\tau(\xi)\sin[s(\xi-y)]dsd\xi \qquad (2.1.23)$$

where $\overline{E}$ is an effective elastic modulus of the host medium given by

$$\overline{E} = \begin{cases} \dfrac{2K_1K_2(\beta_2-\beta_1)}{(K_1+K_2)(c_{12}+c_{33})} & c_{33} < \frac{1}{2}(\sqrt{c_{11}c_{22}} - c_{12}) \\[3mm] \dfrac{2\overline{K}_2^2}{\overline{K}_1(c_{12}+c_{33})} & c_{33} = \frac{1}{2}(\sqrt{c_{11}c_{22}} - c_{12}) \\[3mm] \dfrac{2\beta_4(\overline{K}_1^2+\overline{K}_2^2)}{\overline{K}_1(c_{12}+c_{33})} & c_{33} > \frac{1}{2}(\sqrt{c_{11}c_{22}} - c_{12}) \end{cases} \qquad (2.1.24)$$

24

with

$$K_1 = -(c_{22}c_{33}\beta_2^2 - c_{11}c_{22} + c_{12}^2 + c_{12}c_{33}), K_2 = (c_{22}c_{33}\beta_1^2 - c_{11}c_{22} + c_{12}^2 + c_{12}c_{33})$$

$$\overline{K}_1 = 2c_{22}c_{33}\beta_0^2, \overline{K}_2 = c_{22}c_{33}\beta_0^2 - c_{11}c_{22} + c_{12}^2 + c_{12}c_{33}$$

$$\overline{\overline{K}}_1 = 2\beta_3\beta_4 c_{22}c_{33}, \overline{\overline{K}}_2 = c_{22}c_{33}(\beta_3^2 - \beta_4^2) - c_{11}c_{22} + c_{12}^2 + c_{12}c_{13}$$

and $\overline{F}(s)$ is a function of s given by

$$\overline{F}(s) = \begin{cases} \dfrac{[f_1(s) + f_2(s) + f_3(s) + 1](c_{12} + c_{33})}{\beta_1 K_1[f_2(s) - f_3(s)] + \beta_2 K_2[f_1(s) - 1]} & c_{33} < \dfrac{1}{2}(\sqrt{c_{11}c_{22}} - c_{12}) \\[2mm] \dfrac{(\overline{f}_1 + \overline{f}_2)(c_{12} + c_{33})}{\overline{K}_1(\overline{f}_2 - \overline{f}_3) - (\overline{K}_1 + \overline{K}_2)(\overline{f}_2 + 1)} & c_{33} = \dfrac{1}{2}(\sqrt{c_{11}c_{22}} - c_{12}) \\[2mm] \dfrac{(\overline{\overline{f}}_1 + \overline{\overline{f}}_3)(c_{12} + c_{33})}{\overline{\overline{f}}_1\overline{\overline{K}}_{11} - \overline{\overline{f}}_2\overline{\overline{K}}_{22} + \overline{\overline{f}}_3\overline{\overline{K}}_{33} - \overline{\overline{K}}_{44}} & c_{33} > \dfrac{1}{2}(\sqrt{c_{11}c_{22}} - c_{12}) \end{cases} \quad (2.1.25)$$

where

$$f_1(s) = \frac{\dfrac{E_1}{2E_2}(\dfrac{\beta_2}{\beta_1} + 1) - \dfrac{1}{2E_1E_2}(\dfrac{\beta_2}{\beta_1} - 1) - 1}{\dfrac{E_1E_2}{2}(\dfrac{\beta_2}{\beta_1} - 1) - \dfrac{E_2}{2E_1}(\dfrac{\beta_2}{\beta_1} + 1) + 1}$$

$$f_2(s) = \frac{K_2}{2E_1K_1}[(\frac{\beta_2}{\beta_1} - 1)\frac{1}{E_2} - (\frac{\beta_2}{\beta_1} + 1)E_2 f_1(s)]$$

$$f_3(s) = \frac{E_1K_2}{2K_1}[(\frac{\beta_2}{\beta_1} - 1)E_2 f_1(s) - (\frac{\beta_2}{\beta_1} + 1)\frac{1}{E_2}]$$

$$\overline{f}_1(s) = -\frac{\overline{K}_2(\overline{K}_4 + \overline{K}_5) + E_0^2[\overline{K}_4\overline{K}_5 + \overline{K}_2(\overline{K}_3 + \overline{K}_5) - \overline{K}_3\overline{K}_6]}{E_0^2\overline{K}_1(\overline{K}_3 + \overline{K}_5 - 2\overline{K}_2 + E_0^2\overline{K}_3 - E_0^2\overline{K}_5)}$$

$$\overline{f}_2(s) = -\frac{E_0^2\overline{K}_2(\overline{K}_3 - \overline{K}_5) + \overline{K}_3\overline{K}_6 + \overline{K}_2(\overline{K}_4 - \overline{K}_6) - \overline{K}_4\overline{K}_5}{\overline{K}_1(\overline{K}_3 + \overline{K}_5 - 2\overline{K}_2 + E_0^2\overline{K}_3 - E_0^2\overline{K}_5)}$$

$$\overline{f}_3(s) = -\frac{\overline{K}_4 + \overline{K}_6 + E_0^2(2\overline{K}_2 + \overline{K}_4 - \overline{K}_6)}{E_0^2(\overline{K}_3 + \overline{K}_5 - 2\overline{K}_2 + E_0^2\overline{K}_3 - E_0^2\overline{K}_5)}$$

$$\overline{\overline{f}}_1(s) = -\frac{\overline{\overline{K}}_1(\overline{\overline{K}}_{10}\overline{\overline{K}}_4 - \overline{\overline{K}}_6\overline{\overline{K}}_8) + \overline{\overline{K}}_2(\overline{\overline{K}}_{10}\overline{\overline{K}}_5 + \overline{\overline{K}}_5\overline{\overline{K}}_8 - \overline{\overline{K}}_4\overline{\overline{K}}_9 - \overline{\overline{K}}_6\overline{\overline{K}}_9)}{-\overline{\overline{K}}_1\overline{\overline{K}}_4\overline{\overline{K}}_7 - \overline{\overline{K}}_2\overline{\overline{K}}_5\overline{\overline{K}}_7 + \overline{\overline{K}}_1\overline{\overline{K}}_3\overline{\overline{K}}_8 - \overline{\overline{K}}_1\overline{\overline{K}}_5\overline{\overline{K}}_8 + \overline{\overline{K}}_2\overline{\overline{K}}_3\overline{\overline{K}}_9 + \overline{\overline{K}}_1\overline{\overline{K}}_4\overline{\overline{K}}_9}$$

$$\overline{\overline{f}}_2(s) = -\frac{\overline{\overline{K}}_2(\overline{\overline{K}}_3\overline{\overline{K}}_9 - \overline{\overline{K}}_5\overline{\overline{K}}_7) + \overline{\overline{K}}_1(\overline{\overline{K}}_{10}\overline{\overline{K}}_5 - \overline{\overline{K}}_{10}\overline{\overline{K}}_3 - \overline{\overline{K}}_6\overline{\overline{K}}_9 + \overline{\overline{K}}_6\overline{\overline{K}}_7)}{-\overline{\overline{K}}_1\overline{\overline{K}}_4\overline{\overline{K}}_7 - \overline{\overline{K}}_2\overline{\overline{K}}_5\overline{\overline{K}}_7 + \overline{\overline{K}}_1\overline{\overline{K}}_3\overline{\overline{K}}_8 - \overline{\overline{K}}_1\overline{\overline{K}}_5\overline{\overline{K}}_8 + \overline{\overline{K}}_2\overline{\overline{K}}_3\overline{\overline{K}}_9 + \overline{\overline{K}}_1\overline{\overline{K}}_4\overline{\overline{K}}_9}$$

$$\overline{\overline{f}}_3(s) = -\frac{\overline{\overline{K}}_2(\overline{\overline{K}}_7\overline{\overline{K}}_4 + \overline{\overline{K}}_6\overline{\overline{K}}_7 - \overline{\overline{K}}_3\overline{\overline{K}}_8) + \overline{\overline{K}}_1\overline{\overline{K}}_6\overline{\overline{K}}_8 - \overline{\overline{K}}_{10}(\overline{\overline{K}}_2\overline{\overline{K}}_3 + \overline{\overline{K}}_1\overline{\overline{K}}_4)}{-\overline{\overline{K}}_1\overline{\overline{K}}_4\overline{\overline{K}}_7 - \overline{\overline{K}}_2\overline{\overline{K}}_5\overline{\overline{K}}_7 + \overline{\overline{K}}_1\overline{\overline{K}}_3\overline{\overline{K}}_8 - \overline{\overline{K}}_1\overline{\overline{K}}_5\overline{\overline{K}}_8 + \overline{\overline{K}}_2\overline{\overline{K}}_3\overline{\overline{K}}_9 + \overline{\overline{K}}_1\overline{\overline{K}}_4\overline{\overline{K}}_9}$$

25

with

$$E_0 = e^{\beta_0 |s| H}, \; E_1 = e^{\beta_1 |s| H}, \; E_2 = e^{\beta_2 |s| H}, E_3 = e^{\beta_3 |s| H},$$

$$\overline{K}_3 = \beta_0 H \overline{K}_1 |s| + \overline{K}_2, \; \overline{K}_4 = \beta_0 H \overline{K}_1 |s| - \overline{K}_2,$$

$$\overline{K}_5 = \beta_0 H \overline{K}_1 |s| + \overline{K}_2 + \overline{K}_1, \; \overline{K}_6 = -\beta_0 H \overline{K}_1 s + \overline{K}_2 + \overline{K}_1,$$

$$\overline{\overline{K}}_3 = -\overline{K}_1 \cos(\beta_4 H |s|) - \overline{K}_2 \sin(\beta_4 H |s|),$$

$$\overline{\overline{K}}_4 = -\overline{K}_1 \sin(\beta_4 H |s|) + \overline{K}_2 \cos(\beta_4 H |s|),$$

$$\overline{\overline{K}}_5 = [-\overline{K}_1 \cos(\beta_4 H |s|) + \overline{K}_2 \sin(\beta_4 H |s|)]/E_3^2,$$

$$\overline{\overline{K}}_6 = [-\overline{K}_1 \sin(\beta_4 H |s|) - \overline{K}_2 \cos(\beta_4 H |s|)]/E_3^2,$$

$$\overline{\overline{K}}_7 = [(\beta_3 \overline{\overline{K}}_1 - \beta_4 \overline{\overline{K}}_2) \cos(\beta_4 H |s|) + (\beta_4 \overline{\overline{K}}_1 + \beta_3 \overline{\overline{K}}_2) \sin(\beta_4 H |s|)],$$

$$\overline{\overline{K}}_8 = [(-\beta_3 \overline{\overline{K}}_2 - \beta_4 \overline{\overline{K}}_1) \cos(\beta_4 H |s|) + (\beta_3 \overline{\overline{K}}_1 - \beta_4 \overline{\overline{K}}_2) \sin(\beta_4 H |s|)],$$

$$\overline{\overline{K}}_9 = [(-\beta_3 \overline{\overline{K}}_1 + \beta_4 \overline{\overline{K}}_2) \cos(\beta_4 H |s|) + (\beta_4 \overline{\overline{K}}_1 + \beta_3 \overline{\overline{K}}_2) \sin(\beta_4 H |s|)]/E_3^2,$$

$$\overline{\overline{K}}_{10} = [(-\beta_3 \overline{\overline{K}}_2 - \beta_4 \overline{\overline{K}}_1) \cos(\beta_4 H |s|) + (-\beta_3 \overline{\overline{K}}_1 + \beta_4 \overline{\overline{K}}_2) \sin(\beta_4 H |s|)]/E_3^2.$$

For all three phases presented in Equations (2.1.24) and (2.1.25), $\overline{F}(s)$ tends to $\dfrac{2}{\overline{\overline{E}}}$ when s tends to infinity regardless the thickness of the host medium. This result indicates, as expected, that the singular behaviour of the current problem is independent of the thickness of the host medium. For the case where the shear modulus c_{33} is very small, $c_{33} \longrightarrow 0$, $\overline{E}$ tends to zero. For the case where $c_{33} \longrightarrow \infty$, $\overline{E}$ tends to infinity. It is also interesting to note that for the case of elastic medium with infinite thickness, based on the relation of $\lim\limits_{H \longrightarrow \infty} \overline{F}(s) = \dfrac{2}{\overline{\overline{E}}}$, the resulting strain field along the interface can be obtained as

$$\varepsilon_y(y, 0) = \frac{2}{\pi \overline{\overline{E}}} \int_{-a}^{a} \frac{\tau(\xi)}{y - \xi} d\xi \tag{2.1.26}$$

which shows that the load transfer of the orthotropic host structure is governed by only one parameter $\overline{E}$ for this case. For an isotropic host medium, which corresponds to $c_{33} = \dfrac{c_{11} - c_{12}}{2}$, parameter $\overline{E}$ can be further simplified as $\overline{E} = E/(1 - \nu^2)$ with E and ν being the Young's modulus and the Poisson ratio, respectively.

26

2.2 Governing equations

Consider general case of an elastic medium with thickness H, the compatibility of deformation between the actuator and the host structure indicates that

$$\varepsilon_y^a|_{actuator} = \varepsilon_y|_{host} \quad |y| < a, \quad z = 0 \tag{2.2.1}$$

Substituting (2.1.11) and (2.1.23) into (2.2.1) gives

$$-\frac{1}{\pi} \int_{-a}^{a} \int_{0}^{\infty} [\overline{F}(s) - \frac{2}{\overline{E}}] \tau(\xi) \sin[s(\xi - y)] ds d\xi$$

$$+\frac{2}{\pi \overline{E}} \int_{-a}^{a} \frac{\tau(\xi)}{y - \xi} d\xi + \frac{1}{hE_a} \int_{-a}^{y} \tau(\xi) d\xi = \frac{e_a E_z}{E_a}, \quad |y| < a \tag{2.2.2}$$

To determine interfacial shear stress τ, the singular integral Equations (2.2.2) and (2.1.10) can be normalized to give

$$\left.\begin{array}{c} -\dfrac{a\overline{E}}{2} \displaystyle\int_{-1}^{1} \int_{0}^{\infty} [\overline{F}(s) - \dfrac{2}{\overline{E}}] \overline{\tau}(\zeta) \sin[s(\zeta - \eta)] ds d\zeta \\[3mm] +\displaystyle\int_{-1}^{1} \dfrac{\overline{\tau}(\zeta) d\zeta}{\eta - \zeta} + qv \displaystyle\int_{-1}^{\eta} \overline{\tau}(\zeta) d\zeta = q \quad |\eta| < 1 \\[3mm] \displaystyle\int_{-1}^{1} \overline{\tau}(\zeta) d\zeta = 0 \end{array}\right\} \tag{2.2.3}$$

where

$$\left.\begin{array}{c} \overline{\tau}(\eta) = \tau(a\eta)/\sigma_B, \quad \eta = y/a \\[3mm] q = \dfrac{\pi \overline{E}}{2E_a}, \quad \sigma_B = e_a E_z, v = a/h \end{array}\right\} \tag{2.2.4}$$

Since Equation (2.2.3) is a singular integral equation of the first kind, the solution of it involves a square-root singularity (Muskhelishvili, 1953) at $|\eta| = 1$. Accordingly, the solution of equation (2.2.3) can be generally expressed in terms of the first kind of Chebyshev polynomials, T_j ,as

$$\overline{\tau}(\eta) = \frac{1}{\sqrt{1 - \eta^2}} \sum_{j=0}^{\infty} d_j T_j(\eta) \tag{2.2.5}$$

where $d_0 = 0$ due to $\displaystyle\int_{-1}^{1} \overline{\tau}(\xi) d\xi = 0$.

By truncating the Chebyshev polynomial expansion to the Nth term and satisfying the integral equation in (2.2.3) at the following collocation points along the actuator,

$$\eta_k = \cos\frac{k-1}{N-1}\pi, \quad k = 1, 2, \cdots, N \tag{2.2.6}$$

the unknown coefficients d_j can be determined by solving the following algebraic equations

$$\frac{a\overline{E}}{2}\sum_{j=1}^{N}d_j \begin{cases} (-1)^n \int_0^\infty [\overline{F}(s) - \frac{2}{\overline{E}}]J_j(sa)\cos(sa\eta_k)ds & j = 2n+1 \\ (-1)^{n+1}\int_0^\infty [\overline{F}(s) - \frac{2}{\overline{E}}]J_j(sa)\sin(sa\eta_k)ds & j = 2n \end{cases}$$

$$+\sum_{j=1}^{N}d_j\frac{\sin(j\frac{k-1}{N-1}\pi)}{\sin(\frac{k-1}{N-1}\pi)}[1 + \frac{qv}{\pi j}\sin(\frac{k-1}{N-1}\pi)] = -q/\pi, \quad k = 1, 2, \cdots, N \tag{2.2.7}$$

with J_j $(j = 1, 2\cdots)$ being the Bessel functions of the first kind. The interfacial shear stress can then be determined using Equation (2.2.7). The singular behaviour of the interfacial shear stress at the right tip of the actuator is characterized by the following shear stress singularity factor (SSSF) S

$$S = \lim_{y\to a}[\sqrt{2\pi(a-y)}\tau(y)] = \sigma_B\sqrt{a\pi}\sum_{j=1}^{N}d_j \tag{2.2.8}$$

2.3 Stress distribution

Using the current actuator model, the electrically induced stress field in the host medium can be obtained analytically. According to the general solution given by equations (2.1.19) and (2.1.20) and elastic constitutive relation, the stress distribution in the host medium can be obtained in terms of interfacial shear stress τ by conducting inverse Fourier transform.

For the case where $c_{33} < (\sqrt{c_{11}c_{22}} - c_{12})/2$, the induced stress field is

$$\sigma_y = \frac{1}{\pi}\int_{-a}^{a}\int_0^\infty [K_3 e^{-\beta_1 sz} + K_4 e^{-\beta_2 sz}]\sin[s(u-y)]\tau(u)dsdu \tag{2.3.1}$$

28

$$\sigma_z = \frac{1}{\pi} \int_{-a}^{a} \int_{0}^{\infty} [K_5 e^{-\beta_1 sz} + K_6 e^{-\beta_2 sz}] \sin[s(u - y)]\tau(u)dsdu \qquad (2.3.2)$$

$$\sigma_{yz} = \frac{1}{\pi} \int_{-a}^{a} \int_{0}^{\infty} [K_7 e^{-\beta_1 sz} + K_8 e^{-\beta_2 sz}] \cos[s(u - y)]\tau(u)dsdu \qquad (2.3.3)$$

where

$$K_3 = \frac{c_{11}K_1 + c_{12}K_9\beta_1}{K_{11}}, K_4 = \frac{c_{11}K_2 + c_{12}K_{10}\beta_2}{K_{11}}, K_5 = \frac{c_{12}K_1 + c_{22}K_9\beta_1}{K_{11}}$$

$$K_6 = \frac{c_{12}K_2 + c_{22}K_{10}\beta_2}{K_{11}}, K_7 = \frac{\beta_1}{\beta_1 - \beta_2}, K_8 = \frac{-\beta_2}{\beta_1 - \beta_2}$$

$$K_9 = \frac{\beta_1 K_1 K_2}{c_{33}(c_{12} + c_{33})}, K_{10} = \frac{-\beta_2 K_1 K_2}{c_{33}(c_{12} + c_{33})}, K_{11} = \frac{(\beta_1 - \beta_2)K_1 K_2}{(c_{12} + c_{33})}$$

Using the solution of τ given by (2.2.5) and the following known integral results,

$$\int_{0}^{\infty} J_j(as) \cos(s|y|)e^{-s|z|}ds = \frac{a^j \cos(Ak - \frac{|B|}{2})}{R[(R\cos\frac{|B|}{2} + |z|)^2 + (R\sin\frac{|B|}{2} + |y|)^2]^{j/2}} \qquad (2.3.4)$$

$$\int_{0}^{\infty} J_j(as) \sin(s|y|)e^{-s|z|}ds = \frac{-a^j \sin(Ak - \frac{|B|}{2})}{R[(R\cos\frac{|B|}{2} + |z|)^2 + (R\sin\frac{|B|}{2} + |y|)^2]^{j/2}} \qquad (2.3.5)$$

where

$$R = [(z^2 - y^2 + a^2)^2 + 4y^2 z^2]^{1/4}, B = -|\arccos\frac{z^2 - y^2 + a^2}{R^2}|, A = -\arctan\frac{R\sin\frac{|B|}{2} + |y|}{R\cos\frac{|B|}{2} + |z|}$$

The integration in equations (2.3.1), (2.3.2) and (2.3.3) can be completed and these stress components can be expressed in explicit forms as

$$\sigma_y = \sum_{j=1}^{\infty} d_j \begin{cases} (-1)^n[K_3 F_{1j}(\phi_1, \theta_1) + K_4 F_{1j}(\phi_2, \theta_2)] & j = 2n + 1 \\ (-1)^n[K_3 F_{2j}(\phi_1, \theta_1) + K_4 F_{2j}(\phi_2, \theta_2)] & j = 2n \end{cases} \qquad (2.3.6)$$

$$\sigma_z = \sum_{j=1}^{\infty} d_j \begin{cases} (-1)^n[K_5 F_{1j}(\phi_1, \theta_1) + K_6 F_{1j}(\phi_2, \theta_2)] & j = 2n + 1 \\ (-1)^n[K_5 F_{2j}(\phi_1, \theta_1) + K_6 F_{2j}(\phi_2, \theta_2)] & j = 2n \end{cases} \qquad (2.3.7)$$

$$\sigma_{yz} = \sum_{j=1}^{\infty} d_j \begin{cases} (-1)^{n+1}[K_7 F_{2j}(\phi_1, \theta_1) + K_8 F_{2j}(\phi_2, \theta_2)] & j = 2n + 1 \\ (-1)^n[K_7 F_{1j}(\phi_1, \theta_1) + K_8 F_{1j}(\phi_2, \theta_2)] & j = 2n \end{cases} \qquad (2.3.8)$$

where

$$F_{1j}(\phi_i, \theta_i) = a^{j+1}\frac{\cos(\phi_i j - \theta_i/2)}{\Delta_i}, i = 0, 1, 2$$

$$F_{2j}(\phi_i, \theta_i) = a^{j+1}\frac{\sin(\phi_i j - \theta_i/2)}{\Delta_i}sgn(y), i = 0, 1, 2$$

29

with

$$\theta_1 = -\arctan\left(\frac{2|\beta_1 z||y|}{|\beta_1 z|^2 - |y|^2 + a^2}\right), \theta_2 = -\arctan\left(\frac{2|\beta_2 z||y|}{|\beta_2 z|^2 - |y|^2 + a^2}\right)$$

$$\phi_1 = -\arctan\left(\frac{R_1 \sin(\theta_1/2) + |y|}{R_1 \sin(\theta_1/2) + |\beta_1 z|}\right), \phi_2 = -\arctan\left(\frac{R_2 \sin(\theta_2/2) + |y|}{R_2 \sin(\theta_2/2) + |\beta_2 z|}\right)$$

$$R_1 = \sqrt[4]{(\beta_1{}^2 z^2 - y^2 + a^2)^2 + 4\beta_1{}^2 y^2 z^2}, R_2 = \sqrt[4]{(\beta_2{}^2 z^2 - y^2 + a^2)^2 + 4\beta_2{}^2 y^2 z^2}$$

$$\Delta_1 = R_1[(R_1 \cos(\theta_1/2) + |\beta_1 z|)^2 + (R_1 \sin(\theta_1/2) + |y|)^2]^{j/2}$$

$$\Delta_2 = R_2[(R_2 \cos(\theta_2/2) + |\beta_2 z|)^2 + (R_2 \sin(\theta_2/2) + |y|)^2]^{j/2}$$

For $c_{33} = (\sqrt{c_{11}c_{22}} - c_{12})/2$, the similar procedure can be conducted to obtain stress components in explicit forms as

$$\sigma_y = \sum_{j=1}^{\infty} d_j \begin{cases} (-1)^n[\overline{K}_3 F_{1j}(\phi_0, \theta_0) - z\overline{K}_4 \frac{\partial}{\partial z} F_{1j}(\phi_0, \theta_0)] & j = 2n+1 \\ (-1)^n[\overline{K}_3 F_{2j}(\phi_0, \theta_0) - z\overline{K}_4 \frac{\partial}{\partial z} F_{2j}(\phi_0, \theta_0)] & j = 2n \end{cases} \qquad (2.3.9)$$

$$\sigma_z = \sum_{j=1}^{\infty} d_j \begin{cases} (-1)^n[\overline{K}_5 F_{1j}(\phi_0, \theta_0) - z\overline{K}_6 \frac{\partial}{\partial z} F_{1j}(\phi_0, \theta_0)] & j = 2n+1 \\ (-1)^n[\overline{K}_5 F_{2j}(\phi_0, \theta_0) - z\overline{K}_6 \frac{\partial}{\partial z} F_{2j}(\phi_0, \theta_0)] & j = 2n \end{cases} \qquad (2.3.10)$$

$$\sigma_{yz} = \sum_{j=1}^{\infty} d_j \begin{cases} (-1)^{n+1}[\overline{K}_7 F_{2j}(\phi_0, \theta_0) - z\overline{K}_8 \frac{\partial}{\partial z} F_{2j}(\phi_0, \theta_0)] & j = 2n+1 \\ (-1)^n[\overline{K}_7 F_{1j}(\phi_0, \theta_0) - z\overline{K}_8 \frac{\partial}{\partial z} F_{1j}(\phi_0, \theta_0)] & j = 2n \end{cases} \qquad (2.3.11)$$

where

$$\overline{K}_3 = -\frac{c_{33}[(c_{12}\beta_0{}^2 + c_{11})\overline{K}_1 - 2c_{22}\overline{K}_2\beta_0{}^2]}{\beta_0 \overline{K}_2{}^2}, \overline{K}_4 = \frac{c_{33}(c_{12}\beta_0{}^2 + c_{11})}{\beta_0 \overline{K}_2}$$

$$\overline{K}_5 = 0, \overline{K}_6 = -\frac{1}{\beta_0}, \overline{K}_7 = 1, \overline{K}_8 = -1$$

with

$$\theta_0 = -\arctan\left(\frac{2|\beta_0 z||y|}{|\beta_0 z|^2 - |y|^2 + a^2}\right), \phi_0 = -\arctan\left(\frac{R_0 \sin(\theta_0/2) + |y|}{R_0 \sin(\theta_0/2) + |\beta_0 z|}\right)$$

$$R_0 = \sqrt[4]{(\beta_0{}^2 z^2 - y^2 + a^2)^2 + 4\beta_0{}^2 y^2 z^2}$$

$$\Delta_0 = R_0[(R_0 \cos(\theta_0/2) + |\beta_0 z|)^2 + (R_0 \sin(\theta_0/2) + |y|)^2]^{j/2}$$

30

For $c_{33} > (\sqrt{c_{11}c_{22}} - c_{12})/2$,

$$\sigma_y = \sum_{j=1}^{\infty} d_j \begin{cases} (-1)^n[\overline{\overline{K}}_3 F_{3j}(\phi_3,\theta_3,\phi_4,\theta_4) + \overline{\overline{K}}_4 F_{4j}(\phi_3,\theta_3,\phi_4,\theta_4)] & j = 2n+1 \\ (-1)^n[\overline{\overline{K}}_3 F_{5j}(\phi_3,\theta_3,\phi_4,\theta_4) + \overline{\overline{K}}_4 F_{6j}(\phi_3,\theta_3,\phi_4,\theta_4)] & j = 2n \end{cases} \quad (2.3.12)$$

$$\sigma_z = \sum_{j=1}^{\infty} d_j \begin{cases} (-1)^n[\overline{\overline{K}}_5 F_{3j}(\phi_3,\theta_3,\phi_4,\theta_4) + \overline{\overline{K}}_6 F_{4j}(\phi_3,\theta_3,\phi_4,\theta_4)] & j = 2n+1 \\ (-1)^n[\overline{\overline{K}}_5 F_{5j}(\phi_3,\theta_3,\phi_4,\theta_4) + \overline{\overline{K}}_6 F_{6j}(\phi_3,\theta_3,\phi_4,\theta_4)] & j = 2n \end{cases} \quad (2.3.13)$$

$$\sigma_{yz} = \sum_{j=1}^{\infty} d_j \begin{cases} (-1)^{n+1}[\overline{\overline{K}}_7 F_{3j}(\phi_3,\theta_3,\phi_4,\theta_4) + \overline{\overline{K}}_8 F_{4j}(\phi_3,\theta_3,\phi_4,\theta_4)] & j = 2n+1 \\ (-1)^n[\overline{\overline{K}}_7 F_{5j}(\phi_3,\theta_3,\phi_4,\theta_4) + \overline{\overline{K}}_8 F_{6j}(\phi_3,\theta_3,\phi_4,\theta_4)] & j = 2n \end{cases} \quad (2.3.14)$$

where

$$\overline{\overline{K}}_3 = \frac{c_{33}[c_{12}(\beta_3{}^2 - \beta_4{}^2)\overline{\overline{K}}_1 - 2\beta_3\beta_4 c_{12}\overline{\overline{K}}_2 + c_{11}\overline{\overline{K}}_1]}{\overline{\overline{K}}_9(c_{12} + c_{33})}$$

$$\overline{\overline{K}}_4 = \frac{c_{33}[c_{12}(\beta_3{}^2 - \beta_4{}^2)\overline{\overline{K}}_2 + 2\beta_3\beta_4 c_{12}\overline{\overline{K}}_1 + c_{11}\overline{\overline{K}}_1]}{\overline{\overline{K}}_9(c_{12} + c_{33})}$$

$$\overline{\overline{K}}_5 = 0, \overline{\overline{K}}_6 = -\frac{1}{\beta_4}, \overline{\overline{K}}_7 = 1, \overline{\overline{K}}_8 = -\frac{\beta_3}{\beta_4}, \overline{\overline{K}}_9 = \frac{-\beta_4(\overline{\overline{K}}_1{}^2 + \overline{\overline{K}}_2{}^2)}{c_{12} + c_{33}}$$

with

$$F_{3j} = \frac{1}{2}a^{j+1}[\frac{\cos(\phi_3 j - \theta_3/2)}{\Delta_3} + \frac{\cos(\phi_4 j - \theta_4/2)}{\Delta_4}]$$

$$F_{4j} = -\frac{1}{2}a^{j+1}[\frac{\sin(\phi_3 j - \theta_3/2)}{\Delta_3}sgn(\beta_4 z + y) + \frac{\sin(\phi_4 j - \theta_4/2)}{\Delta_4}sgn(\beta_4 z - y)]$$

$$F_{5j} = \frac{1}{2}a^{j+1}[\frac{\cos(\phi_3 j - \theta_3/2)}{\Delta_3} - \frac{\cos(\phi_4 j - \theta_4/2)}{\Delta_4}]$$

$$F_{6j} = -\frac{1}{2}a^{j+1}[\frac{\sin(\phi_3 j - \theta_3/2)}{\Delta_3}sgn(\beta_4 z + y) - \frac{\sin(\phi_4 j - \theta_4/2)}{\Delta_4}sgn(\beta_4 z - y)]$$

$$\theta_3 = -\arctan(\frac{2|\beta_4 z + y||\beta_3 z|}{|\beta_3 z|^2 - |\beta_4 z + y|^2 + a^2}), \theta_4 = -\arctan(\frac{2|\beta_4 z - y||\beta_3 z|}{|\beta_3 z|^2 - |\beta_4 z - y|^2 + a^2})$$

$$\phi_3 = -\arctan(\frac{R_3\sin(\theta_3/2) + |\beta_4 z + y|}{R_3\sin(\theta_3/2) + |Az|}), \phi_4 = -\arctan(\frac{R_4\sin(\theta_4/2) + |\beta_4 z - y|}{R_4\sin(\theta_4/2) + |\beta_3 z|})$$

$$R_3 = {}^4\sqrt{(\beta_3{}^2 z^2 - (\beta_4 z + y)^2 + a^2)^2 + 4\beta_3{}^2(\beta_4 z + y)^2 z^2}$$

$$R_4 = {}^4\sqrt{(\beta_3{}^2 z^2 - (\beta_4 z - y)^2 + a^2)^2 + 4\beta_3{}^2(\beta_4 z - y)^2 z^2}$$

$$\Delta_3 = R_3[(R_3\cos(\theta_3/2) + |\beta_3 z|)^2 + (R_3\sin(\theta_3/2) + |\beta_4 z + y|)^2]^{j/2}$$

$$\Delta_4 = R_4[(R_4\cos(\theta_4/2) + |\beta_3 z|)^2 + (R_4\sin(\theta_4/2) + |\beta_4 z - y|)^2]^{j/2}$$

31

2.4 Interfacial Debonding

Weak interfacial bonding may result in partial debonding between the actuator and the host medium, which will change the load transfer and may result in degradation of the structure. In this section, attention will be focussed on determining the effect of debonding upon a surface bonded actuator. The actuator considered occupies the region $t_l < y < t_r$, and is assumed partially debonded in $d_l < y < d_r$, as illustrated in Figure 2.3.

Similar to the case involving a perfectly bonded actuator, by making use of the equilibrium equation (2.1.7) and the traction free condition at the two ends of the actuator, the axial strain in the actuator can be expressed in terms of τ as (Wang and Meguid, 2000)

$$\varepsilon_y(y)|_{actuator} = \begin{cases} -\dfrac{1}{E_a h} \displaystyle\int_{t_l}^{y} \tau(\xi)d\xi + \dfrac{e_a}{E_a}E_z & t_l < y < d_l \\[3mm] \dfrac{\sigma_d + e_a E_z}{E_a} & d_l < y < d_r \\[3mm] \dfrac{1}{E_a h}[\sigma_d h - \displaystyle\int_{d_r}^{y} \tau(\xi)d\xi] + \dfrac{e_a}{E_a}E_z & d_r < y < t_r \end{cases} \qquad (2.4.1)$$

where

$$\sigma_d = -\int_{t_l}^{d_l} \frac{\tau(\xi)}{h}d\xi \qquad (2.4.2)$$

is the axial stress in the debonded part of the actuator.

By using the general solution of the host medium, the strain along $z = 0$ in the host material can be expressed in terms of τ as

$$\varepsilon_y(y,0)|_{host} = \frac{2}{\pi \overline{E}}[\int_{t_l}^{d_l} \frac{\tau(\xi)}{y-\xi}d\xi + \int_{d_r}^{t_r} \frac{\tau(\xi)}{y-\xi}d\xi]$$
$$-\frac{1}{\pi}[\int_{t_l}^{d_l} \int_{0}^{\infty} [\overline{F}(s) - \frac{2}{\overline{E}}]\tau(u)\sin[s(u-y)]dsdu$$
$$+\int_{d_r}^{t_r} \int_{0}^{\infty} [\overline{F}(s) - \frac{2}{\overline{E}}]\tau(u)\sin[s(u-y)]dsdu] \qquad (2.4.3)$$

32

The compatibility of deformation between the actuator and the host structure indicates that

$$\varepsilon_y|_{actuator} = \varepsilon_y|_{host} \quad t_l < y < d_l, \ d_r < y < t_r, \quad z = 0 \tag{2.4.4}$$

and

$$u_y(d_r)|_{actuator} - u_y(d_l)|_{actuator} = u_y(d_r,0)|_{host} - u_y(d_l,0)|_{host} \tag{2.4.5}$$

Substituting (2.4.1) and (2.4.3) into (2.4.4) and (2.4.5) gives the following normalized singular integral equations in terms of the interfacial shear stress,

$$\int_{-1}^{1} \frac{\tau^l(\zeta)d\zeta}{\eta_l - \zeta} + \int_{-1}^{1} \frac{\tau^r(\zeta)d\zeta}{\eta_r - \zeta} - \frac{\overline{E}}{2}[c_l \int_{-1}^{1}\int_0^{\infty} [\overline{F}(s) - \frac{2}{\overline{E}}]\tau^l(\zeta)\sin[s(\zeta - \eta_l)]dsd\zeta$$

$$+c_r \int_{-1}^{1}\int_0^{\infty} [\overline{F}(s) - \frac{2}{\overline{E}}]\tau^r(\zeta)\sin[s(\zeta - \eta_r)]dsd\zeta] + \begin{cases} qv_l \int_{-1}^{\eta_l} \tau^l(\zeta)d\zeta = q & |\eta_l| < l \\ -qv_r \int_{\eta_r}^{l} \tau^r(\zeta)d\zeta = q & |\eta_r| < 1 \end{cases} \tag{2.4.6}$$

$$v_l \int_{1}^{\eta_l^*} \int_{-1}^{1} \frac{\tau^l(\zeta)d\zeta}{\eta_l - \zeta} d\eta_l + v_r \int_{\eta_r^*}^{-1} \int_{-1}^{1} \frac{\tau^r(\zeta)d\zeta}{\eta_r - \zeta} d\eta_r$$

$$-\frac{\overline{E}}{2}[v_l c_l \int_{1}^{\eta_l^*} \int_{-1}^{1} \int_0^{\infty} [\overline{F}(s) - \frac{2}{\overline{E}}]\tau^l(\zeta)\sin[s(\zeta - \eta_l)]dsd\zeta d\eta_l$$

$$+v_r c_r \int_{\eta_r^*}^{-1} \int_{-1}^{1} \int_0^{\infty} [\overline{F}(s) - \frac{2}{\overline{E}}]\tau^r(\zeta)\sin[s(\zeta - \eta_r)]dsd\zeta d\eta_r]$$

$$= 2q(v - v_l - v_r)[-\sigma^* + 1] \tag{2.4.7}$$

and

$$\int_{-1}^{1} \tau^l(\zeta)d\zeta = -\frac{\sigma^*}{v_l}, \quad \int_{-1}^{1} \tau^r(\zeta)d\zeta = \frac{\sigma^*}{v_r} \tag{2.4.8}$$

The normalized stresses are given by

$$\tau^l(\zeta) = \tau(a_l\zeta + y_l)/\sigma_B, \quad \tau^r(\zeta) = \tau(a_r\zeta + y_r)/\sigma_B, \quad \sigma^* = \sigma_d/\sigma_B \tag{2.4.9}$$

with

$$\left. \begin{aligned} \eta_l &= (y - y_l)/c_l, \ \eta_r = (y - y_r)/c_r, \ v = a/h, \ v_l = c_l/h, \ v_r = c_r/h \\ c &= \frac{1}{2}(t_r - t_l), \ c_l = \frac{1}{2}(d_l - t_l), \ c_r = \frac{1}{2}(t_r - d_r) \\ y_l &= \frac{1}{2}(d_l + t_l), \ y_r = \frac{1}{2}(t_r + d_r), \ \eta_l^* = 2\frac{v - v_r}{v_l} - 1, \ \eta_r^* = -2\frac{v - v_l}{v_r} + 1 \end{aligned} \right\} \tag{2.4.10}$$

33

Similar to the case where the actuator is perfectly bonded to the host medium, the interfacial shear stress will be square-root singular at the ends of the debonding part and at the tips of the actuator. Therefore, the general solutions of τ^l and τ^r, in (2.4.6), (2.4.7) and (2.4.8), can be expressed in terms of the following expansion of Chebyshev polynomials,

$$\tau^l(\eta_l) = \frac{1}{\sqrt{1-\eta_l^2}} \sum_{j=0}^{\infty} d_j^l T_j(\eta_l), \quad \tau^r(\eta_r) = \frac{1}{\sqrt{1-\eta_r^2}} \sum_{j=0}^{\infty} d_j^r T_j(\eta_r) \qquad (2.4.11)$$

According to Equation (2.4.8), $d_0^l = \dfrac{\sigma^*}{\pi q v_l}$ and $d_0^r = \dfrac{\sigma^*}{\pi q v_r}$.

If the Chebyshev polynomial expansions are truncated to the Nth term, and Equation (2.4.6) is satisfied at the following collocation points at each bonded segment of the actuator given by

$$\eta_{lk} = \eta_{rk} = \eta_k = \cos\frac{k-1}{N-1}\pi, \quad k = 1, 2, \cdots, N \qquad (2.4.12)$$

Equation (2.4.6) reduces to

$$\sum_{j=1}^{N} d_j^l \frac{\sin(j\frac{k-1}{N-1}\pi)}{\sin(\frac{k-1}{N-1}\pi)}[1 + \frac{qv_l}{\pi j}\sin(\frac{k-1}{N-1}\pi)] + \sum_{j=1}^{N} d_j^r[(\eta_{rk}^{*2} - 1)^{1/2} + \eta_{rk}^*]^j/\sqrt{\eta_{rk}^{*2} - 1}$$

$$+\frac{\overline{E}c_l}{2}\sum_{j=1}^{N} d_j^l \left\{ \begin{array}{ll} (-1)^n \int_0^\infty [\overline{F}(s) - \frac{2}{\overline{E}}]J_j(sc_l)\cos(sc_l\eta_k)ds & j = 2n+1 \\ (-1)^{n+1}\int_0^\infty [\overline{F}(s) - \frac{2}{\overline{E}}]J_j(sc_l)\sin(sc_l\eta_k)ds & j = 2n \end{array} \right.$$

$$+\frac{\overline{E}c_r}{2}\sum_{j=1}^{N} d_j^r \left\{ \begin{array}{ll} (-1)^n \int_0^\infty [\overline{F}(s) - \frac{2}{\overline{E}}]J_j(sc_r)\cos(sc_r\eta_{rk}^*)ds & j = 2n+1 \\ (-1)^{n+1}\int_0^\infty [\overline{F}(s) - \frac{2}{\overline{E}}]J_j(sc_r)\sin(sc_r\eta_{rk}^*)ds & j = 2n \end{array} \right.$$

$$+\sigma^*\{\frac{\overline{E}c_l}{2v_l}\int_0^\infty [\overline{F}(s) - \frac{2}{\overline{E}}]J_0(sc_l)\sin(sc_l\eta_k)ds - \frac{\overline{E}c_r}{2v_r}\int_0^\infty [\overline{F}(s) - \frac{2}{\overline{E}}]J_0(sc_r)\sin(sc_r\eta_{rk}^*)ds\}$$

$$+\frac{\sigma^*}{\pi}\{\frac{1}{v_r\sqrt{\eta_{rk}^{*2} - 1}} + q[1 - \frac{k-1}{N-1}]\} = -q/\pi, \quad k = 1, 2, \cdots, N \quad (2.4.13)$$

34

and

$$\sum_{j=1}^{N} d_j^r \frac{\sin(j\frac{k-1}{N-1}\pi)}{\sin(\frac{k-1}{N-1}\pi)}[1 + \frac{qv_r}{\pi j}\sin(\frac{k-1}{N-1}\pi)] - \sum_{j=1}^{N} d_j^l (-1)^j [(\eta_{lk}^{*\,2} - 1)^{1/2} + \eta_{lk}^*]^j / \sqrt{\eta_{lk}^{*\,2} - 1}$$

$$+ \frac{\overline{E}c_r}{2}\sum_{j=1}^{N} d_j^r \left\{ \begin{array}{ll} (-1)^n \int_0^\infty [\overline{F}(s) - \frac{2}{\overline{E}}]J_j(sc_r)\cos(sc_r\eta_k)ds & j = 2n+1 \\[3mm] (-1)^{n+1} \int_0^\infty [\overline{F}(s) - \frac{2}{\overline{E}}]J_j(sc_r)\sin(sc_r\eta_k)ds & j = 2n \end{array} \right.$$

$$+ \frac{\overline{E}c_l}{2}\sum_{j=1}^{N} d_j^l \left\{ \begin{array}{ll} (-1)^n \int_0^\infty [\overline{F}(s) - \frac{2}{\overline{E}}]J_j(sc_l)\cos(sc_l\eta_{lk}^*)ds & j = 2n+1 \\[3mm] (-1)^{n+1} \int_0^\infty [\overline{F}(s) - \frac{2}{\overline{E}}]J_j(sc_l)\sin(sc_l\eta_{lk}^*)ds & j = 2n \end{array} \right.$$

$$+ \sigma^* \{ \frac{\overline{E}c_l}{2v_l}\int_0^\infty [\overline{F}(s) - \frac{2}{\overline{E}}]J_0(sc_l)\sin(sc_l\eta_{lk}^*)ds - \frac{\overline{E}c_r}{2v_r}\int_0^\infty [\overline{F}(s) - \frac{2}{\overline{E}}]J_0(sc_r)\sin(sc_r\eta_k)ds \}$$

$$+ \frac{\sigma^*}{\pi}\{ \frac{1}{v_l\sqrt{\eta_k^2 - 1}} + q\frac{k-1}{N-1} \} = -q/\pi, \quad k = 1, 2, \cdots, N \quad (2.4.14)$$

In addition, Equation (2.4.7) becomes

$$\sigma^*\{-ln[|\eta_l^* + \sqrt{\eta_l^{*2} - 1}||\eta_r^* + \sqrt{\eta_r^{*2} - 1}|] - 2(v - v_l - v_r)q\}$$

$$+ \sigma^*[\frac{\overline{E}c_l}{2}\int_1^{\eta_l^*}\int_0^\infty [\overline{F}(s) - \frac{2}{\overline{E}}]J_0(sc_l)\sin(sc_l\eta_l)dsd\eta_l$$

$$- \frac{\overline{E}c_r}{2}\int_{\eta_r^*}^{-1}\int_0^\infty [\overline{F}(s) - \frac{2}{\overline{E}}]J_0(sc_r)\sin(sc_r\eta_r)dsd\eta_r]$$

$$- \frac{\overline{E}c_l v_l \pi}{2}\sum_{j=1}^{N} d_j^l \left\{ \begin{array}{ll} (-1)^n \int_1^{\eta_l^*}\int_0^\infty [\overline{F}(s) - \frac{2}{\overline{E}}]J_j(sc_l)\cos(sc_l\eta_l)dsd\eta_l & j = 2n+1 \\[3mm] (-1)^{n+1} \int_1^{\eta_l^*}\int_0^\infty [\overline{F}(s) - \frac{2}{\overline{E}}]J_j(sc_l)\sin(sc_l\eta_l)dsd\eta_l & j = 2n \end{array} \right.$$

$$- \frac{\overline{E}c_r v_r \pi}{2}\sum_{j=1}^{N} d_j^r \left\{ \begin{array}{ll} (-1)^n \int_{\eta_r^*}^{-1}\int_0^\infty [\overline{F}(s) - \frac{2}{\overline{E}}]J_j(sc_r)\cos(sc_r\eta_r)dsd\eta_r & j = 2n+1 \\[3mm] (-1)^{n+1} \int_{\eta_r^*}^{-1}\int_0^\infty [\overline{F}(s) - \frac{2}{\overline{E}}]J_j(sc_r)\sin(sc_r\eta_r)dsd\eta_r & j = 2n \end{array} \right.$$

$$+ \sum_{j=1}^{N} d_j^l\{\pi v_l(-1)^j \int_1^{\eta_l^*} [(\eta_l^2 - 1)^{1/2} - \eta_l]^j / \sqrt{\eta_l^2 - 1}d\eta_l$$

$$+ \sum_{j=1}^{N} d_j^r\{-\pi v_r \int_{\eta_r^*}^{-1} [(\eta_r^2 - 1)^{1/2} - \eta_r]^j / \sqrt{\eta_r^2 - 1}d\eta_r\} = 2q(v - v_l - v_r) \quad (2.4.15)$$

where $\eta_{rk}^* = \dfrac{2v - v_r - v_l + v_r\eta_k}{v_r}$, $\eta_{lk}^* = -\dfrac{2v - v_r - v_l - v_l\eta_k}{v_l}$.

35

From these equations, the unknown coefficients d_j^l and d_j^r can be determined. The resulting SSSF at the left and the right tips of the actuator can be expressed in terms of d_j^l and d_j^r as

$$S_l = \sigma_B \sqrt{c_l \pi} \sum_{j=0}^{N} (-1)^j d_j^l, \quad S_r = \sigma_B \sqrt{c_r \pi} \sum_{j=0}^{N} d_j^r \qquad (2.4.16)$$

In addition, the SSSF at the left and the right ends of the debonding part can be obtained as

$$S_{dl} = \sigma_B \sqrt{c_l \pi} \sum_{j=0}^{N} d_j^l, \quad S_{dr} = \sigma_B \sqrt{c_r \pi} \sum_{j=0}^{N} (-1)^j d_j^r \qquad (2.4.17)$$

2.5 Analysis and Discussion

The numerical simulation described in this section is conducted to investigate the effects of the pertinent parameters upon the coupled electromechanical property of an anisotropic structure with a surface bonded piezoelectric actuator subjected to an inplane electric load.

2.5.1 Validation of the actuator model

To verify the validity of the present actuator model to predict the load transfer, the commercially available structure analysis software ANSYS is used to numerically analyze the stress field near a perfectly bonded actuator. In the current analysis, the material constants of the actuator and the matrix are given by (Park and Sun, 1994)

Actuator(PZT-4)

$$c_{11}^{(a)} = 13.9 \times 10^{10}(Pa), c_{12}^{(a)} = 6.78 \times 10^{10}(Pa), c_{13}^{(a)} = 7.43 \times 10^{10}(Pa)$$

$$c_{33}^{(a)} = 11.5 \times 10^{10}(Pa), c_{44}^{(a)} = 2.56 \times 10^{10}(Pa)$$

$$e_{31}^{(a)} = -5.2(C/m^2), e_{33}^{(a)} = 15.1(C/m^2), e_{15}^{(a)} = 12.7(C/m^2)$$

$$\lambda_{11}^{(a)} = 6.45 \times 10^{-9}(C/Vm), \lambda_{33}^{(a)} = 5.62 \times 10^{-9}(C/Vm)$$

36

Two different host media were considered as

Orthotropic medium

$$c_{11}^{(1)} = 13.92 \times 10^{10}(Pa), c_{22}^{(1)} = 160.7 \times 10^{10}(Pa)$$

$$c_{33}^{(1)} = 7.07 \times 10^{10}(Pa), c_{12}^{(1)} = 6.44 \times 10^{10}(Pa)$$

Isotropic medium

$$E^{(2)} = 15.4 \times 10^{11}(Pa), \nu^{(2)} = 0.3$$

The length of the actuator is assumed to be $a = 10h$ and thickness of the host medium is assumed to be infinity, in which $\lim_{H \to \infty} \overline{F}(s) = \frac{2}{\overline{E}}$. The orthotropic and isotropic media have the same effective modulus $\overline{E}$, which results in $q = \frac{\pi \overline{E}}{2E_a} = 3.019$. Figure 2.4 shows the comparison of the interfacial shear stress $\tau^* = \tau/\sigma_B$ distribution determined using the proposed model with the corresponding results from finite element method (FEM). The proposed analytical model predicts that interfacial stress uniquely depends on q in considering the effect of the material properties. It is very interesting to mention that FEM results from orthotropic and isotropic media give very close interfacial stress distributions. The discrepancy between the analytical prediction and the FEM results may be caused by the one-dimensional assumption of the actuator.

In the proposed model, the transverse normal stress σ_z is ignored. FEM analysis has been conducted to examine this assumption. Figure 2.5 shows the effects of the length of the actuator upon $\sigma_z^* = \sigma_z/\sigma_B$ for $H = 8h$ for $q = 2$. For very short actuator $v = a/h = 2$ and 5, significant σ_z^* can be observed even at the centre of the actuator. However, for $v = 10$ and 20, σ_z^* is significant only in the region close to the tip of the actuator, where high stress concentration exists. Figure 2.6 shows the effects of the thickness of the host medium upon σ_z^* for the same material combination in Figure 2.5 with $v = a/h = 10$. It can be observed that the axial stress distribution σ_z^* exists mainly near the tip of the actuator, which will increase

37

with the increase of the thickness of the host medium and eventually approach to coverage when $H > 8h$. Another important parameter, which represents the actuation process, is the maximum axial stress in the actuator. Figure 2.7 shows the comparison of the maximum axial stress $\sigma^*_{max} = \sigma_{max}/\sigma_B$, $\sigma_{max} = -\dfrac{1}{h}\displaystyle\int_{-a}^{0}\tau(y)dy$, determined from the proposed model with FEM results for the case presented in Figure 2.5. It can also be observed that when H/h approaches eight, the result of the proposed model shows good agreement with that from FEM. In addition, compared results in Figure 2.6 and 2.7, it can be found that the normal stress σ^*_z is much smaller than axial stress σ^*_{max}, which shows that normal stress can be ignored for thin actuator ($v > 10$). In conclusion, those comparisons indicate that the actuator model can provide reasonable prediction of the interfacial stress distribution (load transfer) for thin actuators ($v > 10$) which are bonded to the host medium with $H \geq 8h$.

2.5.2 Stress distribution along the interface

Figure 2.8 shows the distribution of the interfacial shear stress between the actuator and the host medium for $v = 10$ and $H = 8h$. The material constants of the orthotropic host medium are

$$c_{11}^{(h)} = 13.92 \times 10^{10}(Pa)$$

$$c_{33}^{(h)} = 7.07 \times 10^{10}(Pa), c_{12}^{(h)} = 6.44 \times 10^{10}(Pa)$$

Different values of c_{22} are used in the analysis, which correspond to different material combination $q = \dfrac{\pi \overline{E}}{2E_a}$. For the case where the actuator is relatively stiff, $q = 0.2$ for example, high shear stress level in the interior part of the actuator is observed. For softer actuator, $q = 5$, interfacial shear stress is mostly concentrated at the tips of the actuator, which corresponds to the so-called 'pin-force' model. Figure 2.9 shows the effect of the thickness of the host medium upon the interfacial shear stress distribution for $\alpha = 10$ and $q = 2$. It is observed that the interfacial shear stress increases with

38

the increase of the thickness of the host medium and approaches a stable distribution which corresponds to the case of an infinite host medium. It can be concluded that when $H \geq 15h$ the effect of the thickness of the host medium upon the interfacial shear stress can be ignored.

2.5.3 Effective modulus $\overline{E}$

One of the most important parameters governing the load transfer between the actuator and the host material is the effective modulus of the host medium $\overline{E}$ given by Equation (2.1.24). Figure 2.10 shows the effect of material anisotropy of the host medium upon the normalized effective modulus $E^* = \overline{E}/c_{11}$ for $\dfrac{c_{12}}{c_{11}} = 0.15$ and $H = 15h$. At this case, the thickness effect of the host medium can be ignored. It is observed that the effective modulus $\overline{E}$ is very sensitive to the shear modulus c_{33}. For cases where c_{22}/c_{11} is small (< 0.3 for example), c_{22} shows a significant effect upon $\overline{E}$, which corresponds to the case where $c_{33} > \dfrac{1}{2}(\sqrt{c_{11}c_{22}} - c_{12})$. In comparison, Figure 2.11 shows the effect of the Poisson ratio $\nu_{yz} = \dfrac{c_{12}}{c_{11}}$ upon $\overline{E}$ for $\dfrac{c_{33}}{c_{11}} = 0.1$ and $H = 15h$. It is interesting to note that the effective modulus is relatively insensitive to the change of the Poisson ratio for $\dfrac{c_{22}}{c_{11}} > 0.5$.

2.5.4 Singular stress field around the actuator

The singular stress field near the tip of the actuator can be obtained by using the substitution that

$$y = a + r\cos\theta, z = r\sin\theta \qquad (2.5.1)$$

and considering the asymptotic property of Equations (2.3.1)-(2.3.14) when $r \longrightarrow 0$.

For $c_{33} < (\sqrt{c_{11}c_{22}} - c_{12})/2$, the singular stress field is given by

$$\sigma_y = S\frac{[K_3 f_1(\beta_1, \theta_1) + K_4 f_1(\beta_2, \theta_2)]}{\sqrt{r\pi}} \qquad (2.5.2)$$

39

$$\sigma_z = S\frac{[K_5 f_1(\beta_1, \theta_1) + K_6 f_1(\beta_2, \theta_2)]}{\sqrt{r\pi}} \qquad (2.5.3)$$

$$\sigma_{yz} = -S\frac{[K_7 f_2(\beta_1, \theta_1) + K_8 f_2(\beta_2, \theta_2)]}{\sqrt{r\pi}} \qquad (2.5.4)$$

where

$$f_1(\beta_i, \theta_i) = \frac{\sin(|\theta_i|/2)}{\sqrt[4]{\cos^2\theta + \beta_i^2 \sin^2\theta}}, f_2(\beta_i, \theta_i) = \frac{\cos(|\theta_i|/2)}{\sqrt[4]{\cos^2\theta + \beta_i^2 \sin^2\theta}}, i = 0, 1, 2$$

$$\theta_0 = \arctan(\frac{\beta_0 \sin\theta}{\cos\theta}), \theta_1 = \arctan(\frac{\beta_1 \sin\theta}{\cos\theta}), \theta_2 = \arctan(\frac{\beta_2 \sin\theta}{\cos\theta})$$

For $c_{33} = (\sqrt{c_{11}c_{22}} - c_{12})/2$, the singular field is

$$\sigma_y = S\frac{[\overline{K}_3 f_1(\beta_0, \theta_0) - \overline{K}_4 a_1 f_1(\beta_0, \theta_0) - \overline{K}_4 a_2 \frac{\partial}{\partial\theta} f_1(\beta_0, \theta_0)]}{\sqrt{r\pi}} \qquad (2.5.5)$$

$$\sigma_z = S\frac{[-\overline{K}_6 a_1 f_1(\beta_0, \theta_0) - \overline{K}_6 a_2 \frac{\partial}{\partial\theta} f_1(\beta_0, \theta_0)]}{\sqrt{r\pi}} \qquad (2.5.6)$$

$$\sigma_{yz} = -S\frac{[\overline{K}_7 f_2(\beta_0, \theta_0) - \overline{K}_8 a_1 f_2(\beta_0, \theta_0) - \overline{K}_8 a_2 \frac{\partial}{\partial\theta} f_2(\beta_0, \theta_0)]}{\sqrt{r\pi}} \qquad (2.5.7)$$

where $a_1 = \sin^2\theta, a_2 = \sin\theta\cos\theta$.

For $c_{33} > (\sqrt{c_{11}c_{22}} - c_{12})/2$, the singular field is

$$\sigma_y = S\frac{[\overline{\overline{K}}_3 \overline{\overline{f}}_1(\theta_3, \theta_4) + \overline{\overline{K}}_4 \overline{\overline{f}}_2(\theta_3, \theta_4)]}{\sqrt{r\pi}} \qquad (2.5.8)$$

$$\sigma_z = S\frac{[\overline{\overline{K}}_5 \overline{\overline{f}}_1(\theta_3, \theta_4) + \overline{\overline{K}}_6 \overline{\overline{f}}_2(\theta_3, \theta_4)]}{\sqrt{r\pi}} \qquad (2.5.9)$$

$$\sigma_{yz} = -S\frac{[\overline{\overline{K}}_7 \overline{\overline{f}}_4(\theta_3, \theta_4) + \overline{\overline{K}}_8 \overline{\overline{f}}_3(\theta_3, \theta_4)]}{\sqrt{r\pi}} \qquad (2.5.10)$$

where

$$\overline{\overline{f}}_1(\theta_3, \theta_4) = \frac{1}{2}[f_3(\theta_3) + f_3(\theta_4)], \overline{\overline{f}}_2(\theta_3, \theta_4) = \frac{1}{2}[f_4(\theta_4) - f_4(\theta_3)]$$

$$\overline{\overline{f}}_3(\theta_3, \theta_4) = \frac{1}{2}[f_4(\theta_3) + f_4(\theta_4)], \overline{\overline{f}}_4(\theta_3, \theta_4) = \frac{1}{2}[f_3(\theta_3) - f_3(\theta_4)]$$

$$f_3(\theta_i) = \frac{\sin(|\theta_i|/2)}{\sqrt[4]{\beta_3^2 \sin^2\theta + (\beta_4\cos\theta + \sin\theta)^2}}$$

$$f_4(\theta_i) = \frac{\cos(|\theta_i|/2)}{\sqrt[4]{\beta_3^2 \sin^2\theta + (\beta_4\cos\theta + \sin\theta)^2}}, i = 3, 4$$

$$\theta_3 = \arctan(\frac{\beta_3 \sin\theta}{\beta_4 \sin^2\theta + \cos\theta}), \theta_4 = \arctan(\frac{\beta_3 \sin\theta}{\beta_4 \sin^2\theta - \cos\theta})$$

40

Figure 2.12 shows the angular distribution of the normalized singular stress field $f = \dfrac{\sqrt{r\pi}\sigma_B}{S}\sigma$ with different angle θ around the tip of the actuator, where σ represents $\sigma_{rr}, \sigma_{\theta\theta}$ and $\sigma_{r\theta}$, respectively. In this figure $\dfrac{c_{22}}{c_{11}} = 11.53$, $\dfrac{c_{12}}{c_{11}} = 0.46$ and $H = 15h$. $\xi = \dfrac{\sqrt{c_{11}c_{22}} - c_{12}}{2c_{33}}$ is assumed to be $0.25, 1, 4$, respectively, representing the three phases discussed before. As expected, the maximum shear stress always occurs at $\theta = 180°$, i.e. along the interface, the maximum $\sigma_{\theta\theta}$ occurs around $\theta = 40° - 60°$ ahead of the actuator, while for σ_{rr}, the maximum is at about $\theta = 130° - 150°$.

Figure 2.13 shows the normalized shear stress singularity factor $S^* = S/\sigma_B\sqrt{\pi h}$ for $\dfrac{c_{12}}{c_{22}} = 0.040$, $\dfrac{c_{33}}{c_{22}} = 0.044$, correspondingly, $q = 3.019$ and $H = 15h$. It shows a significant effect of the material anisotropy c_{11}/c_{22} upon the singular stress field around the tip of the actuator. With the increase of the length of the actuator (a/h), the singular field will approach a steady state, as evidenced by the fact that S^* tends to a constant for large a/h.

2.5.5   Stress distribution in host medium

Figure 2.14 shows the normalized stress distribution $\sigma_y^* = \sigma_y/\sigma_B$ in the host medium for $v = 10$, $\dfrac{c_{22}}{c_{11}} = 11.53$, $\dfrac{c_{12}}{c_{11}} = 0.46$, $\dfrac{c_{33}}{c_{11}} = 0.51$ and $H = 15h$. σ_y was found highly localized in an area near the tip of the actuator. Figure 2.15 shows the corresponding results for $\sigma_{yz}^* = \sigma_{yz}/\sigma_B$. For $z = 0.5h$ and $1.0h$, σ_{yz} undergoes a very sharp reduction around the tip of the actuator before it goes back to its 'normal' value. To further consider this issue, detailed FEM analysis was conducted, which did predict the same phenomenon. The numerical results for $z = 0.5h$ is compared with the corresponding analytical solution in Figure 2.16. A good agreement can be observed. This phenomenon had also been observed in other material combinations.

41

2.5.6 Axial stress and SSSF in central debonded actuator

For the general case of central debonding, the debonded part will not experience interfacial shear stress. However, its effect upon the load transfer will not disappear. In this case, the debonded region will affect the structure by applying a compressive (tensile) stress to the remaining parts of the actuator. Figure 2.17 shows the normalized compressive axial stress $\sigma^* = |\sigma_d|/\sigma_B$, in the debonded part of the actuator for the case where $v = 10$, $q = 2$ and $H = 15h$ with $d = d_l = d_r$. A significant effect of the anisotropic property of the host medium is observed. The axial stress σ^* in debonded part will decrease with the increase of the debonded region. Debonding along the actuator/host medium interface may also dramatically affect the load transfer between the actuator and the host structure. Figure 2.18 shows the shear stress singularity factor $(S^* = S/\sigma_B\sqrt{\pi h})$ at the ends of the debonding located at $|y| < d$, for the case considering in Figure 2.17. A dramatic increase of S^* can be observed with increasing d/a. The results indicate that the electrically induced central debonding of the actuator is an unsteady process, i.e. as soon as the debonding starts to grow, it will keep expanding until full debonding occurs, which is different from the self-arrest edge debonding case.

42
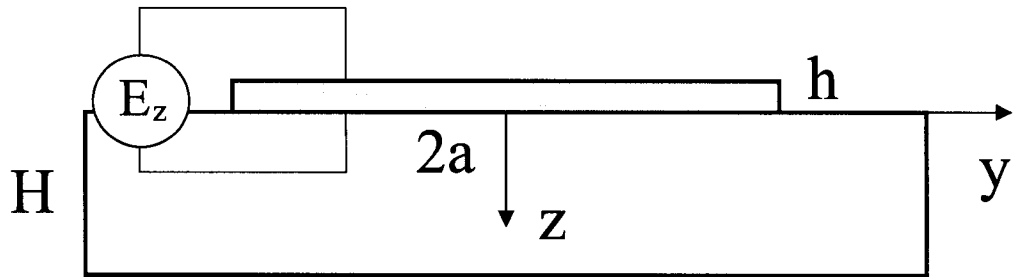
Figure 2.1: An actuator surface bonded to an orthotropic elastic medium
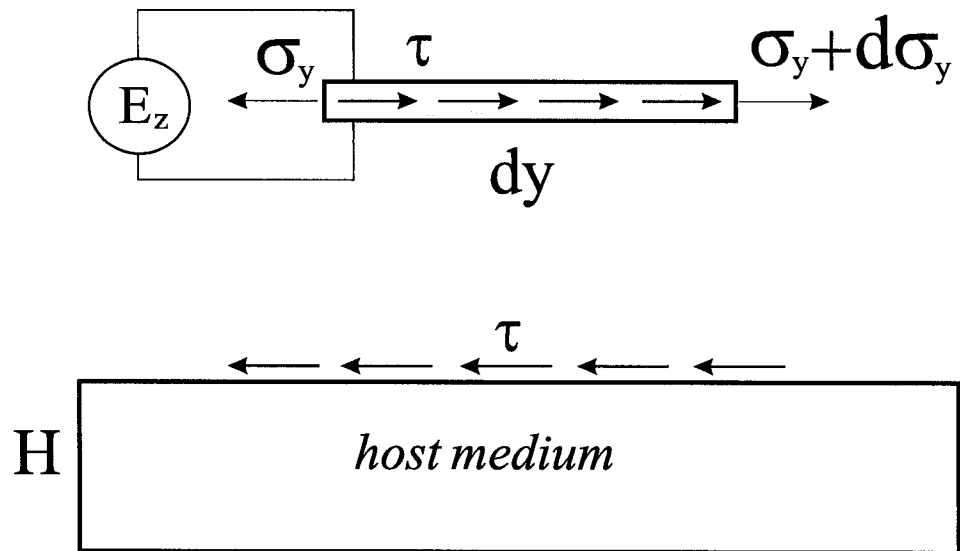
Figure 2.2: An actuator model for surface bonded actuator

43
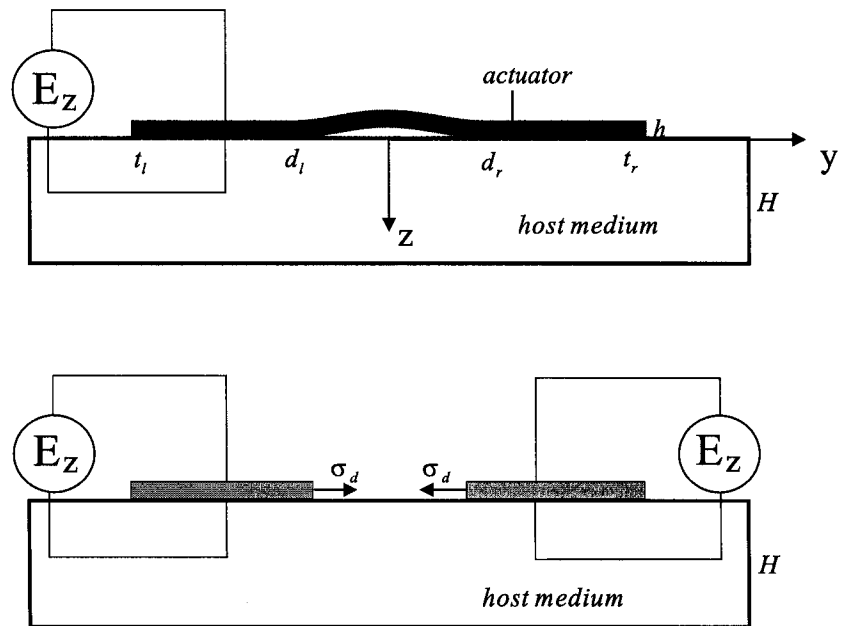
Figure 2.3: An actuator with a central debonding
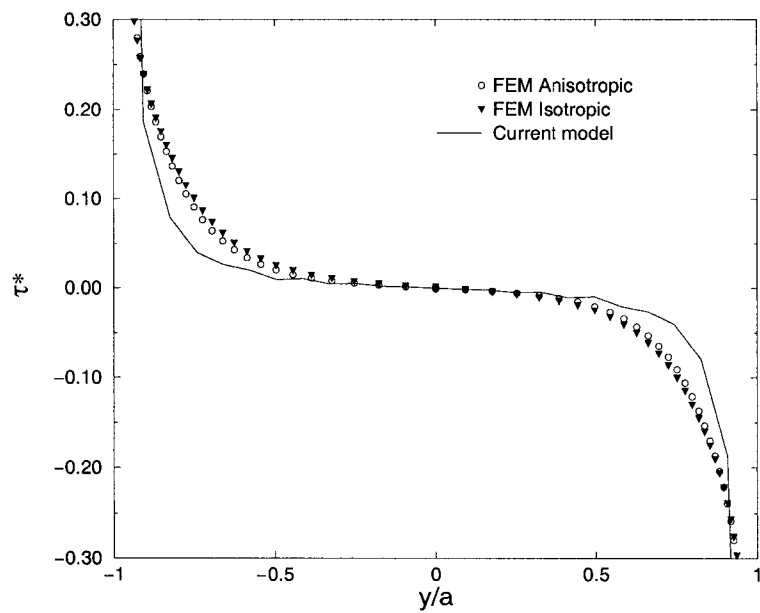
Figure 2.4: Comparison of the interfacial shear stress distribution with FEM results

44
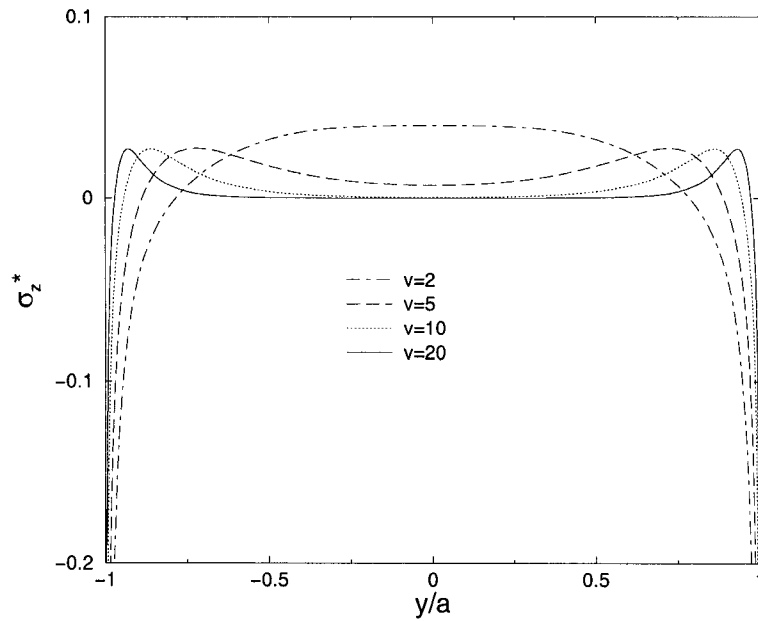
Figure 2.5: The normal stress along the interface for different v
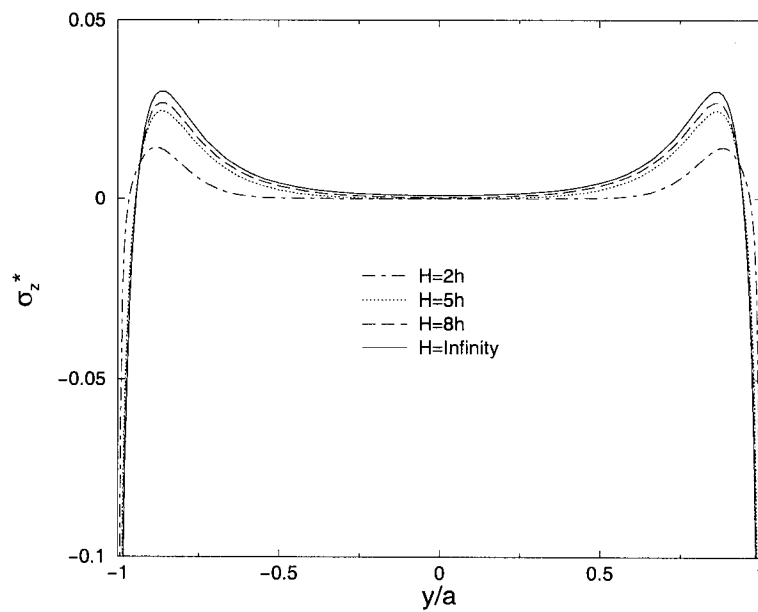
Figure 2.6: The normal stress along the interface for different H

45
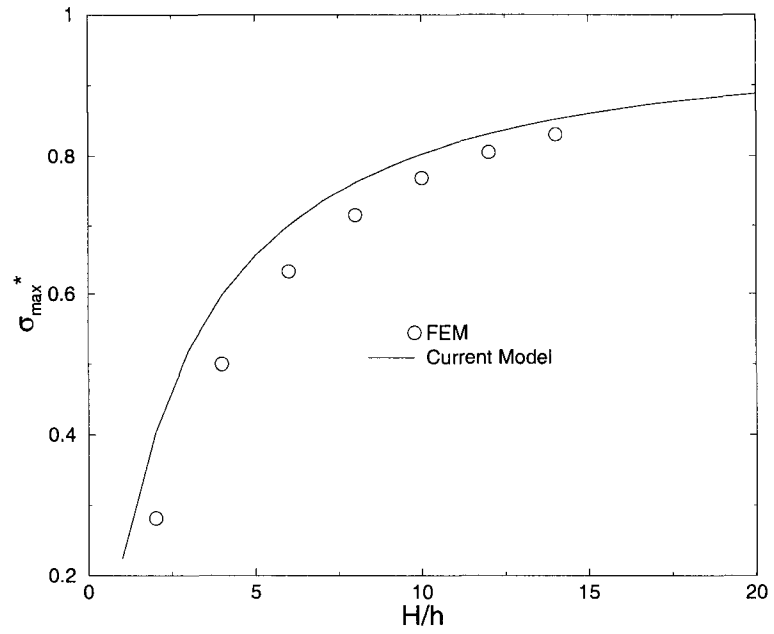
Figure 2.7: Comparison of the maximum axial stress in the actuator with FEM results
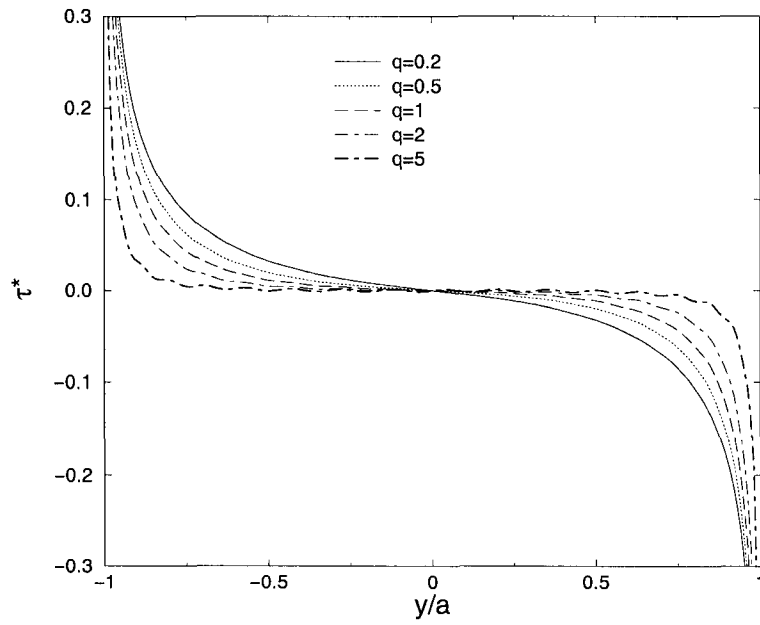
Figure 2.8: The normalize shear stress along the interface for different q

46
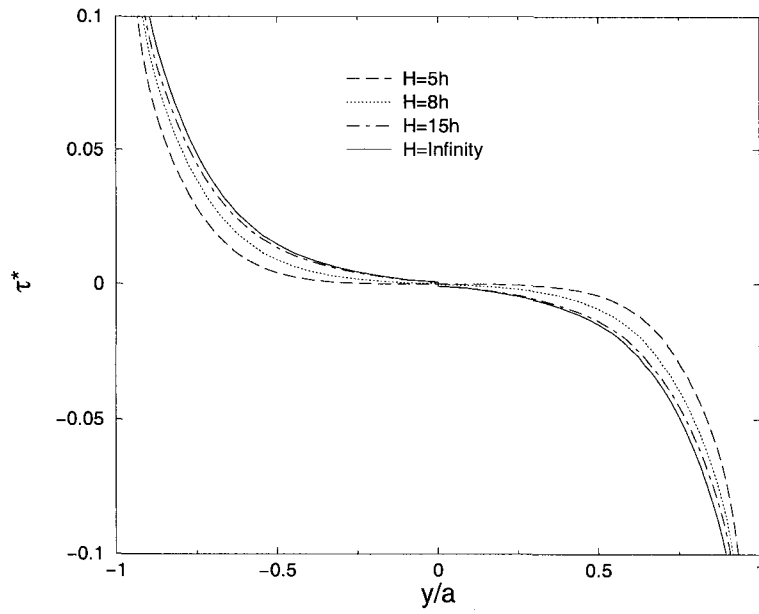
Figure 2.9: The normalize shear stress along the interface for different H
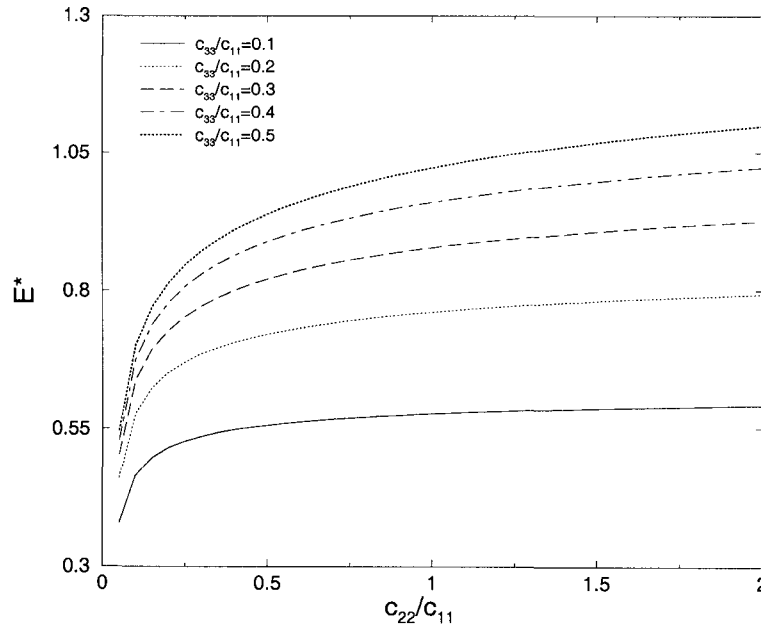
Figure 2.10: Effects of the material anisotropy on the effective modulus

47
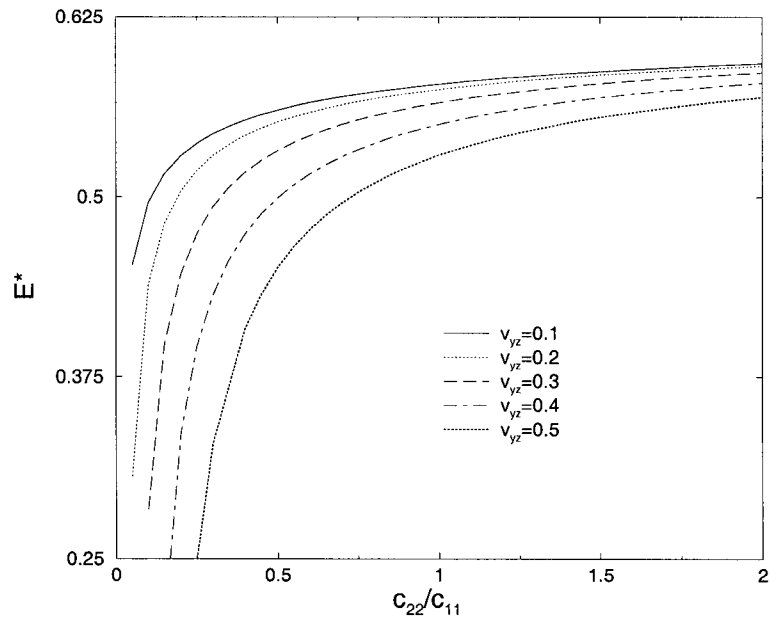
Figure 2.11: Effects of the Poisson ratio on the effective modulus
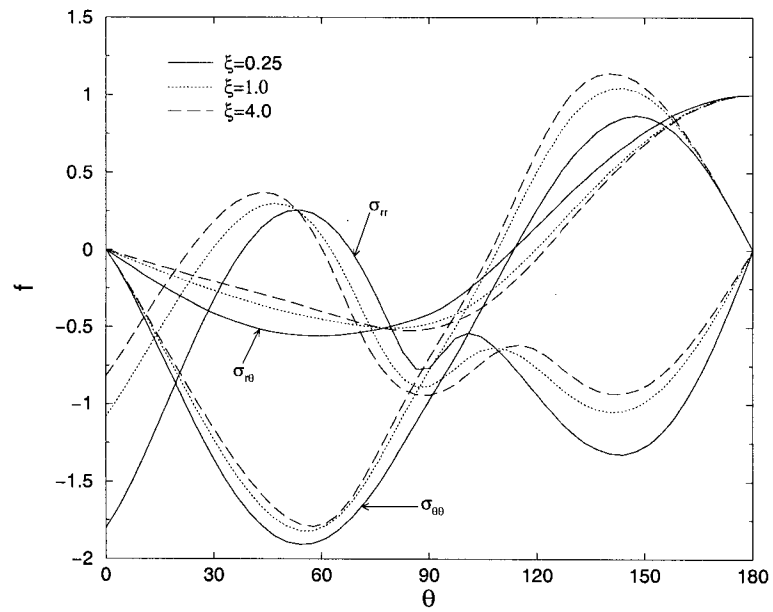
Figure 2.12: Angular distribution of the normalized stress

48
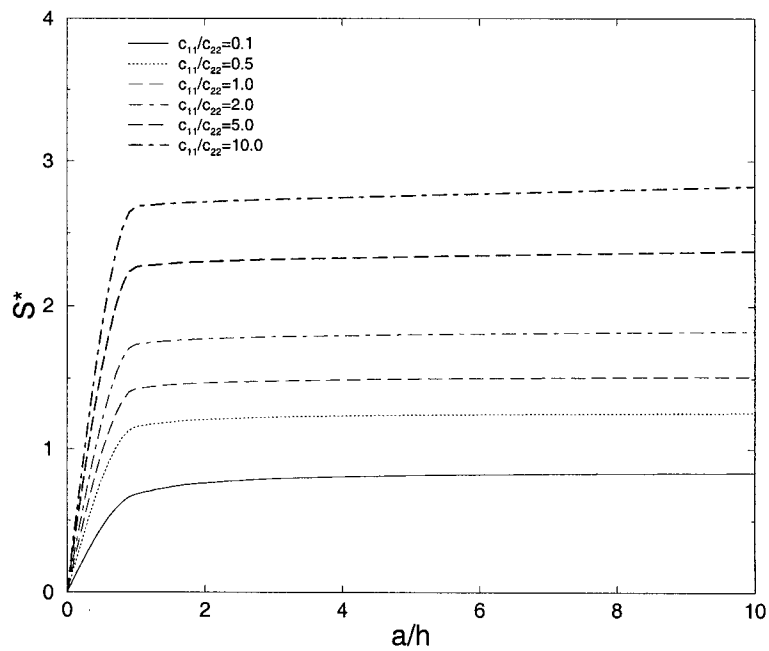
Figure 2.13: Normalized SSSF
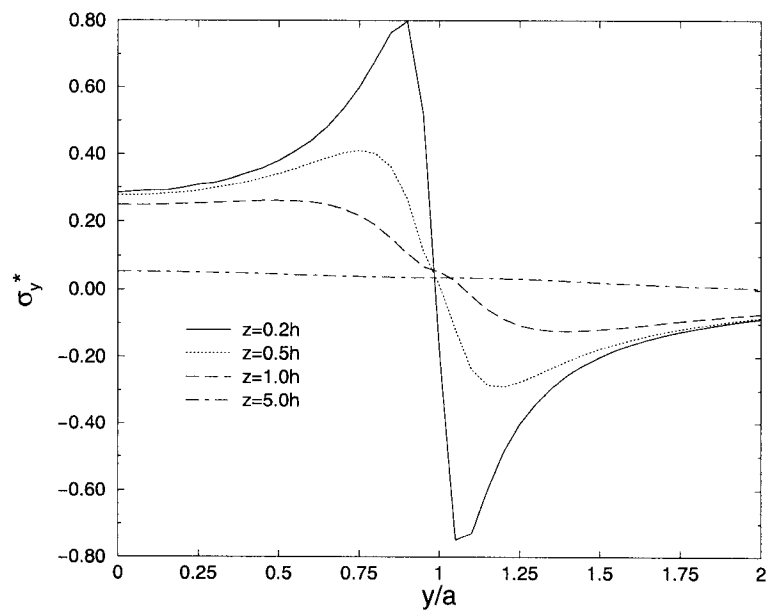
Figure 2.14: Normal stress distribution in the host medium

49
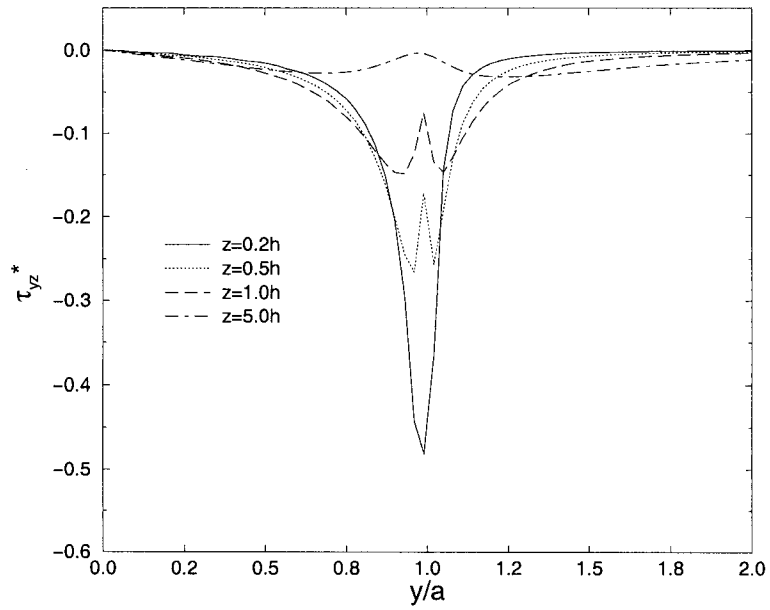
Figure 2.15: Shear stress distribution in the host medium
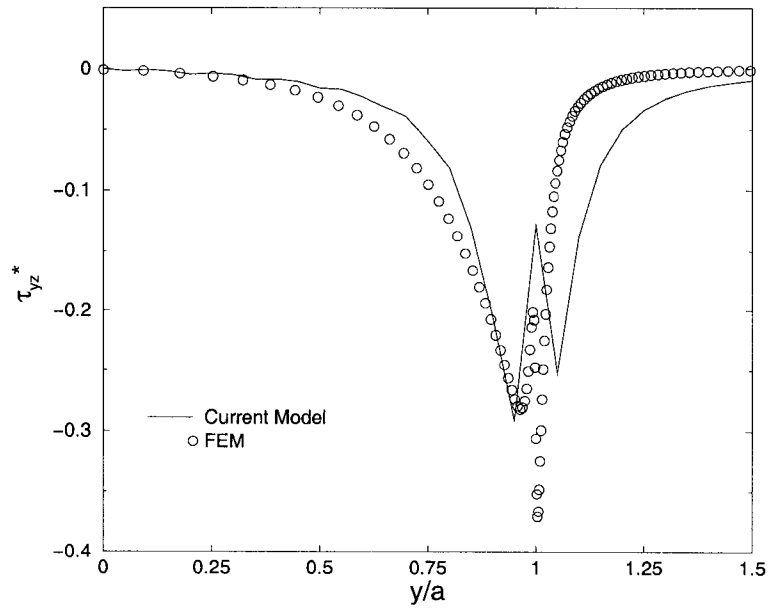
Figure 2.16: Comparison of the analytical shear stress distribution with FEM results

50
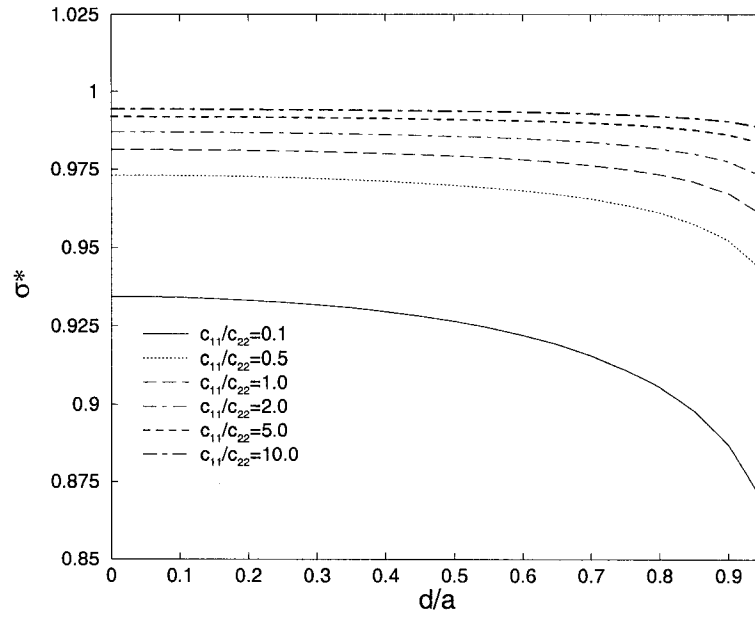
Figure 2.17: The axial stress in a debonded actuator
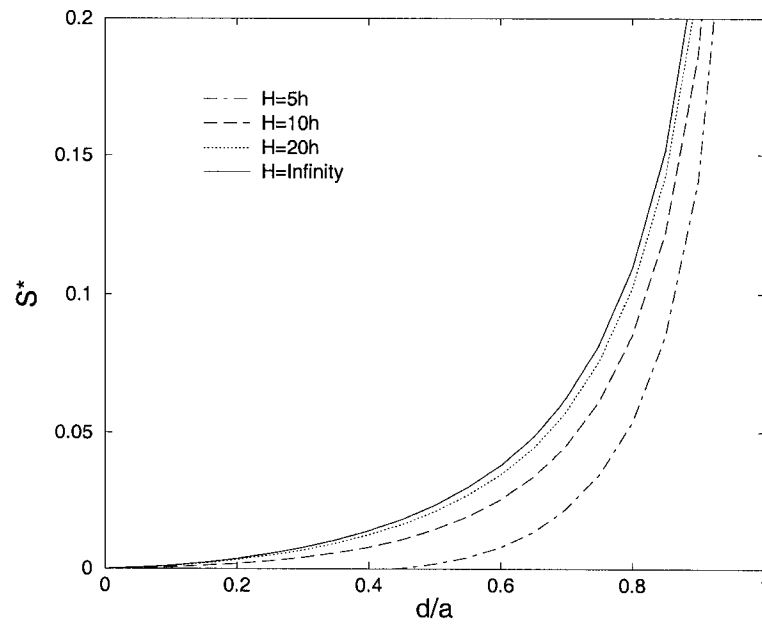
Figure 2.18: The normalized SSSF at the end of the interfacial debonding

51

Chapter 3

Wave Propagation with Surface Bonded Actuators

This chapter provides an analytical and numerical study to simulate the wave propagation in an elastic half plane with surface-bonded piezoceramic actuators under high-frequency electric loads. This solution is based on the developed one dimensional actuator model (Wang, 2000), and the resulting wave propagation induced by a single actuator is mainly focussed by using integral transform method and solving the resulting integral equations. The single actuator solution is then implemented into a Pseudo-Incident Wave method (PsWI) (Wang and Meguid, 1997) to study the wave propagation induced by multiple actuators. Three aspects of the work are examined. The first is concerned with the determination of the effects of the geometry, the material mismatch and the loading frequency upon the resulting waveform, while the second is concerned with the effect of the interaction between actuators upon the induced wave propagation. Finally, the behaviour of the surface Rayleigh wave and far field waveform generated by the surface-bonded piezoelectric actuators are investigated.

52

3.1 Formulation of the Problem

Consider the plane strain problem of M thin piezoceramic actuators surface-bonded to a homogeneous and isotropic elastic insulator, as illustrated in Figure 3.1(a). The half length and the thickness of actuator n are denoted as a_n and h_n, respectively. The position of the centre of actuator n is described by its coordinate in the global coordinate system, $(y_n^0, 0)$. A local coordinate system (y_n, z_n) will be used to describe actuator n with its origin at the centre of the actuator. It is assumed that the poling direction of the actuators is along the z-axis. A voltage between the upper and the lower electrodes of actuator n is applied, which results in an electric field E_z^n of frequency ω along the poling direction of the actuator, $E_z^n = (V_n^- - V_n^+)/h_n$. To study the resulting wave propagation, only the steady state response of the system will be considered. In this case, the displacement, strain, stress and electric fields of the system will generally involve a time factor $\exp(-i\omega t)$. For the sake of convenience, this factor will be suppressed and only the amplitude of the field variables will be considered.

3.2 Wave Propagation due to a Single Actuator

Let us first consider the case where only one actuator is attached to the host medium. The actuator will extend(contract) when an electric field is applied and consequently results in the deformation of the host elastic medium. Detailed description of this process involves the analysis of complicated local stress distribution around the actuator. Because the thickness of the actuator used is very small in comparison with its length, the applied electric field will mainly result in a deformation along the axial direction. Accordingly, the actuator can be modelled as an electroelastic line subjected to the applied electric field and a distributed axial force, τ, as shown in Figure 3.1(b), where τ is the interfacial shear stress transferred between the actuator and

53

the host structure.

3.2.1 The dynamic actuator model

The attention will be focussed on cases where high frequency electric field is applied, which results in a wave propagation with the typical wave length comparable to the length of the actuator. In this case, the inertia effect of the actuator must be considered. According to the actuator model, the equation of motion of the actuator can be expressed as (Wang, 2000)

$$\frac{d\sigma_y^a}{dy} + \tau(y)/h + \rho_a \omega^2 u_y^a = 0 \tag{3.2.1}$$

where ρ_a is the mass density of the actuator. The axial stress in the actuator can be expressed in terms of the axial displacement (u_y^a) and the electric field (E_z) as

$$\sigma_y^a = E_a \frac{\partial u_y^a}{\partial y} - e_a E_z \tag{3.2.2}$$

where E_a and e_a are effective material constants given in Equation (2.1.6).

The two ends of the surface-bonded actuator can be assumed to be traction free, i.e.

$$\sigma_y^a = 0, \quad |y| = a. \tag{3.2.3}$$

Base on the actuator model and boundary conditions, the axial strain of the actuator for an applied τ can be obtained by solving Equation (3.2.1) as

$$\varepsilon_y^a(y) = \varepsilon_E(y) + \frac{\sin k_a(a+y)}{h E_a \sin 2k_a a} \int_{-a}^{a} \cos k_a(\xi - a)\tau(\xi)d\xi$$
$$- \int_{-a}^{y} \cos k_a(\xi - y)\frac{\tau(\xi)}{h E_a}d\xi \tag{3.2.4}$$

where

$$\varepsilon_E(y) = \varepsilon_0 \frac{\cos k_a y}{\cos k_a a} \tag{3.2.5}$$

54

is the axial strain of a free actuator caused by E_z and

$$\varepsilon_0 = \frac{E_z e_a}{E_a}, \quad k_a = \omega/c_a, \quad c_a = \sqrt{E_a/\rho_a} \tag{3.2.6}$$

with k_a and c_a being the wave number and the axial wave speed of the actuator, respectively.

3.2.2 Elastodynamic governing equation

The dynamic plane strain displacement field in a homogeneous isotropic elastic medium is governed by (Achenbach, 1973),

$$u_y = \frac{\partial \Phi}{\partial y} + \frac{\partial \Psi}{\partial z}, \qquad u_z = \frac{\partial \Phi}{\partial z} - \frac{\partial \Psi}{\partial y} \tag{3.2.7}$$

where Φ and Ψ are two displacement potentials which satisfy

$$(\nabla^2 + K^2)\Phi = 0, \qquad (\nabla^2 + k^2)\Psi = 0 \tag{3.2.8}$$

in which the Laplacian operator ∇^2 stands for $\dfrac{\partial^2}{\partial y^2} + \dfrac{\partial^2}{\partial z^2}$ and K and k are two wave numbers defined as

$$K = \omega/c_L, k = \omega/c_T$$

with c_L and c_T being the longitudinal and transverse shear wave speeds of the elastic medium, respectively.

An incident wave and/or an applied electric field will result in a wave propagating in the elastic matrix. The general solution of the induced wave can be determined by solving the governing equations using the Fourier transform with respect to y, which is defined in Equations (2.1.15) and (2.1.16), as

$$\overline{u}_y = -isA(s)e^{-\alpha z} - \beta B(s)e^{-\beta z} \tag{3.2.9}$$

$$\overline{u}_z = -\alpha A(s)e^{-\alpha z} + isB(s)e^{-\beta z} \tag{3.2.10}$$

55

$A(s)$ and $B(s)$ are two unknown functions of s, and α and β are given by

$$\alpha = \begin{cases} \sqrt{s^2 - K^2} & |s|>K \\[2mm] -i\sqrt{K^2 - s^2} & |s|<K \end{cases} \qquad \beta = \begin{cases} \sqrt{s^2 - k^2} & |s|>k \\[2mm] -i\sqrt{k^2 - s^2} & |s|<k \end{cases} \qquad (3.2.11)$$

which ensure that the induced stress field satisfies the radiation condition of the problem. The outgoing wave in the host medium should satisfy the following conditions along its surface,

$$\begin{cases} \sigma_{yz}(y,0) = -\tau & |y| < a \\[2mm] \sigma_{yz}(y,0) = 0 & |y| > a \end{cases} , \quad \sigma_z(y,0) = 0 \qquad (3.2.12)$$

Making using of the general solution of $\bar{u}_y$ and $\bar{u}_z$ and the boundary conditions, the unknown parameters $A(s)$ and $B(s)$ can be determined in terms of τ. Therefore, the resulting dynamic strain in the host medium along the surface can be obtained as

$$\varepsilon_y(y,0)|_{host} = \frac{\lambda_0}{2\pi\mu}[\int_{-a}^{a} \frac{\tau(\xi)}{y-\xi}d\xi - \int_{-a}^{a} \tau(\xi)m_1(y-\xi)d\xi] \qquad (3.2.13)$$

where μ is the shear modulus of the elastic medium, $\lambda_0 = 2(1 - \nu)$ with ν being the Poisson's ratio, and

$$m_1(y - \xi) = \int_0^{\infty} (\frac{2k^2 s\beta}{\lambda_0[(2s^2 - k^2)^2 - 4s^2\alpha\beta]} + 1)\sin s(y - \xi)ds. \qquad (3.2.14)$$

The kernel of the integration in (3.2.14) becomes singular when $(2s^2 - k^2)^2 - 4s^2\alpha\beta$ approaches zero, which corresponds to the well-known Rayleigh wave speed. This singular property will be used in the following discussion to determine the behaviour of Rayleigh wave propagation.

In general cases, an actuator will be subjected to an incident mechanical wave induced by applied load or other actuators. The continuity of deformation between the actuator and the host structure indicates that

$$\varepsilon_y^a(y) = \varepsilon_y(y) + \varepsilon_y^I(y) \quad |y| < a, \quad z = 0 \qquad (3.2.15)$$

where ε_y is the outgoing wave and the superscripts 'a' and 'I' represent the actuator and the incident wave, respectively. By substituting Equations (3.2.4) and (3.2.13)

56

into Equation (3.2.15), the following integral equation can be obtained

$$-qv\frac{\sin k_a(a+y)}{\sin 2k_a a}\int_{-a}^{a}\cos k_a(\xi - a)\tau(\xi)du + qv\int_{-a}^{y}\cos k_a(\xi - y)\tau(\xi)d\xi$$

$$+\int_{-a}^{a}\frac{\tau(\xi)d\xi}{y - \xi} - \int_{-a}^{a}\tau(\xi)m_1(y-\xi)d\xi = \varepsilon_E(y) - \varepsilon_y^I, \quad |y| < a \quad (3.2.16)$$

where

$$q = \frac{\pi\overline{E}}{2E_a}, \overline{E} = \frac{E}{1-\nu^2}, v = \frac{a}{h}$$

with E being the Young's modulus of the host medium. ε_y^I is the strain of the incident field and ε_E is the electric load given by (3.2.5).

Equation (3.2.16) is a first kind of singular integral equation. The general solution of τ can be expressed in terms of Chebyshev polynomials, such that

$$\tau(y) = \sum_{j=0}^{\infty} c_j T_j(y/a)/\sqrt{1 - y^2/a^2} \quad (3.2.17)$$

where $c_0 = 0$ due to $\int_{-a}^{a}\tau(\xi)d\xi = 0$.

If the expansions in (3.2.17) are truncated to the Nth term and Equation (3.2.16) is satisfied at the following collocation points

$$y^l = a\cos[\frac{l-1}{N-1}\pi], \quad l = 1, 2, \cdots, N \quad (3.2.18)$$

N linear algebraic equations in terms of $\{c\} = \{c_1, c_2, \cdots, c_N\}^T$ can be obtained as

$$[A]\{c\} = \{F\} \quad (3.2.19)$$

where the matrix $[A]$ is given by

$$A_{lj} = -\pi\sum_{j=1}^{\infty}c_j\frac{\sin[j\cos^{-1}\eta^l]}{\sin[\cos^{-1}\eta^l]} + qv\sum_{j=1}^{\infty}c_j\int_{\cos^{-1}\eta^l}^{\pi}\cos[\overline{k_a}(\cos\theta - \eta^l)]\cos(j\theta)d\theta$$

$$+\pi\sum_{j=1}^{\infty}c_j\int_{0}^{\infty}P_j^1(\overline{s}, \eta^l)(\frac{2\overline{k}^2\overline{s}\beta}{\lambda_0[(2\overline{s}^2 - \overline{k}^2)^2 - 4\overline{s}^2\overline{\alpha\beta}]} + 1)d\overline{s} - qv\frac{\sin[\overline{k_a}(\eta^l + 1)]}{\sin(2\overline{k_a})}\sum_{j=1}^{\infty}c_jP_j^2$$

In above equations,

$$\eta^l = y^l/a, \quad \overline{K} = Ka, \quad \overline{k} = ka, \quad \overline{k_a} = k_a a, \quad \overline{s} = sa$$

57

and

$$P_j^1(\overline{s}, \eta^l) = J_j(\overline{s}) \begin{cases} (-1)^n \cos(\overline{s}\eta^l) & j = 2n+1 \\ (-1)^{n+1} \sin(\overline{s}\eta^l) & j = 2n \end{cases}$$

$$P_j^2 = J_j(\overline{k}_a) \begin{cases} (-1)^n \sin(\overline{k}_a) & j = 2n+1 \\ (-1)^n \cos(\overline{k}_a) & j = 2n \end{cases} \Bigg\}$$

with J_j $(j = 1, 2 \cdots)$ being the Bessel functions of the first kind. $\overline{\alpha}, \overline{\beta}$ can be obtained from α, β directly, with s, K, k being replaced by $\overline{s}$, $\overline{K}$, $\overline{k}$, respectively.

The loading matrix $\{F\}$ is given by

$$\{F\} = \{\varepsilon_E\} + \{\varepsilon^I\} \tag{3.2.20}$$

with

$$\varepsilon_{Ej} = \frac{\cos \overline{k}_a \eta^j}{\cos \overline{k}_a}, \quad \varepsilon_j^I = -\frac{E_a}{e_a E_z} \varepsilon_y^I(\eta^j, 0)$$

From these equations, the unknown coefficients in $\{c\}$, which represent the interfacial shear stress τ, can be determined. Based on the solution of interfacial shear stress, the singular behaviour near the tips of the actuator can be characterized by a shear stress singularity factor (SSSF), S, defined by

$$S_r = \lim_{y \to a} [\sqrt{2\pi(a-y)}\tau(y)] = \sqrt{a\pi} \sum_{j=1}^{N} c_j$$

$$S_l = \lim_{y \to -a} [\sqrt{2\pi(a+y)}\tau(y)] = \sqrt{a\pi} \sum_{j=1}^{N} (-1)^j c_j \tag{3.2.21}$$

with subscript $'r'$ and $'l'$ representing right and left tips of the actuator, respectively.

3.2.3 Wave propagation and far field solution

By inverse Fourier transform to the general solutions (3.2.9) and (3.2.10) and using the elastic constitutive relation, the general solutions of the induced wave can be obtained as

$$\sigma_y(y, z) = \sum_{j=1}^{N} c_j \begin{cases} (-1)^n \int_0^\infty H_1^s(s, z) J_j(sa) \cos(sy) ds & j = 2n+1 \\ \\ (-1)^{n+1} \int_0^\infty H_1^s(s, z) J_j(sa) \sin(sy) ds & j = 2n \end{cases} \tag{3.2.22}$$

58

$$\sigma_z(y,z) = \sum_{j=1}^{N} c_j \begin{cases} (-1)^n \int_0^\infty H_2^s(s,z) J_j(sa) \cos(sy) ds & j = 2n+1 \\[2mm] (-1)^{n+1} \int_0^\infty H_2^s(s,z) J_j(sa) \sin(sy) ds & j = 2n \end{cases} \tag{3.2.23}$$

$$\sigma_{yz}(y,z) = \sum_{j=1}^{N} c_j \begin{cases} (-1)^n \int_0^\infty H_3^s(s,z) J_j(sa) \sin(sy) ds & j = 2n+1 \\[2mm] (-1)^n \int_0^\infty H_3^s(s,z) J_j(sa) \cos(sy) ds & j = 2n \end{cases} \tag{3.2.24}$$

where $H_1^s(s,z), H_2^s(s,z), H_3^s(s,z)$ are given by

$$H_1^s(s,z) = \frac{2s\beta[(k^2+2\alpha^2)e^{-\alpha z} - (2s^2-k^2)e^{-\beta z}]}{(2s^2-\beta^2)^2 - 4s^2\alpha\beta}$$

$$H_2^s(s,z) = \frac{2s\beta(2s^2-k^2)(e^{-\beta z} - e^{-\alpha z})}{(2s^2-\beta^2)^2 - 4s^2\alpha\beta}$$

$$H_3^s(s,z) = \frac{4s^2\alpha\beta e^{-\alpha z} - (2s^2-k^2)^2 e^{-\beta z}}{(2s^2-\beta^2)^2 - 4s^2\alpha\beta}$$

Although the resulting waveform is very complicated as Equations (3.2.22)-(3.2.24), the fundamental behaviour of the propagating wave can be predicted from wave field far away from the actuator. For any far field point in the polar coordinate, its position can be represented as

$$y = R\cos\theta, \quad z = R\sin\theta, \quad 0 < \theta < \pi \tag{3.2.25}$$

where R denotes the distance from the center of the actuator, θ denotes the position angle with respect to y axis. Making using of the relation of

$$e^{isy} = \cos sy + i \sin sy \tag{3.2.26}$$

the typical stress wave $\sigma_y(y,z)$ in the far field can be rewritten as

$$\sigma_y^f(y,z) = \sigma_y^R + \int_{-\infty}^{\infty} \frac{2N_j^1 J_j(sa)s\beta(k^2+2\alpha^2)e^{-R(\alpha\sin\theta - is\cos\theta)}}{(2s^2-\beta^2)^2 - 4s^2\alpha\beta} ds$$
$$- \int_{-\infty}^{\infty} \frac{2N_j^1 J_j(sa)s\beta(2s^2-k^2)e^{-R(\beta\sin\theta - is\cos\theta)}}{(2s^2-\beta^2)^2 - 4s^2\alpha\beta} ds \tag{3.2.27}$$

59

where σ^R represents the Rayleigh wave field due to the singularity of the above integral and

$$N_j^1 = \begin{cases} \dfrac{(-1)^n}{2} & j = 2n+1 \\[3mm] \dfrac{(-1)^{n+1}}{2i} & j = 2n \end{cases}$$

For $R >> 1$, the Rayleigh wave σ_y^R, which will decay exponentially with the distance from the free surface, will be ignored in the far field solution. The existence of Rayleigh wave along the free surface will be discussed in the next subsection. For equation (3.2.27), since the exponential functions $e^{-R(\beta\sin\theta - is\cos\theta)}$ and $e^{-R(\alpha\sin\theta - is\cos\theta)}$ are rapidly changing functions compared with kernel functions in the above obtained integral, the dominant contribution to the integral comes from the neighborhood of the point $s = s_0$, where $(\beta\sin\theta - is\cos\theta)$ or $(\alpha\sin\theta - is\cos\theta)$ is the smallest, and the accuracy of that dominant contribution improves with increasing R. The method of steepest descent (Achenbach, 1973) takes advantage of this fact by deforming the integration path so that it goes through the saddle point s_0 along the path of steepest decent. For example, for the power function $\lambda_0(s) = \alpha\sin\theta - is\cos\theta$, the saddle point s_0 of function can obtained by $\dfrac{d\lambda_0(s)}{ds} = 0$ as $s_0 = K\cos\theta$. Around the saddle point, the function $\lambda_0(s)$ has the form

$$\lambda_0(s) = \lambda(s)|_{s=s_0} + \frac{1}{2}(s-s_0)^2\lambda''(s)|_{s=s_0} + \cdots \tag{3.2.28}$$

Since along the steepest decent path, the value of $\lambda_0(s) - \lambda(s)|_{s=s_0}$ should be real and positive, the real variable t_0 can be introduced as

$$\frac{1}{2}(s-s_0)^2\lambda_0''(s)|_{s=s_0} = t_0^2 \tag{3.2.29}$$

Similarly, for function $\lambda_1(s) = \beta\sin\theta - is\cos\theta$, the saddle point $s_1 = k\cos\theta$ along the path of steepest decent can be found and the real variable t_1 can be introduced as

$$\frac{1}{2}(s-s_1)^2\lambda_1''(s)|_{s=s_1} = t_1^2 \tag{3.2.30}$$

60

Therefore, the Equation (3.2.27) can be reduced to

$$\sigma_y^f(y, z) = G_0(s)|_{s=s_0} e^{-R\lambda_0(s)|_{s=s_0}} \int_{-\infty}^{\infty} e^{-Rt_0^2}(\frac{ds}{dt_0})dt_0$$
$$- G_1(s)|_{s=s_1} e^{-R\lambda_1(s)|_{s=s_1}} \int_{-\infty}^{\infty} e^{-Rt_1^2}(\frac{ds}{dt_1})dt_1 \qquad (3.2.31)$$

where

$$G_0(s) = \frac{2N_j^1 J_j(sa)s\beta(k^2 + 2\alpha^2)e^{-R(\alpha\sin\theta - is\cos\theta)}}{(2s^2 - \beta^2)^2 - 4s^2\alpha\beta}, \qquad (3.2.32)$$

$$G_1(s) = \frac{2N_j^1 J_j(sa)s\beta(2s^2 - k^2)e^{-R(\beta\sin\theta - is\cos\theta)}}{(2s^2 - \beta^2)^2 - 4s^2\alpha\beta}. \qquad (3.2.33)$$

Based on the fact that t_0^2 and t_1^2 are real function, the direction of the steepest decent path at $s = s_0$ and $s = s_1$ can be determined using

$$arg[\lambda_0^{''}(s)|_{s=s_0} e^{2i\theta_{s0}}] = 0, \quad arg[\lambda_1^{''}(s)|_{s=s_1} e^{2i\theta_{s1}}] = 0 \qquad (3.2.34)$$

as $\theta_{s0} = \theta_{s1} = -\frac{\pi}{4}$. Making use of the following relation

$$\int_{-\infty}^{\infty} e^{-Rt^2} dt = (\frac{\pi}{R})^{\frac{1}{2}} \qquad (3.2.35)$$

the analytical solution for far field elastic wave can be determined as

$$\sigma_y^f = \sum_{j=1}^{N} c_j N_j^1 [f_1(j, \theta)\sqrt{\frac{2\pi K}{R}} e^{i(KR-\frac{\pi}{4})} + f_2(j, \theta)\sqrt{\frac{2\pi k}{R}} e^{i(kR-\frac{\pi}{4})}] \qquad (3.2.36)$$

where

$$f_1(j, \theta) = \frac{g_1(j, \theta)}{m(\theta)}, \quad f_2(j, \theta) = \frac{g_2(j, \theta)}{n(\theta)},$$

$$m(\theta) = (2K^2\cos^2\theta - k^2)^2 + 4k^3\sin\theta\cos^2\theta\sqrt{k^2 - K^2\cos^2\theta}$$

$$n(\theta) = (2k^2\sin^2\theta - k^2)^2 + 4ik^3\sin\theta\cos^2\theta \begin{cases} \sqrt{k^2\cos^2\theta - K^2} & k\cos\theta > K \\ \\ -i\sqrt{K^2 - k^2\cos^2\theta} & k\cos\theta < K \end{cases}$$

$$g_1(j, \theta) = -2KiJ_j(K\cos\theta)\cos\theta\sin\theta\sqrt{k^2 - K^2\cos^2\theta}(k^2 - 2K^2\sin^2\theta)$$

$$g_2(j, \theta) = 2k^2 iJ_j(k\cos\theta)\sin^2\theta\cos\theta(2k^2\cos^2\theta - k^2)$$

61

Similarly, the far field solution of stress components σ_z and σ_{yz} can be obtained as

$$\sigma_z^f = \sum_{j=1}^{N} c_j N_j^1 [f_3(j,\theta)\sqrt{\frac{2\pi K}{R}}e^{i(KR-\frac{\pi}{4})} + f_4(j,\theta)\sqrt{\frac{2\pi k}{R}}e^{i(kR-\frac{\pi}{4})}] \qquad (3.2.37)$$

$$\sigma_{yz}^f = \sum_{j=1}^{N} c_j N_j^2 [f_5(j,\theta)\sqrt{\frac{2\pi K}{R}}e^{i(KR-\frac{\pi}{4})} + f_6(j,\theta)\sqrt{\frac{2\pi k}{R}}e^{i(kR-\frac{\pi}{4})}] \qquad (3.2.38)$$

where

$$N_j^2 = \begin{cases} \dfrac{(-1)^n}{2i} & j = 2n+1 \\[2mm] \dfrac{(-1)^n}{2} & j = 2n \end{cases}$$

and

$$f_3(j,\theta) = \frac{g_3(j,\theta)}{m(\theta)}, \quad f_4(j,\theta) = f_4(j,\theta), \quad f_5(j,\theta) = \frac{g_5(j,\theta)}{m(\theta)}, \quad f_6(j,\theta) = \frac{g_6(j,\theta)}{n(\theta)}$$

$$g_3(j,\theta) = 2KiJ_j(K\cos\theta)\sin\theta\cos\theta\sqrt{k^2 - K^2\cos^2\theta}(2K^2\cos^2\theta - k^2)$$

$$g_4(j,\theta) = -2k^2 iJ_j(k\cos\theta)\sin^2\theta\cos\theta(2k^2\cos^2\theta - k^2)$$

$$g_5(j,\theta) = -4iK^3 J_j(K\cos\theta)\sin^2\theta\cos^2\theta\sqrt{k^2 - K^2\cos^2\theta}$$

$$g_6(j,\theta) = -J_j(k\cos\theta)\sin\theta(2k^2\cos^2\theta - k^2)^2$$

However, for some specific positions $y = 0$ and $z \longrightarrow \infty$, at which the phase of $\lambda_0(z)$ and $\lambda_1(z)$ becomes zero, the method of steepest descents will break down. For this case, an simplified solutions can be directly obtained as

$$\sigma_y^f = \sum_{j=1}^{N} c_j [\frac{W_1(j)}{z}e^{-iKz} + \frac{W_2(j)}{z}e^{-ikz}], \qquad (3.2.39)$$

$$\sigma_z^f = \sum_{j=1}^{N} c_j [\frac{W_3(j)}{z}e^{-iKz} + \frac{W_2(j)}{z}e^{-ikz}], \qquad (3.2.40)$$

$$\sigma_{yz}^f = \sum_{j=1}^{N} c_j [\frac{W_4(j)}{z}e^{-iKz} + \frac{W_5(j)}{z}e^{-ikz}] \qquad (3.2.41)$$

where

$$W_1(j) = \frac{-2N_j^1 J_j(K)\sqrt{k^2 - K^2}k^2 K}{(2K^2 - k^2)^2}, W_2(j) = 2N_j^1 J_j(k), W_5(j) = N_j^2 J_j(k),$$

$$W_3(j) = \frac{2N_j^1 J_j(K)\sqrt{k^2 - K^2}K}{(2K^2 - k^2)}, W_4(j) = \frac{4N_j^2 J_j(K)\sqrt{k^2 - K^2}K^3}{(2K^2 - k^2)^2}.$$

3.3 Rayleigh Wave Propagation

Because of the existence of the free surface, the Rayleigh wave, which propagates along the surface, will be generated. This wave shows no decay during propagation for ideal linear elastic medium and, therefore, is useful for detecting surface defects. To evaluate the behaviour of the Rayleigh wave generated, let consider the stress σ_y along the free surface,

$$\sigma_y(y,0) = \sum_{j=1}^{N} c_j \begin{cases} (-1)^n \int_0^\infty f(s) J_j(sa) \cos(sy)ds & j = 2n + 1 \\ \\ (-1)^{n+1} \int_0^\infty f(s) J_j(sa) \sin(sy)ds & j = 2n \end{cases} \tag{3.3.1}$$

where

$$f(s) = \frac{4(k^2 - K^2)s\beta}{(2s^2 - k^2)^2 - 4s^2\alpha\beta} \tag{3.3.2}$$

It is well known that $F(s) = (2s^2 - k^2)^2 - 4s^2\alpha\beta$ approaches zero at a special value $s = s_r$, i.e. the integral becomes singular when $s \longrightarrow s_r$, where $s_r = \dfrac{\omega}{c_R}$, with c_R being the speed of the Rayleigh wave. $f(s)$ can be rewritten around $s = s_r$ as

$$f(s) \approx \frac{g_r}{s - s_r}, \quad s \longrightarrow s_r \tag{3.3.3}$$

with

$$g_r = \frac{4(k^2 - K^2)s\beta}{F'(s)} \Big|_{s=s_r} \tag{3.3.4}$$

This singular term represents the contribution of the Rayleigh wave. The resulting Rayleigh wave can be separated from (3.3.1) using path integration method and the integral path shown in Figure 3.2. The resulting Rayleigh wave can be obtained as,

$$\sigma_y^R(y,0) = Ae^{i(s_r y + \theta)} \tag{3.3.5}$$

where

$$Ae^{i\theta} = \pi \sum_{j=1}^{N} c_j g_r J_j(s_r a) \begin{cases} (-1)^n i & j = 2n + 1 \\ \\ (-1)^{n+1} & j = 2n \end{cases} \tag{3.3.6}$$

with A and θ being the amplitude and phase angle of the resulting Rayleigh wave.

63

3.4 Interaction between Actuators

For the case where multiple actuators are involved, the interaction between actuators significantly affects the load transfer between the actuators and the host structure. Let us consider a system of M surface bonded actuators. Because of the interaction between different actuators, the incident wave for actuator n includes, in addition to the initial incident wave ε_n^0, wave from other actuators ε_n^p. Therefore, for actuator n subjected to an electric field E_z^n, the total incident wave can be expressed as (Wang, 2000)

$$\varepsilon_n^I = \varepsilon_n^0 + \varepsilon_n^p \tag{3.4.1}$$

The total pseudo incident field of actuator n can be obtained by summing up outgoing waves from all other actuators as

$$\varepsilon_{yn}^p = \sum_{m \neq n}^{M} \varepsilon_{ym}(y_n + y_n^0 - y_m^0, 0), \quad n = 1, 2, \cdots, M \tag{3.4.2}$$

ε_{ym} used in Equation (3.4.2) can be expressed in terms of $\{c\}^m$, using single actuator solution (3.2.19), as

$$\varepsilon_{ym}(y, 0) = [R(y, 0)]\{c\}^m \tag{3.4.3}$$

where

$$[R(y, 0)] = \frac{\lambda_0}{2\pi\mu}[\int_{-a}^{a} \frac{[T(\xi)]}{y - \xi} d\xi - \int_{-a}^{a} [T(\xi)]m_1(y - \xi)d\xi] \tag{3.4.4}$$

with

$$[T(\xi)] = \{T_1(\xi), T_2(\xi), \cdots, T_N(\xi)\} \tag{3.4.5}$$

being the Chebeshev polynomials.

According to the single actuator solution given by (3.2.19), the Chebeshev polynomial expansion coefficients of actuator n, $\{c\}^n = \{c_1^n, c_2^n, \cdots, c_N^n\}^T$, can be determined by

$$[A]^n\{c\}^n = \{F\}^n \tag{3.4.6}$$

64

$[A]^n$ can be obtained directly from matrix $[A]$ with $\overline{k}_a$, q, v being replaced by the corresponding values of actuator n, $\overline{k}_a^n$, q^n, v^n, respectively. And $\{F\}^n$ is the general loads at the collocation points of actuator n, given by

$$\{F\}^n = \{\varepsilon_E\}^n + \{\varepsilon^I\}^n \tag{3.4.7}$$

in which $\{\varepsilon_E\}^n$ is the electric loading acting on collocation points,

$$y_n^l = a_n \cos[\frac{l-1}{N-1}\pi], \quad l = 1, 2, \cdots, N \tag{3.4.8}$$

and $\{\varepsilon^I\}^n$ is the loading induced by total incident wave, given by

$$\varepsilon_{Ej}^n = \frac{\cos \overline{k}_a^n \eta_n^j}{\cos \overline{k}_a^n}, \quad \varepsilon_j^{In} = -\frac{E_a^n}{e_a^n E_z^n}\varepsilon_{yn}^I(\eta_n^j, 0), \quad j = 1, 2, \cdots, N \tag{3.4.9}$$

with $\eta_n^j = y_n^j / a_n$.

Substituting (3.4.1), (3.4.2), (3.4.7) and (3.4.9) into (3.4.6), the following algebraic equations can be obtained,

$$[A]^n\{c\}^n - \sum_{m \neq n}^{M} [Q]^{mn}\{c\}^m = [\varepsilon_E]^n + [Q_0]^n \tag{3.4.10}$$

where $[Q]^{mn}$ and $[Q_0]^n$ are given by

$$[Q_0]^n = -\frac{E_a^n}{e_a^n E_z^n} \left\{ \begin{array}{c} [\varepsilon_{yn}^0(\eta_n^1)] \\ [\varepsilon_{yn}^0(\eta_n^2)] \\ \cdots \\ [\varepsilon_{yn}^0(\eta_n^N)] \end{array} \right\} \tag{3.4.11}$$

and

$$[Q]^{mn} = -\frac{E_a^n}{e_a^n E_z^n} \left\{ \begin{array}{c} [R_m(\eta_n^1 + \eta_n^0 - \eta_m^0, 0)] \\ [R_m(\eta_n^2 + \eta_n^0 - \eta_m^0, 0)] \\ \cdots \\ [R_m(\eta_n^N + \eta_n^0 - \eta_m^0, 0)] \end{array} \right\} \tag{3.4.12}$$

where $\eta_m^0 = y_m^0/a_m$, $\eta_n^0 = y_n^0/a_n$. The Chebyshev polynomial expansion coefficients $\{c\}^n$ can be determined by solving linear equations (3.4.10). The resulting wave propagation can be obtained by superimposing the wave generated by different actuators.

65

Especially, the resulting Rayleigh wave can be determined as:

$$\sigma_y^R(y,0) = Ae^{i(s_r y + \theta)} = \sum_{k=1}^{M} A_k e^{i(s_r y - s_r y_k^0)} \tag{3.4.13}$$

where A and θ are the amplitude and phase angle of the resulting wave, and

$$A_k = \pi \sum_{j=1}^{N} c_j^k g_r J_j(s_r a_k) \begin{cases} (-1)^n i & j = 2n+1 \\ \\ (-1)^{n+1} & j = 2n \end{cases} \tag{3.4.14}$$

with c_j^k being the Chebyshev polynomial expansion coefficients corresponding to actuator k, given by (3.4.10).

3.5 Results and Discussion

This section will be devoted to the discussion of the load transfer from piezoelectric actuators to the host structure and the behaviour of the resulting wave propagation under different geometric and loading conditions.

3.5.1 Validation of the Model

To verify the validity of the current method, consider first the quasistatic behaviour of actuators bonded to an elastic host medium. The PZT-4 piezoelectric actuator is used and the host medium is assumed to be

Host medium

$$E = 2.64 \times 10^{10}(Pa), \nu = 0.3$$

Figure 3.3 shows the normalized interfacial shear stress distribution caused by a single actuator, $\tau^* = \tau/\sigma_B$, $\sigma_B = e_a E_z$ for the case where $v = a/h = 20$, $q = \pi \overline{E}/2E_a = 0.5$. The result is compared with that obtained from finite element analysis using ANSYS. In the current analysis, forty terms in Chebyshev polynomial expansions have been

66

used. In view of the excellent agreement observed between the two solutions, the number of terms used is retained for the remainder of the study.

Figure 3.4 shows the comparison of the normalized local stress distribution $\tau_{yz}^* = \tau_{yz}/\sigma_B$ in the host medium ($z = 0.5a$) with that from finite element analysis using ANSYS for cases where two surface-bonded actuators of equal length are involved, with $v = a/h = 20$, $q = 0.5$ and $2e = 0.5a$, $2e$ being the distance between the two actuators. The comparison indicates that the current model can provide reasonable prediction of the stress field due to interacting actuators.

3.5.2 Dynamic Load Transfer

Figure 3.5 shows the normalized dynamic shear stress distribution $\tau^* = \tau/\sigma_B$ along the interface between an actuator and the matrix for the case where $v = 20$, $q = 0.5$ and $\rho_a/\rho_H = 1$, with ρ_a and ρ_H being the mass density of the actuator and the host medium, respectively. The loading frequency (ka) shows significant effects upon the load transfer, as evidenced by the increase of the stress level in the region of $y = 0.1a \sim 0.7a$ with increasing ka. Similar phenomenon is observed for the dynamic interfacial stress caused by two surface-bonded actuators of the same length, as depicted in Figure 3.6 for the case where $2e = 0.5a$, with $2e$ being the distance between the actuators.

Figure 3.7 shows the effect of the material mismatch upon the dynamic interfacial stress distribution for the case where $ka = 10$, $v = 20$, and $\rho_a/\rho_H = 1$. A higher stress concentration is observed for lower material combination q, corresponding to a stiffer actuator. This result indicates the need to properly select the material combination to increase the actuation efficiency and, at the same time, not to adversely affect the local stress distribution.

Another interesting issue is the local stress field around the tips of the actuators. The variation of the normalized SSSF $S^* = S/\sigma_B\sqrt{\pi a}$ of a single actuator with

67

the loading frequency ka is depicted in Figure 3.8 for the case where $v = 20$ and $\rho_a/\rho_H = 1$. It is observed that the material combination q has significant effects upon the singular stress at the tip of the actuator. It is interesting to note that S^* is not sensitive to the loading frequency until ka approaches 15.

Figure 3.9 shows the dynamic S^* at the right tips of two surface-bonded actuators of equal length subjected to an electric field E_z of frequency ω for the case where $q = 0.5$, $v = 20$, $\rho_a/\rho_H = 1$ and $2e = 0.5a$. The interaction between the actuators increases the stress singularity at the inner tips of the actuators (the right tip of the first actuator) for $ka < 4$. For the outer tips of the actuators(the right tip of the second actuator), S^* is close to that of the single actuator solution for the lower frequency ($ka < 2$). However, for higher frequency ($ka > 2$), significant interacting effect is observed.

Figure 3.10 shows the dynamic S^* at the right tips of three actuators of the same length subjected to an electric field E_z of frequency ω for the case where $q = 0.5$, $v = 20$, $\rho_a/\rho_H = 1$ and $2e = 0.5a$. For lower frequencies ($ka < 2$), S^* of the first actuator is close to that of the second. S^* of the third actuator is similar to that at the outer tips of two interacting actuators, as shown in Figure 3.9. Those results indicate that the interaction effects of the first actuator upon the third one is very small and can be ignored.

3.5.3 Resulting Wave Propagation

Figure 3.11 and Figure 3.12 shows the amplitude of the resulting elastic wave from a single actuator $\sigma_y^* = \sigma_y/\sigma_B$ and $\tau_{yz}^* = \tau_{yz}/\sigma_B$ in the matrix for the case where $ka = 3.0$, $v = a/h = 20$, $q = 0.5$, $\rho_a/\rho_H = 1$. High stress concentration can be observed around the tips of the actuator. The stresses will be reduced with the distance from the actuator and eventually generate a Rayleigh wave, which propagates with a constant amplitude along the surface of the matrix.

68

The stresses σ_y^* and τ_{yz}^*, generated by two actuators of the same length, are depicted in Figure 3.13 and Figure 3.14, respectively, for the case where $ka = 3.0$, $q = 0.5$, $v = 20$, $\rho_a/\rho_H = 1$ and $2e = 0.5a$, with $2e$ being the distance between the actuators. Comparing with the result of the single actuator, more complicated waveform is generated. Similar to the single actuator case, a wave propagating along the surface can be observed, which becomes the Rayleigh wave eventually.

Rayleigh wave propagation is characterized by (3.3.5) and (3.4.13). Figures 3.15 shows the amplitude of the resulting Rayleigh wave $\sigma_y^{R*} = \sigma_y^R/\sigma_B$ for the case $ka = 3.0$, $q = 0.5$, $v = 20$, $\rho_a/\rho_H = 1$. It is interesting to mention that both the position of the actuators and the loading frequency have significant effects upon the the amplitude and phase angle of the resulting wave propagation. For example, for the case where $2e = 0.5a$ and $ka = 2.0$, the amplitude of the Rayleigh wave resulted by two actuators is about two times of that of the single actuator. However, when loading frequency is increased to $ka = 5.0$, the amplitude of the Rayleigh wave resulted by two actuators is smaller than that of the single actuator. Although the resulting amplitude of the Rayleigh wave is low for lower frequencies ($ka < 1.0$), significant increase in σ_y^R can be achieved by using a higher frequency ($ka = 2.0$, for example). Proper combination of the loading frequency and the size and position of the actuators is important in increasing the amplitude of the resulting Rayleigh wave. For $ka = 5.0$, two actuators with $2e = 0.5a$ will result in a high amplitude, which will be significantly reduced when $2e = 1.0a$ is used.

3.5.4 Far field waveform

The wave field far away from the surface bonded actuator, $\sigma_z^{f*} = \sigma_z^f/\sigma_B$, is investigated to show the basic properties of the generated wave propagation. Figure 3.16 shows the comparison of the obtained asymptotic analytical solutions, which are

given in Equations (3.2.36)-(3.2.38) and (3.2.39)-(3.2.41), with those from the numerical results from Equations (3.2.22)-(3.2.24) for the case where $ka = 4.0$, $q = 0.5$, $v = 20$ and $\rho_a/\rho_H = 1$. The very good agreement shows the accuracy of the obtained asymptotic solutions. Figures 3.17 and 3.18 show the far field by using the obtained asymptotic solution for the case where $q = 0.5$, $v = 20$ and $\rho_a/\rho_H = 1$. The loading frequencies $ka = 4$ and $ka = 10$ are used, respectively. It can be found that the main energy of wave field is along the direction $\theta = 40 - 45^0$. It is interesting to mention that the direction of the main energy of far field is not sensitive to the change of the loading frequency, which shows the basic properties of generated wave propagation by surface bonded actuator with the current actuator input.
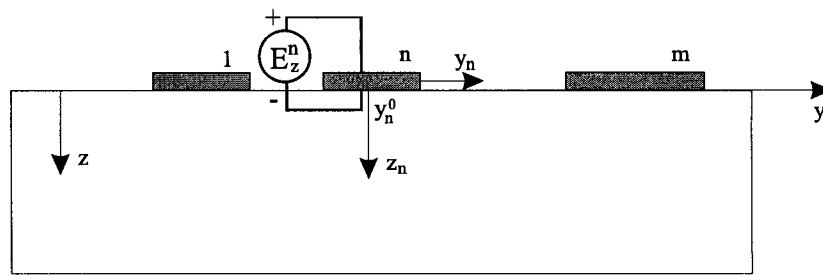
(a)
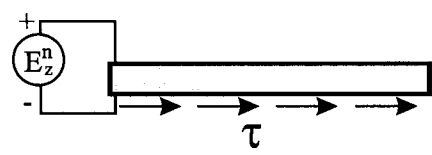
(b)

Figure 3.1: Actuators surface-bonded to an elastic medium
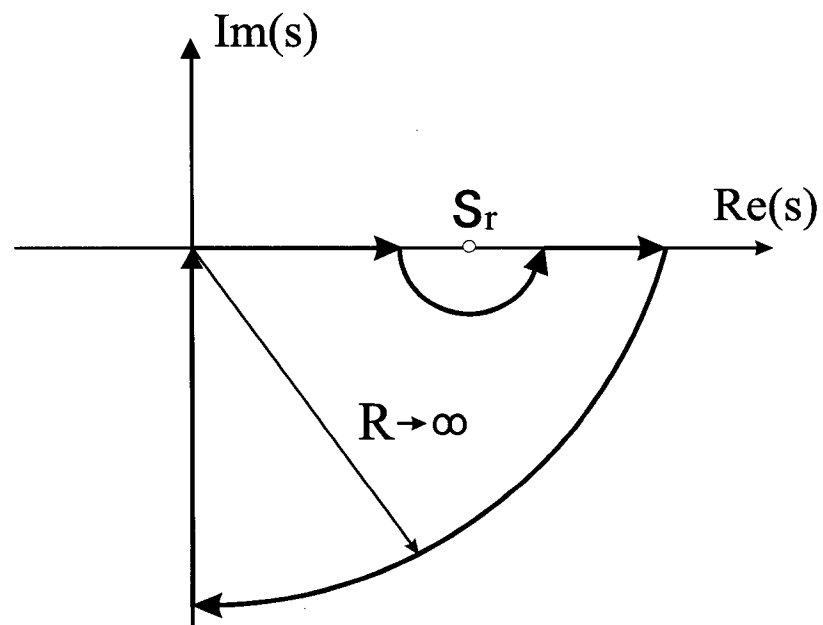
Figure 3.2: Path of integration

71
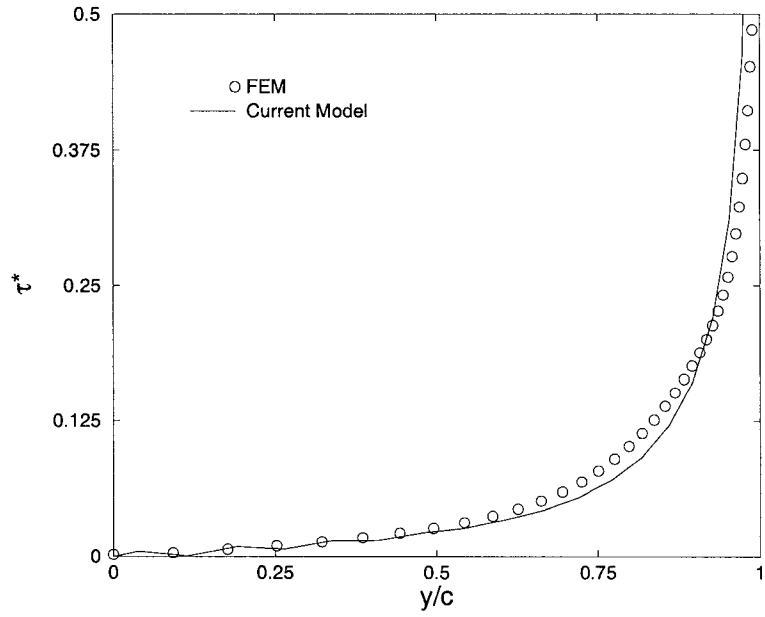
Figure 3.3: The normalized interfacial shear stress
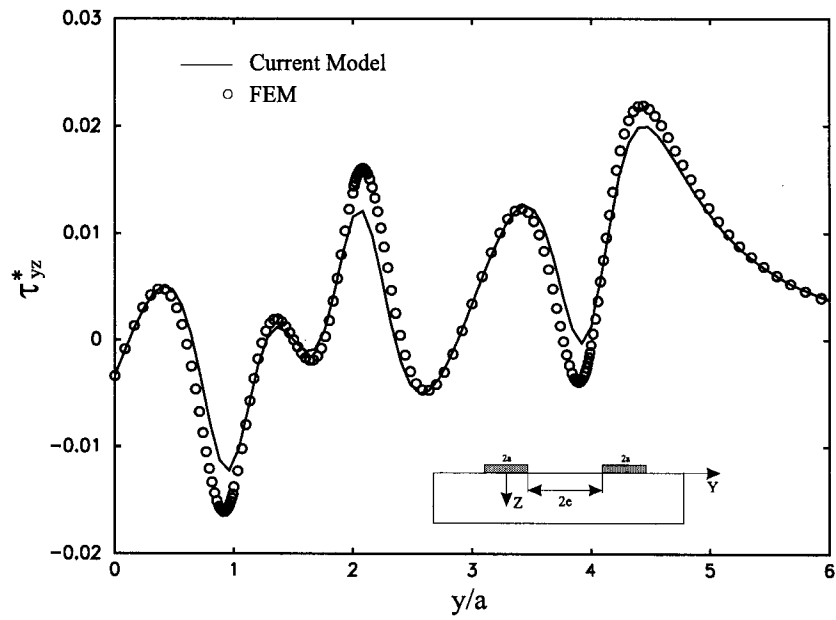
Figure 3.4: The normalized shear stress distribution

72
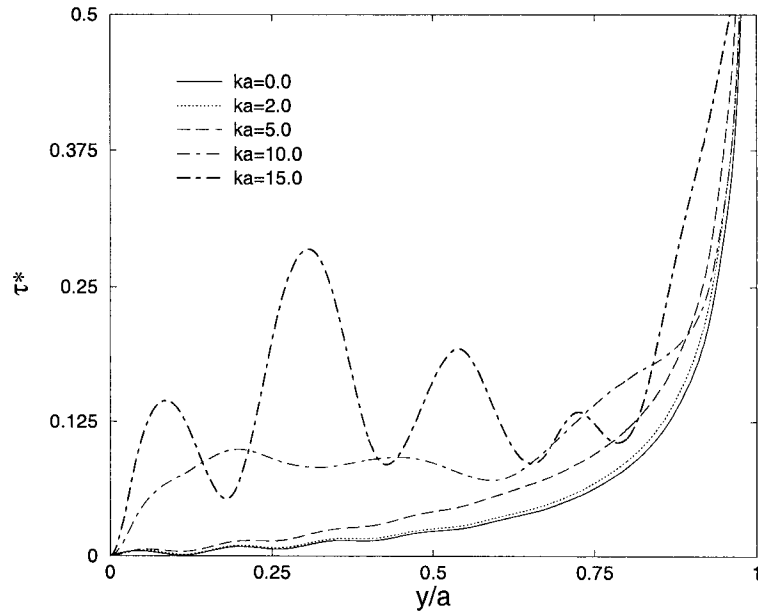
Figure 3.5: The normalized interfacial shear stress: one actuator
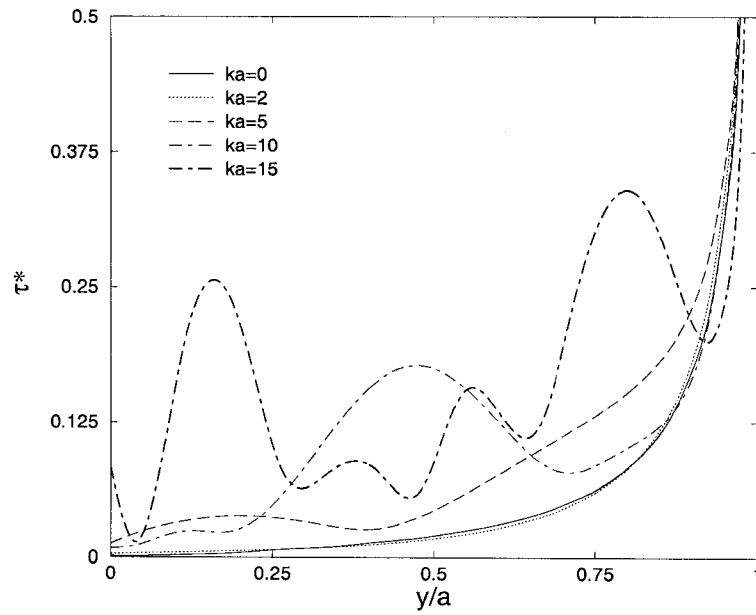
Figure 3.6: The normalized interfacial shear stress: two actuators

73
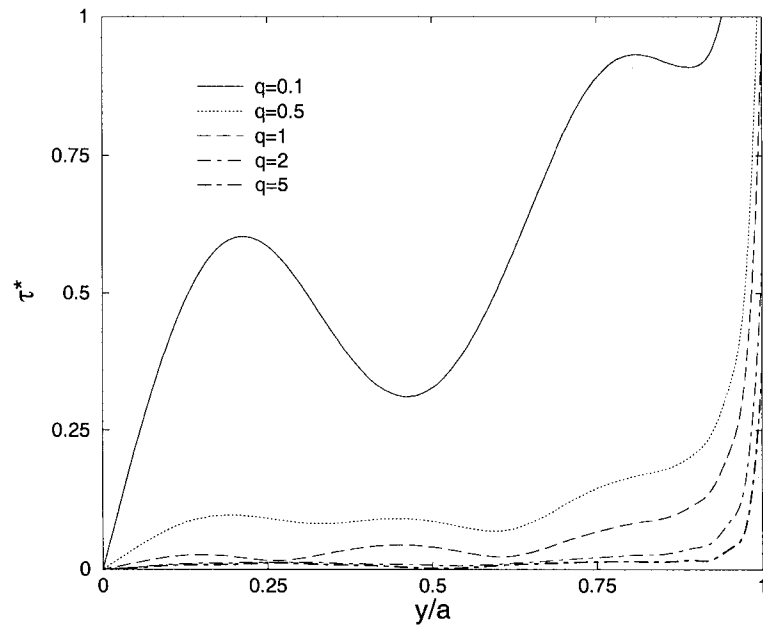
Figure 3.7: Effects of material combination upon the interfacial shear stress
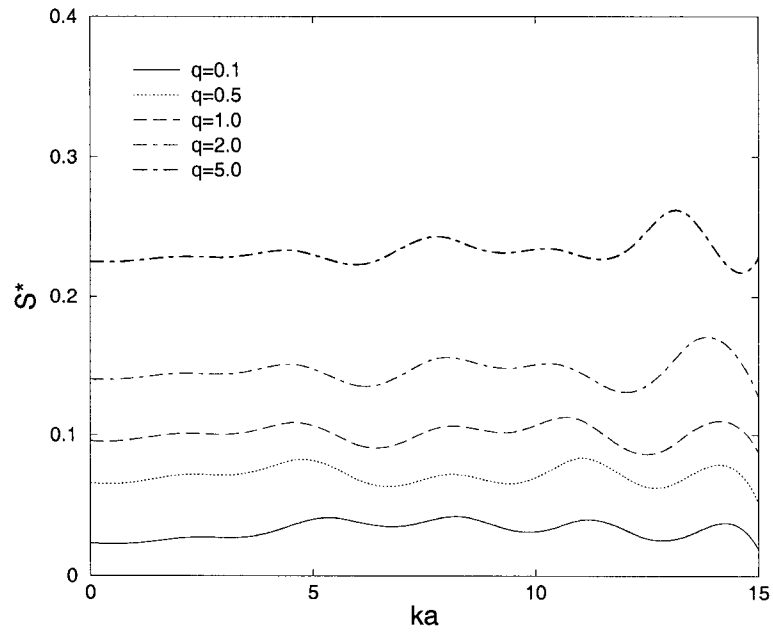
Figure 3.8: The shear stress singularity factor S^*: one actuator

74
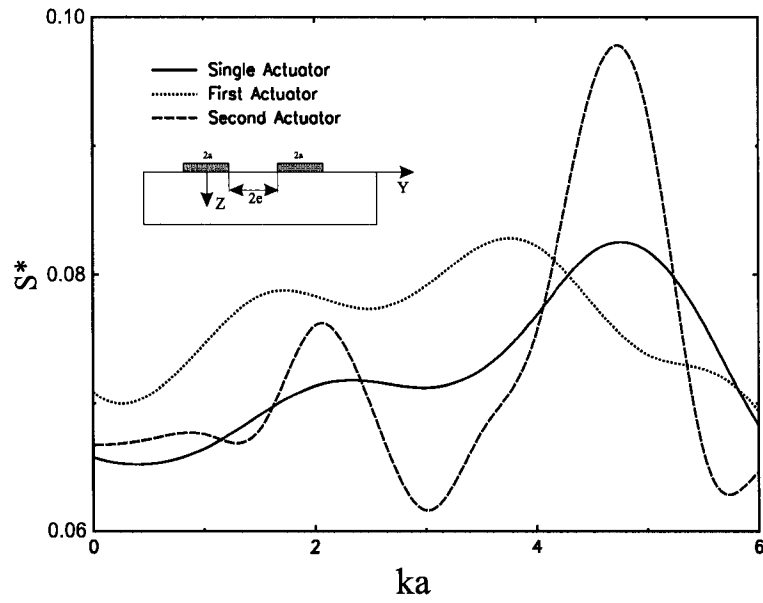
Figure 3.9: The shear stress singularity factor S^*: two actuators
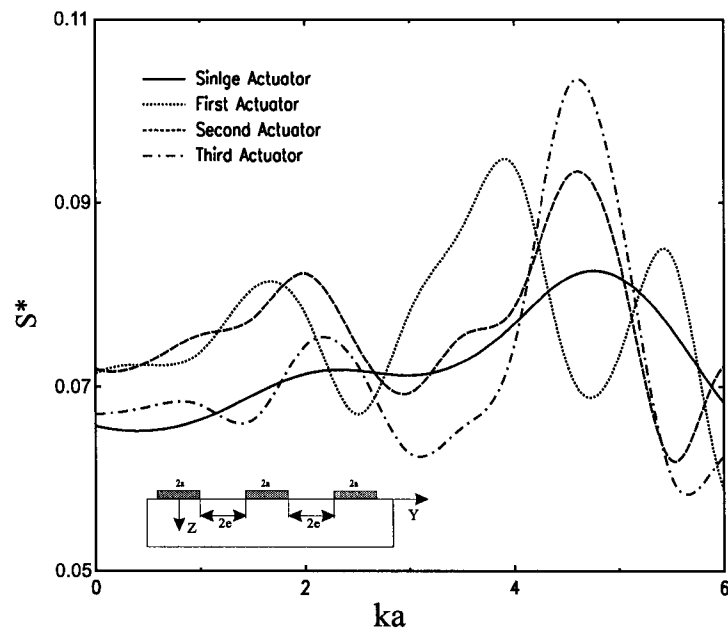
Figure 3.10: The shear stress singularity factor S^*: three actuators

75
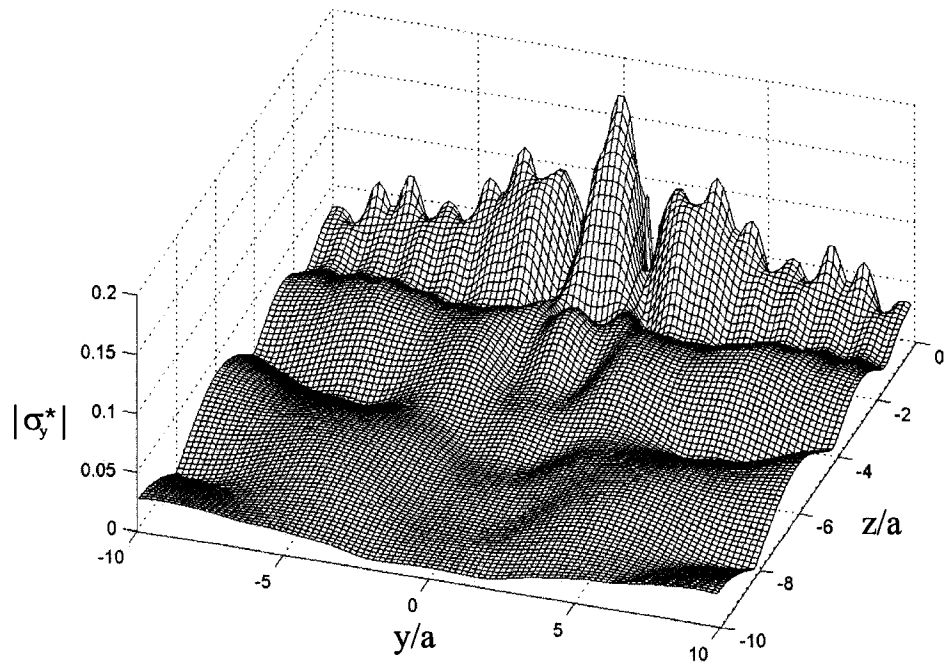
Figure 3.11: Normalized local stress distribution σ_y^* caused by one actuator
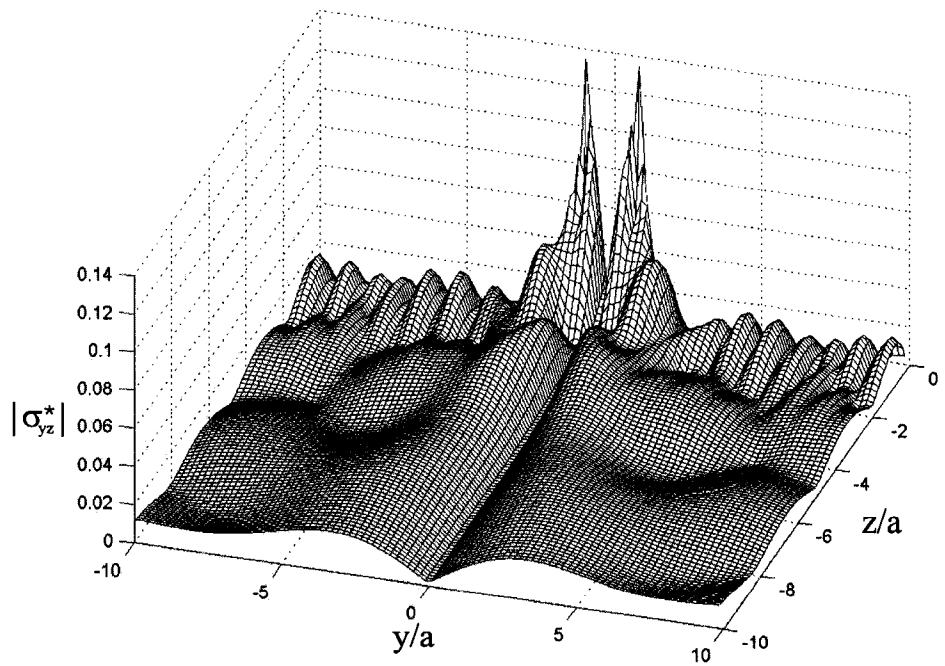
Figure 3.12: Normalized local stress distribution τ_{yz}^* caused by one actuator

76
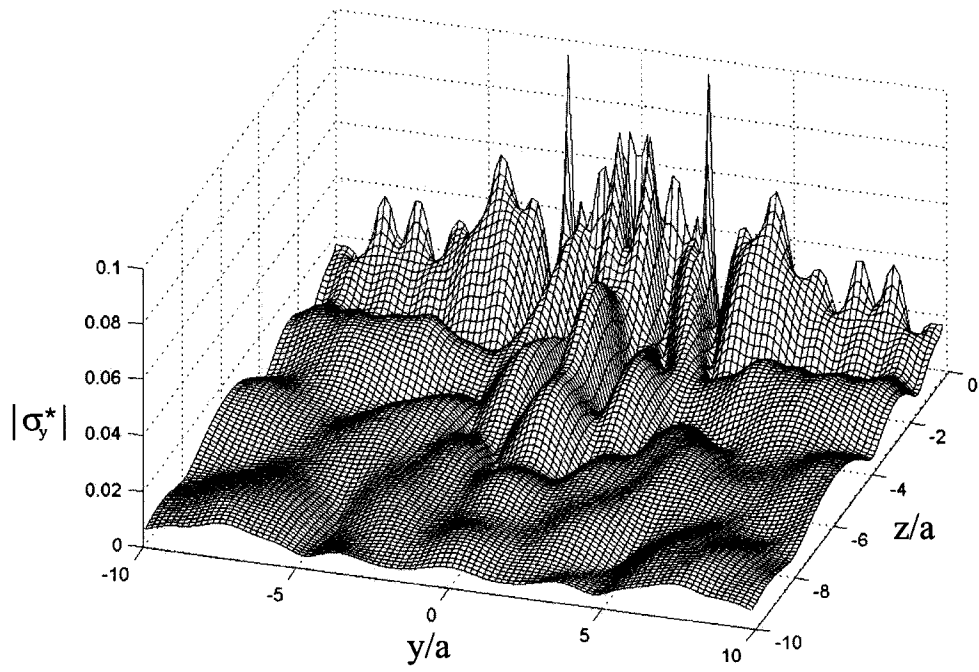
Figure 3.13: Normalized local stress distribution σ_y^* caused by two actuators
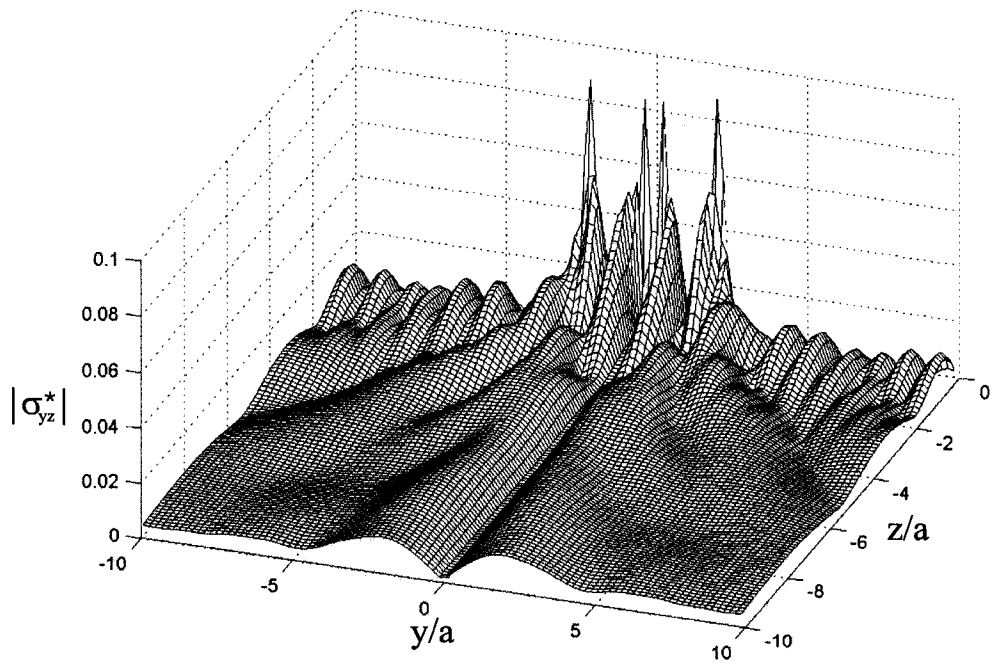
Figure 3.14: Normalized local stress distribution τ_{yz}^* caused by two actuators

77
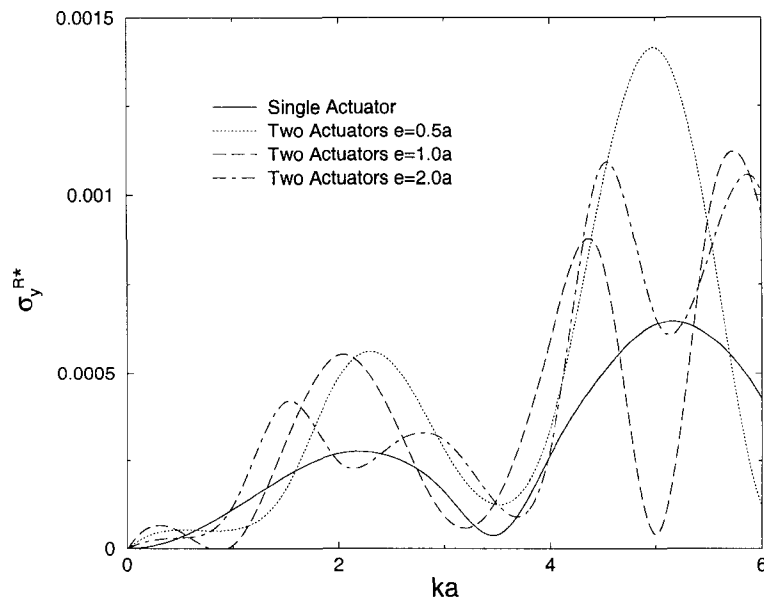
Figure 3.15: The amplitude of the resulting Rayleigh wave
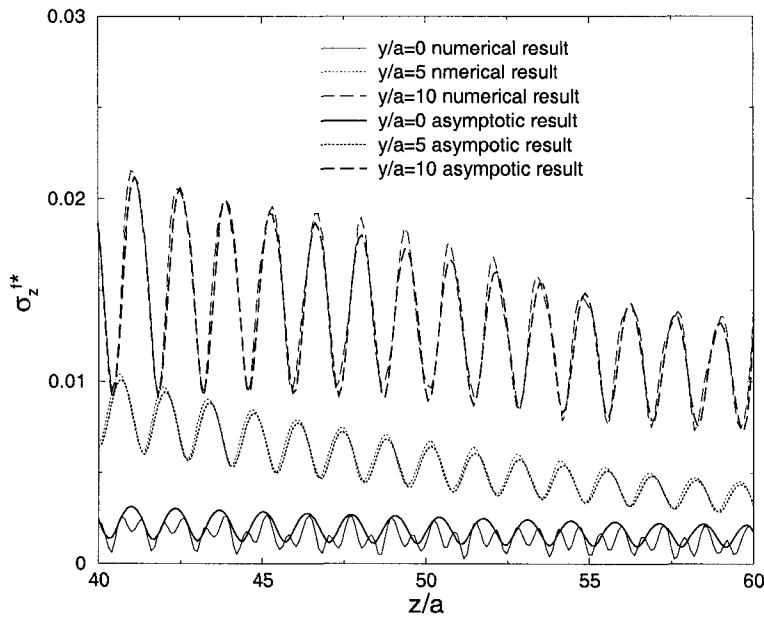
Figure 3.16: The comparison of the far field stress distribution σ_z^{f*}

78
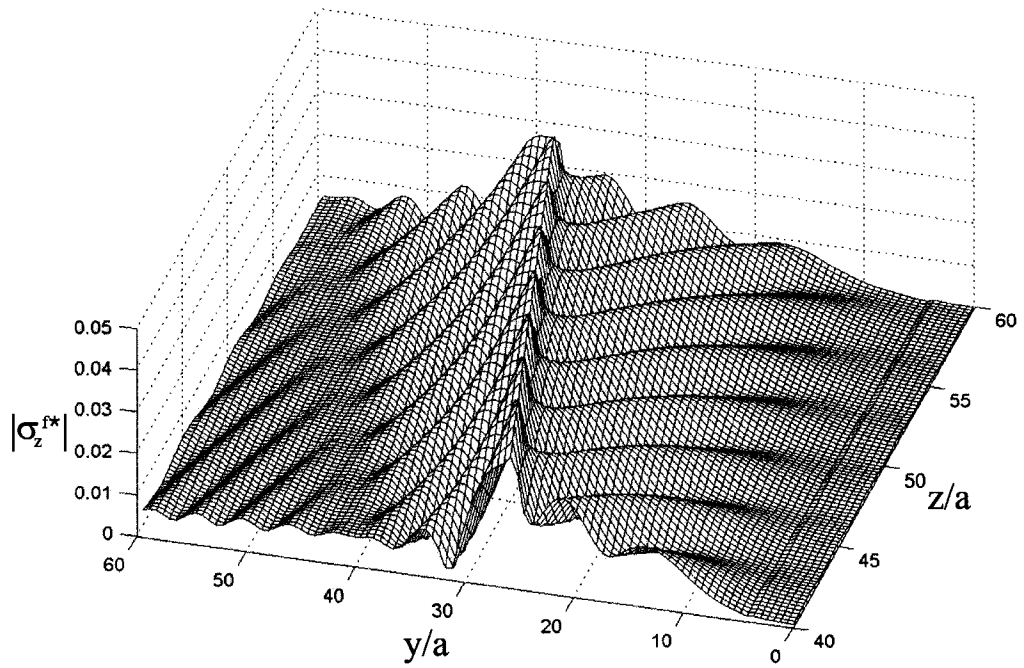
Figure 3.17: The far field stress distribution σ_z^{f*} in the host medium: $ka = 4$
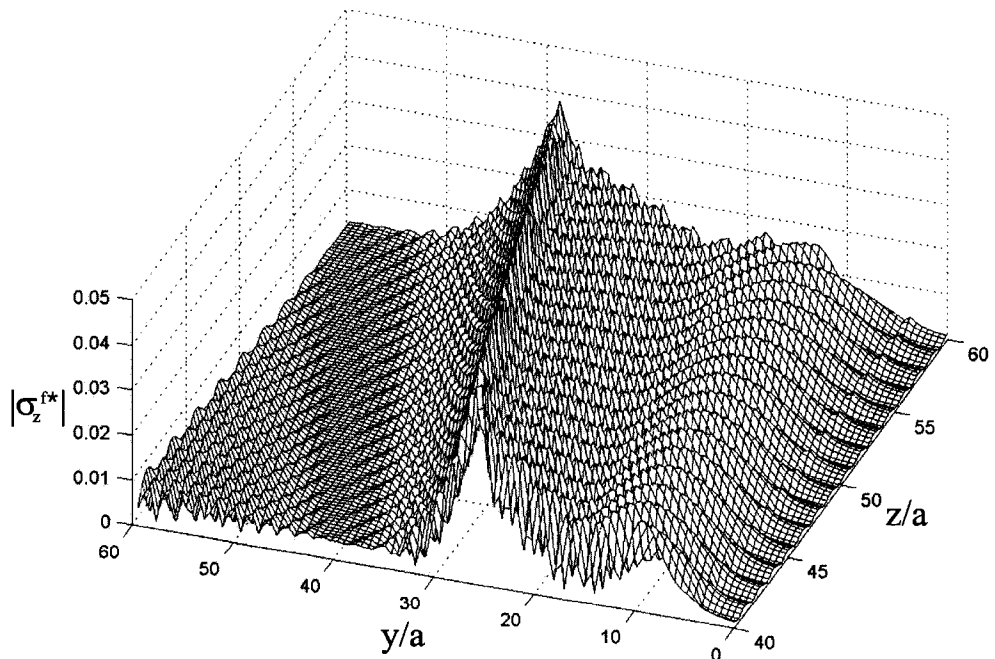
Figure 3.18: The far field stress distribution σ_z^{f*} in the host medium: $ka = 10$

79

Chapter 4

Wave Propagation with Embedded Actuators

This chapter provides a theoretical analysis of the elastic wave propagation in an elastic medium induced by embedded piezoceramic actuators under dynamic electric loads. A modified actuator model involving the deformation in both the transverse and longitudinal directions of the actuators is developed to study the wave propagation induced by multiple actuators. The formulation of the problem is established using the analytical solution of the single actuator problem and the Pseudo-Incident Wave method (PsIW) (Wang and Meguid, 1997). The resulting wave field is determined by solving the resulting integral equations in terms of the interfacial shear stress and transverse displacement of the actuators. Numerical simulation is conducted to evaluate the effects of the geometry, the loading frequency, and the interaction between actuators upon the resulting wave propagation. Especially, the far field waveform is obtained to show the basic properties of the resulting wave propagation.

4.1 Electromechanical behaviour of an actuator

Consider the two-dimensional plane strain problem of M thin-sheet parallel piezoceramic actuators subjected to applied electric fields, which are embedded in a homogeneous and isotropic elastic insulator, illustrated in Figure 4.1. Plane strain model is

80

used to simulate the cases where the width of the actuator is large in comparison with its length. The dimension of the actuator is assumed significantly smaller than that of the host structure. Therefore, the host structure is modelled as an infinite medium. The half length and the thickness of actuator A_n are denoted a_n and h_n, respectively. The position of the centre of actuator A_n is given by (y_n^0, z_n^0) in the global coordinate (y, z). A local coordinate system (y_n, z_n) is used to describe actuator A_n with its origin at the centre of the actuator. It is assumed that the poling direction of the actuator is along its thickness. A voltage between the upper and the lower electrodes of actuator A_n is applied, which results in an electric field of frequency ω along the poling direction of the actuator, $E_z^n = (V_n^- - V_n^+)/h_n$. For the steady state response of the system discussed in this paper, the time factor $\exp(-i\omega t)$, which applies to all field variables, will be suppressed.

4.1.1 Modelling of the embedded actuator

When an electric field is applied to an actuator along its thickness, the actuator will be deformed in both the axial and transverse directions. Because of the continuity of deformation between the actuator and host medium, complicated dynamic stress field will be generated in this material system. Wang (2000) developed a one dimensional actuator model to consider dynamic load transfer between actuator and the host medium. But in this model, the transverse deformation is neglected. In the current study, the effect of transverse strain ε_z^a will be included. In this modified model, it is assumed that the stress and strain components σ_y^a, σ_z^a, ε_y^a, ε_z^a and displacement u_y^a are uniformly distributed across the thickness, and the actuator can be regarded as a one-dimensional electromechanical element. The coupled electromechanical behaviour of an actuator can be described by the following general constitutive relations

$$\sigma_y^a(y) = c_{11}^a \varepsilon_y^a(y) + c_{31}^a \varepsilon_z^a(y) - e_{31}^a E_z \qquad (4.1.1)$$

$$\sigma_z^a(y) = c_{31}^a \varepsilon_y^a(y) + c_{33}^a \varepsilon_z^a(y) - e_{33}^a E_z \qquad (4.1.2)$$

81

where c_{11}^a, c_{31}^a, c_{33}^a, e_{31}^a, and e_{33}^a are elastic and piezoelectric constants of the actuators, and $\varepsilon_y^a(y)$ and $\varepsilon_z^a(y)$ are the axial and transverse strains of the actuator.

According to this model, the interfacial normal and shear stresses transferred between the actuator and the host medium can be replaced by distributed body forces acting along the actuator, as shown in Figure 4.2, in which, τ and σ_z represent the interfacial shear and normal stresses transferred between the actuator and the host medium. The axial and transverse deformations of the actuator are governed by the following equations

$$\frac{d\sigma_y^a}{dy} + \tau(y)/h + \rho_a \omega^2 u_y^a = 0, \tag{4.1.3}$$

$$\varepsilon_z^a(y) = \frac{u_z^{a+} - u_z^{a-}}{h}, \tag{4.1.4}$$

with ρ_a being the mass density of the actuator, u_z^{a+}, u_z^{a-} being the displacements at the upper and lower surfaces of the actuator and h being its thickness.

In the current model, since all the load transfer between actuator and the host medium can be attributed to τ, the two ends of the actuator can be assumed to be traction free, i.e.

$$\sigma_y^a = 0, \quad |y| = a.$$

By making use of the constitutive relations and boundary conditions, the axial strain and the transverse stress of the actuator can be obtained in terms of τ and $u_z^{a+} - u_z^{a-}$ as

$$\varepsilon_y^a(y) = \varepsilon_E(y) - \int_{-a}^{y} \cos k_a(\xi - y) \frac{p(\xi)}{h c_{11}^a} d\xi$$
$$+ \frac{\sin k_a(a+y)}{h c_{11}^a \sin 2k_a a} \int_{-a}^{a} \cos k_a(\xi - a) p(\xi) d\xi \tag{4.1.5}$$

$$\sigma_z^a(y) = \sigma_E(y) + \frac{c_{31}^a \sin k_a(a+y)}{h c_{11}^a \sin 2k_a a} \int_{-a}^{a} p(\xi) \cos k_a(\xi - a) d\xi$$
$$- \frac{c_{31}^a}{h c_{11}^a} \int_{-a}^{y} p(\xi) \cos k_a(\xi - y) d\xi + \frac{c_{33}^a}{h}(u_z^{a+} - u_z^{a-}) \tag{4.1.6}$$

82

with k_a and c_a being the wave number and the axial wave speed of the actuator given by

$$k_a = \omega/c_a, c_a = \sqrt{c_{11}^a/\rho_a} \tag{4.1.7}$$

In Equations (4.1.5) and (4.1.6),

$$p(y) = \tau(y) + hc_{31}^a \frac{d}{dy}(u_z^{a+} - u_z^{a-}), \sigma_E(y) = c_{31}^a \varepsilon_E(y) - e_{33}^a E_z \tag{4.1.8}$$

and

$$\varepsilon_E(y) = \frac{e_{31}^a E_z}{c_{11}^a} \frac{\cos k_a y}{\cos k_a a} \tag{4.1.9}$$

is the strain caused by the free vibration of the actuator.

4.1.2 Deformation of the host medium

According to this model, the deformation of an actuator will result in an interfacial shear stress τ and a transverse displacement $u_z^{a+} - u_z^{a-} = u_z(y, 0^+) - u_z(y, 0^-)$. Correspondingly, the host medium will have a crack-like opening at the site of the actuator. The deformation in z-direction can be represented by the rate of the change of $u_z(y, 0^+) - u_z(y, 0^-)$ along the direction of the actuator

$$\Gamma(y) = \frac{\partial}{\partial y}[u_z(y, 0^+) - u_z(y, 0^-)], \quad |y| < a \tag{4.1.10}$$

and the displacement in y-direction is continuous across the thickness of the actuator, i.e.

$$u_y(y, 0^+) = u_y(y, 0^-). \tag{4.1.11}$$

In addition, the interfacial shear stresses at the upper and the lower surfaces of the 'crack' should satisfy

$$\sigma_{yz}(y, 0^+) - \sigma_{yz}(y, 0^-) = \tau, \quad |y| < a. \tag{4.1.12}$$

83

For the whole plane problem, general solutio of deformation in the host medium can be determined by solving the governing equations (3.2.8) using Fourier transform as

$$
\begin{cases}
\overline{\Phi}_+ = A^+(s)e^{-\alpha z} \quad \overline{\Psi}_+ = B^+(s)e^{-\beta z} \quad z > 0 \\
\\
\overline{\Phi}_- = A^-(s)e^{\alpha z} \quad \overline{\Psi}_- = B^-(s)e^{\beta z} \quad z < 0
\end{cases}
\tag{4.1.13}
$$

$A^+(s)$, $B^+(s)$, $A^-(s)$ and $B^-(s)$ are four unknown functions of s. Making using of the general solution (4.1.13) and the above boundary conditions, the unknown parameters $A^+(s)$, $B^+(s)$, $A^-(s)$ and $B^-(s)$ can be determined in terms of τ and the 'crack' opening $u_z^{a+} - u_z^{a-}$. Therefore, the resulting dynamic strain and stress in the host medium along the surface can be obtained as

$$
\varepsilon_y(y,0)|_{host} = -\frac{1}{2\pi\mu}\left[\int_{-a}^{a} \tau(\xi)n_1(y-\xi)d\xi + \mu\int_{-a}^{a} \Gamma(\xi)n_2(y-\xi)d\xi\right] \tag{4.1.14}
$$

$$
\sigma_z(y,0)|_{host} = -\frac{1}{2\pi}\left[\int_{-a}^{a} \tau(\xi)n_2(y-\xi)d\xi + \mu\int_{-a}^{a} \Gamma(\xi)n_3(y-\xi)d\xi\right] \tag{4.1.15}
$$

where μ is the shear modulus of the host medium and

$$
n_1(y-\xi) = \frac{1}{k^2}\int_0^\infty \frac{s(s^2 - \alpha\beta)}{\alpha}\sin s(\xi - y)ds \tag{4.1.16}
$$

$$
n_2(y-\xi) = \frac{1}{k^2}\int_0^\infty \frac{s(-\gamma + 2\alpha\beta)}{\alpha}\sin s(\xi - y)ds \tag{4.1.17}
$$

$$
n_3(y-\xi) = \frac{1}{k^2}\int_0^\infty \frac{(\gamma^2 - 4s^2\alpha\beta)}{s\alpha}\sin s(\xi - y)ds \tag{4.1.18}
$$

with $\gamma = s^2 + \beta^2$.

The 'crack' opening Γ and the shear stress τ can be determined from the continuity conditions between the actuator and the host medium, given by

$$
\varepsilon_y^a(y) = \varepsilon_y(y,0) + \varepsilon_y^I(y,0),
$$

$$
\sigma_z^a(y) = \sigma_z(y,0) + \sigma_z^I(y,0), \quad |y| < a \tag{4.1.19}
$$

where $\varepsilon_y(y,0)$, $\sigma_z(y,0)$ are the outgoing waves given by (4.1.14) and (4.1.15) and the terms with superscripts $'a'$ and $'I'$ represent the actuator and the incident field,

84

respectively. By substituting Equations (4.1.5), (4.1.6), (4.1.14) and (4.1.15) into Equation (4.1.19), the following integral equations can be obtained

$$-\frac{1}{2\pi\mu} \int_{-a}^{a} [\tau(\xi)n_1(y-\xi) + \mu\Gamma(\xi)n_2(y-\xi)]d\xi$$

$$-\frac{\sin k_a(a+y)}{hc_{11}^a \sin 2k_a a} \int_{-a}^{a} [\tau(\xi) + c_{31}^a \Gamma(\xi)] \cos k_a(\xi - a)d\xi$$

$$+\frac{1}{hc_{11}^a} \int_{-a}^{y} [\tau(\xi) + c_{31}^a \Gamma(\xi)] \cos k_a(\xi - y)d\xi = \varepsilon_E(y) - \varepsilon_y^I(y,0), \quad |y| < a \quad (4.1.20)$$

$$-\frac{1}{2\pi} \int_{-a}^{a} [\tau(\xi)n_2(y-\xi) + \mu\Gamma(\xi)n_3(y-\xi)]d\xi - \frac{c_{33}^a}{h} \int_{-a}^{y} \Gamma(\xi)d\xi$$

$$-\frac{c_{31}^a \sin k_a(a+y)}{hc_{11}^a \sin 2k_a a} \int_{-a}^{a} [\tau(\xi) + c_{31}^a \Gamma(\xi)] \cos k_a(\xi - a)d\xi$$

$$+\frac{c_{31}^a}{hc_{11}^a} \int_{-a}^{y} [\tau(\xi) + c_{31}^a \Gamma(\xi)] \cos k_a(\xi - y)d\xi = \sigma_E(y) - \sigma_z^I(y,0), \quad |y| < a \quad (4.1.21)$$

Equations (4.1.20) and (4.1.21) involve a square-root singularity for both τ and Γ at the ends of the actuator. Therefore, the general solutions of τ and Γ can be expressed in terms of Chebyshev polynomials as

$$\tau(y) = \sum_{j=0}^{\infty} A_j T_j(y/a)/\sqrt{1 - y^2/a^2}, \Gamma(y) = \sum_{j=0}^{\infty} B_j T_j(y/a)/\sqrt{1 - y^2/a^2} \quad (4.1.22)$$

with T_j being Chebyshev polynomials of the first kind and A_j and B_j being unknown constants to be determined. The continuity of displacement $u_z(y,0)$ for $|y| \geq a$ indicates that $\int_{-a}^{a} \Gamma(y)dy = 0$, i.e. $B_0 = 0$. If the expansions in (4.1.22) are truncated to the Nth term and Equations (4.1.20) and (4.1.21) are satisfied at the following collocation points along the length of the actuator, which are defined in (3.4.8), $2N$ linear algebraic equations in terms of $\{c\} = \{A_0, A_1, \cdots, A_{N-1}, B_1, B_2, \cdots, B_N\}^T$ can be obtained as

$$[Q]\{c\} = \{F\} \quad (4.1.23)$$

where

$$[Q_{lj}] = \begin{bmatrix} A_{j-1}^{(1)}(\eta^l) & A_j^{(2)}(\eta^l) \\ A_{j-1}^{(3)}(\eta^l) & A_j^{(4)}(\eta^l) \end{bmatrix}, \quad j = 1, 2, \cdots, N$$

85

with

$$A_j^{(1)}(\eta^l) = -\frac{\overline{K}^2 + \overline{k}^2}{4\mu\overline{k}^2}\frac{\sin[j\cos^{-1}\eta^l]}{\sin[\cos^{-1}\eta^l]} - \frac{1}{2\mu\overline{k}^2}\int_0^\infty P_j^1(\overline{s},\eta^l)(\frac{\overline{s}(\overline{s}^2 - \overline{\alpha}\overline{\beta})}{\overline{\alpha}} - \frac{\overline{K}^2 + \overline{k}^2}{2})d\overline{s}$$
$$+\frac{v}{c_{11}^a}\int_{\cos^{-1}\eta^l}^\pi \cos[\overline{k}_a(\cos\theta - \eta^l)]\cos(j\theta)d\theta - \frac{v\pi\sin[\overline{k}_a(\eta^l + 1)]}{c_{11}^a\sin(2\overline{k}_a)}P_j^2$$

$$A_j^{(2)} = \frac{\overline{K}^2}{2\overline{k}^2}\frac{\sin[j\cos^{-1}\eta^l]}{\sin[\cos^{-1}\eta^l]} - \frac{1}{2\overline{k}^2}\int_0^\infty P_j^1(\overline{s},\eta^l)(\frac{\overline{s}(-\overline{s}^2 - \overline{\beta}^2 + 2\overline{\alpha}\overline{\beta})}{\overline{\alpha}} + \overline{K}^2)d\overline{s}$$
$$+\frac{vc_{13}^a}{c_{11}^a}\int_{\cos^{-1}\eta^l}^\pi \cos[\overline{k}_a(\cos\theta - \eta^l)]\cos(j\theta)d\theta - \frac{v\pi c_{13}^a\sin[\overline{k}_a(\eta^l + 1)]}{c_{11}^a\sin(2\overline{k}_a)}P_j^2$$

$$A_j^{(3)} = \frac{\overline{K}^2}{2\overline{k}^2}\frac{\sin[j\cos^{-1}\eta^l]}{\sin[\cos^{-1}\eta^l]} - \frac{1}{2\overline{k}^2}\int_0^\infty P_j^1(\overline{s},\eta^l)(\frac{\overline{s}(-\overline{s}^2 - \overline{\beta}^2 + 2\overline{\alpha}\overline{\beta})}{\overline{\alpha}} + \overline{k}^2)d\overline{s}$$
$$+\frac{vc_{31}^a}{c_{11}^a}\int_{\cos^{-1}\eta^l}^\pi \cos[\overline{k}_a(\cos\theta - \eta^l)]\cos(j\theta)d\theta - \frac{v\pi c_{13}^a\sin[\overline{k}_a(\eta^l + 1)]}{c_{11}^a\sin(2\overline{k}_a)}P_j^2$$

$$A_j^{(4)} = -\frac{\mu(\overline{K}^2 - \overline{k}^2)}{\overline{k}^2}\frac{\sin[j\cos^{-1}\eta^l]}{\sin[\cos^{-1}\eta^l]} + \frac{v(c_{13}^a)^2}{c_{11}^a}\int_{\cos^{-1}\eta^l}^\pi \cos[\overline{k}_a(\cos\theta - \eta^l)]\cos(j\theta)d\theta$$
$$-\frac{\mu}{\overline{k}^2}\int_0^\infty P_j^1(\overline{s},\eta^l)(\frac{[(\overline{s}^2 + \overline{\beta}^2)^2 - 4s^2\overline{\alpha}\overline{\beta}]}{2\overline{\alpha}\overline{s}} - \overline{K}^2 + \overline{k}^2)d\overline{s}$$
$$-\frac{vc_{33}^a\sin[j\cos^{-1}\eta^l]}{j} - \frac{v\pi(c_{13}^a)^2\sin[\overline{k}_a(\eta^l + 1)]}{c_{11}^a\sin(2\overline{k}_a)}P_j^2$$

$\overline{\alpha}$ and $\overline{\beta}$ can be obtained from (3.2.11) with s, K and k being replaced by $\overline{s}$, $\overline{K}$ and $\overline{k}$, respectively. In these equations,

$$\eta^l = y^l/a, \quad \overline{K} = Ka, \quad \overline{k} = ka \quad \overline{k_a} = k_a a, \quad \overline{s} = sa, \quad v = \frac{a}{h}.$$

The general loading $\{F\}$ used in equation (4.1.23) is given by

$$F_l = \varepsilon_E(\eta^l) - \varepsilon^I(\eta^l, 0) \quad l = 1, 2, \cdots, N$$
$$F_{l+N} = \sigma_E(\eta^l) - \sigma^I(\eta^l, 0) \quad l = 1, 2, \cdots, N \tag{4.1.24}$$

From Equation (4.1.23), the unknown coefficient $\{c\}$ and, therefore, τ and Γ can be obtained. The outgoing wave of an actuator is governed by its interfacial stress τ

86

and its 'crack' opening Γ, which can be obtained in terms of the coefficients of the Chebyshev polynomial expansion, $\{c\}$, as

$$\sigma_y(y,z) = -\frac{1}{k^2}\sum_{j=0}^{N} A_j \int_0^{\infty} H_1^e(s,z^n)P_j^1(s,y)ds - \frac{\mu}{k^2}\sum_{j=1}^{N} B_j \int_0^{\infty} H_2^e(s,z)P_j^1(s,y)ds \quad (4.1.25)$$

$$\sigma_z(y,z) = -\frac{1}{k^2}\sum_{j=0}^{N} A_j \int_0^{\infty} H_3^e(s,z^n)P_j^1(s,y)ds - \frac{\mu}{k^2}\sum_{j=1}^{N} B_j \int_0^{\infty} H_4^e(s,z)P_j^1(s,y)ds \quad (4.1.26)$$

$$\sigma_{yz}(y,z) = \frac{sgn(z)}{k^2}\sum_{j=0}^{N} A_j \int_0^{\infty} H_5^e(s,z)P_j^3 ds + \frac{sgn(z)\mu}{k^2}\sum_{j=1}^{N} B_j \int_0^{\infty} H_6^e(s,z)P_j^3 ds \quad (4.1.27)$$

where

$$H_1^e(s,z) = \frac{s\gamma}{2\alpha}e^{-\alpha|z|} - s\beta e^{-\beta|z|}, \quad H_2^e(s,z) = -\frac{(2\alpha^2+k^2)\gamma}{2\alpha s}e^{-\alpha|z|} + 2s\beta e^{-\beta|z|}$$

$$H_3^e(s,z) = -\frac{s\gamma}{2\alpha}e^{-\alpha|z|} + s\beta e^{-\beta|z|}, \quad H_4^e(s,z) = \frac{\gamma^2}{2\alpha s}e^{-\alpha|z|} - 2s\beta e^{-\beta|z|}$$

$$H_5^e(s,z) = s^2 e^{-\alpha|z|} - \frac{\gamma}{2}e^{-\beta|z|}, \quad H_6^e(s,z) = \gamma(-e^{-\alpha|z|} + e^{-\beta|z|})$$

$$P_j^3(s,y) = J_j(sa) \begin{cases} (-1)^n \sin(sy) & j = 2n+1 \\ (-1)^n \cos(sy) & j = 2n \end{cases}$$

It should be mentioned that in addition to the singular shear stress τ along the interface between the actuators and the host medium, the normal stress along the actuator will also be singular, which can be expressed as

$$\sigma_z = \frac{1}{\pi k^2}[\frac{K^2}{2}\int_{-a}^{a}\frac{\tau(\xi)}{\xi-y}d\xi - \mu(K^2-k^2)\int_{-a}^{a}\frac{\Gamma(\xi)}{\xi-y}d\xi] + \text{higher order terms} \quad (4.1.28)$$

The singular behaviour of the interfacial shear stress at the tips of the actuator can be characterized by a shear stress singularity factor (SSSF), S, defined by (3.2.21), can be expressed in terms of A_j as being

$$S_l = \sqrt{a\pi}\sum_{j=0}^{N}(-1)^j A_j, \quad S_r = \sqrt{a\pi}\sum_{j=0}^{N} A_j \quad (4.1.29)$$

87

Similarly, the singular behaviour of the normal stress σ_z ahead of the actuator can be characterized by a normal stress intensity factor (NSIF), N, defined by

$$
\begin{aligned}
N_r &= \lim_{y \to a}[\sqrt{2\pi(a-y)}\sigma_z] \\
N_l &= \lim_{y \to -a}[\sqrt{2\pi(a+y)}\sigma_z]
\end{aligned}
$$

(4.1.30)

which can be expressed in terms of A_j and B_j as being

$$
\begin{aligned}
N_l &= \frac{\sqrt{a\pi}}{2(1-\nu)}[\frac{1-2\nu}{2}\sum_{j=0}^{N}(-1)^j A_j + \mu\sum_{j=1}^{N}(-1)^j B_j] \\
N_r &= \frac{\sqrt{a\pi}}{2(1-\nu)}[\frac{1-2\nu}{2}\sum_{j=0}^{N} A_j + \mu\sum_{j=1}^{N} B_j]
\end{aligned}
$$

(4.1.31)

Following the method for the surface bonded actuator case by assuming,

$$
y = R\cos\theta, z = R\sin\theta, \quad 0 < \theta < 2\pi
$$

(4.1.32)

where R denotes the distance from the center of the actuator, θ denotes the position angle with respect to y axis, the approximation analytical solution for far field elastic wave can be determined by using steepest decent method as

$$
\begin{aligned}
\sigma_y^f &= \sum_{j=0}^{N} A_j[f_1(j,\theta)\sqrt{\frac{2\pi K}{R}}e^{i(KR-\frac{\pi}{4})} + f_2(j,\theta)\sqrt{\frac{2\pi k}{R}}e^{i(kR-\frac{\pi}{4})}]N_j^1 \\
&+ \sum_{j=1}^{N} B_j[f_3(j,\theta)\sqrt{\frac{2\pi K}{R}}e^{i(KR-\frac{\pi}{4})} + f_4(j,\theta)\sqrt{\frac{2\pi k}{R}}e^{i(kR-\frac{\pi}{4})}]N_j^1
\end{aligned}
$$

(4.1.33)

$$
\begin{aligned}
\sigma_z^f &= \sum_{j=0}^{N} A_j[f_5(j,\theta)\sqrt{\frac{2\pi K}{R}}e^{i(KR-\frac{\pi}{4})} + f_6(j,\theta)\sqrt{\frac{2\pi k}{R}}e^{i(kR-\frac{\pi}{4})}]N_j^1 \\
&+ \sum_{j=1}^{N} B_j[f_7(j,\theta)\sqrt{\frac{2\pi K}{R}}e^{i(KR-\frac{\pi}{4})} + f_8(j,\theta)\sqrt{\frac{2\pi k}{R}}e^{i(kR-\frac{\pi}{4})}]N_j^1
\end{aligned}
$$

(4.1.34)

$$
\begin{aligned}
\sigma_{yz}^f &= \sum_{j=0}^{N} A_j[f_9(j,\theta)\sqrt{\frac{2\pi K}{R}}e^{i(KR-\frac{\pi}{4})} + f_{10}(j,\theta)\sqrt{\frac{2\pi k}{R}}e^{i(kR-\frac{\pi}{4})}]N_j^2 \\
&+ \sum_{j=1}^{N} B_j[f_{11}(j,\theta)\sqrt{\frac{2\pi K}{R}}e^{i(KR-\frac{\pi}{4})} + f_{12}(j,\theta)\sqrt{\frac{2\pi k}{R}}e^{i(kR-\frac{\pi}{4})}]N_j^2
\end{aligned}
$$

(4.1.35)

88

where

$$f_1(j,\theta) = \frac{i(2K^2\cos\theta^2 - k^2)\cos\theta J_j(K\cos\theta)}{2}, f_2(j,\theta) = ik^2\sin^2\theta\cos\theta J_j(k\cos\theta),$$

$$f_3(j,\theta) = -\frac{i(k^2 - 2K^2\sin^2\theta)(2K^2\cos\theta^2 - k^2)J_j(K\cos\theta)}{2K^2\cos\theta},$$

$$f_4(j,\theta) = -2ik^2\sin^2\theta\cos\theta J_j(k\cos\theta),$$

$$f_5(j,\theta) = \frac{i(k^2 - 2K^2\cos^2\theta)\cos\theta J_j(K\cos\theta)}{2}, f_6(j,\theta) = -ik^2\sin^2\theta\cos\theta J_j(k\cos\theta),$$

$$f_7(j,\theta) = \frac{i(k^2 - 2K^2\cos^2\theta)^2 J_j(K\cos\theta)}{2K^2\cos\theta}, f_8(j,\theta) = 2ik^2\sin^2\theta\cos\theta J_j(k\cos\theta),$$

$$f_9(j,\theta) = K^2\cos^2\theta|\sin\theta|J_j(K\cos\theta), f_{10}(j,\theta) = -\frac{(K^2\cos^2\theta - k^2)|\sin\theta|J_j(k\cos\theta)}{2},$$

$$f_{11}(j,\theta) = -\frac{(2K^2\cos^2\theta - k^2)|\sin\theta|J_j(K\cos\theta)}{2},$$

$$f_{12}(j,\theta) = (2K^2\cos^2\theta - k^2)|\sin\theta|J_j(k\cos\theta).$$

For some specific position $y = 0$ and $z \longrightarrow \infty$ where the steepest decent method will break down, an approximation integral solution can be obtained by solving the integral directly as

$$\sigma_y^f = \sum_{j=0}^{N} A_j[\frac{W_1(j)}{|z|}e^{-iK_z} + \frac{W_2(j)}{|z|}e^{-ik_z}] - \mu\sum_{j=1}^{N} B_j[\frac{W_3(j)}{|z|}e^{-iK_z} - 2\frac{W_2(j)}{|z|}e^{-ik_z}] \quad (4.1.36)$$

$$\sigma_z^f = \sum_{j=0}^{N} A_j[\frac{W_4(j)}{|z|}e^{-iK_z} - \frac{W_2(j)}{|z|}e^{-ik_z}] - \mu\sum_{j=1}^{N} B_j[\frac{W_5(j)}{|z|}e^{-iK_z} - 2\frac{W_2(j)}{|z|}e^{-ik_z}] \quad (4.1.37)$$

$$\sigma_{yz}^f = \sum_{j=0}^{N} A_j[\frac{W_6(j)}{|z|}e^{-iK_z} - \frac{W_7(j)}{|z|}e^{-ik_z}] + \mu\sum_{j=1}^{N} B_j[\frac{W_8(j)}{|z|}e^{-iK_z} + \frac{W_9(j)}{|z|}e^{-ik_z}] \quad (4.1.38)$$

where

$$K_z = K|z|, \quad k_z = k|z|,$$

$$W_1(j) = \frac{J_j(K)(2K^2 - k^2)}{2k^2}N_j^1, \quad W_2(j) = J_j(k)N_j^1,$$

$$W_3(j) = \frac{J_j(K)(2K^2 - k^2)^2}{2K^2k^2}N_j^1, W_4(j) = -J_j(K)N_j^1, W_5(j) = \frac{J_j(K)(2K^2 - k^2)k^2}{K^2}N_j^1,$$

$$W_6(j) = K^2 J_j(K)N_j^2, \quad W_7(j) = (2K^2 - k^2)J_j(k)N_j^2/2,$$

$$W_8(j) = (2K^2 - k^2)J_j(K)N_j^2, \quad W_9(j) = (2K^2 - k^2)J_j(k)N_j^2.$$

4.2 Multiple actuators

For the case where multiple actuators are involved, the interaction between actuators may significantly affect the load transfer between the actuators and the host medium, and, therefore, change the resulting waveform. The interaction effect can be simulated using a newly developed Pseudo-Incident Wave technique (Wang and Meguid, 1997).

For a specific actuator A_n, the total incident wave can be expressed as

$$\varepsilon_{yn}^I = \varepsilon_y^0 + \varepsilon_{yn}^p \tag{4.2.1}$$

$$\sigma_{zn}^I = \sigma_z^0 + \sigma_{zn}^p \tag{4.2.2}$$

where ε_y^0 and σ_z^0 are the mechanical incident waves due to external loading, ε_{yn}^p and σ_{zn}^p are the unknown pseudo-incident waves from other actuators. The pseudo incident field of actuator A_n can be obtained by summing up outgoing waves from all other actuators as

$$\varepsilon_{yn}^p = \sum_{\substack{m=1 \\ m \neq n}}^{M} \varepsilon_{ym}(y_n + y_n^0 - y_m^0, z_n^0 - z_m^0), \tag{4.2.3}$$

$$\sigma_{zn}^p = \sum_{\substack{m=1 \\ m \neq n}}^{M} \sigma_{zm}(y_n + y_n^0 - y_m^0, z_n^0 - z_m^0), \tag{4.2.4}$$

with $n = 1, 2, \cdots, M$.

According to the single actuator solutions given by (4.1.23), the Chebeshev polynomial expansion coefficients of actuator A_n, $\{c\}^n = \{A_0^n, A_1^n, \cdots, A_{N-1}^n, B_1^n, B_2^n, \cdots, B_N^n\}^T$, can be determined by

$$[Q]^n \{c\}^n = \{F\}^n \tag{4.2.5}$$

where $[Q]^n$ can directly obtained from $[Q]$ with k_a, q, v, α, β being replaced by k_a^n, q_n, v_n, α_n, β_n, respectively, and

$$\{F\}^n = \{f_E\}^n + \{f_I\}^n \tag{4.2.6}$$

90

with $\{f_E\}^n$ and $\{f_I\}^n$ being the applied electric load and the incident field at the collocation points of actuator A_n given by

$$\{f_E\}^n = \left\{ \begin{array}{c} \varepsilon_E^n(y_n^1) \\ \varepsilon_E^n(y_n^2) \\ \cdots \\ \varepsilon_E^n(y_n^N) \\ \sigma_E^n(y_n^1) \\ \sigma_E^n(y_n^2) \\ \cdots \\ \sigma_E^n(y_n^N) \end{array} \right\}, \{f_I\}^n = -\left\{ \begin{array}{c} \varepsilon_{y_n}^I(y_n^1) \\ \varepsilon_{y_n}^I(y_n^2) \\ \cdots \\ \varepsilon_{y_n}^I(y_n^N) \\ \sigma_{z_n}^I(y_n^1) \\ \sigma_{z_n}^I(y_n^2) \\ \cdots \\ \sigma_{z_n}^I(y_n^N) \end{array} \right\}$$

The incident wave $\{f_I\}^n$ of actuator A_n can be obtained based on Equations (4.2.1) and (4.2.2) as

$$\{f_I\}^n = \{R_0\}^n + \sum_{m \neq n}^{M} [R]^{mn}\{c\}^m \tag{4.2.7}$$

where

$$\{R_0\}^n = \left\{ \begin{array}{c} \varepsilon_{y_n}^0(y_n^1) \\ \varepsilon_{y_n}^0(y_n^2) \\ \cdots \\ \varepsilon_{y_n}^0(y_n^N) \\ \sigma_{z_n}^0(y_n^1) \\ \sigma_{z_n}^0(y_n^2) \\ \cdots \\ \sigma_{z_n}^0(y_n^N) \end{array} \right\}, [R]^{mn} = \left\{ \begin{array}{cc} [G^{(1)}(y_{mn}, z_{mn})] & [G^{(2)}(y_{mn}, z_{mn})] \\ [G^{(3)}(y_{mn}, z_{mn})] & [G^{(4)}(y_{mn}, z_{mn})] \end{array} \right\} \tag{4.2.8}$$

are the applied mechanical incident wave and the scattering matrix induced by other actuators at the collocation points of the actuator A_n, with $y_{mn}^l = y_n^l + y_n^0 - y_m^0$, $z_{mn} = z_n^0 - z_m^0$.

91

In above equations, the matrices $[G^{(i)}(y, z)], i = 1, 2, 3, 4$ are given by

$$G_{jl}^{(1)} = -\frac{1}{2\mu k^2} \int_0^\infty P_j^1(s, y^l)[\frac{s^3}{\alpha}e^{-\alpha|z|} - s\beta e^{-\beta|z|}]ds$$

$$G_{jl}^{(2)} = -\frac{1}{2k^2} \int_0^\infty P_j^1(s, y^l)[-\frac{s\gamma}{\alpha}e^{-\alpha|z|} + 2s\beta e^{-\beta|z|}]ds$$

$$G_{jl}^{(3)} = -\frac{1}{2k^2} \int_0^\infty P_j^1(s, y^l)[-\frac{s\gamma}{\alpha}e^{-\alpha|z|} + 2s\beta e^{-\beta|z|}]ds$$

$$G_{jl}^{(4)} = -\frac{\mu}{2k^2} \int_0^\infty P_j^1(s, y^l)[\frac{\gamma^2}{\alpha s}e^{-\alpha|z|} - 4s\beta e^{-\beta|z|}]ds$$

Substituting (4.2.6), (4.2.7) into (4.2.5), the following algebraic equations can be obtained,

$$[Q]^n\{c\}^n - \sum_{m \neq n}^M [R]^{mn}\{c\}^m = [f_E]^n + [R_0]^n, \quad n = 1, 2, \cdots, M \qquad (4.2.9)$$

from which $\{c\}^n$ can be determined. The total resulting wave propagation can be obtained by superimposing the wave generated by different actuator which is expressed in terms of $\{c\}^n$.

4.3 Results and discussion

This section will be devoted to the discussion of the dynamic electromechanical behaviour of piezoelectric actuators embedded in an elastic medium under electric loading. Specifically, it is desired to determine the effect of different actuator parameters and the interaction between actuators upon the generated wave propagation in the host medium.

4.3.1 Static load transfer

To validate the actuator model, consider first the quasi-static load transfer between the actuator and the host medium. The material constants of the actuator are assumed to be PZT-4.

Figure 4.3 shows normalized shear stress distribution, $\tau^* = \tau/\sigma_B$, $\sigma_B = e_{33}^a E_z$, along the interface between the actuator and the host medium with different length-to-thickness ratio $v = a/h = 5, 10, 20$, respectively, for the case where $q = \pi\mu/c_{11}^a = $

0.14. A comparison is made with finite element results using the structural analysis software ANSYS. Excellent agreement is observed between the solutions even for a short actuator with $v = 5$.

Figure 4.4 shows the normalized normal stress distribution $\sigma_z^* = \sigma_z/\sigma_B$ along the interface for the same case as presented in Figure 4.3. It is observed that with the decrease of v the transverse stress σ_z increases, indicating that it is necessary to consider the effect of transverse deformation for short actuators. Comparison with the corresponding finite element results shows very good agreement.

To evaluate the effect of transverse deformation of the actuator, the shear stress $\sigma_{yz}^* = \sigma_{yz}/\sigma_B$ in the host medium distribution along $z = 0.5a$, is shown in Figure 4.5 and compared with the finite element result and that from a simplified line model of the actuator (Wang and Meguid, 1999), in which the transverse deformation of the actuator is ignored, i.e., $\Gamma = 0$. The comparison shows significant improvement of the current actuator model in predicting the local stress field.

4.3.2 Dynamic load transfer

Figure 4.6 shows the normalized dynamic shear stress distribution $\tau^* = \tau/\sigma_B$ along the interface for the case where $v = 20$, $q = 1.5$, $\rho_a/\rho_H = 1$, with ρ_a and ρ_H being the mass density of the actuator and the host structure, respectively. It is observed that, in the frequency range considered, higher shear stress level can be observed with increasing loading frequency.

Figure 4.7 shows the normalized dynamic transverse stress $\sigma_z^* = \sigma_z/\sigma_B$ along the interface for the same case as presented in Figure 4.6. It is found that the effect of the loading frequency upon the transverse stress σ_z^* is much stronger than that for the shear stress. Significant transverse stress is observed for high frequencies ($ka = 12$), for example). It should be mentioned that the existence of high transverse stress may result in a wave propagating mainly in the direction perpendicular to the actuator,

93

which is similar to that generated by traditional piezoelectric transducers.

Another interesting issue is the stress concentration around the tips of the actuator. Figures 4.8 and 4.9 show the normalized shear stress singular factor (SSSF) $S^* = S/\sigma_B\sqrt{\pi a}$ and the normalized normal stress intensity factor (NSIF) $N^* = N/\sigma_B\sqrt{\pi a}$ for the case where $v = 20$ and $\rho_a/\rho_H = 1$. Those results show the dramatic effects of the material combination, q, upon S^*. It is interesting to mention that both S^* and N^* are not sensitive to the loading frequency. This result indicates that the variation of load transfer with loading frequency happens mainly in the interior region of the interface, which is away from the tips.

4.3.3 Interaction between actuators

The interaction between actuators may significantly change the resulting load transfer and the waveform. Figure 4.10 shows the normalized dynamic interfacial shear stress, $\xi_\tau = \tau/\tau^{single}$, of an actuator interacting with a collinear actuator of equal length. τ^{single} is the corresponding shear stress distribution of a single actuator and ξ_τ represents the disturbance of the shear stress due to the interaction. In this case, the two actuators are subjected to the same applied electric field E_z, $v = 20$, $q = 0.46$, $\rho_a/\rho_H = 1$ and $2e = 0.5a$, with $2e$ being the distance between the inner tips of the actuators. The shear stress increases significantly due to the interaction of the actuators, especially for relatively high frequencies ($ka > 3$) and the interior range of the actuator.

The effect of interaction between these actuators upon the transverse stress, $\xi_\sigma = \sigma_z/\sigma_z^{single}$, is shown in Figure 4.11, with σ_z^{single} being the normal stress distribution along the interface due to a single actuator. Unlike the shear stress, the interaction effect may be reduced with the increase of the loading frequency.

4.3.4 Wave propagation

Figure 4.12 shows the amplitude of $\sigma_z^* = \sigma_z/\sigma_B$ in the elastic matrix caused by

94

one actuator subjected to a harmonic electric field, located at $|y/a| < 1$ and $z/a = 0$, for the case where $ka = 3.0$, $v = 20$, $q = 0.46$, $\rho_a/\rho_H = 1$. In this case, recognizable wave propagation in both the axial and transverse directions can be observed. Figure 4.13 shows the amplitude of $\sigma_z^* = \sigma_z/\sigma_B$ in the matrix caused by the same actuator for higher loading frequency $ka = 20.0$. Significantly stronger wave propagation in z-direction is observed. This is believed to be caused by the higher transverse stress σ_z along the actuator-matrix interface, as shown in Figure 4.7. Detailed simulation for different loading frequency k, material mismatch q and actuator dimension h and a indicates that stronger wave propagation in the transverse direction perpendicular to the actuator can be generated by (i) using higher frequency loading, (ii) increasing the thickness or the length of the actuator while the same E_z is applied, (iii) using higher material mismatch q. The interfacial transverse stress may play a more important role in generating high frequency wave propagation than that of the interfacial shear stress.

The normalized stresses $\sigma_z^* = \sigma_z/\sigma_B$, $\sigma_y^* = \sigma_y/\sigma_B$ caused by two collinear actuators of equal length is depicted in Figures 4.14 and 4.15 for the case where $ka = 5.0$, $v = 20$, $q = 0.46$, $\rho_a/\rho_H = 1$. The centers of the two actuators are at $y/a = -1.5, z/a = 0$ and $y/a = 1.5, z/a = 0$ in the global coordinate system. Similar to the single actuator cases, stronger wave propagation characterized by higher amplitude of the resulting wave in z-direction can be observed. Different waveforms can be generated by adjusting the position and size of the actuators. Figure 4.16 shows $\sigma_z^* = \sigma_z/\sigma_B$ distribution caused by three equally spaced collinear actuators of equal length, for the cases where $ka = 10.0$, $v = 20$, $q = 0.46$, and $\rho_a/\rho_H = 1$. The centers of the three actuators are at $y/a = -6.0, z/a = 0$, $y/a = 0, z/a = 0$ and $y/a = 6.0, z/a = 0$ in the global coordinate system. Because of the symmetry of the problem, only the second and the third actuators are included in Figure 4.16. For this specific case, the interacting effect becomes very weak as evidenced by the almost symmetric

distribution of σ_z around the third actuator. It should be mentioned that the current arrangement of actuators enables the generation of wave propagation in a larger area, in comparison with that by two actuators.

4.3.5 Far field waveform

Figure 4.17 shows the comparison of $\sigma_z^{f*} = \sigma_z^f/\sigma_B$ from the obtained asymptotic analytical solution with that from the numerical result for the case where $ka = 10.0$, $q = 0.5$, $v = 20$ and $\rho_a/\rho_H = 1$. The very good agreement shows the validate of the obtained asymptotic solutions. Figure 4.18 shows the wave field far away from the embedded actuator, σ_z^{f*}, for the case where $ka = 4.0$, $q = 0.5$, $v = 20$ and $\rho_a/\rho_H = 1$. It can be found that the main wave energy propagates along z direction. Figure 4.19 shows the corresponding result for loading frequency $ka = 10.0$. It is observed that the energy will mainly propagate along z direction and the focus range of the wave energy will be reduced with the increase of the loading frequency, which shows the basic properties of the far field waveform caused by using embedded actuators.
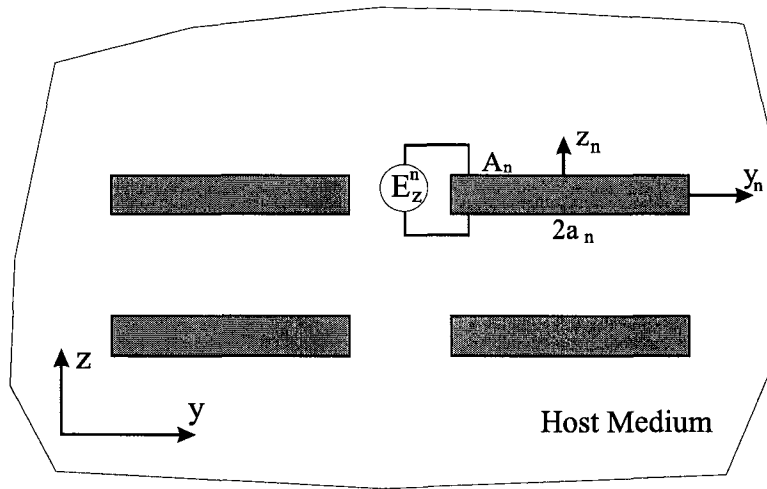
Figure 4.1: Multiple embedded piezoelectric actuators
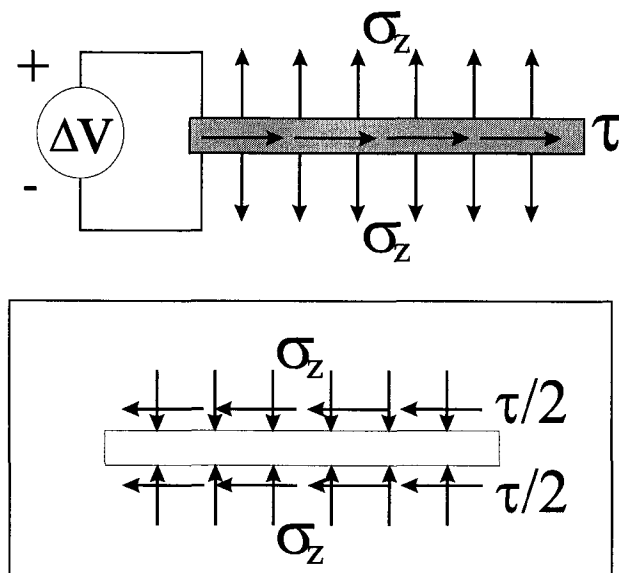
Figure 4.2: Actuator model for embedded actuator

97
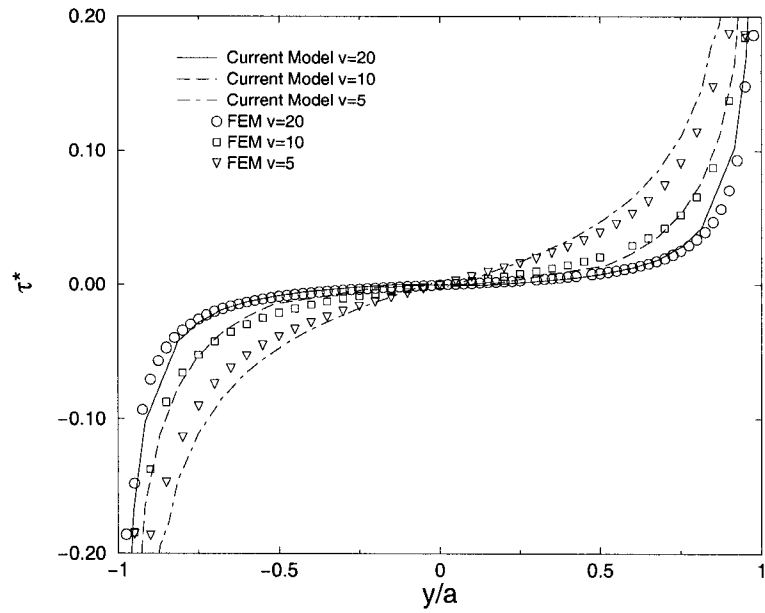
Figure 4.3: The interfacial shear stress distribution: static state
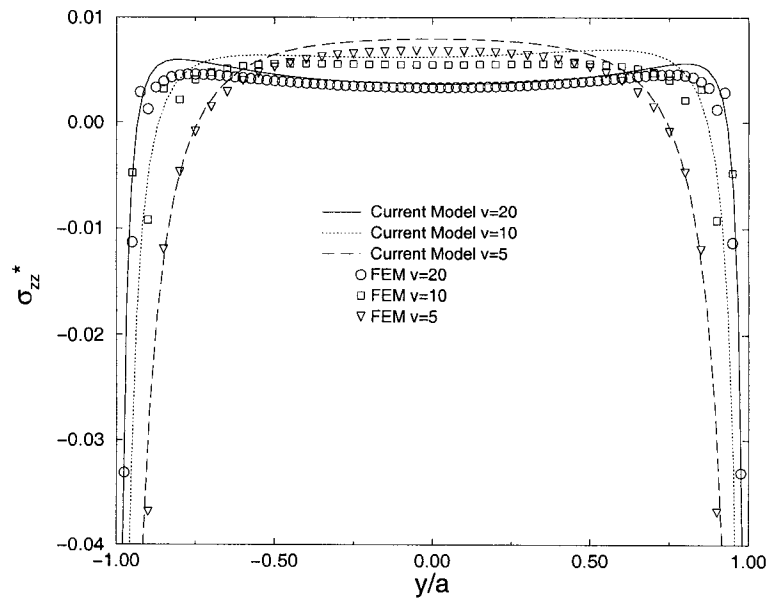
Figure 4.4: The interfacial normal stress distribution: static state

98
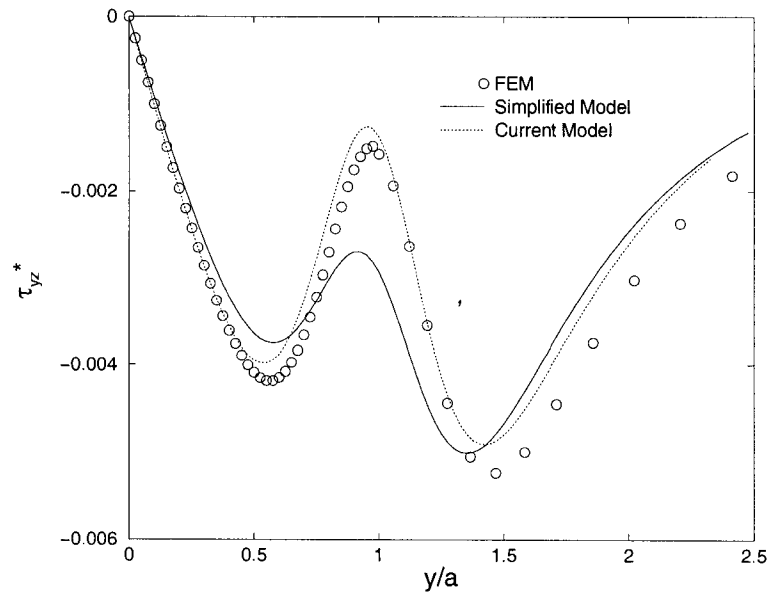
Figure 4.5: The shear stress distribution
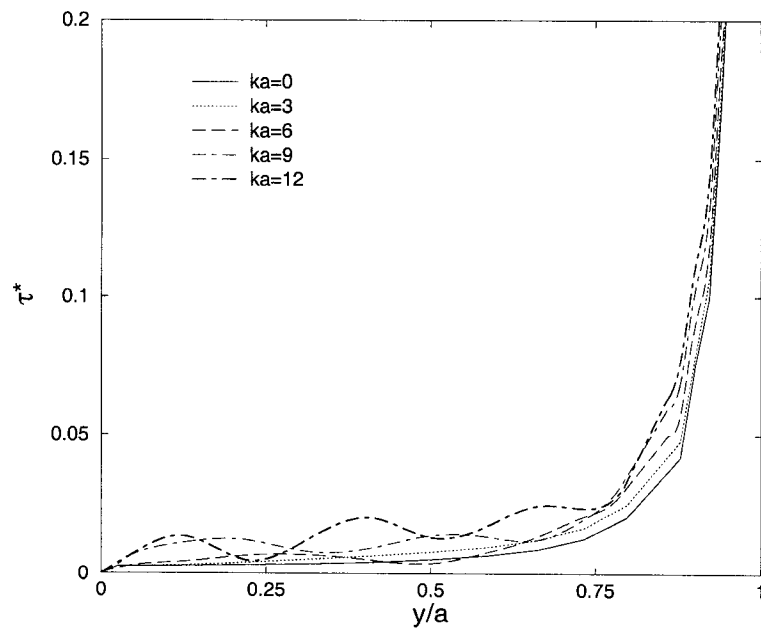
Figure 4.6: The interfacial shear stress distribution: dynamic state

99
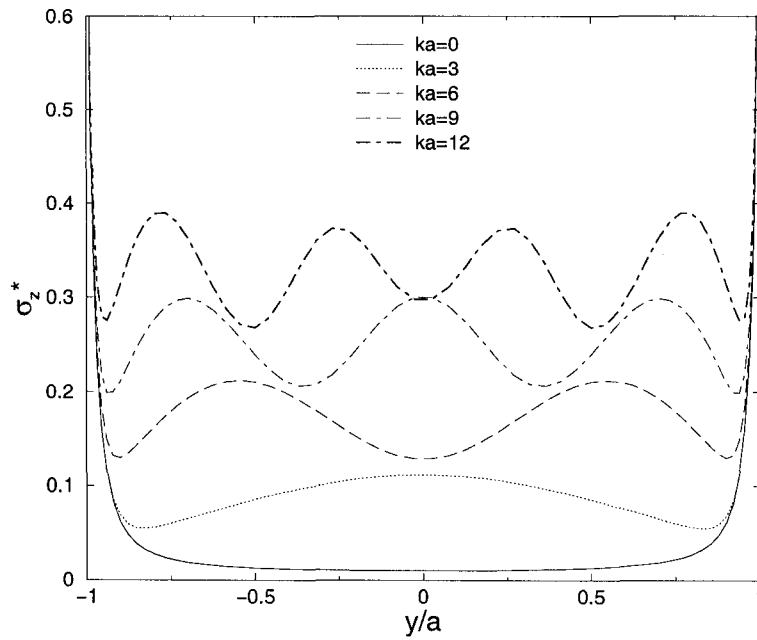
Figure 4.7: The interfacial normal stress distribution: dynamic state
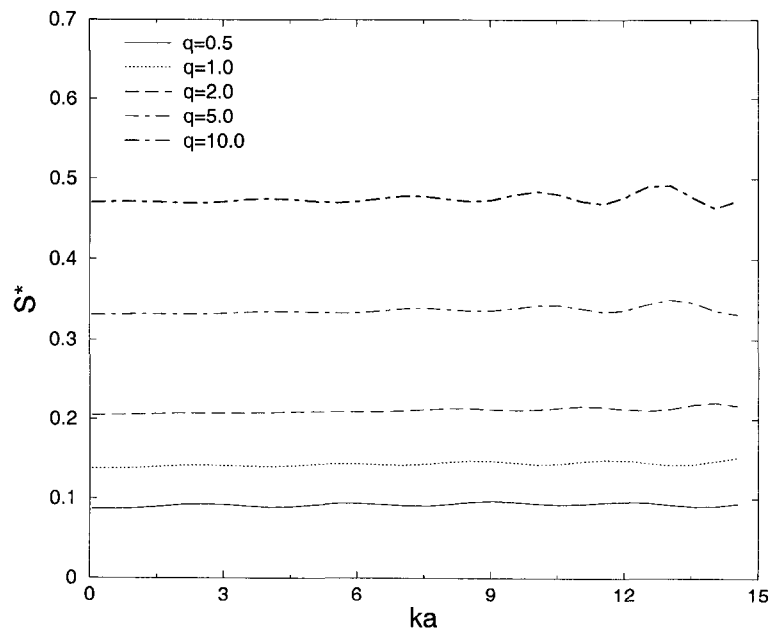
Figure 4.8: The normalized shear stress singularity factor S^*

100
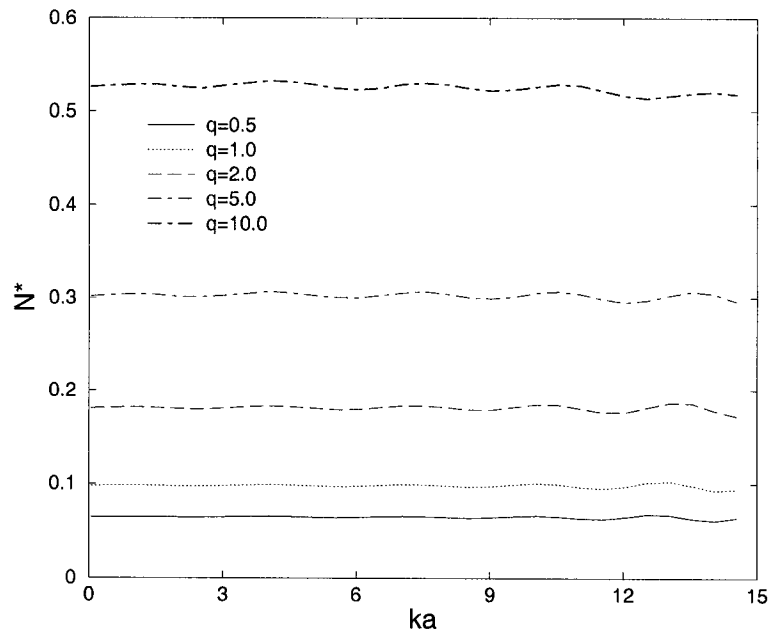
Figure 4.9: The normalized normal stress singularity factor N^*
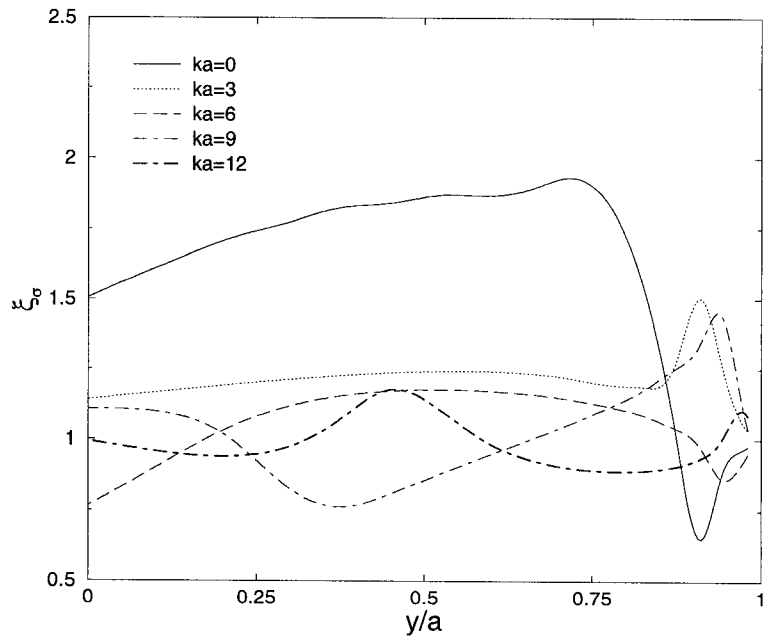
Figure 4.10: The interaction effect upon the interfacial shear stress

101
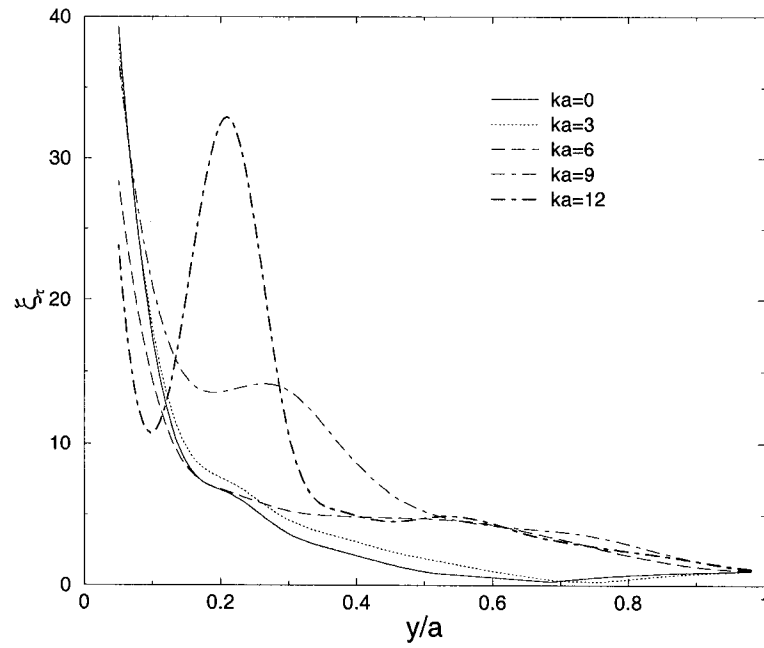
Figure 4.11: The interaction effect upon the interfacial normal stress
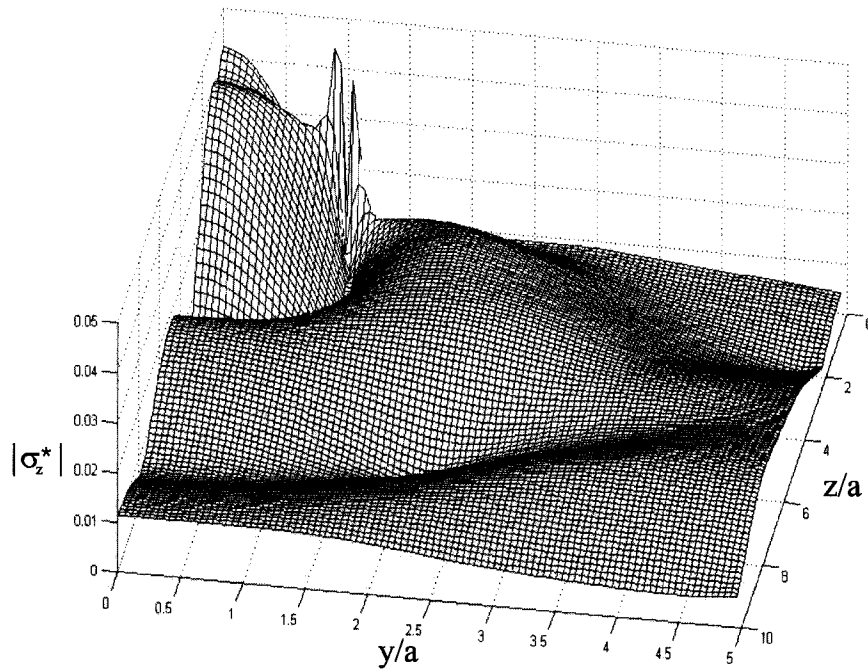
Figure 4.12: The stress distribution σ_z^* in the host medium: $ka = 3$

102
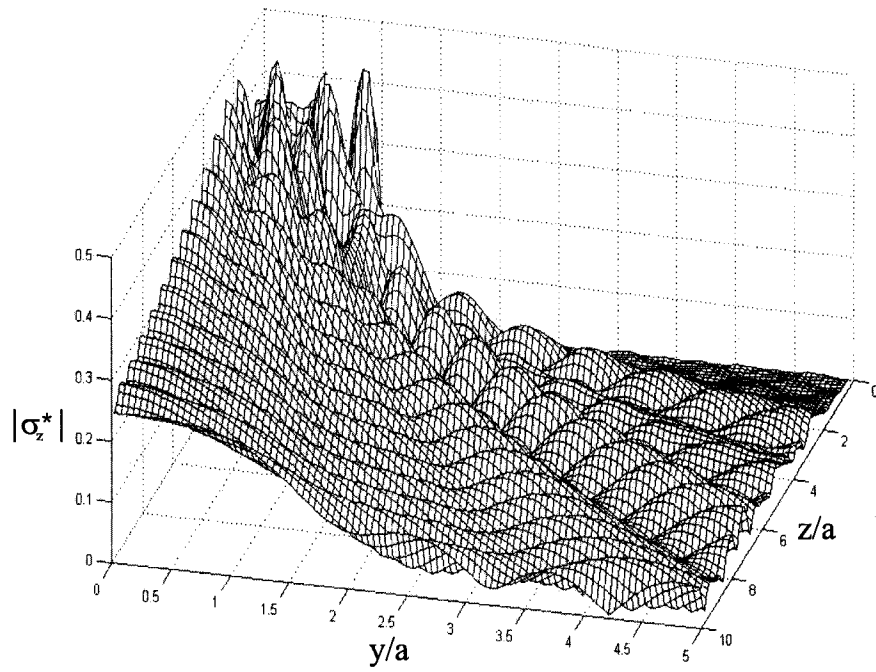
Figure 4.13: The stress distribution σ_z^* in the host medium: $ka = 10$
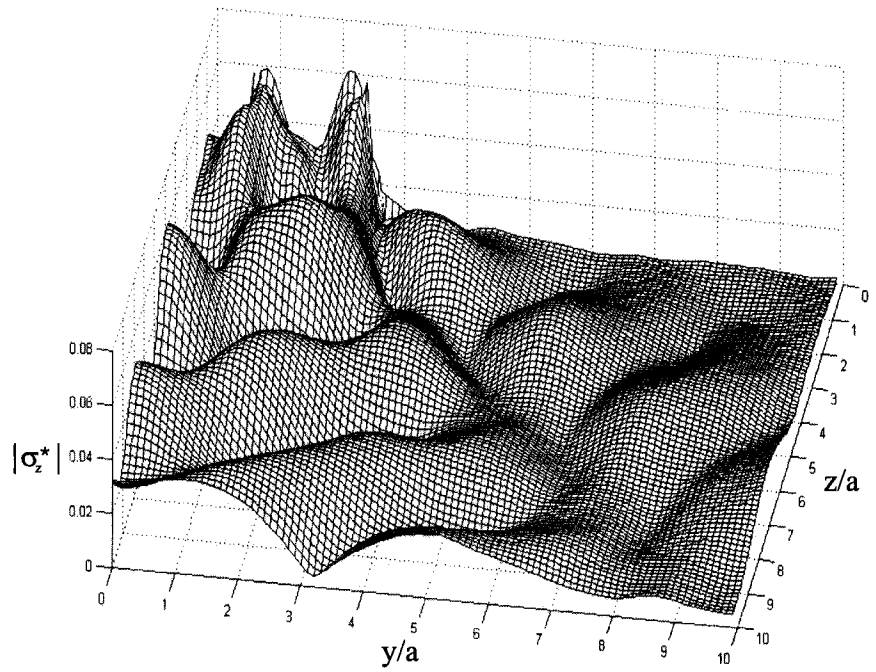
Figure 4.14: The stress distribution σ_z^* in the host medium for two actuators

103
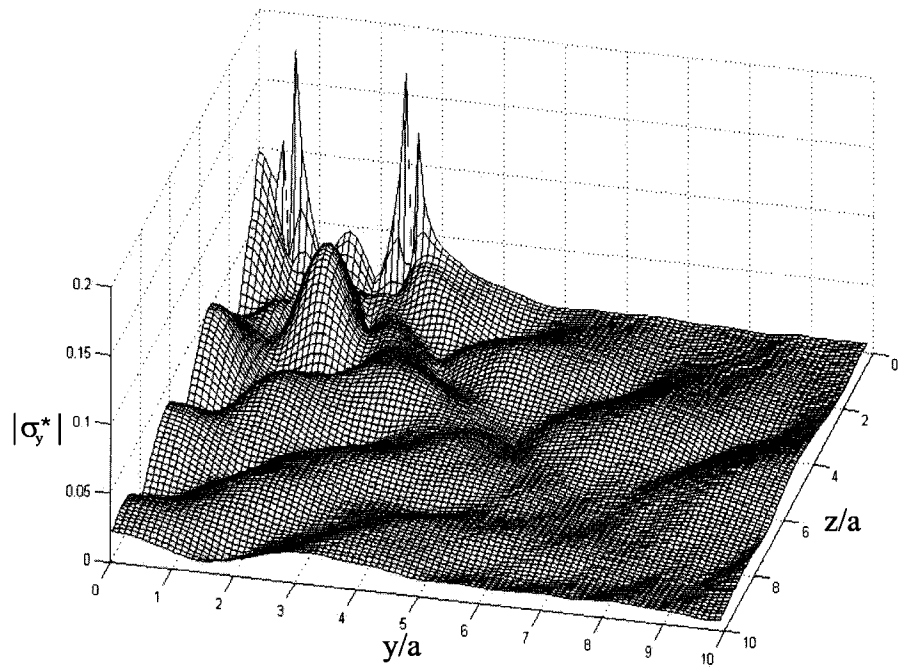
Figure 4.15: The stress distribution σ_y^* in the host medium for two actuators
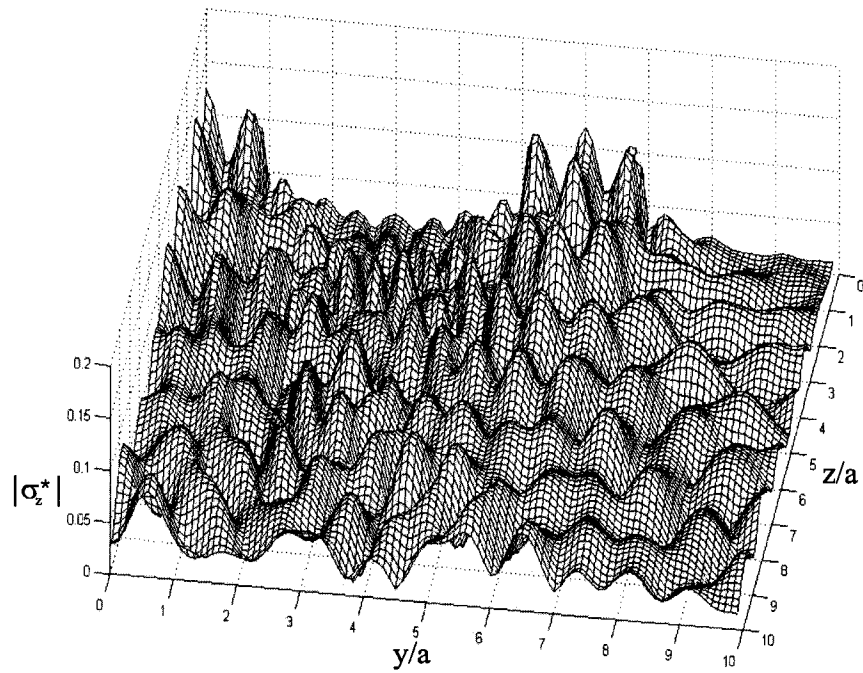
Figure 4.16: The stress distribution σ_z^* in the host medium for three actuators

104
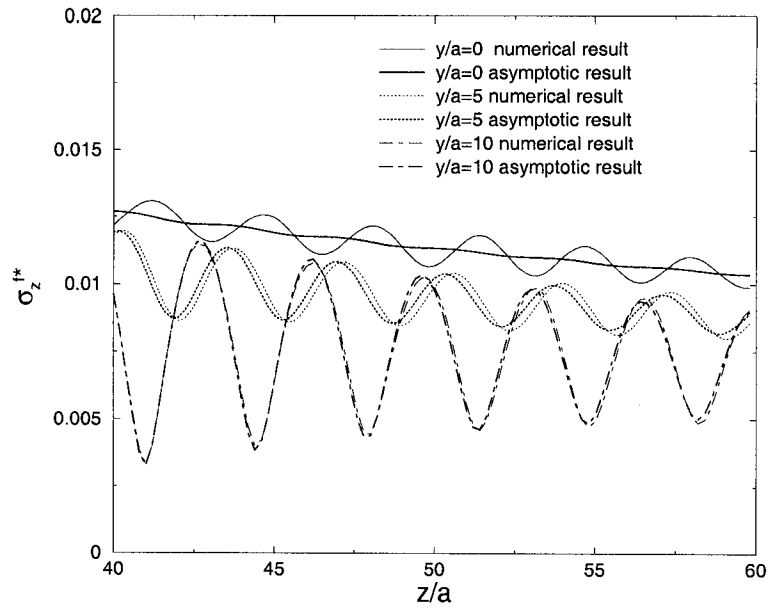
Figure 4.17: The comparison of the far field stress distribution σ_z^{f*}
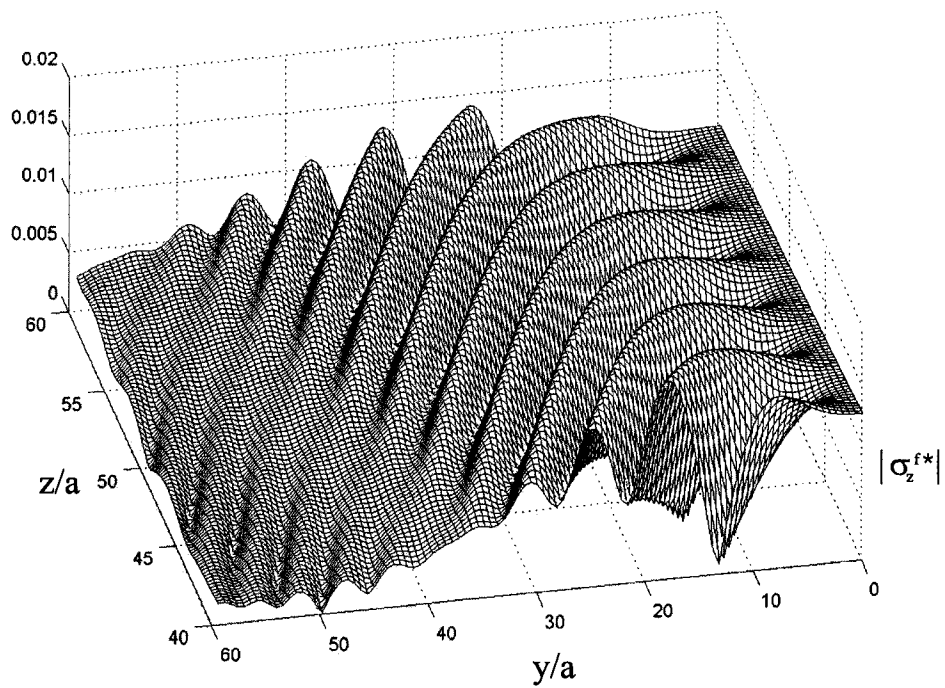
Figure 4.18: The far field stress distribution σ_z^{f*} in the host medium: $ka = 4$

105
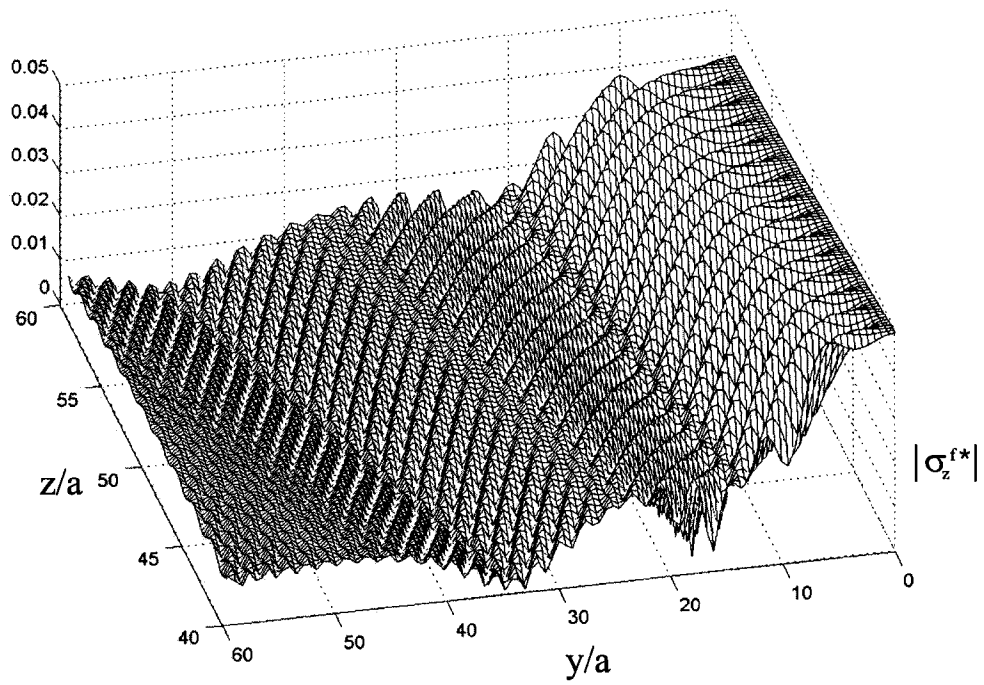
Figure 4.19: The far field stress distribution σ_z^{f*} in the host medium: $ka = 10$

106

Chapter 5

Elastic Wave Propagation in a Cracked Medium

Based on the results obtained in the previous chapters, the wave propagation in a cracked elastic medium induced by an embedded piezoelectric actuator is studied to determine the information of embedded cracks using a piezoelectric actuator/sensor system. The main objectives of this Chapter are to (i) develop a basic understanding of the effects of the crack upon the wave field generated by the actuator, and (ii) determine the characteristics of the crack using the information of scattering waves, which can be measured by a sensor system. A comprehensive theoretical description is given to investigate the dynamic behaviour between the actuator and crack based on the newly developed actuator model and Pseudo-Incident Wave method. The reversed scattering waves can be obtained by solving an elastodynamic problem using sensor signals as boundary conditions. The results are then used in an imaging technique to identify cracks.

5.1 Formulation of the problem

A piezoelectric actuator embedded in a material can generate complicated elastic wave propagation, which depends on the geometry of the actuator, the loading frequency and the material mismatch between the actuator and the host medium (Wang, 2000).

107

To explore the potential of using this type of wave propagation to identify damages, an important question to be answered is how to describe the resulting wave propagation in damaged medium and whether the generated wave can provide useful information for damage identification. The current study will be focussed on this issue, especially the interaction between piezoelectric actuators and cracks.

The problem envisaged is the plane strain deformation of a thin piezoceramic actuator embedded in an isotropic elastic medium with an arbitrarily located and oriented crack, as illustrated in Figure 5.1. Two rectangular coordinate systems (y, z) and (ξ, η) are employed to characterize the actuator and the crack. The position of the centre of the crack is given by (y_c, z_c) in coordinate system (y, z). The distance between the centre of the crack and the centre of the actuator is e. The inclination angle and the orientation angle of the crack with respect to the y-axis are θ and ϕ. The respective half-lengthes of the crack and the actuator are c and a. It is assumed that the poling direction of the actuator is along the z-axis. A voltage between the upper and the lower electrodes of the actuator is applied, which results in an electric field E_z of frequency ω along the poling direction of the actuator, $E_z = (V^- - V^+)/h$, with V^-, V^+ and h being the electric potentials at the lower and the upper electrodes, and the thickness of the actuator. In this paper, the steady state response of the system is discussed. The corresponding time factor $\exp(-i\omega t)$, which applies to all the field variables, will be suppressed and only the amplitudes of them will be considered.

In response to the applied electric field, elastic wave propagation in the host medium is generated, which can be described using the PsIW technique. The original problem, shown in Figure 5.1(a), can be decomposed into two subproblems shown in Figure 5.1(b) and 5.1(c). In subproblem (b) the actuator is subjected to the applied electric field and a pseudo-incident wave W_a^P, while in subproblem (c) the crack is subjected to a pseudo-incident wave W_c^P. The pseudo-incident waves can be related to the outgoing wave from the actuator W_a^{out} and the scattering wave from the crack

108

W_c^{sc} as

$$W_a^P = W_c^{sc}, \quad W_c^P = W_a^{out}. \tag{5.1.1}$$

5.2 Actuator-Induced Wave Propagation

Based on the superposition shown in Figure 5.1, the original problem is reduced to a single actuator problem and a single crack problem, which are coupled with the relation being given by Equation (5.1.1). These two problems will be discussed in the following subsections.

5.2.1 Outgoing waves from the actuator

Consider now a thin actuator, subjected to an applied electric field E_z and a pseudo-incident wave W_a^P, as shown in Figure 5.1(b). Based on the developed actuator model, the axial strain $\varepsilon_y^a(y)$ and the transverse stress $\sigma_z^a(y)$ of the actuator can be obtained in terms of τ and $(u_z^{a+} - u_z^{a-})$ by conducting a dynamic electromechanical analysis of the actuator element. The elastic field in the host medium can also be expressed in terms of τ and $(u_z^{a+} - u_z^{a-})$ through an elastodynamic analysis. The detailed discussion can be found in Chapter 4.

The continuity conditions between the actuator and the host medium can be expressed as

$$\varepsilon_y^a(y) = \varepsilon_y^{out}(y,0) + \varepsilon_{ya}^P(y,0), \tag{5.2.1}$$

$$\sigma_z^a(y) = \sigma_z^{out}(y,0) + \sigma_{za}^P(y,0), \tag{5.2.2}$$

$$u_z^{a+} - u_z^{a-} = (u_z^+ - u_z^-)^{out} \tag{5.2.3}$$

where superscript $'a'$, $'out'$ and $'P'$ represent the actuator, the outgoing wave in the host medium and the pseudo-incident wave field, respectively. Making use of the results for ε_y^a and σ_z^a and the continuity conditions given in (5.2.1)-(5.2.3), the

109

following integral equations for determining τ and $(u_z^{a+} - u_z^{a-})$ can be obtained

$$-\frac{1}{2\pi\mu}\int_{-a}^{a}[\tau(\xi)n_1(y-\xi) + \mu\Gamma(\xi)n_2(y-\xi)]d\xi$$

$$-\frac{\sin k_a(a+y)}{hc_{11}^a \sin 2k_a a}\int_{-a}^{a}[\tau(\xi) + c_{31}^a\Gamma(\xi)]\cos k_a(\xi - a)d\xi$$

$$+\frac{1}{hc_{11}^a}\int_{-a}^{y}[\tau(\xi) + c_{31}^a\Gamma(\xi)]\cos k_a(\xi - y)d\xi = \varepsilon_E(y) - \varepsilon_{ya}^P(y,0), \quad |y| < a \quad (5.2.4)$$

$$-\frac{1}{2\pi}\int_{-a}^{a}[\tau(\xi)n_2(y-\xi) + \mu\Gamma(\xi)n_3(y-\xi)]d\xi - \frac{c_{33}^a}{h}\int_{-a}^{y}\Gamma(\xi)d\xi$$

$$-\frac{c_{31}^a \sin k_a(a+y)}{hc_{11}^a \sin 2k_a a}\int_{-a}^{a}[\tau(\xi) + c_{31}^a\Gamma(\xi)]\cos k_a(\xi - a)d\xi$$

$$+\frac{c_{31}^a}{hc_{11}^a}\int_{-a}^{y}[\tau(\xi) + c_{31}^a\Gamma(\xi)]\cos k_a(\xi - y)d\xi = \sigma_E(y) - \sigma_{za}^P(y,0), \quad |y| < a \quad (5.2.5)$$

where $\varepsilon_{ya}^P(y,0)$ and $\sigma_{za}^P(y,0)$ are the strain and stress components caused by the pseudo-incident wave field at the location of the actuator.

By solving the integral equations, which involve a square-root singularity, using the Chebyshev polynomials of the first kind, the outgoing wave of the actuator W_a^{out}, which propagates in the host medium and is governed by the interfacial stress τ and the transverse deformation Γ, can then be obtained in terms of $\{c\} = \{c_0^1, c_1^1, \cdots, c_{N-1}^1, c_1^2, c_2^2, \cdots, c_N^2\}^T$ as

$$\left.\begin{array}{l}\sigma_y^{out}(y,z) = \{[M^1(y,z)]\}\{c\} \\[4pt] \sigma_z^{out}(y,z) = \{[M^2(y,z)]\}\{c\} \\[4pt] \sigma_{yz}^{out}(y,z) = \{[M^3(y,z)]\}\{c\} \\[4pt] u_y^{out}(y,z) = \{[M^4(y,z)]\}\{c\} \\[4pt] u_z^{out}(y,z) = \{[M^5(y,z)]\}\{c\}\end{array}\right\} \quad (5.2.6)$$

where

$$M_j^1(y,z) = \begin{cases} -\dfrac{1}{k^2}\displaystyle\int_0^\infty [\dfrac{s\gamma}{2\alpha}e^{-\alpha|z|} - s\beta e^{-\beta|z|}]P_{j-1}^1 ds & j = 1, \cdots, N \\[18pt] -\dfrac{\mu}{k^2}\displaystyle\int_0^\infty [-\dfrac{(2\alpha^2 + k^2)\gamma}{2\alpha s}e^{-\alpha|z|} + 2s\beta e^{-\beta|z|}]P_{j-N}^1 ds & j = N+1, \cdots, 2N \end{cases}$$

110

$$M_j^2(y,z) = \begin{cases} -\dfrac{1}{k^2}\displaystyle\int_0^\infty [-\dfrac{s\gamma}{2\alpha}e^{-\alpha|z|} + s\beta e^{-\beta|z|}]P_{j-1}^1 ds & j = 1,\cdots,N \\[4ex] -\dfrac{\mu}{k^2}\displaystyle\int_0^\infty [\dfrac{\gamma^2}{2\alpha s}e^{-\alpha|z|} - 2s\beta e^{-\beta|z|}]P_{j-N}^1 ds & j = N+1,\cdots,2N \end{cases}$$

$$M_j^3(y,z) = \begin{cases} \dfrac{sgn(z)}{k^2}\displaystyle\int_0^\infty [s^2 e^{-\alpha|z|} - \dfrac{\gamma}{2}e^{-\beta|z|}]P_{j-1}^2 ds & j = 1,\cdots,N \\[4ex] \dfrac{sgn(z)\mu}{k^2}\displaystyle\int_0^\infty [\gamma(-e^{-\alpha|z|} + e^{-\beta|z|})]P_{j-N}^2 ds & j = N+1,\cdots,2N \end{cases}$$

$$M_j^4(y,z) = \begin{cases} \dfrac{1}{\mu k^2}\displaystyle\int_0^\infty [-\dfrac{s^2}{2\alpha}e^{-\alpha|z|} + \dfrac{\beta}{2}e^{-\beta|z|}]P_{j-1}^2 ds & j = 1,\cdots,N \\[4ex] \dfrac{1}{k^2}\displaystyle\int_0^\infty [\dfrac{\gamma}{2\alpha}e^{-\alpha|z|} - \beta e^{-\beta|z|}]P_{j-N}^2 ds & j = N+1,\cdots,2N \end{cases}$$

$$M_j^5(y,z) = \begin{cases} -\dfrac{sgn(z)}{\mu k^2}\displaystyle\int_0^\infty [\dfrac{\alpha}{2}(e^{-\alpha|z|} - e^{-\beta|z|})]P_{j-1}^1 ds & j = 1,\cdots,N \\[4ex] \dfrac{sgn(z)}{k^2}\displaystyle\int_0^\infty [\dfrac{\gamma}{2s}e^{-\alpha|z|} - se^{-\beta|z|}]P_{j-N}^1 ds & j = N+1,\cdots,2N \end{cases}$$

with $\gamma = s^2 + \beta^2$.

5.2.2 Scattering waves by the crack

Consider now the elastodynamic behaviour of a single crack as shown in Figure 5.1(c). The crack is assumed to lie on the ξ-axis with its centre coinciding with the origin of coordinate system (ξ, η). The crack is subjected to a pseudo-incident wave W_c^P with its boundary condition being

$$\sigma_{\xi\eta}(\xi,0) = -\sigma_{\xi\eta c}^P(\xi) \quad \sigma_\eta(\xi,0) = -\sigma_{\eta c}^P(\xi) \quad |\xi| < c \tag{5.2.7}$$

$$u_\xi(\xi,0^+) - u_\xi(\xi,0^-) = 0 \quad u_\eta(\xi,0^+) - u_\eta(\xi,0^-) = 0 \quad |\xi| > c \tag{5.2.8}$$

where $\sigma_{\xi\eta c}^P(\xi)$, $\sigma_{\eta c}^P(\xi)$ represent the stress components due to the pseudo-incident wave, and $u_\xi(\xi,0^+)$, $u_\xi(\xi,0^-)$, $u_\eta(\xi,0^+)$, $u_\eta(\xi,0^-)$ are displacements in ξ and η directions at the upper and the lower surfaces of the crack.

111

Introduce the following dislocation density functions

$$m(\xi) = \frac{\partial}{\partial \xi}[u_\xi(\xi, 0^+) - u_\xi(\xi, 0^-)], \quad n(\xi) = \frac{\partial}{\partial \xi}[u_\eta(\xi, 0^+) - u_\eta(\xi, 0^-)] \qquad (5.2.9)$$

which govern the stress field of the cracked medium (Meguid and Wang, 1995). Conducting elastodynamic analysis of the cracked medium and making use of the continuity conditions of σ_η and $\sigma_{\xi\eta}$ at $\eta = 0$ and the boundary conditions given in (5.2.7) and (5.2.8), the following singular integral equations in terms of functions $m(\xi)$ and $n(\xi)$ can be obtained,

$$\int_{-c}^{c} \frac{m(w)}{w - \xi} dw + \int_{-c}^{c} m(w) \int_0^\infty [\frac{(s^2 + \beta^2)^2 - 4s^2\alpha\beta}{2(K^2 - k^2)s\beta} - 1] \sin[s(w - \xi)] ds dw$$

$$= -\frac{4\pi(1 - \nu^2)}{E} \sigma_{\xi\eta c}^P(\xi) \ , \quad |\xi| < c \ (5.2.10)$$

$$\int_{-c}^{c} \frac{n(w)}{w - \xi} dw + \int_{-c}^{c} n(w) \int_0^\infty [\frac{(s^2 + \beta^2)^2 - 4s^2\alpha\beta}{2(K^2 - k^2)s\alpha} - 1] \sin[s(w - \xi)] ds dw$$

$$= -\frac{4\pi(1 - \nu^2)}{E} \sigma_{\eta c}^P(\xi) \ , \quad |\xi| < c \ (5.2.11)$$

and

$$\int_{-c}^{c} m(w) dw = 0, \quad \int_{-c}^{c} n(w) dw = 0. \qquad (5.2.12)$$

where E and ν are Young's modulus and Poisson's ratio of the host medium.

Since Equations (5.2.10) and (5.2.11) are square-root singular, $m(w)$ and $n(w)$ can be expressed in term of Chebyshev polynomials,

$$m(w) = \sum_{j=0}^{N} \frac{d_j^1}{\sqrt{1 - w^2/c^2}} T_j(w/c), \quad n(w) = \sum_{j=0}^{N} \frac{d_j^2}{\sqrt{1 - w^2/c^2}} T_j(w/c). \qquad (5.2.13)$$

From the orthogonality conditions of the Chebyshev polynomials, Equation (5.2.12) reduces to $d_0^1 = 0$ and $d_0^2 = 0$. If the Equation (5.2.13) is satisfied at N collocation points along the length of the crack

$$\xi^l = c \, \cos(\frac{l - 1}{N - 1}\pi) \ , \quad l = 1, 2, \cdots, N \qquad (5.2.14)$$

112

The following $2N$ linear algebraic equations can be reduced as (Meguid and Wang, 1995)

$$[B]\{d\} = \{W\} \qquad (5.2.15)$$

$[B]$ is a known matrix given as

$$[B_{lj}] = \begin{bmatrix} f_j(\eta^l) & 0 \\ 0 & g_j(\eta^l) \end{bmatrix}$$

with

$$f_j(\xi^l) = \frac{\sin\left[j\cos^{-1}\xi^l\right]}{\sin\left[\cos^{-1}\xi^l\right]} + c\int_0^\infty [\frac{\gamma^2 - 4s^2\alpha\beta}{2(K^2 - k^2)s\beta} - 1]P^1(s,\xi^l)ds$$

$$g_j(\xi^l) = \frac{\sin\left[j\cos^{-1}\xi^l\right]}{\sin\left[\cos^{-1}\xi^l\right]} + c\int_0^\infty [\frac{\gamma^2 - 4s^2\alpha\beta}{2(K^2 - k^2)s\alpha} - 1]P^1(s,\xi^l)ds$$

In above equations, $\{W\}$ is the applied load with

$$W_l = -\frac{4\pi(1 - \nu^2)}{E}\sigma_{\xi\eta}^{IK}(\xi^l), \quad W_{N+l} = -\frac{4\pi(1 - \nu^2)}{E}\sigma_\eta^{IK}(\xi^l), \quad l = 1, 2, \cdots, N \quad (5.2.16)$$

The scattering wave from the crack can finally be expressed in terms of $\{d\} = \{d_1^1, d_2^1, \cdots, d_N^1, d_1^2, d_2^2, \cdots, d_N^2\}$ as

$$\left.\begin{aligned} \sigma_\xi^{sc}(\xi,\eta) &= \{[R^1(\xi,\eta)]\}\{d\} \\ \sigma_\eta^{sc}(\xi,\eta) &= \{[R^2(\xi,\eta)]\}\{d\} \\ \sigma_{\xi\eta}^{sc}(\xi,\eta) &= \{[R^3(\xi,\eta)]\}\{d\} \\ \varepsilon_\xi^{sc}(\xi,\eta) &= \{[R^4(\xi,\eta)]\}\{d\} \\ \varepsilon_\eta^{sc}(\xi,\eta) &= \{[R^5(\xi,\eta)]\}\{d\} \\ \varepsilon_{\xi\eta}^{sc}(\xi,\eta) &= \{[R^6(\xi,\eta)]\}\{d\} \end{aligned}\right\} \qquad (5.2.17)$$

where

$$R_j^1(y,z) = \begin{cases} \dfrac{sgn(z)\lambda c}{k^2}\displaystyle\int_0^\infty [(s^2 - \nu\alpha^2)e^{-\alpha|z|} - (\alpha^2 - \nu s^2)e^{-\beta|z|}]P_j^1 ds & j = 1, \cdots, N \\[2em] \dfrac{\lambda c}{2k^2}\displaystyle\int_0^\infty [\dfrac{\gamma(\nu\alpha^2 - s^2)}{s\alpha}e^{-\alpha|z|} - 2(1 - \nu)s\beta e^{-\beta|z|}]P_{j-N}^2 ds & j = N + 1, \cdots, 2N \end{cases}$$

113

$$R_j^2(y,z) = \begin{cases} -\dfrac{\lambda\, sgn(z)c}{k^2}\displaystyle\int_0^\infty \gamma(e^{-\alpha|z|} - e^{-\beta|z|})P_j^1 ds & j = 1,\cdots,N \\[4mm] -\dfrac{\lambda(1-\nu)c}{4k^2}\displaystyle\int_0^\infty [\dfrac{\gamma^2}{\alpha s}e^{-\alpha|z|} - 4s\beta e^{-\beta|z|}]P_{j-N}^2 ds & j = N+1,\cdots,2N \end{cases}$$

$$R_j^3(y,z) = \begin{cases} \dfrac{\mu c}{2k^2}\displaystyle\int_0^\infty [\dfrac{\gamma^2}{s\beta}e^{-\beta|z|} - 4s\alpha e^{-\alpha|z|}]P_j^1 ds & j = 1,\cdots,N \\[4mm] \dfrac{\mu\, sgn(z)}{k^2}\displaystyle\int_0^\infty [\gamma(-e^{-\alpha|z|} + e^{-\beta|z|})]P_{j-N}^2 ds & j = N+1,\cdots,2N \end{cases}$$

$$R_j^4(y,z) = \begin{cases} -\dfrac{sgn(z)c}{k^2}\displaystyle\int_0^\infty [s^2 e^{-\alpha|z|} - \dfrac{\gamma}{2}e^{-\beta|z|}]P_j^1 ds & j = 1,\cdots,N \\[4mm] -\dfrac{c}{2k^2}\displaystyle\int_0^\infty [-\dfrac{\gamma}{2\alpha}e^{-\alpha|z|} - \beta e^{-\beta|z|}]P_{j-N}^2 ds & j = N+1,\cdots,2N \end{cases}$$

$$R_j^5(y,z) = \begin{cases} -\dfrac{sgn(z)c}{k^2}\displaystyle\int_0^\infty [-\alpha^2 e^{-\alpha|z|} + \dfrac{\gamma}{2}e^{-\beta|z|}]P_j^1 ds & j = 1,\cdots,N \\[4mm] -\dfrac{c}{k^2}\displaystyle\int_0^\infty [-\dfrac{\gamma\alpha}{2s}e^{-\alpha|z|} + s\beta e^{-\beta|z|}]P_{j-N}^2 ds & j = N+1,\cdots,2N \end{cases}$$

$$R_j^6(y,z) = \begin{cases} \dfrac{c}{2k^2}\displaystyle\int_0^\infty [\dfrac{\gamma^2}{s\beta}e^{-\beta|z|} - 4s\alpha e^{-\alpha|z|}]P_j^1 ds & j = 1,\cdots,N \\[4mm] \dfrac{sgn(z)}{k^2}\displaystyle\int_0^\infty [\gamma(-e^{-\alpha|z|} + e^{-\beta|z|})]P_{j-N}^2 ds & j = N+1,\cdots,2N \end{cases}$$

where $\lambda = \dfrac{E(1-\nu)}{(1-2\nu)(1+\nu)}$, $\mu = \dfrac{E}{2(1+\nu)}$.

5.2.3 Dynamic interaction between the actuator and the crack

The dynamic interaction between the actuator and the crack may significantly affect the resulting waveform. Based on the Pseudo Incident Wave method discussed in the above section, as represented by Equation (5.1.1), the continuity condition

114

between the actuator and the host medium, Equations (5.2.1) and (5.2.2) can be expressed as

$$\varepsilon_y^a(y) = \varepsilon_y^{out}(y) + \varepsilon_{yc}^{sc}(y) \tag{5.2.18}$$

$$\sigma_z^a(y) = \sigma_z^{out}(y) + \sigma_{zc}^{sc}(y) \tag{5.2.19}$$

where ε_{yc}^{sc} and σ_{zc}^{sc} are the scattering wave from the crack, which can be determined from Equation (5.2.17) as

$$\varepsilon_{yc}^{sc}(y,0) = \varepsilon_\xi^{sc}(\overline{\xi},\overline{\eta})\cos^2\phi + \varepsilon_\eta^{sc}(\overline{\xi},\overline{\eta})\sin^2\phi - \varepsilon_{\xi\eta}^{sc}(\overline{\xi},\overline{\eta})\sin\phi\cos\phi \tag{5.2.20}$$

$$\sigma_{zc}^{sc}(y,0) = \sigma_\xi^{sc}(\overline{\xi},\overline{\eta})\sin^2\phi + \sigma_\eta^{sc}(\overline{\xi},\overline{\eta})\cos^2\phi + \sigma_{\xi\eta}^{sc}(\overline{\xi},\overline{\eta})\sin 2\phi \tag{5.2.21}$$

with

$$\overline{\xi} = -e\cos(\phi - \theta) + y\cos\phi, \quad \overline{\eta} = e\sin(\phi - \theta) - y\sin\phi \tag{5.2.22}$$

Similarly, for the crack, the boundary condition, given in Equation (5.2.7), can be rewritten as

$$\sigma_{\xi\eta}(\xi) = -\sigma_{\xi\eta}^{out}(\xi) \tag{5.2.23}$$

$$\sigma_\eta(\xi) = -\sigma_\eta^{out}(\xi) \tag{5.2.24}$$

where $\sigma_{\xi\eta}^{out}(\xi)$ and $\sigma_\eta^{out}(\xi)$ are the outgoing wave from the actuator, given by

$$\sigma_\eta^{out}(\xi,0) = \sigma_y^{out}(\overline{y},\overline{z})\sin^2\phi + \sigma_z^{out}(\overline{y},\overline{z})\cos^2\phi - \sigma_{yz}^{out}(\overline{y},\overline{z})\sin 2\phi \tag{5.2.25}$$

$$\sigma_{\xi\eta}^{out}(\xi,0) = [\sigma_z^{out}(\overline{y},\overline{z}) - \sigma_y^{out}(\overline{y},\overline{z})]\sin\phi\cos\phi + \sigma_{yz}^{out}(\overline{y},\overline{z})\cos 2\phi \tag{5.2.26}$$

with

$$\overline{y} = e\cos\theta + \xi\cos\phi, \quad \overline{z} = e\sin\theta + \xi\sin\phi \tag{5.2.27}$$

Substituting Equations (5.2.20) and (5.2.21) into Equations (5.2.4) and (5.2.5), and Equations (5.2.25) and (5.2.26) into (5.2.10) and (5.2.11), respectively, results in a system of coupled linear algebraic equations, representing the interaction between

115

the actuator and the crack. The Chebyshev polynomial expansion coefficients $\{c\}$ and $\{d\}$ can then be determined by solving those algebraic equations. The total resulting waves in the host medium can then be obtained by superimposing the outgoing wave induced by the actuator and the scattering wave by the crack as

$$\{\sigma^T\} = \{\sigma^{out}\} + \{\sigma^{sc}\} = [K]\{c\} + [T][L]\{d\} \tag{5.2.28}$$

where

$$\{\sigma^T\} = \left\{ \begin{array}{c} \sigma_y^T(y,z) \\ \sigma_z^T(y,z) \\ \sigma_{yz}^T(y,z) \end{array} \right\} \tag{5.2.29}$$

with

$$[K(y,z)] = \left\{ \begin{array}{c} M^1(y,z) \\ M^2(y,z) \\ M^3(y,z) \end{array} \right\} \tag{5.2.30}$$

and

$$[T] = \left\{ \begin{array}{ccc} \cos^2\phi & \sin^2\phi & -\sin 2\phi \\ \sin^2\phi & \cos^2\phi & \sin 2\phi \\ \dfrac{\sin 2\phi}{2} & -\dfrac{\sin 2\phi}{2} & \cos 2\phi \end{array} \right\}, [L] = \left\{ \begin{array}{c} R^1(\xi^*,\eta^*) \\ R^2(\xi^*,\eta^*) \\ R^3(\xi^*,\eta^*) \end{array} \right\} \tag{5.2.31}$$

with $\xi^* = (y - y_c)\cos\phi + (z - z_c)\sin\phi$, $\eta^* = -(y - y_c)\sin\phi + (z - z_c)\cos\phi$.

5.3   Crack detection using scattering waves

To theoretically evaluate the possibility of identifying embedded cracks, the resulting wave propagation due to an actuator interacting with a crack is further used to simulate sensor signals of a cracked medium in response to an electrically loaded piezoelectric actuator. 'Sensors' are assumed to be arranged along $z = z_0$ and be able to provide the displacement distribution. The displacements at the 'sensor' locations given in the previous section are used as the sensor signals. Since the location and property of the actuator will always be known, the outgoing wave of the actuator can

116

be determined theoretically when the effect of the crack upon the actuator, which is of second order in nature, can be ignored. Therefore, sensor signals corresponding to scattering waves from cracks can be obtained by eliminating outgoing waves from the 'measured signals'. In the following discussion, attention will be focussed on only the scattering wave from the crack.

After the displacements caused by the scattering wave from the crack along $z = z_0$ are obtained from 'sensor signals', a reverse process of scattering wave propagation will be considered. The conjugate of the displacement field along $z = z_0$ is used as the boundary condition to generate a reverse wave propagation, which is given by

$$u_y(y, z_0) = [u_y^{sc}(y, z_0)]^\dagger, \quad u_z(y, z_0) = [u_z^{sc}(y, z_0)]^\dagger \tag{5.3.1}$$

where superscript $'\dagger'$ represents the conjugate of a complex number. Using the Fourier transform with respect to y and solving an elastodynamic boundary problem, the conjugate of the displacement field of the reverse wave can be obtained as

$$[u_y^r(y, z)]^\dagger = \frac{1}{\pi} \int_{-\infty}^{\infty} [u_y^{sc}]^\dagger \int_0^\infty \frac{(s^2 e^{-\alpha|z-z_0|} - \alpha\beta e^{-\beta|z-z_0|})}{s^2 - \alpha\beta} \cos s(\xi - y) ds d\xi +$$
$$\frac{sgn(z - z_0)}{\pi} \int_{-\infty}^{\infty} [u_z^{sc}]^\dagger \int_0^\infty \frac{s\beta(e^{-\alpha|z-z_0|} - e^{-\beta|z-z_0|})}{s^2 - \alpha\beta} \sin s(\xi - y) ds d\xi \tag{5.3.2}$$

$$[u_z^r(y, z)]^\dagger = \frac{sgn(z - z_0)}{\pi} \int_{-\infty}^{\infty} [u_y^{sc}]^\dagger \int_0^\infty \frac{s\alpha(e^{-\alpha|z-z_0|} - e^{-\beta|z-z_0|})}{s^2 - \alpha\beta} \sin s(\xi - y) ds d\xi +$$
$$\frac{1}{\pi} \int_{-\infty}^{\infty} [u_z^{sc}]^\dagger \int_0^\infty \frac{(-\alpha\beta e^{-\alpha|z-z_0|} + s^2 e^{-\beta|z-z_0|})}{s^2 - \alpha\beta} \cos s(\xi - y) ds d\xi \tag{5.3.3}$$

from which the reverse wave can be easily determined.

This reverse wave field is then used to identify cracks based on an imaging process. Berkout (1985) and Wapenaar et al. (1987) proposed that the image of a structure can be obtained by correlating the reverse scattering waves and the outgoing waves from the source. This method is modified in the current study to generate the image of cracks using the actuator-induced wave. For any frequency ω, following value, which represents the degree of correlation between scattering and outgoing (incident

for crack) waves, is used to form the image of point (y, z),

$$< R(y, z, \omega) >= \frac{1}{s^2(\omega)} \underline{u}^r(y, z, \omega)[\underline{u}^{out}(y, z, \omega)]^\dagger \tag{5.3.4}$$

where $s^2(\omega) = \int_{-\infty}^{\infty} \int_{-\infty}^{\infty} \underline{u}^{out}(y, z, \omega)[\underline{u}^{out}(y, z, \omega)]^\dagger dy dz$ denotes a scaling factor for frequency ω, $[\underline{u}^{out}(y, z, \omega)]^\dagger$ denotes the conjugate of $\underline{u}^{out}(y, z, \omega) = \{u_y^{out}, u_z^{out}\}$, and $\underline{u}^r(y, z, \omega) = \{u_y^r, u_z^r\}$.

Multiple frequencies will be used to enhance the quality of the image. The final image of the structure could be obtained by superimposing the effect of all frequencies,

$$I(y, z) = Re(\sum_i < R(y, z, \omega_i) >) \tag{5.3.5}$$

where $Re <>$ represents the real part of a function.

5.4 Results and Discussion

This section will be devoted to determining the effects of different crack parameters upon the generated wave propagation in the host medium and identifying cracks by using scattering wave signals.

5.4.1 Interaction between actuator and crack

To verify the validity of the current method, consider first the quasi-static interaction between an actuator and a crack with $c/a = 1.0$, $e/a = 1.0$, $\theta = 90°$, $\phi = 0°$. The PZT-4 piezoelectric actuator is used and the material constants of the host medium are assumed to be,

Host medium

$$E = 3.08 \times 10^{10}(Pa), \nu = 0.3.$$

Figure 5.2 shows the comparison of the normalized stress distribution $\sigma_z^{T*} = \sigma_z^T/\sigma_B$, $\sigma_B = e_a E_z$, along $z/a = 0.5$ with that obtained from finite element analysis using ANSYS for the case where material mismatch $q = \pi\mu/c_{11}^a = 0.46$, and the

118

length-thickness ratio $v = a/h = 20$. The excellent agreement observed between the two solutions shows that the proposed actuator model and the Pseudo Incident Wave method used are suitable for dealing with the interaction between the actuator and the crack.

Consider now the dynamic interaction between a crack and an actuator. The effect of the interaction upon the shear stress singularity factor (Wang, 2000) $S^* = S/S^0$ at the right tip of the actuator for different e/a and loading frequencies is shown in Figure 5.3, for the case where $c/a = 1.0$, $\theta = 90°$, $\phi = 0°$, $q = 0.46$, $v = 20$ and $\rho_a/\rho_H = 1$, with ρ_a and ρ_H being the mass density of the actuator and the host structure, respectively. The shear stress singularity factor (SSSF) S is defined as $S = \lim_{y \to a}[\sqrt{2\pi(a-y)}\tau(y)]$ and can be expressed in terms of $\{c\}$ as $S = \sqrt{a\pi}\sum_{j=0}^{N}c_j^1$. S_0 is the SSSF of the actuator in the absence of the crack. A significant increase of S^* with the increase of the loading frequency for $e < 3a$ can be observed. However, the interaction between the actuator and crack can be ignored when the distance between them is significantly greater than the length of the actuator and the crack, such as $e > 5a$.

5.4.2 Resulting wave propagation

Figure 5.4 shows the stress component $\sigma_z^{out*} = \sigma_z^{out}/\sigma_B$ of the resulting wave propagation induced by the actuator in the host medium in absence of crack for the case where $ka = 5$, $q = 0.46$, $v = 20$, $\rho_a/\rho_H = 1$. Significant decay of the wave field with increasing distance from the actuator can be observed. It is interesting to mention, however, that the wave field is stronger in z-direction, which is perpendicular to the actuator. The result indicates that the piezoelectric actuator could effectively illuminate a sector around z-axis.

Figure 5.5 shows the scattering wave propagation $\sigma_z^{sc*} = \sigma_z^{sc}/\sigma_B$ in the host medium for the case where $e/a = 10$, $c/a = 1$, $\theta = 90°$, $\phi = 0°$ caused by the

119

incident wave field given in Figure 5. Similar scattering wave propagation can be observed for $\sigma_{y*}^{sc} = \sigma_y^{sc}/\sigma_B$. It can be found that stronger scattering wave propagation appears in the direction perpendicular to the crack. The scattering wave propagation $\sigma_z^{sc*} = \sigma_z^{sc}/\sigma_B$ in the host medium for the case where the actuator and the crack are perpendicular to each other with $e/a = 10$, $c/a = 1$, $\phi = 90°$, $\theta = 90°$ is depicted in Figure 5.6. In this case, the strongest scattering wave propagates along $\pm 45°$ directions with respect to z-axis.

5.4.3 Crack determination

To demonstrate the feasibility of using actuator-generated-wave to identify cracks, simulation is conducted to image an embedded crack by using the numerical results discussed above as the 'sensor' signals. The configurations considered are $e/a = 10$, $c/a = 1$, $\phi = 90°$, $\theta = 0°$. The outgoing wave u_y^{out} and u_z^{out} generated by the actuator in the absence of the crack is used as the incident wave for the crack. The outgoing field near the position of the crack is shown in Figure 5.7 for $ka = 18$. When this incident wave reaches the surface of the crack, the scattering wave will be induced. Displacements at a total of 321 points evenly distributed along $z_0 = 0$ within $-16a < y < 16a$ are used to simulate sensor signals. Figure 5.8 shows the reversed scattering wave field $\underline{u}^r = \{u_y^r, u_z^r\}$. The convergence of the reverse scattering wave into the position of the crack (centred at $y = y_c$, $z = z_c$) can be clearly observed. This result is then used to get the image of the crack based on Equation (5.3.5). A series of frequencies $ka = 3 + (i - 1), i = 1, \cdots, 18$ are considered to generate the image. Figure 5.9(a) shows the image for one frequency $ka = 10$, which contains the information of the crack but also significant pseudo images. Figure 5.9(b) gives the result for $ka = 4, 6, 8, 10, 12$, showing improved quality of the image. Figure 5.10 shows the image of the crack based on eighteen frequencies, $ka = 3, 4, \cdots, 20$. It can be observed that the position, size and orientation of the crack can be clearly

120

identified. It should be noted that the image of the crack can be further improved by eliminating pseudo images which will change with the use of different frequencies.

121
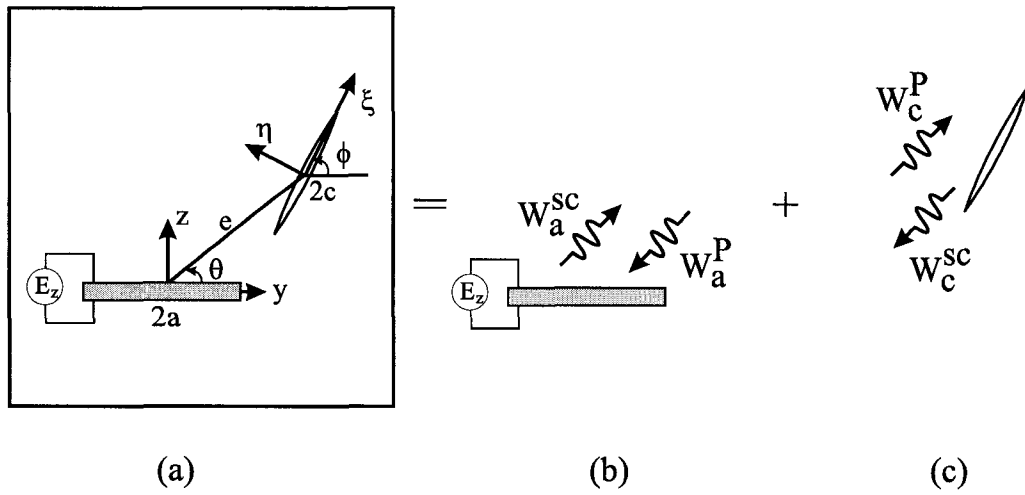
Figure 5.1: Decomposition of elastic waves in the cracked medium
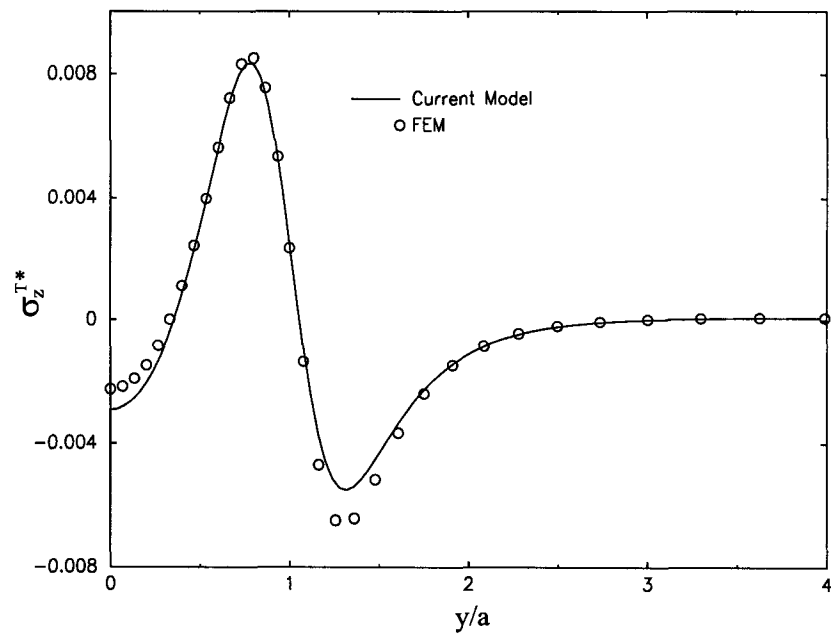
Figure 5.2: Comparison of the total resulting wave with FEM result

122
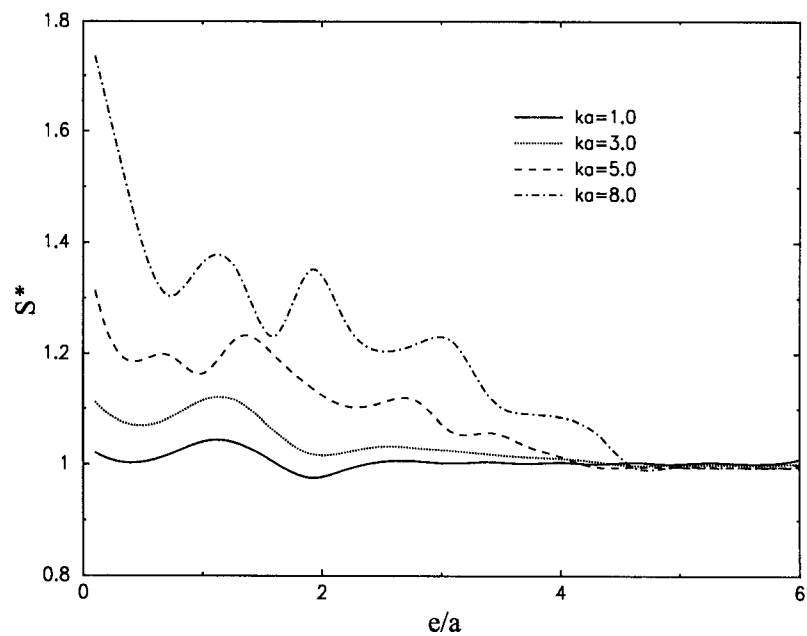
Figure 5.3: The effect of interaction upon S at the tip of the actuator
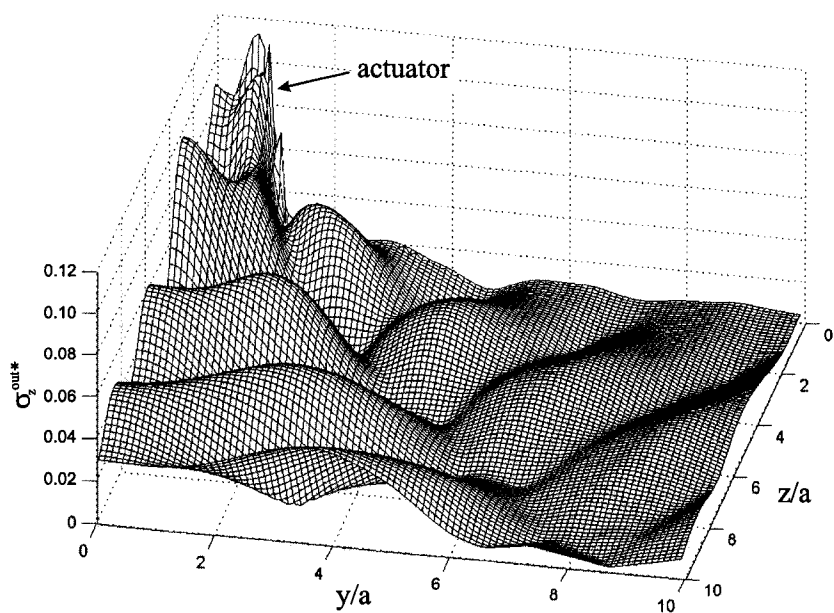
Figure 5.4: Outgoing wave propagation generated by the actuator

123
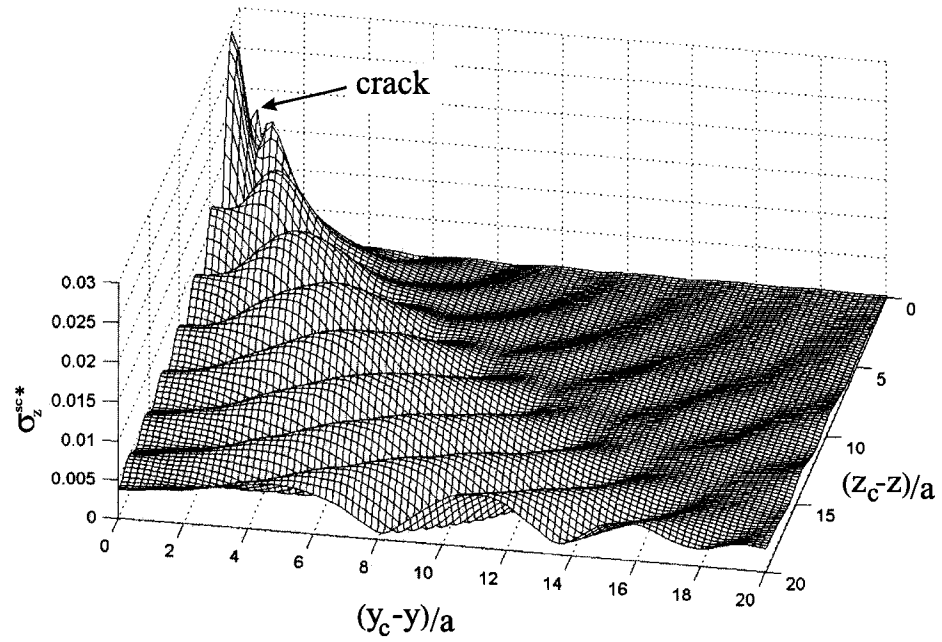
Figure 5.5: Scattering wave propagation induced by the embedded crack: $\theta = 0°$
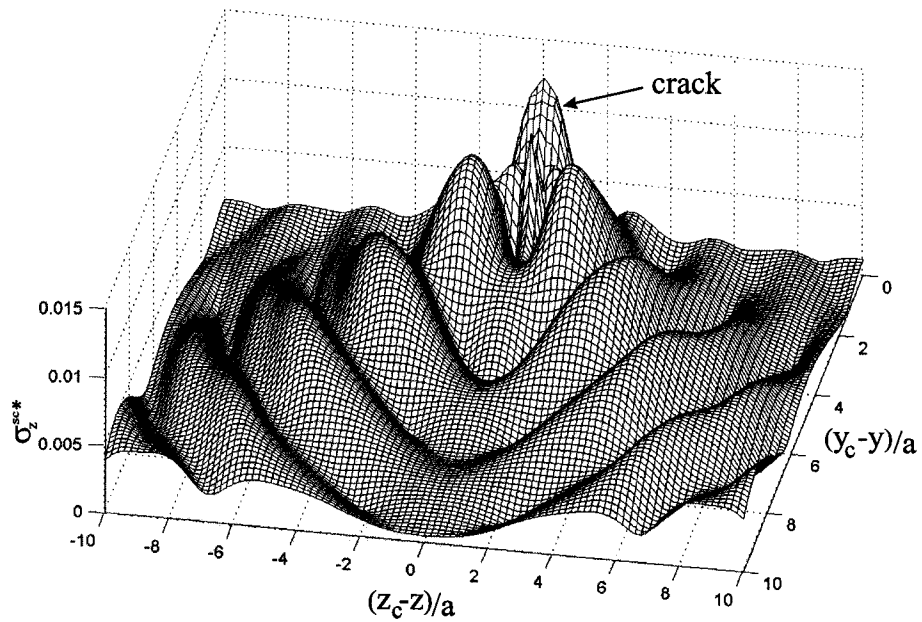
Figure 5.6: Scattering wave propagation induced by the embedded crack: $\theta = 90°$

124
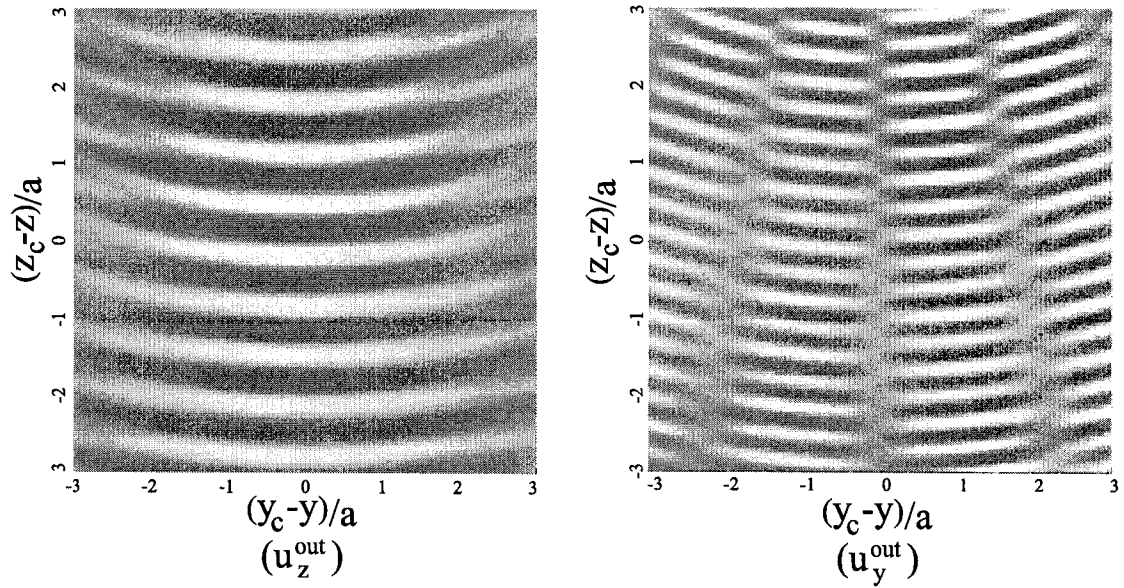
Figure 5.7: The outgoing wave field near the position of the crack
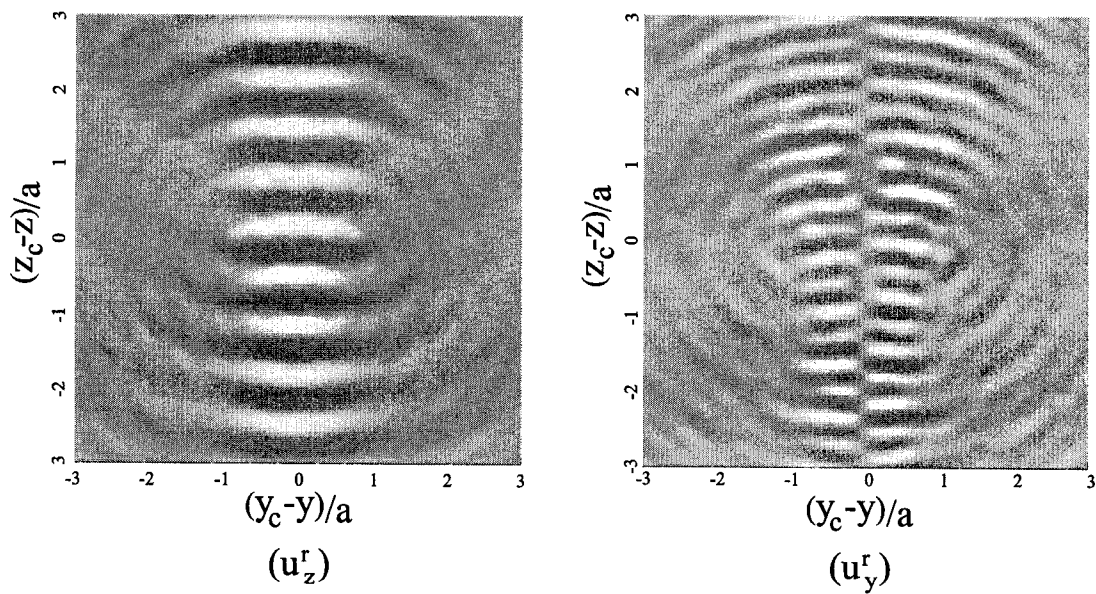
Figure 5.8: The reversed scattering wave field near the position of the crack

125
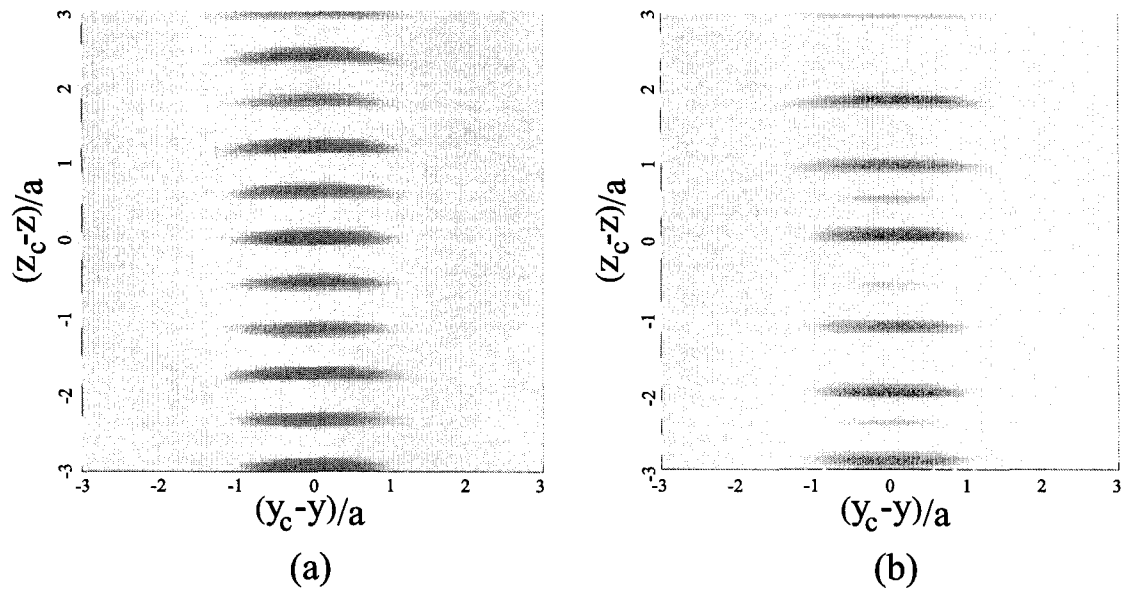
Figure 5.9: The preliminary image of the crack: (a) based on one frequency result (b) based on five frequencies' results
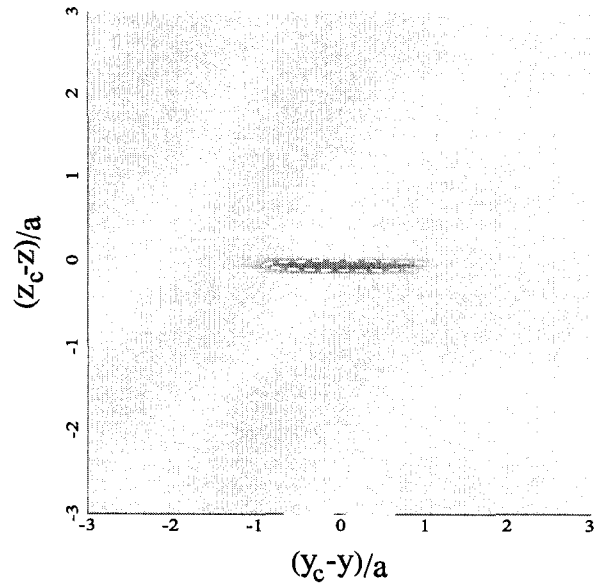
Figure 5.10: The final image of the crack for harmonic wave cases

126

Chapter 6

Identification of Embedded Cracks Using Reverse Elastic Waves

As discussed in Chapter 5, in order to obtain good image results many different loading frequency results should be used, which make this method numerical cumbersome and unfavorable for experiment work. It should be noted that the relation of the transient signals and harmonic signals can be established by the Fourier transform, from which the summation process for harmonic signals can be replaced by analyzing transient wave signals directly. In this Chapter, a theoretical study of identifying multiple cracks in plane elastic media using transient surface signals induced by a dynamic excitation is presented. The focus of this study is to develop a quantitative understanding of the relation between surface signals and the location and characteristics of embedded cracks. An elastodynamic analysis is first conducted using Fourier transform to separate the surface response due to scattering waves by cracks from the total surface signals. The obtained scattering wave signals are then used as boundary conditions to induce a reverse elastic wave propagation in the elastic medium. An imaging technique is used to determine the sizes, shapes and positions of existing cracks. Typical numerical simulation results are presented to show the feasibility and accuracy of the current method.

127

6.1 Formulation of the problem

Consider a plane strain problem of a homogeneous isotropic elastic half plane with embedded cracks, as shown in Figure 6.1(a). A coordinate system (y, z) is used to describe the elastic medium. It is assumed that surface displacements u_y^m, u_z^m are known as sensor signals in $-a < y < a$, $z = 0$, which will be used to determine the sizes, shapes and locations of the embedded cracks. The half plane model is used to simulate the case where the cracks are small in size and, therefore, other boundaries are 'far away' from them. To induce elastic wave propagation, a dynamic excitation is applied on the surface of the medium, represented by a force $F(t)$ as shown in Figure 6.1(a). As a result, an incident elastic wave $\mathbf{U}^I = \{u_y^I, u_z^I\}$ is induced. When the incident wave reaches the cracks, a scattering wave will be generated, which will propagate back to the surface of the medium. The resulting displacements along the surface are measured as surface signals $\mathbf{U}^m = \{u_y^m, u_z^m\}$.

To separate the scattering wave by cracks from the total signal, the original problem will be decomposed into two subproblems b and c, as shown in Figure 6.1. Subproblem b represents the scattering wave from the crack $\mathbf{U}^{sc} = \{u_y^{sc}, u_z^{sc}\}$, which travels in an infinite medium. Subproblem c describes the response of the half plane to surface loading, $\mathbf{U}^s = \{u_y^s, u_z^s\}$. In Figure 6.1(c), $F(t)$ is the applied force and $-\sigma$, $-\tau$ are the normal and shear forces corresponding to that induced by subproblem b. Correspondingly, the measured signal along the surface can be decomposed into

$$\mathbf{U}^m(y, t) = \mathbf{U}^s(y, t) + \mathbf{U}^{sc}(y, t). \tag{6.1.1}$$

$\mathbf{U}^{sc}$ will be used to identify the characteristics of the cracks.

6.1.1 Surface signals processing

To determine the scattering wave $\mathbf{U}^{sc}$ from the cracks, displacements of the scattering field $\mathbf{U}^{sc}$ along $z = 0$ are needed as the boundary condition for subproblem 6.1(b).

128

This boundary condition can be determined theoretically using measured signals $\mathbf{U}^m$ by conducting a detailed elastodynamic analysis.

The dynamic behaviour of a homogeneous isotropic elastic medium under plane strain deformation is governed by the following wave equations (Achenbach, 1973)

$$\nabla^2 \Phi - \frac{1}{c_L^2}\frac{\partial^2 \Phi}{\partial^2 t} = 0, \qquad \nabla^2 \Psi - \frac{1}{c_T^2}\frac{\partial^2 \Psi}{\partial^2 t} = 0 \qquad (6.1.2)$$

where the Laplacian operator ∇^2 stands for $\dfrac{\partial^2}{\partial y^2} + \dfrac{\partial^2}{\partial z^2}$ with $c_L = \sqrt{\dfrac{\lambda + 2\mu}{\rho}}$ and $c_T = \sqrt{\dfrac{\mu}{\rho}}$ being the longitudinal and transverse wave velocities of the elastic medium, respectively. Φ and Ψ are two complex displacement potentials, from which displacements can be determined,

$$u_y = \frac{\partial \Phi}{\partial y} + \frac{\partial \Psi}{\partial z}, \qquad u_z = \frac{\partial \Phi}{\partial z} - \frac{\partial \Psi}{\partial y} \qquad (6.1.3)$$

Fast Fourier Transform (FFT) with respect to time t and Fourier Transform (FT) with respect to y will be used in the current study, which are defined by

$$f^F(\omega) = \frac{1}{N}\sum_{n=0}^{N-1} f(t_n)e^{-j\omega t_n}, \quad f(t) = \sum_{k=0}^{N-1} f^F(\omega_k)e^{j\omega_k t} \qquad (6.1.4)$$

and

$$\bar{g}(s) = \frac{1}{2\pi}\int_{-\infty}^{\infty} g(y)e^{isy}dy, \quad g(y) = \int_{-\infty}^{\infty} \bar{g}(s)e^{-isy}ds \qquad (6.1.5)$$

where the superscript 'F' represents FFT, and '$-$' represents FT. $\omega_k = \dfrac{2\pi k}{N\triangle t}$, $t_n = n\triangle t$ with $\triangle t$ being the time step and N being the the total number of the time steps used in FFT.

Applying FFT and FT to (6.1.2) results in

$$\frac{\partial^2 \Phi}{\partial^2 z} + (k^2 - s^2)\Phi = 0, \qquad \frac{\partial^2 \Psi}{\partial^2 z} + (K^2 - s^2)\Psi = 0 \qquad (6.1.6)$$

where $k = \dfrac{\omega}{c_L}$ and $K = \dfrac{\omega}{c_T}$ are two wave numbers. For the problem shown in Figure 6.1(c), the general solution of the wave due to the surface loading can be determined from Equation (6.1.6) as

$$\overline{\Phi}^F = A(s)e^{-\alpha z}, \quad \overline{\Psi}^F = B(s)e^{-\beta z} \qquad (6.1.7)$$

129

where $A(s)$ and $B(s)$ are unknown functions of s, and

$$\alpha = \begin{cases} \sqrt{s^2 - K^2} & |s| > K \\ -i\sqrt{K^2 - s^2} & |s| < K \end{cases} \qquad \beta = \begin{cases} \sqrt{s^2 - k^2} & |s| > k \\ -i\sqrt{k^2 - s^2} & |s| < k \end{cases} \tag{6.1.8}$$

The boundary conditions along the surface can be written as

$$\overline{\sigma}_y^F = -\overline{\sigma}^F + F^F(\omega), \quad \overline{\sigma}_{xy}^F = -\overline{\tau}^F \tag{6.1.9}$$

where $F^F(\omega)$, $\overline{\sigma}^F$, $\overline{\tau}^F$ are the FFT of $F(t)$, FFT and FT of σ and τ. By making use of the general solution (6.1.7), the boundary conditions (6.1.9) and the constitutive relations, the unknown functions $A(s)$ and $B(s)$ can be obtained in terms of $\overline{\sigma}^F$, $\overline{\tau}^F$ and $F^F(\omega)$. Accordingly, the induced surface displacements can be obtained as

$$(\overline{u}_y^s)^F = \frac{1}{\mu\Delta}\{-\beta(s^2 + \beta^2)\overline{\tau}^F + is[(s^2 + \beta^2) - 2\alpha\beta](\overline{\sigma}^F - F^F)\} \tag{6.1.10}$$

$$(\overline{u}_z^s)^F = \frac{1}{\mu\Delta}\{-is[(s^2 + \beta^2) + 2\alpha\beta]\overline{\tau}^F - \alpha(s^2 - \beta^2)(\overline{\sigma}^F - F^F)\} \tag{6.1.11}$$

where μ is the shear modulus of the host medium and $\Delta = (2s^2 - k^2)^2 - 4s^2\alpha\beta$.

For the scattering wave shown in Figure 16.1(b), the relation between the displacement and stress fields can be similarly established. For the upper half plane $z < 0$, the scattering wave can be determined by solving the governing equation (6.1.6) as

$$\overline{\Phi}^F = C(s)e^{\alpha z}, \quad \overline{\Psi}^F = D(s)e^{\beta z} \tag{6.1.12}$$

where $C(s)$ and $D(s)$ are unknown functions of s. Making using of this general solution, the displacements and stresses along $z = 0$ can be calculated. The relation between them can then be determined as

$$\overline{\sigma}^F = \frac{is\mu(s^2 + \beta^2 - 2\alpha\beta)}{s^2 - \alpha\beta}(\overline{u}_y^{sc})^F + \frac{\mu\beta(s^2 - \beta^2)}{s^2 - \alpha\beta}(\overline{u}_z^{sc})^F \tag{6.1.13}$$

$$\overline{\tau}^F = \frac{\mu\alpha(s^2 - \beta^2)}{s^2 - \alpha\beta}(\overline{u}_y^{sc})^F - \frac{is\mu(s^2 + \beta^2 - 2\alpha\beta)}{s^2 - \alpha\beta}(\overline{u}_z^{sc})^F \tag{6.1.14}$$

Substituting Equations (6.1.10)-(6.1.11) and (6.1.13)-(6.1.14) into Equation (6.1.1), the displacements along $z = 0$ due to the scattering elastic wave from the cracks, $\mathbf{U}^{sc}$,

130

shown in Figure 6.1(b), can be obtained in terms of the measured surface displacement $\mathbf{U}^m$ and the applied surface force F as

$$(\overline{u}_y^{sc})^F = \frac{1}{2}(\overline{u}_y^m)^F + \frac{is(s^2 + \beta^2 - 2\alpha\beta)}{2\alpha(s^2 - \beta^2)}(\overline{u}_z^m)^F + \frac{is[(s^2 + \beta^2) - 2\alpha\beta]}{2\mu\Delta}F^F \quad (6.1.15)$$

$$(\overline{u}_z^{sc})^F = \frac{1}{2}(\overline{u}_z^m)^F - \frac{is(s^2 + \beta^2 - 2\alpha\beta)}{2\beta(s^2 - \beta^2)}(\overline{u}_y^m)^F - \frac{\alpha(s^2 - \beta^2)}{2\mu\Delta}F^F \quad (6.1.16)$$

The inverse FT of displacements u_y^{sc} and u_z^{sc} along $z = 0$, given by Equations (6.1.15) and (6.1.16), can be expressed as

$$(u_y^{sc})^F(y) = \frac{1}{2}(u_y^m)^F(y) + \frac{1}{2\pi}\int_{-\infty}^{\infty}(u_z^m)^F(\xi)\int_0^\infty \frac{s(s^2 + \beta^2 - 2\alpha\beta)}{\alpha(s^2 - \beta^2)}\sin s(y - \xi)dsd\xi$$

$$+\frac{F^F}{2\pi\mu}\int_0^\infty \frac{s[(s^2 + \beta^2) - 2\alpha\beta]}{\Delta}\sin syds \quad (6.1.17)$$

$$(u_z^{sc})^F(y) = \frac{1}{2}(u_z^m)^F(y) - \frac{1}{2\pi}\int_{-\infty}^{\infty}(u_y^m)^F(\xi)\int_0^\infty \frac{s(s^2 + \beta^2 - 2\alpha\beta)}{\beta(s^2 - \beta^2)}\sin s(y - \xi)dsd\xi$$

$$-\frac{F^F}{2\pi\mu}\int_0^\infty \frac{\alpha(s^2 - \beta^2)}{\Delta}\cos syds \quad (6.1.18)$$

For the case where u_y^m and u_z^m are measured in $|y| < a$, $(u_y^m)^F$ and $(u_z^m)^F$ can be expressed in terms of Chebyshev polynomials as

$$(u_y^m)^F(y) = \sum_{j=0}^\infty A_j T_j(y/a)/\sqrt{1 - y^2/a^2}, \quad (6.1.19)$$

$$(u_z^m)^F(y) = \sum_{j=0}^\infty B_j T_j(y/a)/\sqrt{1 - y^2/a^2} \quad (6.1.20)$$

The coefficients A_j and B_j can be determined by using the orthogonality properties of the Chebyshev polynomials.

The mathematical singularity in above equations has been removed in the numerical calculation. In the current analysis, 32 terms in Chebyshev polynomial expansions have been used. The scattering waves in FFT domain can then be obtained in terms

131

of A_j and B_j as

$$(u_y^{sc})^F(y) = \frac{1}{2}(u_y^m)^F(y) - \frac{K^2}{2k^2}\sum_{j=0}^{N}A_j\frac{\sin\left(j\frac{l}{N+1}\pi\right)}{\sin\left(\frac{l}{N+1}\pi\right)} +$$

$$\frac{1}{2\pi k^2}\sum_{j=0}^{N}A_j\begin{cases}(-1)^n\int_0^\infty[\dfrac{s(s^2+\beta^2-2\alpha\beta)}{\alpha}-K^2]J_j(sa)\cos(sy)ds & j=2n+1\\[3mm](-1)^{n+1}\int_0^\infty[\dfrac{s(s^2+\beta^2-2\alpha\beta)}{\alpha}-K^2]J_j(sa)\sin(sy)ds & j=2n\end{cases}$$

$$+\frac{F^F}{2\pi\mu}\int_0^\infty\frac{s[(s^2+\beta^2)-2\alpha\beta]}{\Delta}\sin syds \quad (6.1.21)$$

$$(u_z^{sc})^F(y) = \frac{1}{2}(u_z^m)^F(y) + \frac{K^2}{2k^2}\sum_{j=0}^{N}B_j\frac{\sin\left(j\frac{l}{N+1}\pi\right)}{\sin\left(\frac{l}{N+1}\pi\right)} +$$

$$\frac{1}{2\pi k^2}\sum_{j=0}^{N}B_j\begin{cases}(-1)^n\int_0^\infty[\dfrac{s(s^2+\beta^2-2\alpha\beta)}{\beta}-K^2]J_j(sa)\cos(sy)ds & j=2n+1\\[3mm](-1)^{n+1}\int_0^\infty[\dfrac{s(s^2+\beta^2-2\alpha\beta)}{\beta}-K^2]J_j(sa)\sin(sy)ds & j=2n\end{cases}$$

$$-\frac{F^F}{2\pi\mu}\int_0^\infty\frac{\alpha(s^2-\beta^2)}{\Delta}\cos syds \quad (6.1.22)$$

with J_j ($j=1,2\cdots$) being the Bessel functions of the first kind. Inverse FFT is then applied to generate the boundary condition of the reverse scattering wave along $z=0$ at the time domain.

6.1.2 Simulation of direct wave propagation

In this study, to deal with the complicated wave-crack interaction phenomena, the structural analysis software ANSYS will be used to simulate elastic wave propagation in cracked elastic media. Simple bilinear quadrilateral isoparametric element (four nodes "PLANE42" element) has been chosen for spatial discretization in the present investigation with the uniform mesh size.

Modelling elastic wave propagation in a continuous medium through a discretization in time and in space may introduce several errors associated with different numerical parameter effect. To avoid some of these errors the spatial and temporal grids

132

should be chosen carefully. The accuracy of the transient elastic wave modelling depends strongly on the number of nodes per wave length. In order to reduce grid dispersion, at least ten to fifteen nodes per shortest wavelength are required. In additional, the temporal discretization should be such that the wave does not propagate the smallest spatial resolution in one time step, i.e.

$$\Delta t < \frac{2}{3} \frac{min(\Delta y, \Delta z)}{c_{max}} \qquad (6.1.23)$$

where $min(\Delta y, \Delta z)$ is minimum spatial resolution in the structure and c_{max} is the maximum wave propagation velocity in the structure, i.e., longitudinal wave velocity for isotropic solids.

To simulate wave propagation over a enough period of time, it is necessary to model a very large domain to avoid reflections from boundaries. But this solution is not practicable as it requires high storage space and memory for computation. As a result, in the analysis of the elastic wave propagation in the half plane domain using FEM, three unbounded edges of the computation domain must be truncated by artificial boundaries to render the computational domain finite. The boundary conditions that eliminate these spurious reflection are known as the Non-Reflecting Boundary Conditions (NRBC) for elastic waves. In current study, 'unified boundary condition' (White et al., 1977) is adopted as

$$\left\{ \begin{array}{c} \sigma_{nn} \\ \sigma_{nt} \end{array} \right\} = \left[\begin{array}{cc} ac_L & 0 \\ 0 & bc_T \end{array} \right] \left\{ \begin{array}{c} \frac{\partial u_y}{\partial t} \\ \frac{\partial u_z}{\partial t} \end{array} \right\} \qquad (6.1.24)$$

where $[\sigma] = \{\sigma_{nn}, \sigma_{nt}\}^T$ represents the stresses normal and shear to the boundary, a and b are the dimensionless parameters. A spring-damper element ("COMBIN42" element in ANSYS) is used to simulate a boundary condition, which enables the effective elimination of unwanted reflected waves from the boundary of the finite element model.

133

6.1.3 Reverse wave propagation

Let us focus on the scattering wave from the cracks as shown in Figure 6.1(b). The determined displacement along $z = 0$ in the previous section will be used to generate a reverse wave propagation to simulate the scattering wave.

During this process, instead of increasing time t, the wave field with decreasing t from a specific moment $t = T$ will be considered. Since governing equation (6.1.2) contains only the second order derivative with respect to time t, its format will not be changed if a new parameter is introduced,

$$t^r = T - t \tag{6.1.25}$$

where t^r denotes the reverse time for the process of reverse propagation of waves, $T = N\Delta t$ denotes the total time span of the surface signal. t^r is measured backwards in time domain from $t = T$ to $t = 0$. Using t^r in Equation (6.1.2), a reverse wave can be generated to simulate the scattering wave propagation in the medium caused by cracks before it reaches the surface. The reverse propagation of the scattering wave can be represented as a boundary value problem with the following boundary and initial conditions,

$$u_y^r(y, 0, t^r) = u_y^{sc}(y, 0, T - t), \quad u_z^r(y, 0, t^r) = u_z^{sc}(y, 0, T - t), \tag{6.1.26}$$

$$u_y^r(y, z, 0) = 0, \quad u_z^r(y, z, 0) = 0, \tag{6.1.27}$$

$$\dot{u}_y^r(y, z, 0) = 0, \quad \dot{u}_z^r(y, z, 0) = 0. \tag{6.1.28}$$

u_y^{sc} and u_z^{sc} are given by Equations (6.1.15) and (6.1.16) in the previous section. $\dot{u}_y^r$ and $\dot{u}_z^r$ are initial velocities, i.e. the first derivation of u_y^r and u_z^r to t^r.

To simplify the problem, this boundary value problem is also solved using the finite element software ANSYS to generate the reverse scattering wave. The resulting displacements of the scattering wave from the cracks can then be used to identify the embedded cracks.

134

6.1.4 Imaging cracks

To develop an understanding of the quantitative relation between the scattering wave and the properties of the cracks, an imaging method based on reverse scattering wave propagation is used. In a cracked medium, a scattering wave is excited at the time when the incident wave from the source impinges on a point of the crack surface. The amplitude of the excited scattering field at this moment corresponds to the feature of the crack surface. Based on this idea, the image of a specific point in the material is formed by extracting the amplitude of the scattering wave at that point when the incident wave arrives. It should be mentioned that unlike the migration technique in geophysical applications, where only one type of seismic wave is used, both longitudinal (P) and transverse (S) waves need to be included in the current study. As a result, two arrival times corresponding to incident P and S waves need to be considered in identifying cracks.

For homogenous linear material, the time for incident P wave to reach point (y, z) from the excitation source, t^I, is given by

$$t_L^I = \sqrt{(y - y_0)^2 + (z - z_0)^2}/c_L \qquad (6.1.29)$$

where (y_0, z_0) is the position of the source loading. The corresponding time for the reverse propagating wave field is then

$$t_L^r = T - t_L^I \qquad (6.1.30)$$

Similarly, the reverse time for incident S wave to reach a specific point (y, z) can be determined with c_L being replaced by c_T in Equations (6.1.29) and (6.1.30).

The image of any point (y, z) can be obtained by extracting the amplitude of the displacement field of the scattering wave at this point at the moment of $t_L^r = T - t_L^I$ given by (6.1.30). The resulting image of this point can be expressed as

$$\mathbf{I}_L(y, z) = \mathbf{U}^r(y, z, t_L^r) \qquad (6.1.31)$$

135

where $\mathbf{I}_L = \{|u_y|_L, |u_z|_L\}$ is the amplitude of the displacement field of the scattering wave. Since either u_y or u_z can be used to form the image, two possible images can be obtained. In addition, if S incident wave is used two more images can be generated.

For either P or S incident wave, the final image of the cracks is obtained by using the amplitude of the scattering displacement field by integrating u_y and u_z images, i.e.

$$I^{final}(y, z) = \sqrt{(u_y|_{L+T})^2 + (u_z|_{L+T})^2} \tag{6.1.32}$$

A complete image could be obtained by adding up all of these images. This stacking process will increase the signal-to-noise ratio.

It should be mentioned that for a pulse-like excitation, as used in the current study, P and S waves usually propagate separately without overlapping when impinge on the embedded cracks. However, since the scattering wave field is generally caused by both incident P and S waves, during the imaging process using incident P wave, part of the imaging wave energy induced by incident S wave can also be extracted, which may influence the quality of the image. Similarly, some of the scattering wave induced by the incident P wave may affect the image quality using incident S wave. The coupling between P and S incident waves may result in pseudo images of the cracks. This type of pseudo images can be eliminated by considering different excitation conditions. Examples of dealing with $P - S$ coupling will be presented in the next section.

6.2 Numerical results

This section is devoted to the numerical simulation of identifying different cracks using surface signals for determining their positions, dimensions and shapes. Simulation is also conducted to show the feasibility of using signals from a limited number of surface points for identifying cracks.

136

6.2.1 The dynamic excitation and surface signal

The elastic constants of the material are assumed to be

$$\lambda = 5.20 \times 10^{10}(Pa), \mu = 2.68 \times 10^{10}(Pa), \rho = 2572(kg/m^3)$$

with λ and μ being the Lame's constants and ρ the mass density.

To generate an elastic wave propagation, a concentrated normal surface force F(t) is applied at $y = 0$, as shown in Figure 6.1(a). To reduce the possible distortion of the waveform during propagation, a narrow band signal is used, which is given by

$$F(t) = P[H(t) - H(t - N_p/f_0)](1 - \cos\frac{2\pi f_0 t}{N_p})\sin 2\pi f_0 t \qquad (6.2.1)$$

where $H(t)$ is the Heaviside step function, f_0 is the central frequency, P is the amplitude of the force, and N_p controls the duration of the excitation signal.

The surface response corresponding to this load depends on the geometries of embedded cracks. In the current study, the 'measured' surface signal corresponding to different crack geometries is simulated using the FEM to overcome the difficulties associated with the complicated crack geometry. The infinite boundary involved in the current problem is dealt with using the special element with viscous boundaries discussed in section 6.1.2 to eliminate the reflected wave.

The first case considered is a crack of length $6mm$ parallel to the surface with its centre being at $(0mm, 20mm)$. The excitation load used is defined by $f_0 = 1MHz$, $N_p = 1$ and $P = 10KN$. A high frequency has been used to ensure reasonable resolution of the image. The resulting displacement u_z at the loading point and at $(16mm, 10mm)$ is shown in Figures 6.2 and 6.3, respectively. Separation of P and S waves is observed in Figure 6.3. Both P and S waves retain the original shape of the input signal, indicating that the distortion of the waveform is effectively suppressed by choosing the narrow band excitation signal given by (6.2.1). By conducting the FEM analysis, surface response can be determined. Figure 6.4 shows the results of

137

the surface displacements u_z^m at $y_i = -24 + 6 \times (i-1)mm, i = 1, \cdots, 4$, in which the surface signal corresponding to the applied load is removed.

As discussed in previous sections, shown in Figure 6.1(b), the 'measured signal' can not be used directly in determining the scattering wave. The displacements of the scattering field along $y = 0$ are needed. To achieve this, the resulting surface displacements from the FEM analysis are transformed into FFT and FT domain using Equations (6.1.4) and (6.1.5). The time span T used is $T = 20\mu s$. The transformed surface signals are then used in Equations (6.1.15) and (6.1.16) to determine u_x^{sc} and u_y^{sc} of the scattering wave along $y = 0$. Figure 6.4 shows the comparison between u_z^m and u_z^{sc} at the four surface points mentioned before. It is observed that although the shapes of the signals are similar, their amplitudes are significantly different, indicating the importance of considering the effect of the surface.

Figure 6.5 shows the displacement components u_y^{sc} and u_z^{sc} of the scattering waves along $y = 0$, with the gray scale corresponding to the amplitude of the wave field. Due to the symmetry of the problem, only the result for $y > 0$ is shown. Elastic wave mode conversion due to wave reflection is observed, including PP and PS waves representing the scattering P and S waves caused by incident P wave, and SP and SS waves representing the scattering P and S waves caused by incident S wave. The data given in Figure 6.4 will be used as the boundary conditions of the reverse wave in identifying cracks. According to this figure, a time span of $20\mu s$ is long enough to ensure that the surface signals in the range $|y| < 24mm$ can be completely recorded. The hyperbolic curves for the corresponding scattering waves show that a sensor range $|y| < 24mm$ is large enough for representing the wave propagation. The time span and sensor range identified here will be used in the following examples.

6.2.2   Reverse waves and imaging cracks

Figure 6.6 shows four snapshots of u_z^r in the process of reverse propagation of waves at different times by using reverse sensor signals in Figure 6.5 as boundary

138

condition. Corresponding wave component u_z^r can also be obtained. As shown in Figure 6.6, the reversed scattering waves carry all the energy backwards along the same paths over which they previously propagated forward. The energy converges to a focus in time and space domain, which represents the information of the crack. The dash lines in Figure 6.6 represent the imaging points for incident P and S waves at the corresponding time.

The images of the cracked medium can be obtained from the scattering field shown in Figure 6.6 using Equations (6.1.29) and (6.1.30). In frame (a), the scattering wave field begins to propagate towards the cracks, the wavefronts of the corresponding P and S waves are out of the plotted area at this time. In frame (b), the scattering wave from crack induced by the incident S wave is focussed back to the crack and the points corresponding to the incident S wave at this time are imaged (dash line). In frame (c), the scattering wave from the crack induced by the incident P wave is focussed back to the crack and the points corresponding to incident P and S waves at this time are imaged (dash lines). In frame (d), the scattering wave continued its downward propagation, which would not be coincident with the incident waves.

Figure 6.7 shows the images by using incident P and S waves. Frames (a) and (b) are the images for displacement component u_z and u_y, respectively, using incident P wave. Frames (c) and (d) are the corresponding images for u_z and u_y using incident S wave. Comparing the images in frames (a)-(d), it can be found that the images using incident P wave are different from those using incident S wave. The existence of pseudo images of cracks is because of the coupling between P and S waves due to the complicated reflection of elastic waves. To eliminate these pseudo images, a different excitation force acting at $y = -6mm$ along the surface is applied to generate new images. Figure 6.8 shows the corresponding images. Comparing these images to previous ones, the pseudo images of the crack can be easily identified. After eliminating the pseudo images in Figure 6.7 and 6.8 and using Equation (6.1.32),

the image of the crack can be obtained as shown in Figure 6.9. The dash line in this figure represents the real crack position. Figure 6.10 shows the image of a longer crack of length $18mm$, which is parallel to the surface and its centre is at $(0mm, 20mm)$. Surface signals within $|y| < 24mm$ are used for imaging the crack. It is interesting to see that even for the current case where the sensor range is in the same order of the crack length, satisfactory result is obtained. The location of the image of the crack is very close to its real position. Some discrepancy in the size and the shape of the crack is observed, which may be caused by the finite width of the waveform and the distortion of it during propagation.

6.2.3 Complicated geometries

Simulation has also been conducted for more complicated crack configurations. Figure 6.11 shows the image of an inclined crack of length $6mm$ with its centre at $(0, 20mm)$ and the inclination angle being $45°$. The dash line represents the real crack position. The image provides a reasonable prediction of the orientation of the crack. However, it should be mentioned that even though the migration algorithm itself has no angle restrictions, very steeply angled cracks will not produce good images unless the source-recorder geometry is such that the response of these cracks can be well recorded.

Figure 6.12 shows the image of a wedge shape crack with its centre being at $(0, 20mm)$, half length $8mm$ and the inclination angle $45°$. The dash line represents the real crack position. As shown in this figure, the image can provide the most information about the kind of crack, although the real wedge is a little bit longer than the imaged result. To produce high quality images for this kind of complicated shape cracks, the multiplicity of actuators and sensors that are typical of surface surveys is required. Another way to improve the image quality is to increase the frequency of the excitation. Figure 6.13 shows the image of two collinear cracks of length $6mm$. Their centres are located at $(-6mm, 20mm)$ and $(6mm, 20mm)$ and are parallel to the surface. Surface signals in $|y| < 30mm$ are used in the current imaging

140

process. Very good agreement between the image of the cracks and their real position is observed. The capability to image multiple cracks is a very important property of the current reverse wave technique, which make this technique very favorable in comparison with other interpretation methods, for which multiple cracks may result in difficulties.

6.2.4 Use of limited signals

In the above examples, extensive numbers of surface signals are used as the boundary conditions to generate the reverse scattering wave field. However, in the evaluation of a real structure, the number of the surface signals is limited by the number and dimension of sensors attached to the surface. To study the availability of the current technique for detecting cracks when signals are limited, simulations have been conducted for cases where only discrete signals along the surface are available. Figure 6.14 shows the scattering wave signals received at 13 equally spaced points along the surface with $y_i = -24 + 4 \times (i-1)mm, i = 1, \cdots, 13$, caused by a single crack as discussed in Figure 6.5.

In order to increase the resolution of the image, a complete 'surface signals' are constructed by interpolation based on the polynomial curve fitting using the least-square method. Figure 6.15 shows the image of the crack using the interpolation data with the dash line representing the real crack position. The result is similar to that shown in Figure 6.9, which is obtained using the signals along the whole area of $|y| < 24mm$. The current result shows the potential of the developed technique for identifying embedded cracks using surface signals measured by limited surface sensors.
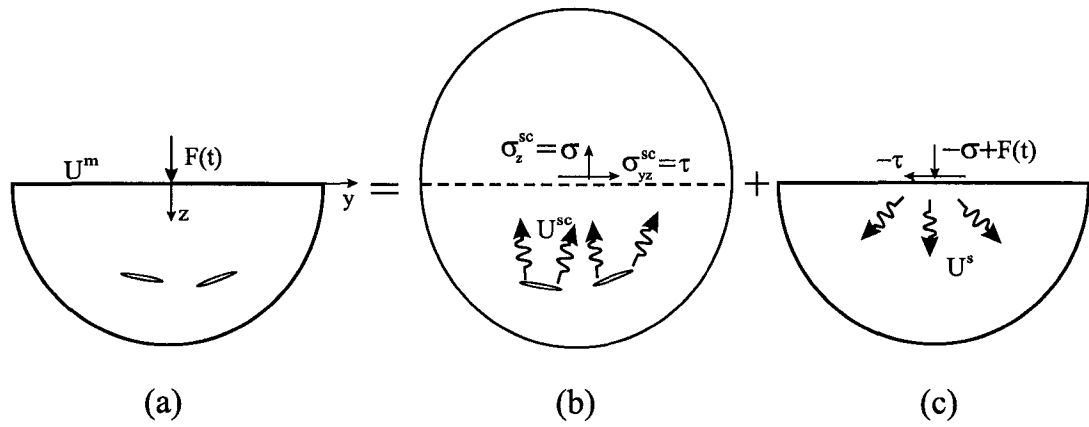
141

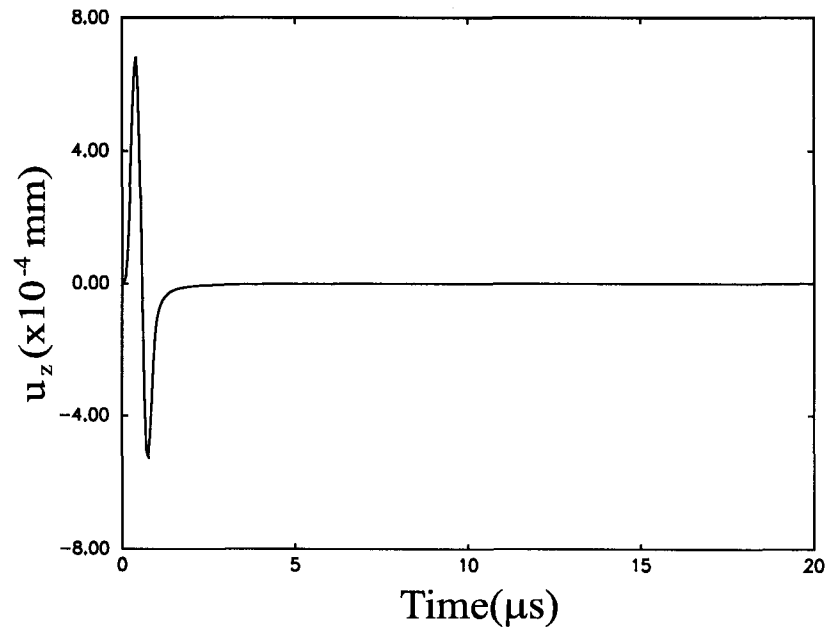Figure 6.1: Decomposition of elastic waves in the cracked medium

Figure 6.2: Surface displacement due to the applied dynamic force

142
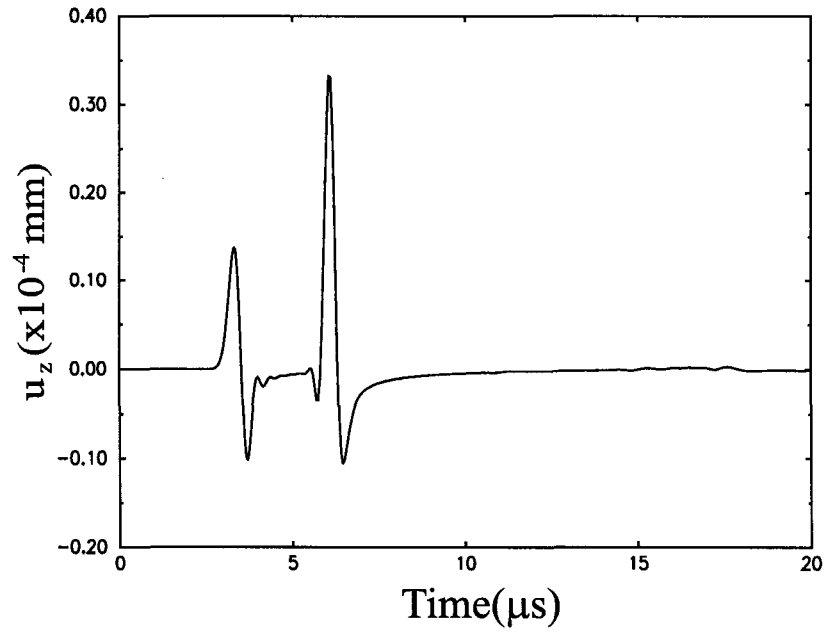
Figure 6.3: Displacement due to the incident wave
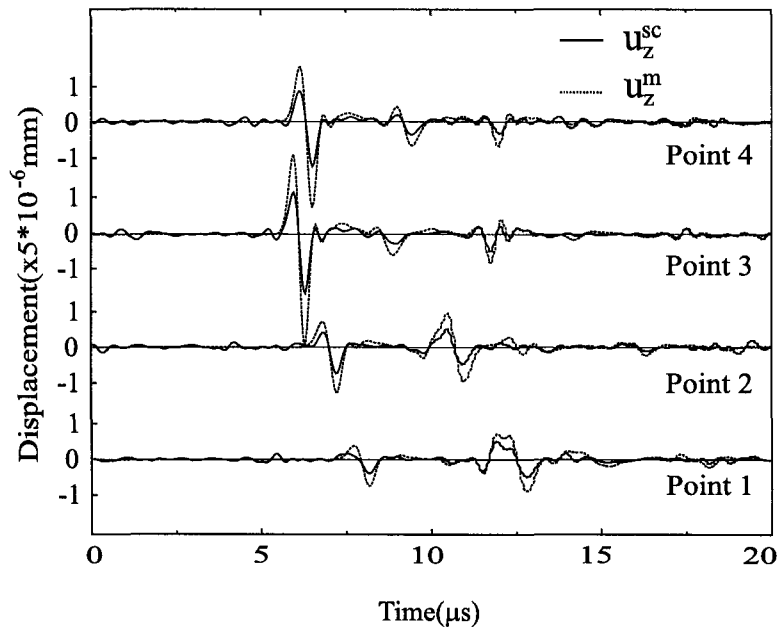
Figure 6.4: Surface displacements u_z^m and u_z^{sc} of the cracked medium

143
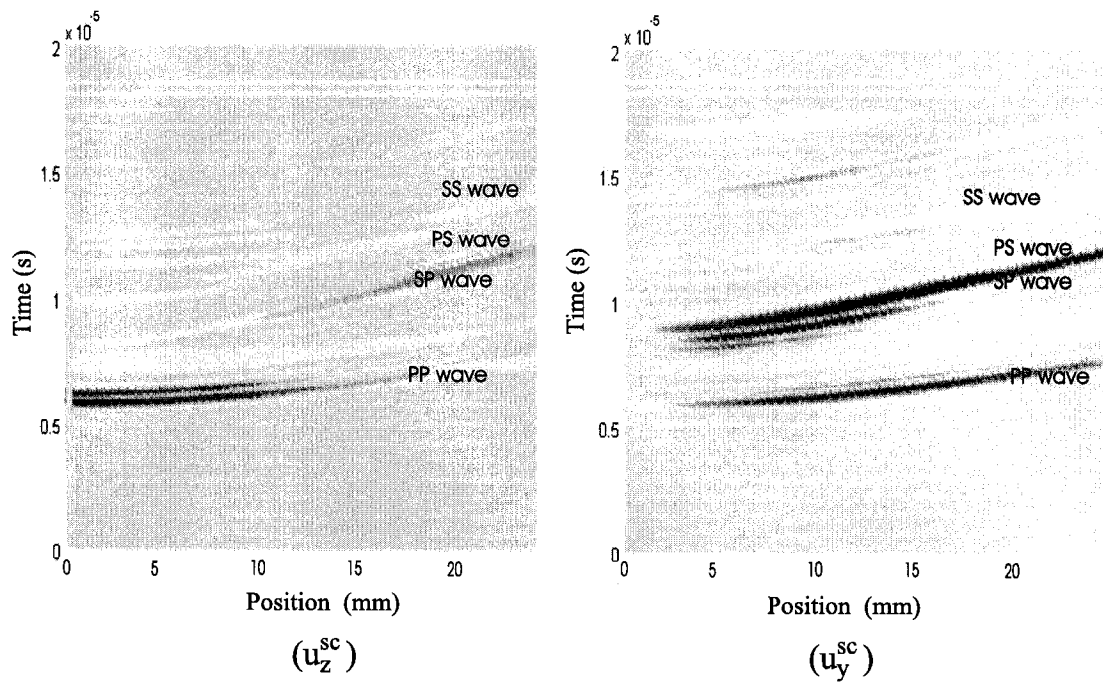
Figure 6.5: Surface displacements of the scattering wave u_z^{sc} and u_y^{sc}
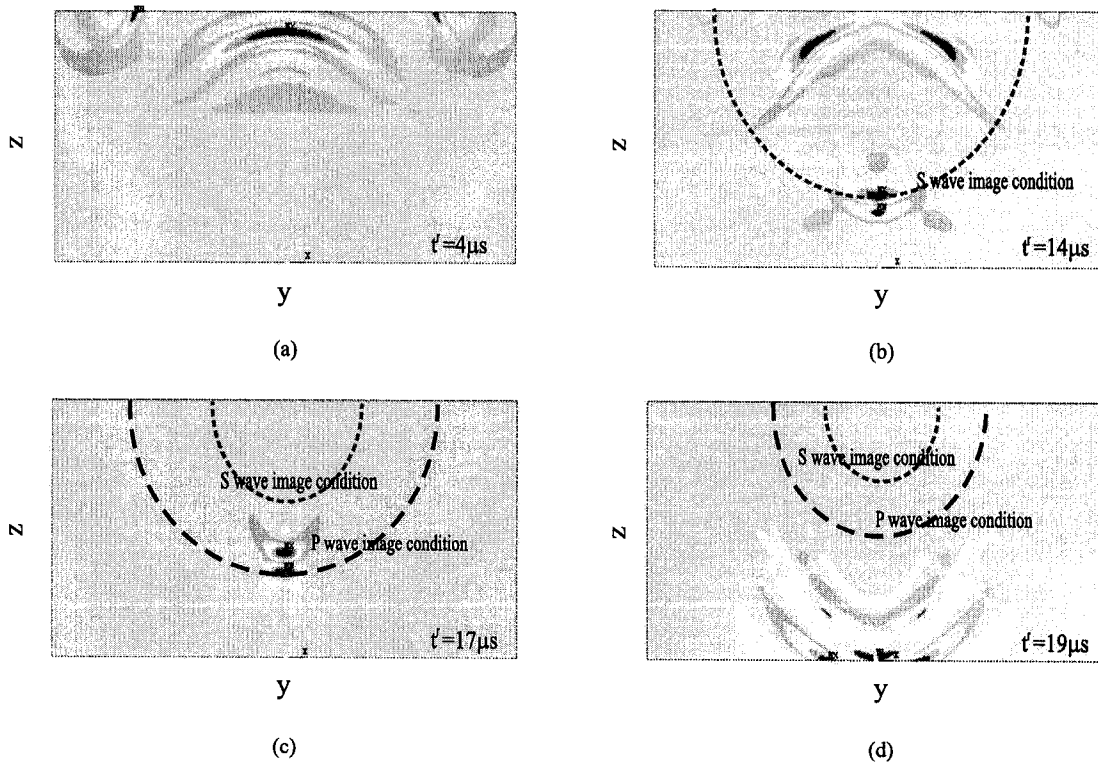
Figure 6.6: The reverse scattering wave

144
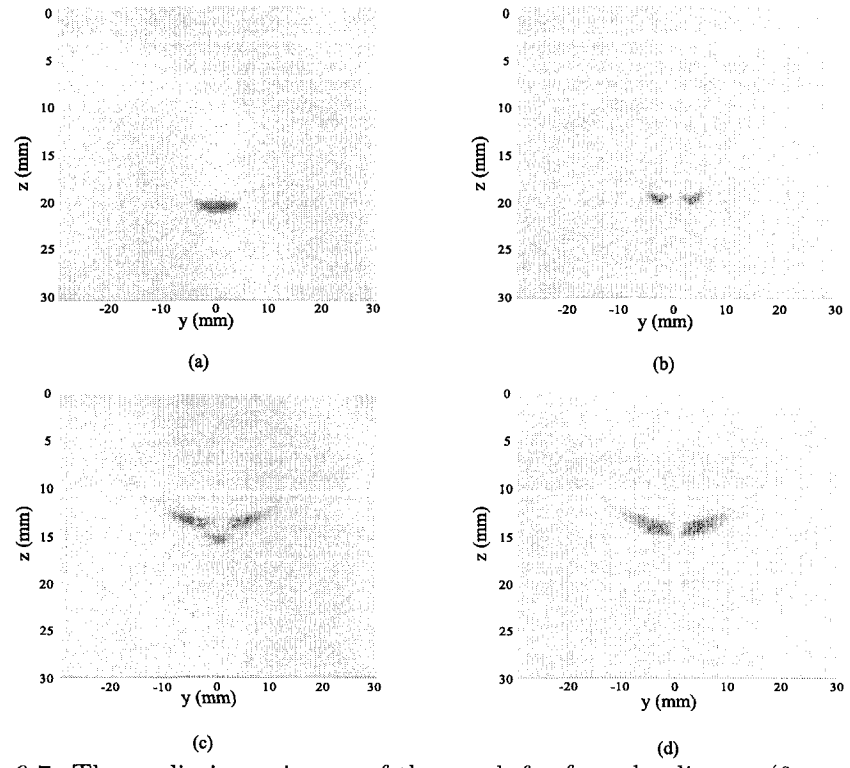
Figure 6.7: The preliminary image of the crack for force loading at $(0mm, 0mm)$
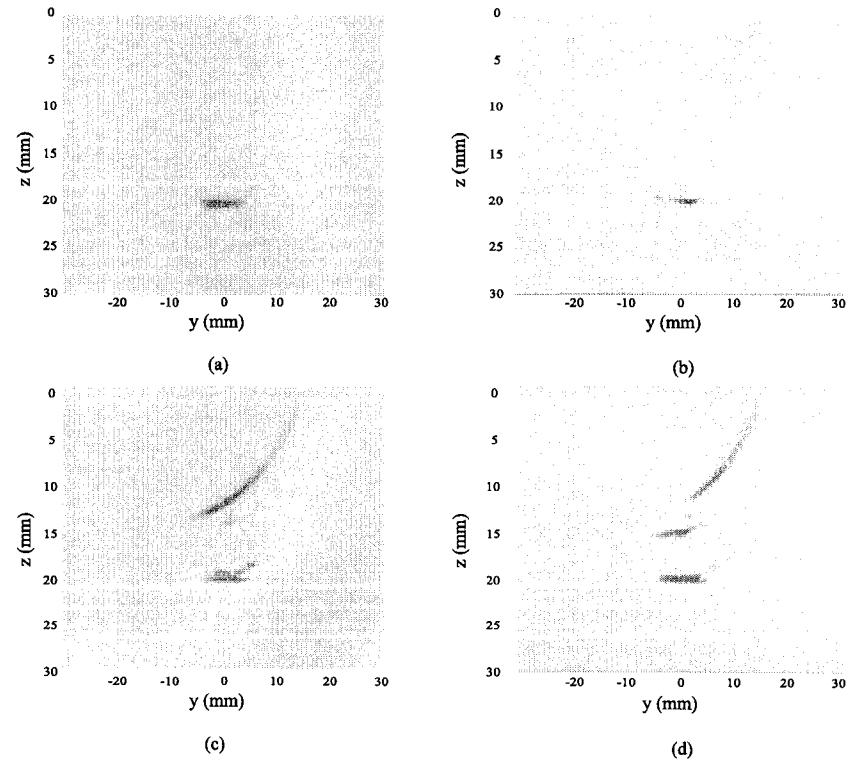
Figure 6.8: The preliminary image of the crack for force loading at $(-6mm, 0mm)$

145
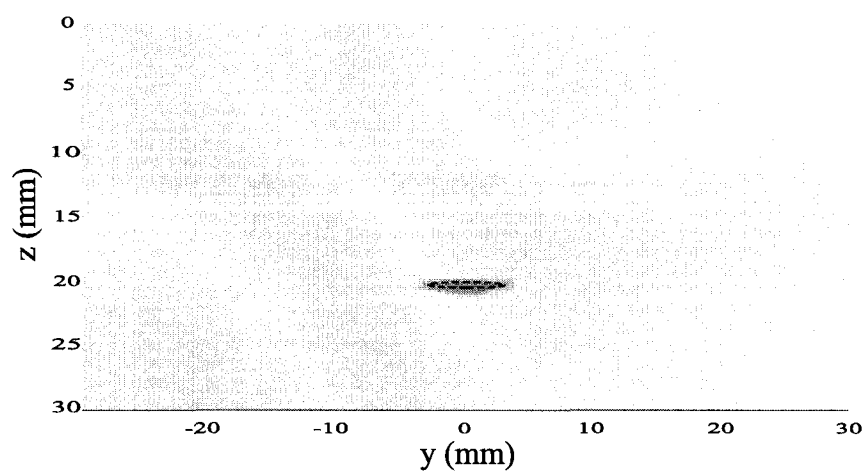
Figure 6.9: The final image of the crack with length $6mm$
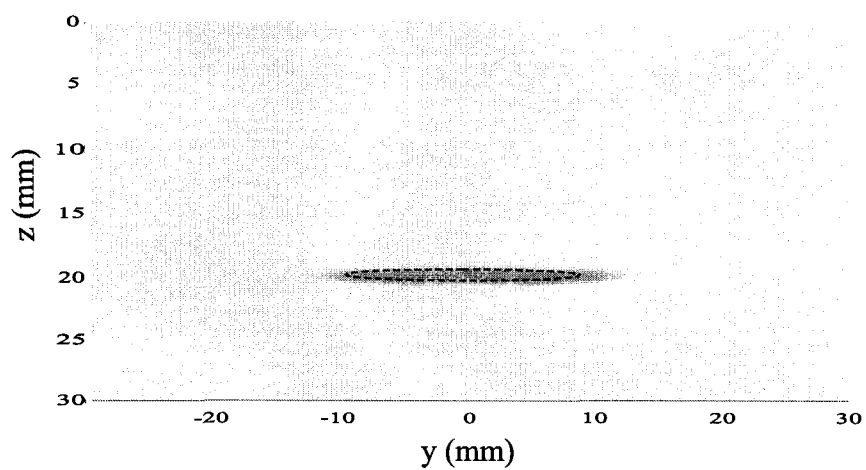
Figure 6.10: The final image of the crack with length $18mm$

146
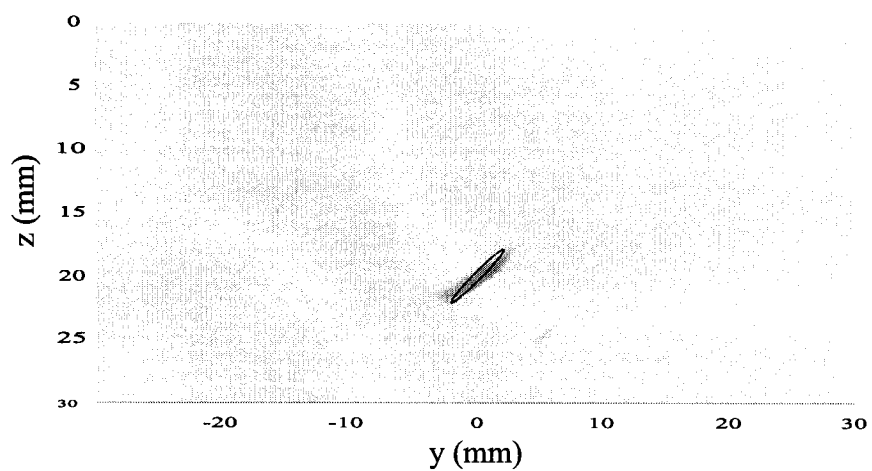
Figure 6.11: Image of the inclined crack with orientation 45°
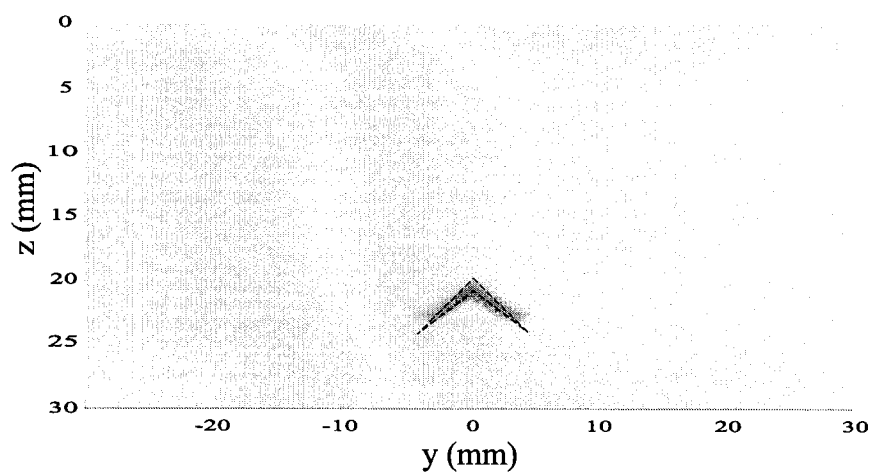
Figure 6.12: Image of the wedged crack

147
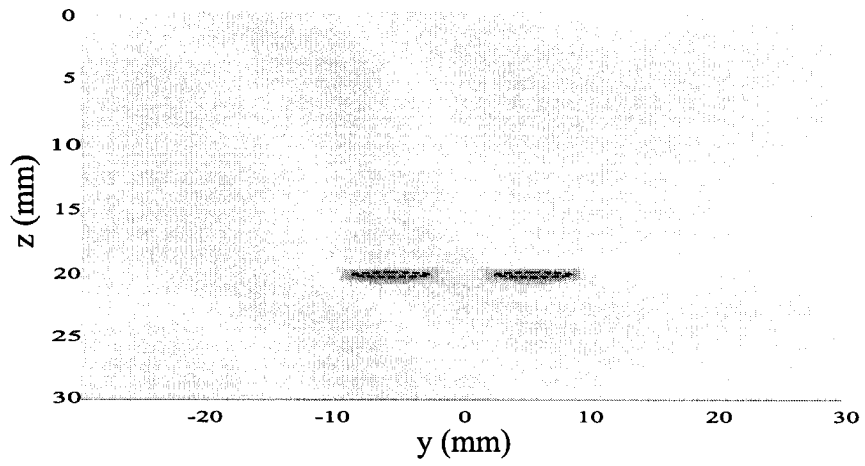
Figure 6.13: Image of the two collinear cracks
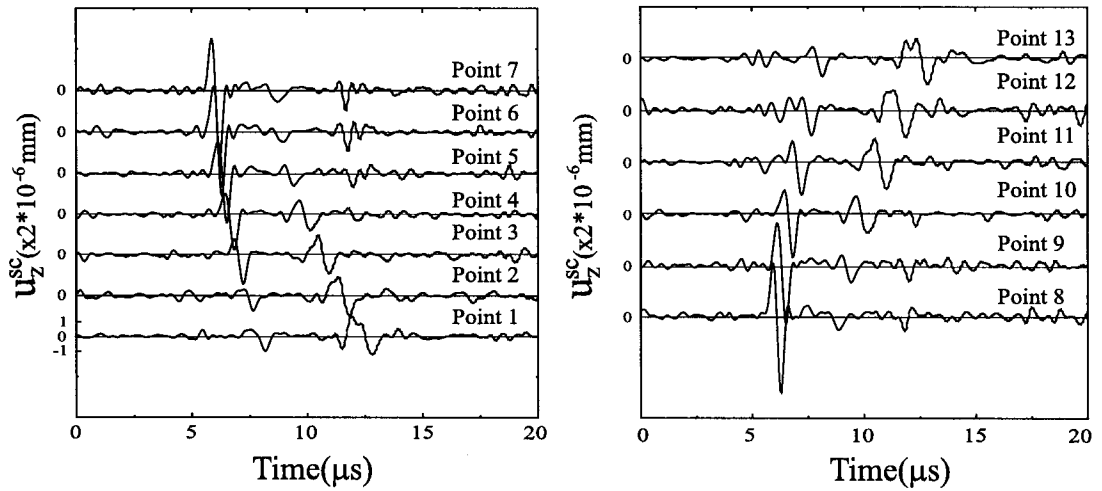
Figure 6.14: Surface displacements at the discrete points

148
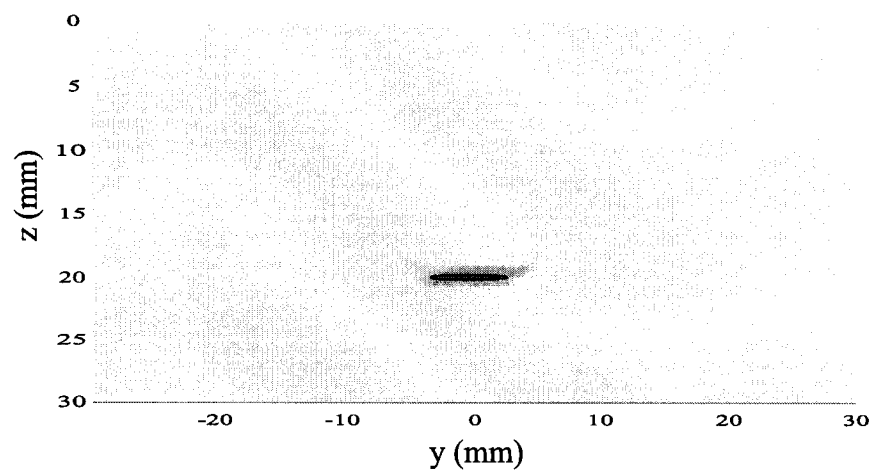
Figure 6.15: Image of the crack by using the discrete signals

149

Chapter 7

Structural Integrity Analysis with a Piezoelectric Acutuator/Sensor System

As discussed in Chapter 6, the proposed imaging scheme needs all two components of displacement on the measurement surface, and it is very difficult for any device to perform this task in the same time. For surface bonded piezoelectric actuator/sensor system, the electric voltage or electric potential, which is related to change of mechanical strain, is measured. This Chapter provides a theoretical study of a damage identification technique, which uses a piezoelectric sensors system attached to an elastic medium to quantitatively detect embedded cracks. A reverse wave field is generated using surface signals from piezoelectric sensors, which is further used to evaluate embedded cracks based on an imaging technique. The simulation is based on the use of the Cagniard-de Hoop method. Numerical examples are provided to show the feasibility of using surface bonded sensors/actuator system to determine the location, size and shape of different embedded cracks.

7.1   Statement of the problem

Because of their capability of capturing signals of wide bandwidth, piezoelectric sensors in forms of thin sheets show great potential in structural health monitoring.

150

Because they are small in size, these sensors can be used at almost any position of a structure, thus provide rich information at interested points along the surface of the structure. In a typical health monitoring system, when elastic waves are generated, reflected waves from embedded cracks will be captured by these sensors. The development of techniques to subtract information of cracks from the stored sensor waveforms plays a central role in the quantitative identification of them. In the current study, signals from a piezoelectric sensor system are assumed known and are used to provide images of embedded cracks in an elastic medium. Thin sheet piezoelectric sensors bonded to a structure will be able to provide only the information of the tangential deformation at the surface of the structure. Therefore, only strain in the tangential direction will be used as the sensor signals.

Consider now a plane strain problem of a half infinite isotropic elastic insulator with multiple cracks, as shown in Figure 7.1. A coordinate system (y, z) is used to describe the elastic medium. In order to detect the cracks in the material a piezoelectric actuators/sensors array is surface-bonded. The half length and the thickness of the actuator/sensor $A_n, n = 1, 2, 3, \cdots$ are denoted as a_n and h_n. The actuators/sensors are electroded on both sides. The electric potential will, therefore, be uniform across the surface of any actuator/sensor.

7.1.1   One-dimensional sensor model

When one of the piezoelectric elements, which is used as an actuator, is electrically excited by applying a transient electric voltage across its upper and lower electrodes, an elastic wave will be generated, which travels into the host medium. This wave will be reflected by embedded cracks and eventually reaches the sensors. Sensor signals in forms of electric potentials will be generated and recorded.

Because of the difficulties associated with the complicated bonding/interface conditions caused by the actuators/sensors and cracks, Fininte Element (FE) method

is used to simulate this process to generate the 'sensor signal' for further usage in crack identification. The simulation is based on the commercially available software ANSYS using the coupled field element "PLANE 13". A non-reflection boundary is used to simulate the infinite medium. The simulation is carefully controlled to ensure accuracy and stability of the results. The voltage across the upper and lower electrodes of the sensor can be directly determined. Since these electrodes are not electrically connected except by the sensor itself, the relation between the measured voltage and the strain of the sensor can be obtained based on an open-loop mode of the sensor.

For a thin sensor, the axial strain, which will dominately generate the electric voltage, can be assumed to be uniform across the thickness of the sensor. Therefore, the relation between the electric displacement D_z, the axial strain ε_y^s and the electric field E_z can be expressed as

$$D_z = e_s \varepsilon_y^s + \lambda_s E_z \tag{7.1.1}$$

where

$$
\begin{aligned}
e_s &= e_{13}^s - e_{33}^s \frac{c_{13}^s}{c_{33}^s} \quad plane\ strain \\
\lambda_s &= \lambda_{33}^s + \frac{(e_{33}^s)^2}{c_{33}^s} \quad plane\ strain
\end{aligned}
\tag{7.1.2}
$$

are effective material constants, c_{11}^s, c_{13}^s, c_{33}^s, e_{31}^s, e_{33}^s and λ_{33}^s are elastic and piezoelectric constants of the sensors.

When the sensor operates in an open loop situation and there is no external electric field applied (Tzou, 1993),

$$D_z = 0 \tag{7.1.3}$$

The electric charge will be collected on the electrodes and will produce an electric potential. The voltage across the electrodes of the sensor A_n can be obtained by integrating the electric filed as

$$V^{out} = \frac{e_s h_n}{2 a_n \lambda_s} \int_{-a_n}^{a_n} \varepsilon_y^s dy \tag{7.1.4}$$

152

7.1.2 Elastic wave back propagation

In this study, since the sensors are thin and small in size, the perturbation effects of the bonded sensor to the sensed wave field are ignored so that the received sensor signal ε_y^s can be regarded as the scattering wave field induced by the embedded crack ε_y^{sc}. The 'measured' sensor strain will be used to identify the embedded cracks. A reverse wave field, which represents the wave field before it reaches the sensors, will first be generated using the signals. In this study, the following boundary condition problem is suggested to back propagate wave field as

$$\varepsilon_y^r(y, 0, t^r) = \varepsilon_y^{sc}(y, 0, T - t), \quad \sigma_z^r(y, 0, t^r) = 0, \tag{7.1.5}$$

where T denotes total time span of the received signals. It should be mentioned that since $\sigma_z^r = 0$ is used as the boundary condition, the generated wave will also include partially the effect of the surface, in addition to the scattering wave from the cracks. Numerical results indicates that, for impulse type excitation, the use of $\sigma_z^r = 0$ will mainly disturb the amplitude but not the wave arrival time and propagation path. Correspondingly, the location and dimension of the cracks will not be significantly affected.

The back propagated wave field can be obtained by solving the elastodynamic boundary problem instead of using FEM method, since very neatly analytical solutions for this case can be obtained and strain boundary condition is difficult to apply for FEM. Applying the two side Laplace transform with respect to y and one side Laplace transform with respect to t, which are defined as (Achenbach, 1973),

$$f^L(s) = \int_{-\infty}^{\infty} f(y)e^{-sy}dy, \quad f(y) = \frac{1}{2\pi i} \int_{s_0-i\infty}^{s_0+i\infty} f^L(s)e^{sy}ds \tag{7.1.6}$$

$$\widetilde{f}(p) = \int_{0}^{\infty} f(t)e^{-pt}dt, \quad f(t) = \frac{1}{2\pi i} \int_{p_0-i\infty}^{p_0+i\infty} \widetilde{f}(p)e^{pt}dp \tag{7.1.7}$$

where the superscripts 'L' and '$\sim$' represent two side and one side Laplace transform, respectively, the governing equations, which is given in (6.1.2), can be reduced to the

153

following ordinary differential equations as

$$\frac{d^2\widetilde{\Phi}^L}{dz^2} - (\frac{p^2}{c_L^2} - s^2)\widetilde{\Phi}^L = 0, \tag{7.1.8}$$

$$\frac{d^2\widetilde{\Psi}^L}{dz^2} - (\frac{p^2}{c_T^2} - s^2)\widetilde{\Psi}^L = 0 \tag{7.1.9}$$

where Φ and Ψ are two complex displacement potentials, c_L and c_T are the longitudinal and transverse shear wave velocities of the elastic medium, respectively. The general solution of equations (7.1.8) and (7.1.9) can be determined as

$$\widetilde{\Phi}^L = E(p,s)e^{-\sqrt{\frac{p^2}{c_L^2} - s^2}z}, \ \widetilde{\Psi}^L = F(p,s)e^{-\sqrt{\frac{p^2}{c_T^2} - s^2}z} \tag{7.1.10}$$

This solution ensures that the induced wave field satisfies the radiation condition of the problem. Making using of the above general solutions and boundary conditions, the unknown parameters $E(p,s)$ and $F(p,s)$ can be determined. The resulting displacements in the host medium can then be obtained as

$$\widetilde{u}_y^L = -2c_T^2(\frac{\eta}{p} e^{-p\sqrt{\frac{1}{c_L^2} - \eta^2}z} - \frac{\eta^2 - \frac{1}{2c_T^2}}{p\eta} e^{-p\sqrt{\frac{1}{c_T^2} - \eta^2}z})\widetilde{\varepsilon}_y^L \tag{7.1.11}$$

$$\widetilde{u}_z^L = -\frac{2c_T^2}{p}(\sqrt{\frac{1}{c_L^2} - \eta^2}e^{-p\sqrt{\frac{1}{c_L^2} - \eta^2}z} + \frac{\eta^2 - \frac{1}{2c_T^2}}{\sqrt{\frac{1}{c_T^2} - \eta^2}}e^{-p\sqrt{\frac{1}{c_T^2} - \eta^2}z})\widetilde{\varepsilon}_y^L \tag{7.1.12}$$

where $\eta = \frac{s}{p}$.

Equations (7.1.11) and (7.1.12) need to be inverted into time-space domain. For the first term of $\widetilde{u}_y^L$, inversion of the two side Laplace transform requires evaluation of the following integral

$$\widetilde{I}_{yL} = \frac{1}{2\pi i}\int_{\eta_0-i\infty}^{\eta_0+i\infty} \eta e^{-p(\sqrt{\frac{1}{c_L^2} - \eta^2}z - \eta y)} d\eta \tag{7.1.13}$$

which has branch points $\eta = \pm\frac{1}{c_L}$. To complete the inversion, path integration will be produced and cuts are introduced in the complex η plane along the real axis from the branch points to infinity. Figure 7.2 shows the branch points, the cuts of the integrand as well as the path of integration along the imaginary axis employed in Equation

154

(7.1.13). In the following this integral has to be converted into an integration along a new path, from which the inverse Laplace transform can be obtained by inspection. The desired new path of integration in the η-plane is defined by

$$\sqrt{\frac{1}{c_L^2} - \eta^2} z - \eta y = t \tag{7.1.14}$$

Equation (7.1.14) can be solved for η to obtain

$$\eta_{L\pm}(r,\theta,t) = -\frac{t}{r}\cos\theta \pm i(\frac{t^2}{r^2} - \frac{1}{c_L^2})^{\frac{1}{2}}\sin\theta \tag{7.1.15}$$

where $r^2 = y^2 + z^2$ and $\tan\theta = \dfrac{z}{y}$. The integration along the vertical path is then transferred to the hyperbola obtained above, as shown in Figure 7.2. For the path, t runs from ∞ to $\dfrac{r}{c_L}$ in the lower branch of the hyperbola and then from $\dfrac{r}{c_L}$ to ∞ in the upper branch. So the integration along the imaginary axis can be replaced by an integration along the hyperbola as a function of t

$$\widetilde{I}_{yL} = \frac{1}{2\pi i}\{\int_{\frac{r}{c_L}}^{\infty} (\eta)_{\eta=\eta_{L+}}e^{-pt}\frac{\partial\eta_{L+}}{\partial t}dt + \int_{\infty}^{\frac{r}{c_L}} (\eta)_{\eta=\eta_{L-}}e^{-pt}\frac{\partial\eta_{L-}}{\partial t}dt\} \tag{7.1.16}$$

The above integral can be simplified to

$$\widetilde{I}_{yL} = \frac{1}{2\pi i}\int_{\frac{r}{c_L}}^{\infty} [(\eta)_{\eta=\eta_{L+}}\frac{\partial\eta_{L+}}{\partial t} - (\eta)_{\eta=\eta_{L-}}\frac{\partial\eta_{L-}}{\partial t}]e^{-pt}dt \tag{7.1.17}$$

from which, the inverse Laplace transform I_{yL} can be obtained as

$$I_{yL} = \frac{\sin\theta\cos\theta}{r\pi}(\frac{t^2}{r^2} - \frac{1}{c_L^2})^{-\frac{1}{2}}(2\frac{t^2}{r^2} - \frac{1}{c_L^2})H(t - \frac{r}{c_L}) \tag{7.1.18}$$

with H is Heaviside step function.

The second term of $\widetilde{u}_y^L$, which includes a pole at $\eta = 0$, can be reduced by inversion of the two-sided Laplace transform as

$$\widetilde{I}_{yT} = -\frac{1}{2\pi i}\int_{\eta_0-i\infty}^{\eta_0+i\infty} \frac{\eta^2 - \frac{1}{2c_T^2}}{\eta}e^{-p(\sqrt{\frac{1}{c_L^2}-\eta^2}z-\eta y)}d\eta \tag{7.1.19}$$

By defining a path

$$\eta_{T\pm}(r,\theta,t) = -\frac{t}{r}\cos\theta \pm i(\frac{t^2}{r^2} - \frac{1}{c_T^2})^{\frac{1}{2}}\sin\theta \tag{7.1.20}$$

155

and considering the pole at $\eta = 0$, which is shown in 7.3, I_{yT} can be similarly determined as

$$I_{yT}(y, z, t) = \frac{1}{2}\delta(t - \frac{r}{c_T})[H(y) - H(-y)]$$

$$-\frac{\sin\theta\cos\theta}{2r\pi}(\frac{t^2}{r^2} - \frac{1}{c_T^2})^{-\frac{1}{2}}[-\frac{1}{c_T^4}(\frac{t^2}{r^2} - \frac{\sin^2\theta}{c_T^2})^{-1} + 2(2\frac{t^2}{r^2} - \frac{1}{c_T^2})]H(t - \frac{r}{c_T}) \quad (7.1.21)$$

Therefore, the reversed wave field in the host medium can be obtained as

$$u_y^r(r, \theta, t) = -2c_T^2 \int_0^\infty \varepsilon_y^r(r, 0, \tau)[I_{yL}(r, \theta, t - \tau) + I_{yT}(r, \theta, t - \tau)]d\tau, \quad (7.1.22)$$

$$u_z^r(r, \theta, t) = -2c_T^2 \int_0^\infty \varepsilon_y^r(r, 0, \tau)[I_{zL}(r, \theta, t - \tau) + I_{zT}(r, \theta, t - \tau)]d\tau \quad (7.1.23)$$

where

$$I_{zL}(y, z, t) = -\frac{1}{r\pi}(\frac{t^2}{r^2} - \frac{1}{c_L^2})^{-\frac{1}{2}}[2\frac{t^2}{r^2}(\cos^2\theta - \sin^2\theta) - \frac{\cos^2\theta}{c_L^2}]H(t - \frac{r}{c_L}) \quad (7.1.24)$$

$$I_{zT}(y, z, t) = \frac{1}{2r\pi}(\frac{t^2}{r^2} - \frac{1}{c_T^2})^{-\frac{1}{2}}(\cos^2\theta - \sin^2\theta)(2\frac{t^2}{r^2} - \frac{1}{c_T^2})H(t - \frac{r}{c_T}) \quad (7.1.25)$$

7.2 Results and discussion

This section is devoted to the numerical simulation of identifying cracks using surface sensor signals for determining their positions, dimensions and shapes.

The material constants of piezoelectric actuators and sensors and the structure being monitored are assumed to be,

Actuator and sensor

$$c_{11}^{(s)} = 3.61 \times 10^9 (Pa), c_{12}^{(s)} = 1.4 \times 10^9 (Pa), c_{13}^{(s)} = 1.4 \times 10^9 (Pa)$$

$$c_{33}^{(s)} = 1.63 \times 10^9 (Pa), c_{44}^{(s)} = 0.59 \times 10^9 (Pa)$$

$$e_{31}^{(s)} = 7.68 \times 10^{-3} (C/m^2), e_{33}^{(s)} = -30.7 \times 10^{-3} (C/m^2), e_{15}^{(s)} = -11.5 \times 10^{-3} (C/m^2)$$

$$\lambda_{11}^{(s)} = 0.061 \times 10^{-9} (C/Vm), \lambda_{33}^{(s)} = 0.067 \times 10^{-9} (C/Vm)$$

Host medium

$$\lambda = 5.20 \times 10^{10} (Pa), \mu = 2.68 \times 10^{10} (Pa), \rho = 2572 (kg/m^3)$$

156

The voltage applied to the actuator is

$$V(t) = V_0[H(t) - H(t - N_p/f_0)](1 - \cos\frac{2\pi f_0 t}{N_p})\sin 2\pi f_0 t$$

with $f_0 = 1MHz$, $N_p = 1$ and $V_0 = 10V$.

7.2.1 Sensor signals

Consider the case where a crack of $6mm$ long, parallel to the surface and centred at $(0mm, 20mm)$. 25 equally spaced actuators/sensors with $v = a_i/h_i = 20, a_i = 0.5mm, y_i = -24 + 2 \times (i - 1)mm, i = 1, \cdots, 25$ are used. The actuator is at $(0mm, 0mm)$. Electric potential will be generated at these sensors in response to the actuator. The 'measured' voltage at a sensor will be used to derive the average strain of the sensor using Equation (7.1.4). This average strain will be used approximately as the strain at the centre of the sensor in crack identification. For the sensor centred at $(0mm, 2mm)$, Figure 7.4 shows the comparison between the average strain obtained from 'measured' voltage and the real strain at its centre. In this figure, the incident waves from the actuator have already been muted by subtracting the wave field without crack. The comparison agrees well, which means that one-dimensional sensor model can be used to predict strain field of the sensor. In the following discussion, strain obtained from sensor signals are regarded as the strain at the centre of the sensor. Figure 7.5 shows the scattering strain wave field ε_y^{sc} along the measurement surface, in which wave fields at points other than the sensors' position are extrapolated by using polynomial curve fitting. This result will be used as input data for reverse wave propagation process.

7.2.2 Reverse wave technique and crack imaging

After the scattering wave field along the surface is obtained, the reverse wave field can be obtained by solving the proposed boundary value problem. Figure 7.6 displays four snapshots of reverse wave component u_z^r at different times. The moment, $t^r = T - t$, at which the snapshots are taken are $t^r = 4, 14, 17, 19\mu s$, respectively. In

157

Figure 7.6a, the wave field is propagating toward the crack. The scattering wave energy from the crack is focussed back to the crack at time $t^r = 14, 17\mu s$ for S and P waves in Figure 7.6b,c, respectively,. In Figure 7.6d, the scattering energy continued its downward propagation. At each moment, the points which satisfy the imaging conditions, which are given in Equation (6.1.29), are imaged by extracting the amplitude of the wave field at these points.

Figure 7.7 shows the images by using incident S and P waves for the single crack case discussed. Frame (a) and (b) are the image results based on displacement components u_z^r and u_y^r, respectively, using S wave image condition. Frame (c) and (d) are the image results based on displacement components u_z^r and u_y^r, respectively, using P wave image condition. Comparing the images in frames (a)-(d), it can be found that the images by using incident P wave are different from those by using incident S wave. To uniquely determine the location of the crack, an additional case using a different actuator is considered. Figure 7.8 shows the corresponding image results for the same problem with position of the actuator at $(y_0, z_0) = (-6mm, 0)$. After compared with the two image results, the pseudo images, which is mainly resulted from P wave image condition, can be easily eliminated. The final image of the crack can be obtained as shown in Figure 7.9 based on Equation (6.1.32). The dash line superimposed in this figure represents the real crack position. Similar result for a longer crack of $18mm$, which is centred at $(0, 20mm)$, is shown in Figure 7.10. The very good agreement shows the feasibility of using the proposed technique to reversely propagate scattering wave and image the crack.

7.2.3   Imaging using different numbers of sensors

The number of sensors used in a specific area of a health monitoring system is usually limited since the dimension of sensors can not be too small. The effect of sensor numbers used on the quality of images is shown in Figure 7.11 for the case used in Figure 7.9. Frames (a)-(d) are the final image results of the structure for total

158

25,17,9,5 equal spaced sensors within the same range (-24mm, 24mm), respectively. In frame (a), the image result can clearly identify the information of the embedded crack, and the image result in frame (b) is very similar to that in frame (a), which shows that distance between the sensors for the current problem is still good enough to obtain good information of the embedded crack. In frame (c), the image result begins to diffuse around the position of the embedded crack, the more diffuse phenomenon can be observed in frame (d), which shows limitation of the sensor's number used. The parameter's optimization about the number of the sensors and corresponding loading frequency used could be further studied to ensure good image results.

7.2.4 Image of multiple cracks

Figure 7.12 shows the image of two collinear cracks of length $6mm$. Their centres are located at $(-6mm, 20mm)$ and $(6mm, 20mm)$ and are parallel to the surface. Very good agreement is observed. It should be mentioned that capability to image multiple cracks is an important property of the current reverse wave technique, which makes this technique very favorable comparison with traditional pulse-echo methods.

159
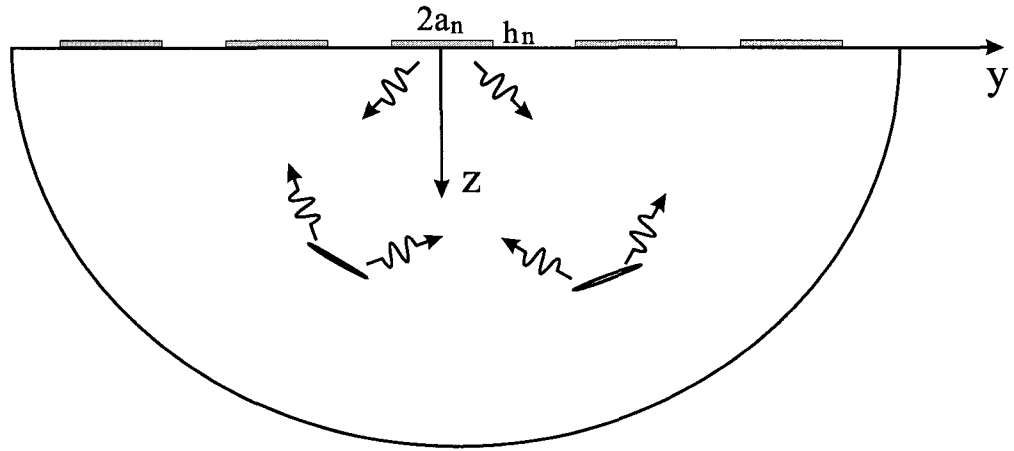
Figure 7.1: Piezoelectric actuators/sensors surface-bonded to the cracked medium
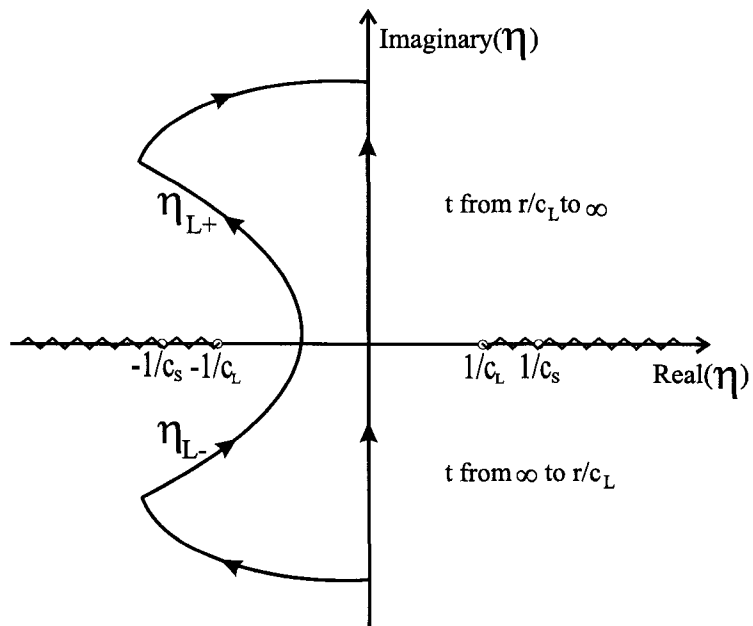
Figure 7.2: The integral path the first term of $\widetilde{u}_y^L$

160
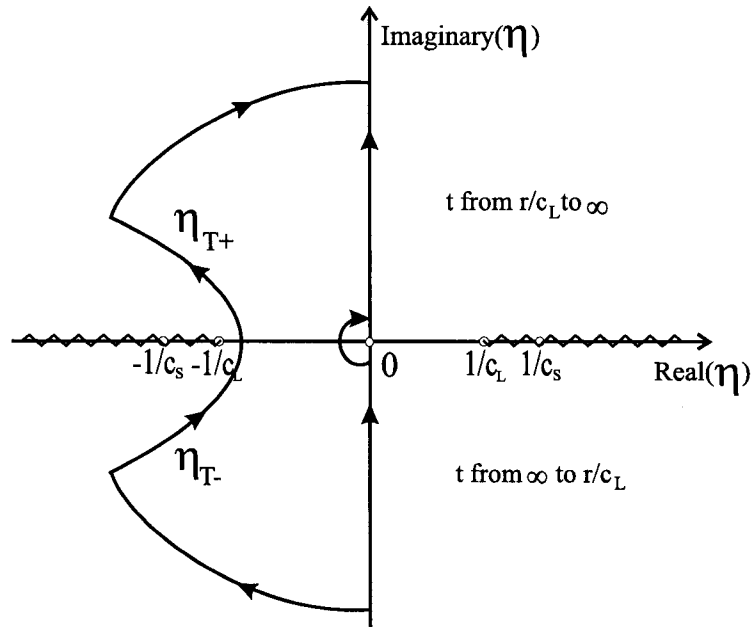
Figure 7.3: The integral path the second term of $\widetilde{u}_y^L$
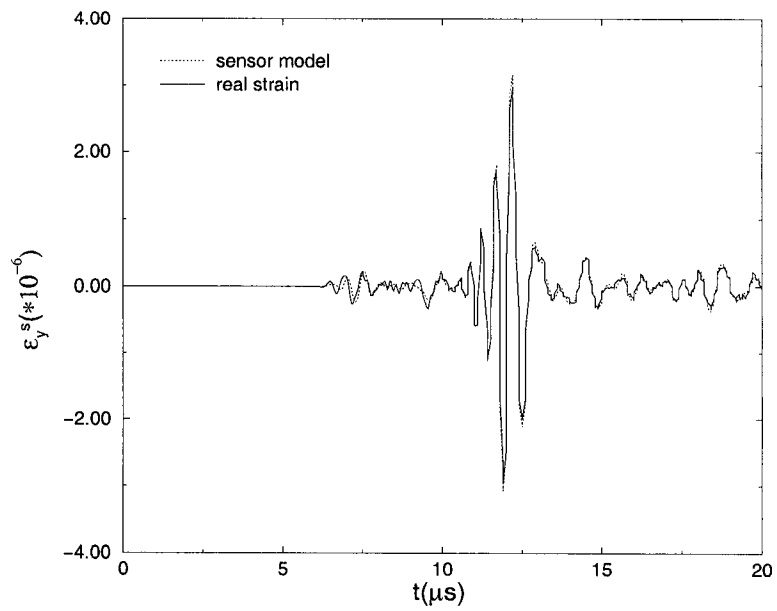
Figure 7.4: Comparison of the real strain with sensor measurement

161
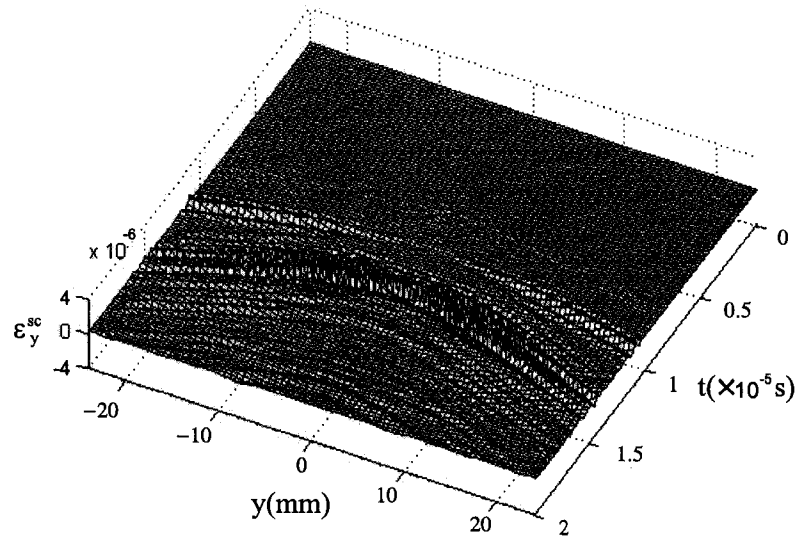
Figure 7.5: Surface signal due to the scattering wave from the crack
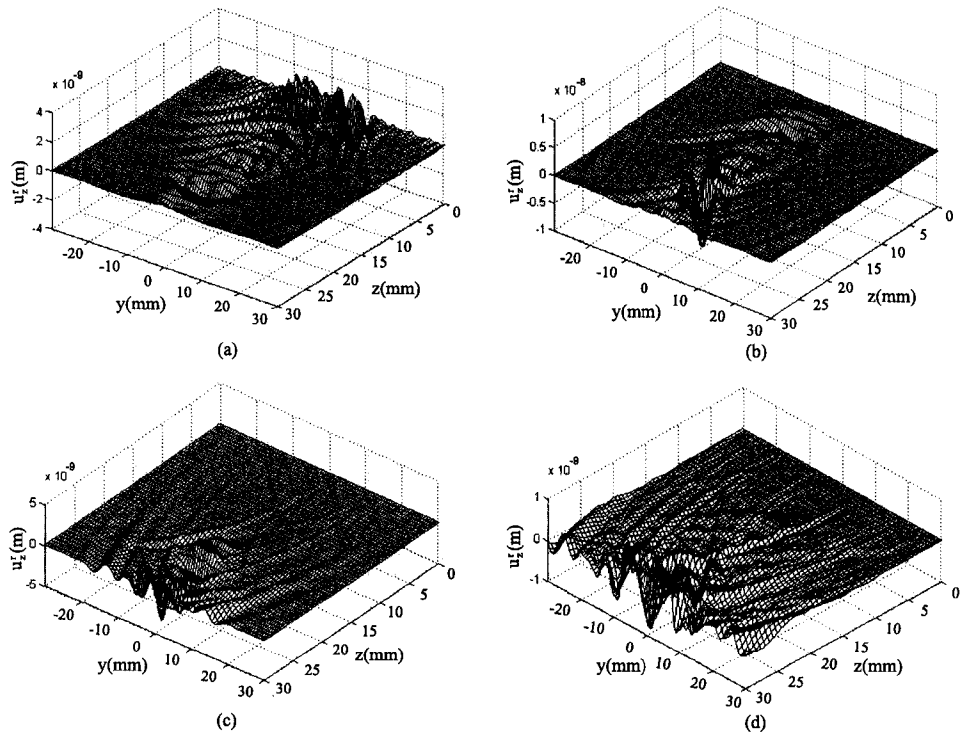
Figure 7.6: The reverse scattering wave

162
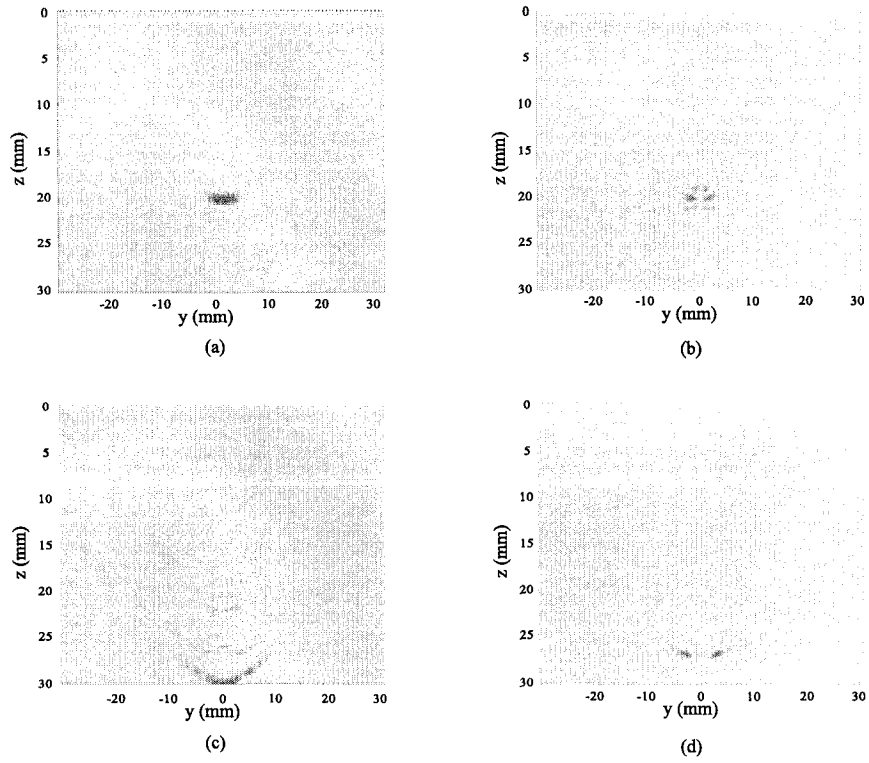
Figure 7.7: The preliminary image of the crack with actuator at $(0mm, 0mm)$
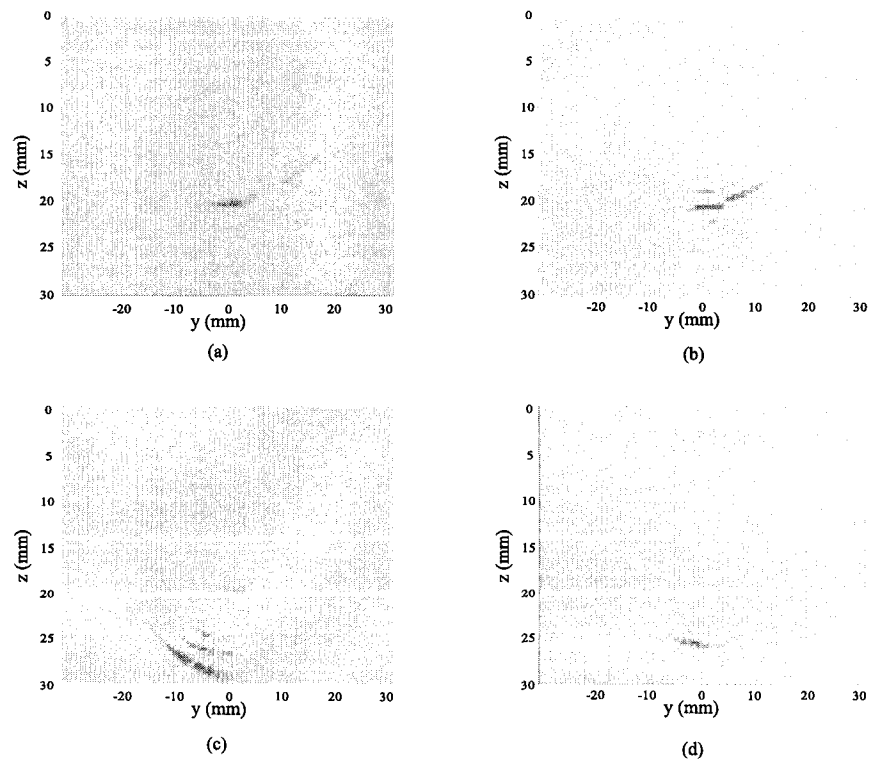
Figure 7.8: The preliminary image of the crack with actuator at $(-6mm, mm)$

163
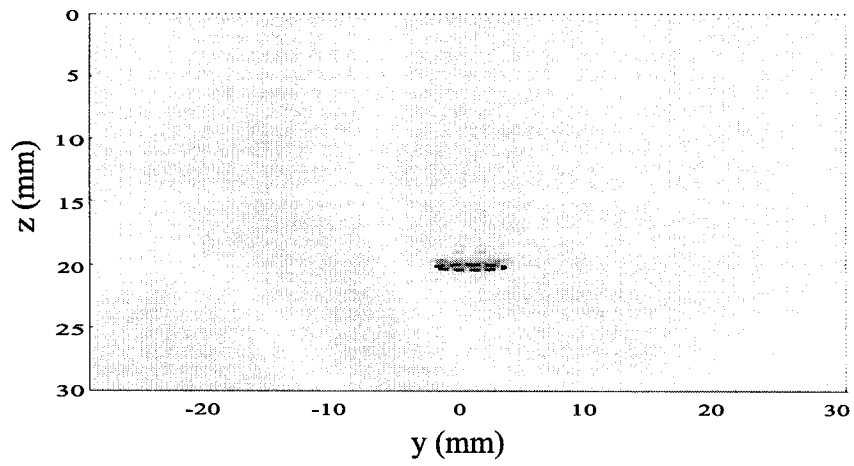
Figure 7.9: The final image of the crack with length $6mm$
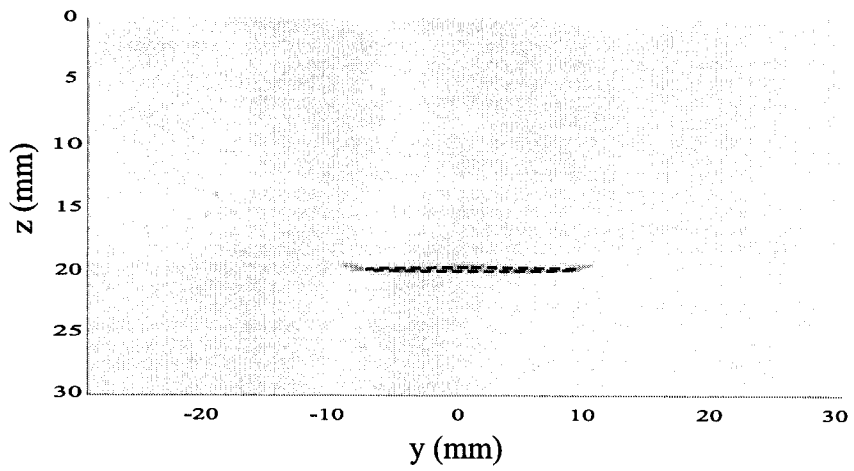
Figure 7.10: The final image of the crack with length $18mm$

164
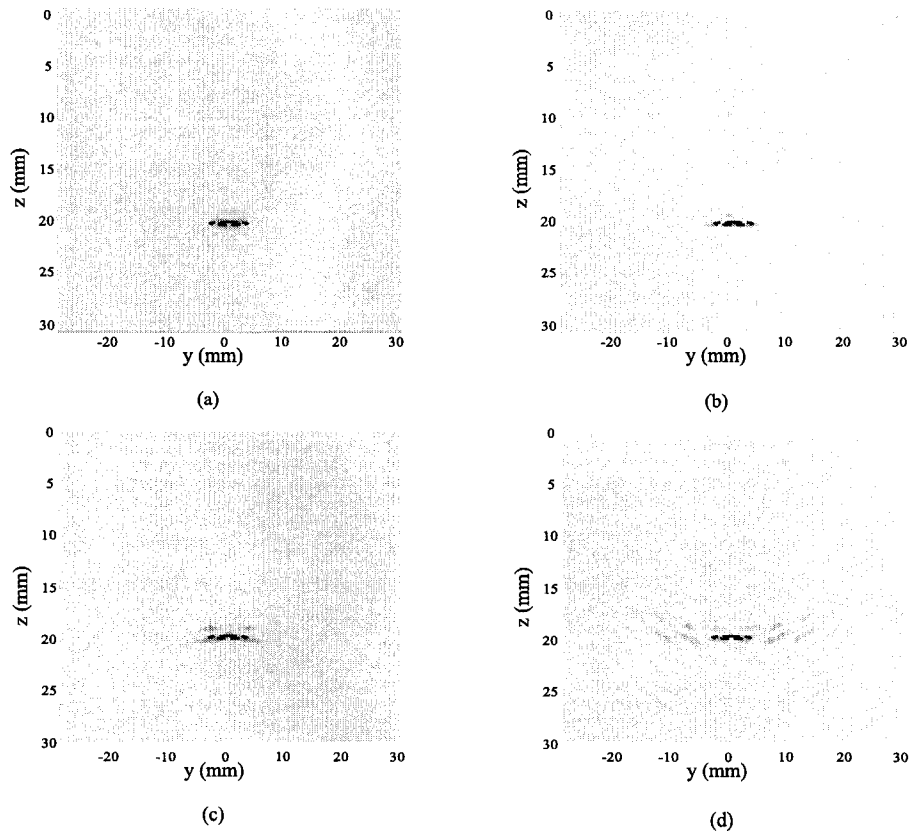
Figure 7.11: The final image results by using different sensor numbers
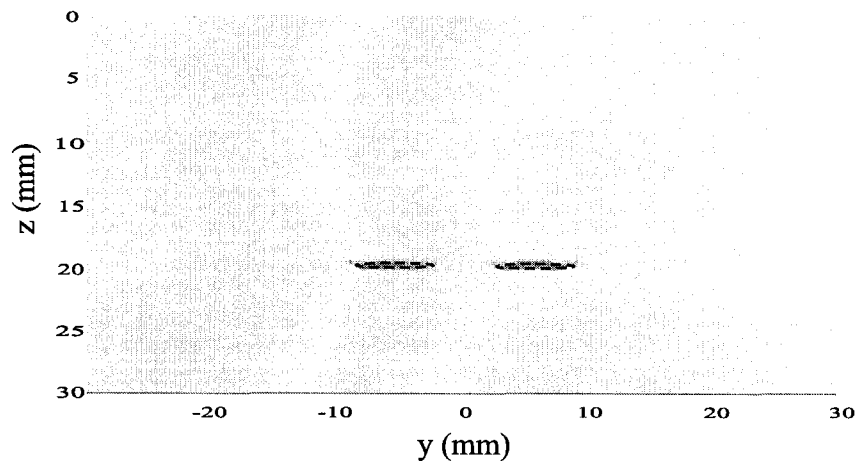
Figure 7.12: Image of the two collinear cracks

165

Chapter 8

Discussion and Conclusions

8.1 Conclusions

Throughout this study, three major issues essential to the establishment of a structural health monitoring system using piezoelectric actuators/sensors are studied (i) a one dimensional actuator model has been modified and used to simulate the mechanical field in elastic media due to surface bonded or embedded piezoelectric actuator, (ii) the wave propagation induced by different piezoelectric actuators are systematically studied through numerical simulation, and (iii) a reverse wave technique is proposed as an interpretation method to find the information of embedded cracks.

Specific contributions and conclusions of this study to the field of the research can be summarized as follows:

(a) The one dimensional actuator model (Wang and Meguid, 2000) is used to consider the static coupled electromechanical behaviour of a piezoelectric actuator bonded to an orthotropic elastic medium under plane electric loading. The effects of the geometry, the material mismatch, the material anisotropy and interfacial debonding upon the load transfer between the actuator and the host structure are determined and discussed.

(b) The one dimensional actuator model (Wang, 2000) is used and modified to consider dynamic electromechanical behaviour of actuators surface-bonded to and/or

166

embedded in an isotropic elastic medium. The significant effects of loading frequency upon interfacial transverse stress between the actuators and the host structure are observed, which shows the importance of including the interfacial transverse stress for embedded actuators.

(c) The wave propagation generated by surface-bonded and embedded piezoelectric actuators is analytically studied. The interaction between actuators is simulated by using newly developed Pseudo-Incident Wave method (Wang and Meguid, 1997). The numerical simulation conducted indicates the effects of the geometry of the actuators, the material combination and the loading frequency upon the resulting wave propagation. The basic properties of the wave field is demonstrated by the analytical solution of the wave field far away from the actuators.

(d) To use the piezoelectric actuator-generated wave to detect cracks, a reverse wave technique is developed to identify embedded cracks in the elastic medium. The technique is based on the usage of the scattering waves from the cracks in response to the actuators, which can be measured by distributed piezoelectric sensors. This technique has been used for both harmonic and transient waves. Images of embedded cracks are obtained using newly proposed algorithms. Numerical simulations show that the current technique can accurately determine the locations, dimensions, and shapes of cracks.

8.2 Future studies

Based on the results of the work done in this thesis, the additional investigations in a number of areas, which could be further conducted, are suggested as follows:

(a) The current study is limited to two dimensional models. Considering the fact that structures are always three dimensional, further study and detailed simulation using 3-D model will be an important topic for a real SHM system. Piezoelectric actuator and sensor models for three dimensional cases should be developed to generate

167

the elastic wave and receive the scattering wave in 3-D structure.

(b) Extensive experimental work is needed to verify the proposed technique and proper actuator/sensor systems need to be designed for further studies. The piezoelectric materials are surface-bonded to the structure as actuators and sensors to generate and collect the elastic waves, respectively. A waveform generator generates the high frequency excitation signal. The excited signal is first amplified by a power amplifier, then drives PZT actuators to generate transient waves. PZT sensors will collect the waves and convert them into electrical signals and recorded as an input signals to find out the information of embedded crack by using the proposed technique.

168

Bibliography

[1] Achenbach, J.D., 2002, "Modelling for quantitative non-destructive evaluation", *Ultrasonics*, 40(1-8): 1-10.

[2] Achenbach, J.D., 2000, "Quantitative nondestructive evaluation", *International Journal of Solids and Structures*, 37(1-2): 13-27.

[3] Achenbach, J.D., 1973, "Wave propagation in elastic solids", North-Holland Publishing Company, Amsterdam.

[4] Aldraihem, O.J. and Khdeir, A.A., 2000, "Smart beams with extension and thickness-shear piezoelectric actuators", *Smart Materials and Structures*, 9(1): 1-9.

[5] Alleyne, D.N. and Cawley, P., 1992a, "Optimization of Lamb wave inspection techniques", *NDT and E International*, 25(1): 11-22.

[6] Alleyne, D.N. and Cawley, P., 1992b, "The interaction of Lamb wave with defects" , *IEEE Transactions on Ultrasonics, Ferroelectrics and Frequency Control*, 39(3): 381-397.

[7] Ashley, S., 1995, "Smart Skis and other Adaptive Structures", *Mechanical Engineering*, November:76-81.

[8] Ayres, J.W., Rogers, C.A. and Chaudhry Z., 1996, "Qualitative health monitoring of a steel bridge joint via piezoelectric actuator/sensor patches", *the SPIE Nondestructive Evaluation Technique for Aging Infrastructure and Manufacturing*, December:1-8.

[9] Bailey, T. and Hubbard, J.E., 1985, "Distributed piezoelectric polymer active vibration control of a cantilever beam", *AIAA Journal of Guidance Control*, 6: 605-611.

[10] Bakker, M.C.M., Verweij, M.T. and Hubbard, J.E., 2003, "An approximation to the far field and directivity of elastic wave transducers", *Journal of the Acoustical Society of America*, 111(3): 1177-1188.

[11] Banks, H.T. and Smith, R.C., 1995, "The modelling of piezoceramic patch interactions with shells, plates, and beams", *Quarterly of Applied Mathematics*, LIII:353-381.

[12] Banks, H.T., Smith, R.C. and Wang, Y., 1996, "Smart Material Structures: Modelling, Estimation and Control", Masson, John Wiley and Sons, Paris.

[13] Bar-Cohen Y. and Lih, S.S., 2000, "Progress And Challenges to NDE of Composites Using Obliquely Insonified Ultrasonic Waves" *45th International SAMPE Symposium and Exhibition*, Long Beach CA, May 21-25,.

[14] Bar-Cohen, Y., 2000, "Emerging NDE Technologies and Challenges at the Beginning of the 3rd Millennium - Part I." *Material Evaluation*, 58(1): 17-30.

[15] Batra, R.C., Liang, X.Q. and Yang, J.S., 1996, "The vibration of a simply supported rectangular elastic plate due to piezoelectric actuators " *International Journal of Solids and Structures*, 33(11): 1597-1618.

[16] Berkhout, A.J. and Wappenaar, C.P.A., 1987, "One-way versions of the Kirchhoff integral", *Geophysics*, 54(4): 460-467.

[17] Benjeddou, A., Trindade, M.A. and Ohayon, R., 2000, "Piezoelectric actuation mechanisms for intelligent sandwich structures", *Smart Materials and Structures*, 9(3): 328-335.

[18] Biemans, C., Staszewski, W.J., Boller, C. and Tomlinson, G.R., 1999, "Crack detection in metallic structures using using piezoceramic sensors", *Key Engineering Materials*, 167(1): 112-121.

[19] Boller, C., 2000, "Next Generation Structural Health Monitoring and its Integration into Aircraft Design", *International Journal of Systems Science*, 31: 1333-1349.

[20] Boller, C., 1998, "State of the art and trends in using smart materials and systems in transportation vehicles", *Proceedings of the Institution of Mechanical Engineers Part I-Journal of Systems and Control Engineering*, 212 (I3): 149-158.

[21] Burke S.E. and Hubbard J.E., 1991, "Distributed transducer vibration control of thin plates", *Journal of the Acoustical Society Of America*, 90(2): 937-944.

[22] Carino, N.J., Sansalone, M. and Hsu, N. N., 1986, "A point source-point receiver pulse-echo technique for flaw detection in concrete", *ACI Journal*, 83: 199-208.

[23] Capineri, L., Tattersall, H.G., Temple, J.A.G. and Silk, M.G., 1995, "Time of flight diffraction tomography for NDT applications", *Ultrasonics*, 5: 275-288.

[24] Chang, F.K., 1995, "Built-in damage diagnostics for composite structures", *Proceedings of the 10th International Conference on Composite Structures*, 5: 283-289.

[25] Chang, W. and Mcmechan, G.A., 1986, "Reverse-time migration of offset profiling data using the excitation-time image condition", *Geophysics*, 51: 67-84.

[26] Chien, L.S., 1997, "In-situ damage detection of plates by migration technique", *Proceedings of the 38th AIAA/ASME/ASCE/AHS/ASC Structures, Structural Dynamics and Material Conference*, Kissimmee, FL, AIAA-97-1225, 1110-1114.

[27] Charles, H., Keilers, J. and Change, F.K., 1995, "Identification delamination in composite beams using built-in piezoelectrics: Part I experiment and analysis", *Journal of Intelligent Material and Structural System*, 6: 649-663.

[28] Chiu, W.K., Galea, S.C., Koss, L.L. and Rajic, N., 2000, "Damage detection in bonded repairs using piezoceramics", *Smart Materials and Structures*, 9: 466-475.

[29] Chiu, W.K., Heller, M. and Jones, R., 1997, "Determination of the stress components of an array of piezoelectric sensors: a numerical study", *Smart Materials and Structures*, 6: 152-160.

[30] Claerbout, J.F., 1976, "Fundamentals of Geophysical Data Processing", McGrew-Hill, New York.

[31] Claerbout, J.F., 1985, "Imaging the Earth's Interior", Blackwell Scientific Publication, Boston.

[32] Crawley, E.F., 1994, "Intelligent structure for aerospace: a technology overview and assessment", *AIAA Journal*, 32(8): 1689-1699.

[33] Crawley, E.F. and Anderson, E.H., 1990, "Detailed models of piezoelectric actuation of beams", *Journal of Intelligent Material Systems and Structures* 1: 4-25.

[34] Crawley, E.F. and Luis, D.J., 1987, "Use of piezoelectric actuators as elements of intelligent structures", *AIAA Journal*, 25(10): 1373-1385.

[35] Crawley, E.F. and Lazarus, K.B., 1991, "Induced strain actuation of isotropic and anisotropic plates", *AIAA Journal*, 29(6): 944-951.

[36] Dalton R.P., Cawley P. and Lowe M., 2001, "The potential of Guided Waves for monitoring large areas of metallic aircraft fuselage structure", *Journal of Nondestructive Evaluation*, 20: 29-46.

[37] Datta, D. and Kishore, N.N., 1996, "Features of ultrasonic wave propagation to identify defects in composite materials modelled by finite element method", *NDT and E International*, 4: 213-223.

[38] Deutsch, W., Cheng, J. and Achanbach, J., 1997, "Self-focusing of rayleigh waves and lamb waves with a linear phased array", *Research in Nondestructive Evaluation*, 9: 81-95.

[39] De-Hoop, A.T., 1995, "Handbook of Radiation and Scattering of Waves", Academic Press, London.

[40] Docherty, P., 1991, "A brief comparison of some Kirchhoff integral formulas for migration and inversion", *Geophysics*, 56: 1164-1169.

[41] Dimitriadis, E. K., Fuller, C.R. and Rogers, C.A., 1991, "Piezoelectric actuators for distributed noise and vibration excitation of thin plates", *ASME Journal of Vibration and Acoustics*, 13: 100-107.

[42] Duune J. P., Pitt D.M. and Sofge D.A., 2001, "Recent advances in active damage interrogation", *Proceedings of the 42nd AIAA SDM conference*, Seattle, WA.

[43] Esmersoy C. and Oristaglio, M., 1988, "Reverse-time wave-field extrapolation, imaging, and inversion", *Geophysics*, 53(7): 920-931.

[44] Fink, M., 1992, "Time reversal of ultrasonic field-part 1: basic principles", *IEEE Transaction on Ultrasonics, Ferroelectrics and Frequency Control*, 39(5): 555-592.

[45] Fink, M., 1993, "Time reverse mirror", *Journal of Physics D: Applied Physics*, 26: 1333-1350.

[46] Fukunaga, H., Hu, N. and Chang, F.K., 2001, "Structural damage identification using piezoelectric sensors", *International Journal of Solids and Structures*, 39: 393-418.

[47] Fu, L., 1987, "Mechanics aspects of NDE by sound and ultrasound", *Applied Mechanics Reviews*, 35: 1047-1057.

[48] Gandhi, M.V. and Thompson, B.S., 1992, *Smart materials and structures*, Chapman Hall, London.

[49] Giurgiutiu, V. and Zagrai, A. N., 2002, "Embedded Self-Sensing Piezoelectric Active Sensors for Online Structural Identification", *ASME Journal of Vibration and Acoustics*, (124): 116-125.

[50] Giurgiutiu, V. Zagrai, A., and Bao, J., 2002a, "Embedded Active Sensors For In-Situ Structural Health Monitoring of Thin-Wall Structures", *ASME Journal of Pressure Vessel Technology*, 124: 134-145.

[51] Giurgiutiu, V., Zagrai, A. and Bao, J., 2002b, "Piezoelectric wafer embedded active sensors for aging aircraft structural health monitoring", *Structural Health Monitoring*, 1(1): 41-61.

[52] Giurgiutiu V., Bao J. and Zhao W., 2001, "Active Sensor Wave Propagation Health Monitoring of Beam and Plate Structures", *Proceedings of the 8th International SPIE Symposium on Smart Structures and Materials*, Newport Beach, CA.

[53] Giurgiutiu, V. and Zagrai, A., 2000, "Characterization of Piezoelectric Wafer Active Sensors", *Journal of Intelligent Material Systems and Structures*, 11(12): 959-976.

[54] Giurgiutiu, V. and Roger, C.A., 1996, "Modelling of the electro-mechanical (E/M) impedance response of a damaged composite beam", *Adaptive Structures and Materials Systems*, 87: 39-46.

[55] Gobin, P.F., Jayet, Y., Baboux, J.C., Salvia, M., Chateauminois, A., Abry, J.C. and Giraud, G., 2000, "New trends in non-destructive evaluation in relation to the smart materials concept", *International Journal of Systems Science*, 31(11): 1351-1359.

[56] Gorman, M.R. and Prosser, W.H., 1996, "Application of normal mode expansion to AE waves in finite plates", *ASME Journal of Applied Mechanics*, 63(2): 555-557.

[57] Guo, Z., Achenbach, J.D. and Krishnaswamy, S., 1997, "EMAT generation and laser detection of single Lamb modes", *Ultrasonics*, 35: 423-429.

[58] Ha, S.K., Kerlers, C., and Chang, F.K., 1992, "Finite Element Analysis of Composite Structures Containing Distributed Piezoelectric Sensors and Actuators", *AIAA Journal*, 30: 772-780.

[59] Han, J.H. and Lee, I., 1998, "Analysis of composite plates with piezoelectric actuators for vibration control using layerwise displacement theory", *Composites, Part B*, 29: 519-672.

174

[60] Hagood, N.W., Chung, W.H. and Von Flotow, A., 1990, "Modelling of piezo-electric actuator dynamics for active structural control", *Journal of Intelligent Materials Systems and Structures*, 1: 327-354.

[61] Hickman, G.A., Gerardi, J.J. and Feng, Y., 1991, "Application of smart structures to aircraft health monitoring", *Journal of Intelligent Materials Systems and Structures*, 2: 411-430.

[62] Hoummady, M., Campitelli, A. and Wlodarski, W., 1997, "Acoustic wave sensors: design, sensing mechanisms and applications", *Smart Materials and Structures*, 6: 647-657.

[63] Hsu, N.N., Simmons, J.A. and Hardy, S.C., 1997, "An approach to acoustic emission signal analysis-theory and experiment", *Material Evaluation*, 35: 100-106.

[64] Im, S. and Atluri, S.N., 1989, "Effects of a piezo-actuator on a finite deformation beam subjected to general loading", *AIAA Journal*, 27: 1801-1807.

[65] Kessler, S.S. and Spearing S.M., 2002a, "Damage detection in composite materials using Lamb wave methods", *Smart Materials and Structures*, 11(2): 269-278.

[66] Kessler, S.S. and Spearing, S.M., 2002b, "Damage detection in composite materials using frequency response methods ". *Composite Part B*, 33(1): 87-95.

[67] Keilers, C.H. and Change, F.K., 1995a, "Identification delamination in composite beams using built-in piezoelectrics: Part I-experimental and analysis", *Journal of Intelligent Materials Systems and Structures*, 6: 649-663.

[68] Keilers, C.H. and Change, F.K., 1995b, "Identification delamination in composite beams using built-in piezoelectrics: Part II-an identification method", *Journal of Intelligent Materials Systems and Structures*, 6: 664-679.

[69] Kino, G.S., Barnett, D.M., Grayeli, N., Herrmann, G., Hunter, J.B., Ilic, D.B., Johnson, G.C., King, R.B., Scott, M.P., Shyne, J.C. and Steele, C.R., 1980, "Acoustic measurements of stress fields and microstructure", *Journal of Nondestructive Evaluation*, 1(1): 67-77.

175

[70] Koh, Y.L., Chiu, W.K., Marshall, I.H., Rajic, N. and Galea, S.C., 2001, "Detection of disbonding in a repair patch by means of an array of lead zirconate titanate and polyvinylidene fluoride sensors and actuators", *Smart Materials and Structures*, 10: 946-962.

[71] Kromine A.K., Fomitchov, P.A., Krishnaswamy, S. and Achenbach, J.D., 2000, "Laser ultrasonic detection of surface breaking discontinuities: Scanning laser source technique", *Material Evaluation*, 58(2): 173-177.

[72] Kudva, J.N., Marabtidis, C., Gentry, J. and Blazic, E., 1993, "Smart structures concepts for aircraft structural health monitoring", *Proceedings of SPIE on Smart Structures and Intelligent Systems*, Albuquerque, New Mexico, 1917: 964-971.

[73] Kundu, T. and Maslov, K., 1997, "Material interface inspection by Lamb waves", *International Journal of Solids and Structures*, Albuquerque, 34(29): 3885-3901.

[74] Kuo, T. and Dai, T., 1984, "Kirchhoff elastic wave migration for the case of noncoincident source and receiver", *Geophysics*, 49: 1223-1238.

[75] Langenberg, K.J., Barmann, R., Marklein, R., Irmer, S., Muller, H., Brandfass, M. and Potzkai, B., 1999, "Inverse scattering with acoustic, electromagnetic, and elastic waves as applied in nondestructive evaluation", In *Wavefield Inversion (Wrigin, Ed.)*, Springer-Verlag, Vienna.

[76] Langenberg, K.J., Hannemann, R., Kaczorowski, T., Marklein, R., Koehler, B., Schurig, C. and Walte, F., 2000, "Application of modelling techniques for ultrasonic austenitic weld inspection", *NDT and E International*, 33(7): 465-480.

[77] Lee, C.K. and Moon, F.C., 1989, "Laminated Piezopolymer plates for torsion and bending sensors and actuators", *Journal of the Acoustic Society of America*, 85(6): 2432-2439.

[78] Lee, C.K. and Moon, F.C., 1991, "Modal sensors/actuators", *ASME Journal of Applied Mechanics*, 57: 434-441.

[79] Lee, C.K. and Osullivan, T.C., 1991, "Piezoelectric strain gages", *Journal of the Acoustic Society of America*, 90(2): 945-953.

[80] Lee, S.S. and Sun, S.W., 1994, "Variation formulation for Timoshenko beam element by separtation of deformation mode", *Commun. Num. Meth. Eng*, 10(8): 599-610.

[81] Lim, Y.H., Gopinathan, S.V., Varadan, V.V. and Varadan, V. K., 1999, "Finite element simulation of smart structures using an optimal output feedback controller for vibration and noise control", *Smart Materials and Structures*, 8: 324-337.

[82] Lin, M.W. and Rogers, C.A., 1993a, "Modelling of the actuation mechanism in a beam structure with induced strain actuators", *Proceedings of AIAA/ASCE/ASME/ASC 34th Structures, Structural Dynamics and Materials Conference*, AIAA Inc., Washington, DC, Part VI, 3608-3617, La Jolla, CA. 19-22 April.

[83] Lin, M.W. and Rogers, C.A., 1993b, "Actuation response of a beam structure with induced strain actuators", *Adaptive Structures and Material Systems*, AD 35: 129-139.

[84] Lin, X. and Yuan, F.G., 2000, "Pre-stack reverse time migration in structural health monitoring", *41st AIAA/ASME/ASCE/AHS/ASc Structures, Structural Dynamics and Materials Conference and Exhibit*, Atlanta, 1984-1994.

[85] Lin, X. and Yuan, F.G., 2001a, "Detection of multiple damages by prestack reverse time migration". *AIAA Journal*, 39 (11): 2206-2215.

[86] Lin, X. and Yuan, F.G., 2001b, "Damage detection of a plate using migration techniques". *Journal of Intelligent Materials Systems and Structures*, 12(7): 469-482.

[87] Liu, P.L., Tsai, C.D. and Wu, T.T., 1997, "Imaging of surface breaking concrete cracks using transient elastic waves", *NDT and E International*, 5: 323-331.

177

[88] Lorenz, M., Wal, L.F. and Berkout, A.J., 1991, "Ultrasonic imaging multi-saft; nondestructive characterization of defects in steel components", *Nondestructive Testing and Evaluation*, 6: 149-161.

[89] Ludwig, R. and Lord, W., 1988, "Finite element study of ultrasonic wave propagation and scattering in an aluminum block", *Materials Evaluation*, 46: 108-113.

[90] Maalej, M., Karasaridis, A., Pantazopoulou, S. and Hatzinakos, D., 2002, "Structural health monitoring of smart structures", *Smart Materials and Structures*, 11(4): 581-589.

[91] Mal, A., 2001, "NDE for health monitoring of aircraft and aerospace structures", *7th ASME NDE Topical Conference*, 20: 149-155.

[92] Mall, S., 2002, "Integrity of graphite/epoxy laminate embedded with piezoelectric sensor/actuator under monotonic and fatigue loads", *Smart Materials and Structures*, 11: 527-533.

[93] Mast, M.D., 2001, "Quantitative flaw reconstruction from ultrasonic surface wavefields measured by electronic speckle pattern interferometry", *IEEE Transactions on Ultrasonics Ferroelectrics Ferroeletrics and Frequency Control*, 48(2): 432-444.

[94] Meguid S.A. and Wang X.D., 1995, "On the dynamic interaction between a microdefect and a main crack", *Proc. R. Soc. London, Series A*, 448: 449-464.

[95] Miller, D., Oristaglio, M. and Beylkin, G., 1987, "A new slant on seismic imaging: migration and integral geometry", *Geophysics*, 52(7): 943-964.

[96] Mitchell, J.A. and Reddy, J.N., 1995, "A study of embedded piezoelectric layers in composite cylinders", *ASME Journal of Applied Mechanics*, 62: 166-173.

[97] Moetakef, M.A., Joshi, S.P. and Lawrence, K.L., 1996, "Elastic wave generation by piezoceramic patches", *AIAA Journal*, 34(10): 2110-2117.

[98] Monkhouse, R.S.C., Wilcox, P.W. and Cawley, P., 1997, "Flexible interdigital PVDF transducers for the generation of Lamb waves in structures", *Ultrasonics*, 35: 489-498.

178

[99] Moulin, E., Assaad, J., Delebarre, C. and Osmont, D., 1999, "Lamb waves generation using a transverse embedded in a composite plate", *Proceedings of the 12th International Conference on Composite Materials*, Paris.

[100] Muskhelishvili, N.I., 1953, Some Basic Problems of the Mathematical Theory of Elasticity, Noordhoff, Groningen.

[101] Nam K., 1999, "Acoustic emission from surface fatigue cracks in SS41 steel", *Fatigue and Fracture of Engineering Materials and Structures*, 22(12): 1103-1109.

[102] Okafor, A.C., Chandrashekhara, K. and Jiang, Y.P., 1996, "Delamination prediction in composite beam with built-in piezoelectric devices using modal analysis and neural network", *Smart Materials and Structures*, 5: 338-347.

[103] Park S.B. and Sun C.T., 1994. "Crack Extension in Piezoelectric Materials", *SPIE*. 2189: 357-368.

[104] Park, G.P., Cudney, H.H. and Inman, D.J., 2000, "An integrated health monitoring technique using structural impendance sensors", *Journal of Intelligent Materials Systems and Structures*, 11: 448-455.

[105] Pao, Y.H., 1983, "Elastic wave in solids", *ASME Journal of Applied Mechanics*, 50(4B): 1152-1164.

[106] Pao, Y.H., 1976, "Huygens' principle, radiation conditions, and integral formulas for the scattering of elastic waves", *Journal of the Acoustic Society of America*, 59(6): 1361-1371.

[107] Pearson, S.R., Owen, J.S. and Choo, B.S., 2001, "The use of vibration signatures to detect flexural cracking in reinforced concrete bridge decks", *Proceedings of the 4th International Conference on Damage Assessment of Structures (DAMAS 2001)*, Cardiff, Wales, UK, June 25th-28th.

[108] Qui, J. and Tani. J., 1995, "Vibration Control of a Cylindrical Shell Using Distributed Piezoelectric Sensors and Actuators", *Journal of Intelligent Material Systems and Structures*, 6(4): 474-481.

179

[109] Reddy, J.N., 1997, "Mechanics of Laminated Composite Plates", Theory and Analysis, CRC Press, Boca Raton, FL.

[110] Reddy, J.N., 1999, "On laminated composite plates with integrated sensors and actuators", *Engineering Structures*, 21:568-593.

[111] Richard, J.S. and Cudney, H.H., 1993, "Modelling Multiple Layer Piezoelectric Actuators in Active Structural Control", *Proceedings of SPIE*, 1916: 231-243.

[112] Ryu, D.H. and Wang, K.W., 2002, "Characterization of surface bonded piezo-electric actuators on curved beams", *Smart Materials and Structures*, 11: 377-388.

[113] Samuel, P. and Pines. D., 1997, "Health Monitoring/Damage Detection of a Rotorcraft Planetary Geartrain Using Piezoelectric Sensors", *Proceedings of SPIEs 4th Annual Symposium on Smart Structures and Materials*, San Diego, CA, 3041:44-53.

[114] Schulz, M.J., Pai, P.F. and Inman, D.J., 1999, "Health monitoring and active control of composite structures using piezoelectric patches", *Composite Part B*, 30: 54-72.

[115] Sirohi, J. and Chopra, I., 2000, "Fundamental Understanding of Piezoelectric Strain Sensors", *Journal of Intelligent Materials Systems and Structures*, 11: 246-257.

[116] Sohn, J.I., Lee, S., Song, Y.H., Choi, S.Y., Cho, K.I. and Nam, K.S., 2001, "Patterned selective growth of carbon nanotubes and large field emission from vertically well-aligned carbon nanotube field emitter arrays", *Applied Physics Letters*, 78(7): 901-903.

[117] Sun, R. and Mcmechan G.A., 1986, "Pre-stack reverse time migration for elastic waves with application to synthetic offset vertical seismic profiles", *Proceedings of The IEEE*, 74: 457-465.

[118] Takadoya, M., Notake, M., Kitahara, M., Achenbac, J.D., Guo, Q.C. and Peterson, M.L., 1992, "Neural network approach to the inverse problem of crack depth determination from ultrasonic backscattering data", *IUTAM Symposium on Inverse Problems in Engineering Mechanics*, Tokyo, 413-422.

[119] Tan, K.S., Guo, N., Wong, B.S. and Tui, C.G., 1995, "Experimental evaluation of delamination in composite plates by the use of Lamb waves", *Composites Science and Technology*, 53: 77-84.

[120] Tauchert, T.R., 1992, "Piezothermoelastic behaviour of a laminated plate", *Journal of Thermal Stresses*, 15: 25-37.

[121] Thomas, G., 1995, "Overview of nondestructive evaluation technologies", *Proceedings of SPIE on Nondestructive of Aging Aircraft, Airports Aerospace hardware, and Materials*, Oakland, Californis, 2455: 5-9.

[122] Tracy, M., Roh, Y.S. and Chang, F.K., 1996, "Impact damage diagnosis for composite structures using built-in actuators and sensors", *Proceedings of SPIE on Smart Structures and Materials*, Lyon, France, 2779: 118-123.

[123] Tracy, M. and Chang, F.K., 1998, "Identifying impacts in composite plates with piezoelectric strain sensors, Part I: theory", *Journal of Intelligent Materials Systems and Structures*, 9(11): 920-928.

[124] Tzou, H.S. and Gadre, M., 1989, "Theoretical-Analysis Of A Multi-Layered Thin Shell Coupled With Piezoelectric Shell Actuators For Distributed Vibration Controls", *Journal Of Sound And Vibration*, 132(3): 433-450.

[125] Tzou, H.S. and Tseng, C.I., 1991, "Distributed vibration control and identification of coupled elastic/piezoelectric systems", *Mechanical Systems and Signal Processing*, 5: 215-231.

[126] Tzou, H.S. and Zhong, J.P., 1993, "Electromechanics And Vibrations Of Piezoelectric Shell Distributed Systems", *Journal Of Dynamic Systems Measurement And Control*, 115(3): 506-517.

[127] Tzou, H.S. and Ye, R., 1994, "Piezothermoelasticity and precision control of piezoelectric systems: theory and finite element analysis", *Journal of Vibration and Acoustics*, 116:489-495.

[128] Varadan, V.K., Wu, Z., Bao, X.Q. and Varadan, V.V., 1993, "Light weight robot using piezoelectric motor, sensor and actuator", *Adaptive Structures and Material Systems*, 35: 141-148.

[129] Varadan, V.V., Kim, J. and Varadan, V.K., 1997, "Modelling of piezoelectric sensor fidelity", *IEEE Transactions on Ultrasonics, Ferroelectrics, and Frequency Control*, 44(3): 538-547.

[130] Veidt, M., Liu, T. and Kitipornchai, S., 2001, "Analysis of piezoelectric sensor to detect flexural waves", *Journal of Guidance, Control and Dynamics*, 24(5): 960-966.

[131] Wang, B.T., 1996, "Characterization of transfer functions for piezoceramic and conventional transducers", *Journal Of Intelligent Material Systems and Structures*, 7(4): 390-398.

[132] Wang, B.T. and Rogers, C.A., 1991, "Laminate plate theory for spatially distributed induced strain actuators", *Journal of Composite Materials*, 25:433-452.

[133] Wang, B.T. and Chen, R.L., 2000, "The use of piezoceramic transducers for smart structural testing", *Journal of Intelligent Materials Systems and Structures*, 11: 713-723.

[134] Wang, D.H. and Huang, S.L., 2000, " Health monitoring and diagnosis for flexible structures with PVDF piezoelectric film sensor array", *Journal of Intelligent Materials Systems and Structures*, 11: 482-491.

[135] Wang, Q. and Quek, S.T., 2002, "A model for the analysis of beams with embedded piezoelectric layers", *Journal of Intelligent Materials Systems and Structures*, 11: 61-70.

[136] Wang, X.D., 2000, "Coupled electromechanical behaviour of piezoelectric actuators in smart structures". *Journal of Intelligent Material Systems and Structures*, 10: 232-241.

[137] Wang X.D. and Meguid S.A., 1997, "Diffraction of SH-wave by interacting matrix crack and an inhomogeneity", *ASME Journal of Applied Mechanics*, 64: 568-575.

[138] Wang, X.D. and Meguid, S.A., 2000, "On the electroelastic behaviour of a thin piezoelectric actuator attached to an infinite host structure", *International Journal of Solids and Structures*, 37:3231-3251.

[139] Wang X.D. and Huang G.L., 2003a, "Identification of embedded cracks using reverse elastic waves", 19th Canadian Congress of Applied Mechanics, CANCAM 2003.

[140] Wang X.D. and Huang G.L., 2003b, "On the elastic wave propagation induced by a network of piezoelectric actuators", *Acta Mechanica*, 160: 1-18.

[141] Wang X.D. and Huang G.L., 2002a, "Wave propagation induced by multiple piezoelectric actuators in electromechanical structures", *ASME Journal of Pressure Vessel Technology*, 124: 311-318.

[142] Wang X.D. and Huang G.L., 2002b, "Ultrasonic imaging of structural damages using integrated sensor signals", Proceedings of the 14th US National Congress of Theoretical and Applied Mechanics (USNCTAM14), Blacksburg, VA, June 23-28.

[143] Wang X.D. and Huang G.L., 2001a, "Wave propagation in electromechanical structures: induced by surface-bonded piezoelectric actuators", *Journal of Intelligent Material Systems and Structures*, 12: 105-115.

[144] Wang X.D. and Huang G.L., 2001b, "Wave propagation in electromechanical structures: induced by embedded piezoelectric actuators", *Journal of Intelligent Material Systems and Structures*, 12: 117-125.

[145] Wang X.D. and Huang G.L., 2001c, "Modelling and analysis of piezoelectric actuators in anisotropic structures", *Acta Mechanica*, 155: 45-63.

[146] Wang X.D. and Huang G.L., 2001d, "The electromechanical behaviour of a piezoelectric actuator bonded to an anisotropic elastic medium", *Internation Journal of Solids and Structures*, 38: 4721-4740.

[147] Wang X.D. and Huang G.L., 2001e, "Wave propagation induced by multiple piezoelectric actuators in electromechanical structures", *The 7th NDE Topical Conference, ASME*, San Antonio, Texas, April 23-25.

[148] Wang X.D. and Huang G.L., 2001f, "Elastic wave propagation induced by piezo-electric actuators for health monitoring of structures", *The Thirteenth International Conference on Composite Materials*, Beijing, China, June 25-29.

[149] Wang X.D. (Keynote lecture) and Huang G.L., 2000, "Electromechanical behaviour of anisotropic elastic media with surface bonded piezoelectric actuators", *The Third International Conference on Mechanics and Materials in Design*, May 29-31, Orlando, Florida.

[150] Wang, X.M. and Shen, Y.P., 2001, "On the characterization of piezoelectric actuators attached to structures", *Smart Materials and Structures*, 7: 389-395.

[151] Wapenaar, C.P.A. and Haime, G.C., 1990, "Elastic extrapolation of primary seismic P and S waves", *Geophysical Prospecting*, 38: 23-60.

[152] White, W., Valliappan, S. and Lee, I.K., 1977, "Unified boundary for finite dynamic models", *Journal of the Engineering Mechanics Division, ASCE.*, 103: 949-963.

[153] Wiggins, J.W., 1984, "Kirchhoff integral extrapolation and migration of non-planar data", *Geophysics*, 49(8): 1239-1248.

[154] Wu, T., 1999, "Elastic wave propagation and nondestructive evaluation of materials", *Proc. Natl. Sci. Counc. Roc(A)*, 23(6): 703-714.

[155] Wu, T. and Gong, J., 1993, "Application of transient elastic waves to the non-destructive evaluation of plate structure with cavity or inclusion", *Journal of the Acoustic Society of America*, 90(3): 1453-1460.

[156] Yang, S. and Ngol, B., 1999, "General sensor equation and actuator equation for the theory of laminated piezoelectric plates", *Smart Materials and Structures*, 8: 411-415.

[157] Zhu, J.M. and Lines L.R., 1998, "Comparison of kirchhoff and reverse-time migration methods with applications to prestack depth imaging of complex structures", *Geophysics*, 63(4): 1166-1176.